

Nano-Impact Voltammetry

A thesis submitted for the degree of Doctor of Philosophy
in Physical and Theoretical Chemistry

Thomas R. Bartlett

St. John's College

2017

Abstract

This thesis introduces new concepts to the study of nanoparticles by nano-impact voltammetry. Utilising the special chemistries of metal halide and metal oxide nanoparticles, the use of the nano-impact technique is expanded beyond quantitative sizing towards the study of the in-situ synthesis and detection of nanoparticles, reversible agglomeration behaviour and the fabrication of nanoelectrode arrays. Nano-impact voltammetry is also demonstrated to be an informative tool for the tracking of chemical and photochemical conversion reactions of metal halide nanoparticles and for the mechanistic determination of metallic nanoparticle growth during synthesis. The use of forced convection to gain improvements in the detection limit achievable for the *direct*-impact of metallic nanoparticles is also reported.

Initially, the work reported herein looks at the *direct-impact* voltammetry of previously unstudied nanomaterials; mercury(I) chloride, silver bromide and bismuth oxide. The first sizing of metal halide nanoparticles is reported as well as a method for synthesising particles through the electrolytic induced implosion of a nanoscale metal halide layer on a liquid electrode. The "upper-limit" of the nano-impact technique is also quantified through the use of silver bromide and silver nanoparticles with diameters approaching 100 nm successfully studied.

Next, bismuth oxide nanoparticles are studied by the nano-impact method to probe the reversible agglomeration of particles. By reducing impacting bismuth oxide nanoparticles at the electrode, bismuth deposits are shown to result and can be imaged by scanning electron microscopy. Through the analysis of these deposits, in combination with nanoparticle tracking analysis, experimental evidence for the voltammetrically induced de-agglomeration of nanoparticles is proposed.

In the subsequent chapter, nano-impact voltammetry is employed in the study of photochemical reactions. First, the photochemical reduction of silver bromide nanoparticles to

silver nanoparticles is followed both by ultra-violet visible spectroscopy and nano-impacts, allowing mechanistic determination of the conversion process. Second, the nano-impact technique is used in combination with ultra-violet visible spectroscopy and transmission electron microscopy for the mechanistic determination of the photochemical Ostwald ripening of silver nanoprisms from silver nanoseeds.

Finally, the inter-play between nano-impacts and electrode arrays is reported. Through the electrolysis of impacting silver bromide nanoparticles, it is shown that a functional silver nanoelectrode array can be formed. The formed nanoelectrode array is characterised by the electrocatalytic reduction of hydrogen peroxide. The lowest reported detection limit for silver nanoparticles is also reported, through the combination of a random array of microelectrodes and a specially developed, custom built, and characterised wall-jet flow cell.

Acknowledgements

The story of my DPhil began 5 years ago at Infineum, Oxfordshire. A quirk of fate brought Mike Hollas to my desk whilst I was looking up DPhil opportunities. He looked over my shoulder and said “if you’re looking at doing electrochemistry you should check out Richard Compton’s group”. It’s a funny thing how random acts can have long lasting effects. If it weren’t for that brief conversation all those years ago, I might never have found my way to the Compton group. For that, Mike Hollas deserves special thanks as the initiator of what was to come.

Predominantly I owe my thanks to Prof. Richard Compton for giving me the opportunity to work and learn in the group for the past three years. It’s not been the easiest road. I’ve learnt the hard way that research has its ups and downs. However, you guided me through these times with a steady hand and I have now reached a place where I can be proud of my achievements. To all the Compton group members, past and present, I thank you. You made the lab an inviting place to work. I spent many good evenings in various pubs around the city at group drinks and ate vast amounts of cake at birthdays. In particular I would like to thank Patty, Her Shuang and Eddy, who guided me through my first year. There was a lot of electrochemistry to learn and without your help I don’t know how I would have made it through. I would also like to thank Stan who, alongside an unfathomable amount of coffee, got me through my final year as a DPhil student. The Anglo-Russian dream team achieved great things.

Lastly I would like to thank my dear wife Aimie. Whilst I have had many helpers at work to get me through the tough times, she was the one who was always there when I left at the end of the day. Without her I would never have made it as far as I have.

Publication List

The publications which contributed to this thesis are listed in order of appearance.

Metal-Halide Nanoparticle Formation: Electrolytic and Chemical Synthesis of Mercury(I) Chloride Nanoparticles, T. R. Bartlett, C. Batchelor-McAuley, K. Tschulik., K. Jurkschat, R. G. Compton, *ChemElectroChem,* **2015**, *2*, 522-528.

Electrochemical Nanoparticle Sizing Via Nano-Impacts: How Large a Nanoparticle Can Be Measured? T. R. Bartlett, S. V. Sokolov, R. G. Compton, *ChemistryOpen,* **2015**, *140*, 600-605.

Bi_2O_3 Nanoparticle Clusters: *Reversible* Agglomeration Revealed by Imaging and Nano-Impact Experiments, T. R. Bartlett, S. V. Sokolov, J. Holter, N. P. Young, R. G. Compton, *Chem. - Eur. J.*, **2016**, *22*, 7408-7414.

Nanoparticle Photochemistry via Nano-Impacts, T. R. Bartlett, S. V. Sokolov, R. G. Compton, *Russ. J. Electrochem,* **2016**, *52(12)*, 1131-1136.

Tracking of Photochemical Ostwald Ripening of Nanoparticles Through Voltammetric Atom Counting, T. R. Bartlett, S. V. Sokolov, B. J. Plowman. N. P. Young, R. G. Compton, *Nanoscale*, **2016**, *8*, 16177-16181.

Nanoelectrode Array Formation by Electrolytic Nanoparticle Impacts, T. R. Bartlett, J. Holter, N. P. Young, R. G. Compton *Nanoscale*, **2016**, *8*, 13908-13914.

Femtomolar Detection of Silver Nanoparticles by Flow-Enhanced Direct-Impact Voltammetry at a Microelectrode Array, S. V. Sokolov†, T. R. Bartlett†, P. Fair, S. Fletcher, R. G. Compton, *Anal. Chem.,* **2016**, *88(17),* 8908-8912.

Glossary

Roman Symbols

Symbol	Definition	Units
a	Diameter of a jet nozzle	m
A	Electrode area	m^2
A_{abs}	Absorbance	
A_r	Relative atomic mass	
c	Speed of light in a vacuum ($\sim 2.99 \times 10^8$)	$m\ s^{-1}$
c^*	Bulk concentration of a species	$mol\ dm^{-3}$
d	Edge length of a prism	m
D	Diffusion coefficient	$m^2\ s^{-1}$
D_∞	Hypothetical diffusion coefficient at infinite temperature	$m^2\ s^{-1}$
E	Potential difference (two electrode system)	V
E_a	Activation energy for diffusion	$J\ mol^{-1}$
E_f^0	Formal potential	V
$E_{p,a}$	Anodic peak potential	V
$E_{p,c}$	Cathodic peak potential	V
eV	Kinetic energy of an electron (1 keV)	eV
F	Faraday constant (~96485)	$C\ mol^{-1}$
G	Gibbs energy	$J\ mol^{-1}$
h	Planck constant	$m^2\ kg\ s^{-1}$
h_p	Thickness of prism	m
I	Current	A
I_{lim}	Limiting current	A
I_p	Peak current	A
I_{step}	Increase in current during a step	A
J	Flux	$mol\ m^{-2}\ s^{-1}$
J_a	Anodic flux	$mol\ m^{-2}\ s^{-1}$
J_c	Cathodic flux	$mol\ m^{-2}\ s^{-1}$
J_{conv}	Convectional flux	$mol\ m^{-2}\ s^{-1}$
k_a	Anodic rate constant	$m\ s^{-1}$
k_B	Boltzmann constant	$J\ K^{-1}\ molecule^{-1}$
k_c	Cathodic rate constant	$m\ s^{-1}$

k^0	Standard electrochemical rate constant	m s^{-1}
l	Layer thickness	m
L	Path length	m
M	Moles per particle	mol $particle^{-1}$
m_e	Mass of an electron	kg
M_p	Moles per prismatic particle	mol $particle^{-1}$
M_s	Moles per spherical particle	mol $particle^{-1}$
m_T	Mass transport coefficient	mol m^{-2} s^{-1}
M_w	Molecular mass	g mol^{-1}
n	Number of electrons transferred per molecule	
N_A	Avogadro constant (6.022×10^{23})	mol^{-1}
n_m	Number of moles of the species	mol
N_{molec}	Number of molecules	
n'	Sum of the electrons transferred before the rate determining electron transfer	
q	Scattering vector	
Q	Charge	C
R	Gas constant (~8.314)	J mol^{-1} K^{-1}
r_e	Electrode radius	m
R_e	Reynolds number	
r_h	Spherical hydrodynamic radius	m
r_{np}	Radius of a nanoparticle	m
t	Time	s
T	Temperature	K
$U_{e,}$	Electrophoretic mobility	m^2 s^{-1} V^{-1}
V	Local fluid velocity	m^3 s^{-1}
V_f	Volumetric flow rate	m^3 s^{-1}
V_p	Volume of particle	m^3
x	Cartesian co-ordinate	m
$\sqrt{\langle x^2 \rangle}$	Root mean square displacement (1D)	m
y	Cartesian co-ordinate	m
z	Cartesian co-ordinate	m
Z	Electrical charge of a species	C

Greek Symbols

Symbol	Definition	Units
α	Cathodic transfer coefficient	
$\boldsymbol{a'_{n+1}}$	Transfer coefficient of the rate determining electron transfer	
$\boldsymbol{\alpha_j}$	Activity of species *j*	
β	Anodic transfer coefficient	
γ	Activity coefficient	
δ	Nernst diffusion layer thickness	m
δ_H	Hydrodynamic layer thickness	m
ε	Dielectric constant	
ε_0	Vacuum permittivity	
ζ	Zeta potential	
η	Viscosity of a medium	kg m^{-1} s^{-1}
θ_{dls}	Scattering angle	o
κ^{-1}	Debye length	m
κa	Ratio of the Debye length and the NP radius	
$f(\kappa a)$	Henry function	
μ_j	Chemical potential	
μ_j^0	Standard chemical potential	
$\bar{\mu}_j$	Electrochemical potential	
λ	Wavelength of the incident light	m
λ_{max}	Absorption maximum	m
λ_e	Wavelength of an electron	m
Λ,	Matsuda and Ayabe parameter	V s^{-1}
ν	Scan rate	V s^{-1}
ρ	Density	kg m^{-3}
τ	Time delay between two consecutive signals	s
υ	Kinematic viscosity	kg m^{-1} s^{-1}
ϕ	Potential of the phase in which a species is present	V
$\Delta\phi$	Potential difference (single electrode)	V
ϕ_M	Electrical potential of the electrode	V
ϕ_S	Electrical potential of the solution	V
ψ_{salt}	Ionic strength of the solvent	mol kg^{-1}
ω	Rotation speed	rpm

Other Symbols

Symbol	Definition	Units
$c(q,\tau)$	Correlation function	
$[I(q)]$	Average scattered light intensity	
$I(q,t)$	Scattered light intensity at time, t	
I	Transmitted light intensity	
I_0	Incident light intensity	
n	Refractive index of the solvent	
$[\ ]^0$	Standard concentration (1 mol dm^{-3})	mol dm^{-3}

Abbreviations

Abbreviation	Meaning
Au@Ag	Silver shell – gold core nanoparticle
CE	Counter electrode
CF	Carbon fibre
CL	Cathodoluminescence
CV	Cyclic voltammetry
CVD	Chemical vapour deposition
C_{60}	Buckminsterfullerence
DLS	Dynamic light scattering
EBIC	Electron beam induced current
EDX	Energy dispersive X-ray spectroscopy
EELS	Electron emission loss spectroscopy
GC	Glassy carbon
IHP	Inner-Helmholtz Plane
IUPAC	International Union of Pure and Applied Chemistry
LSPR	Localised surface plasmon resonance
LSW	Linear sweep voltammetry
MX	Metal halide
NEA	Nanoelectrode array

NEE	Nanoelectrode ensemble
NP	Nanoparticle
NTA	Nanoparticle tracking analysis
NTP	1,4-nitrothiophenol
OHP	Outer-Helmholtz Plane
PEEK	Polyether ether ketone
PVK	Poly(N-vinylcarbazole)
RAM	Random electrode array
RDE	Rotating disk electrode
REF	Reference electrode
SCE	Saturated mercury-mercury chloride electrode
SEM	Scanning electron microscopy
SERS	Surface enhanced raman spectroscopy
SHE	Standard hydrogen electrode
TEM	Transmission electron microscopy
UV-Vis	Ultraviolet-visible spectroscopy
WE	Working electrode

Contents

1 An Introduction to Electrochemistry 1

1.1 The Nernst Equation 1

1.2 The Double Layer 4

1.3 Electrode Kinetics 6

1.4 The Electrochemical Cell 8

1.5 Mass Transport 10

1.5.1 Diffusion 10

1.5.2 Migration 12

1.5.3 Convection 12

1.6 Electrochemical Methods 13

1.6.1 Chronoamperometry. 13

1.6.2 Linear Sweep Voltammetry, Cyclic Voltammetry and Tafel Analysis . . 15

1.7 Electrodes: From the Macroscale to the Nanoscale 22

1.8 Electrode Arrays 24

1.8.1 Microelectrode Arrays 25

1.8.2 Nanoelectrode Arrays 27

1.9 Electrodes Under Flow: Rotating Disk and Wall-Jet Electrodes 29

2 Nanoparticles and Characterisation Techniques 33

2.1 An Introduction to Nanoparticles 33

2.2 Characterisation and Detection Methods 34

2.2.1 Dynamic Light Scattering and Nanoparticle Tracking Analysis 34

2.2.2 Ultraviolet-Visible Spectroscopy 39

2.2.3 Zeta Potential 41

2.2.4 Electron Microscopy 43
2.2.5 Stripping and Dissolution Voltammetry 46
2.2.6 Nano-Impact Voltammetry 48
3 Experimental Methods 53
3.1 Chemicals 53
3.2 Electrochemical Instrumentation 55
3.3 Non-Electrochemical Methods 57
3.3.1 Ultraviolet-Visible Spectroscopy 57
3.3.2 Scanning Electron Microscopy 57
3.3.3 Transmission Electron Microscopy 57
3.3.4 Nanoparticle Tracking Analysis 58
3.4 Nanoparticle Synthesis 58
3.4.1 Mercury(I) Chloride Nanoparticles 58
3.4.2 Silver Bromide Nanoparticles 58
3.4.3 Silver Nanoprisms 59
4 Nano-Impact Voltammetry of Metal Halide Nanoparticles 60
4.1 Metal-halide Nanoparticle Formation: Electrolytic and Chemical Synthesis of Mercury(I) Chloride Nanoparticles 61
4.1.1 Introduction 61
4.1.2 Experimental 63
4.1.3 Results and Discussion 65
4.1.4 Conclusions 75
4.2 Electrochemical Nanoparticle Sizing Via Nano-Impacts: How Large a Nanoparticle Can be Measured? 78

4.2.1 Introduction 78
4.2.2 Experimental 79
4.2.3 Results and Discussion 79
4.2.4 Conclusions 88
5 Nano-Impact Voltammetry of Metal Oxide Nanoparticles 89
5.1 Bi_2O_3 Nanoparticle Clusters: *Reversible* Agglomeration Revealed by Imaging and Nano-Impact Experiments 89
5.1.1 Introduction 89
5.1.2 Experimental 91
5.1.3 Results and Discussion 92
5.1.4 Conclusions 102
6 Nano-Impact Photochemistry 103
6.1 Nanoparticle Photochemistry via Nano-Impacts 103
6.1.1 Introduction 103
6.1.2 Experimental 106
6.1.3 Results and Discussion 107
6.1.4 Conclusions 114
6.2 In-situ Tracking of Photochemical Ostwald Ripening Through Voltammetric Atom Counting 114
6.2.1 Introduction 114
6.2.2 Experimental 116
6.2.3 Results and Discussion 117
6.2.4 Conclusions. 126

7 Nano-Impact Voltammetry and Electrode Arrays 127

7.1 Nanoelectrode Array Formation by Electrolytic Nanoparticle Impacts . . . 127

7.1.1 Introduction 127

7.1.2 Experimental 129

7.1.3 Results and Discussion 130

7.1.4 Conclusions 140

7.2 Femtomolar Detection of Silver Nanoparticles by Flow-Enhanced Direct-Impact Voltammetry at a Microelectrode Array 140

7.2.1 Introduction 140

7.2.2 Experimental 143

7.2.3 Results and Discussion 149

7.2.4 Conclusions 154

8 Conclusions and Future Work 155

9 Bibliography 157

Chapter 1

An Introduction to Electrochemistry

In this chapter the electrochemical concepts necessary for the understanding and appreciation of the work undertaken in this thesis are covered. For more detailed and comprehensive explanations on electrochemistry please refer to the textbooks *Understanding Voltammetry*[1] and *Electrochemical Methods: Fundamentals and Applications*[2], which provide an excellent introduction to electrochemical fundamentals and techniques.

1.1 The Nernst Equation

Consider the general case of a reactant, *A*, in dynamic equilibrium with a product, *B*, through the transfer of an electron, e^-, at an electrode:

$$A + e^- \rightleftarrows B\,. \tag{1.10}$$

Species *A* is said to be reduced to *B* by the transfer of this electron. When an electrode is immersed into a solution of *A* and *B* the number of electrons transferred between the two species is insignificantly small and no measurable change in concentration of either species can be observed. It is the transfer of this charged species, e^-, that differentiates electrochemical equilibria to those of chemical equilibria. In electrochemical experiments the transfer of the electron occurs at an electrode leading to a charge difference between the electrode and solution. This difference in charge establishes a difference in potential and the electrochemical equilibrium responsible for creating the potential difference is known as a potential determining equilibrium. The potential difference and hence the position of the equilibrium is determined through a combination of both the chemical potential, μ_j, and electrical energies of the involved species. The chemical potential of a species *j* is given by:

$$\mu_j = \left(\frac{\partial G}{\partial n_{m,j}}\right)_{T, n_{m,i} \neq n_{m,j}}, \quad (1.11)$$

where G is the Gibbs energy, $n_{m,j}$ is the number of moles of the species and T is the temperature. For ideal solution species the chemical potential can be expressed as:

$$\mu_j = \mu_j^0 + RTln\frac{[j]}{[\ ]^0}, \quad (1.12)$$

where μ_j^0 is the standard chemical potential of *j*, R is the gas constant (8.314 J mol^{-1} K^{-1}), $[j]$ is the concentration of *j* and $[\ ]^0$ is the standard concentration. For pure solids or liquids:

$$\mu_j \cong \mu_j^0 . \quad (1.13)$$

The combination of both μ_j and the electrical energy can be expressed as the electrochemical potential, $\bar{\mu}_j$:

$$\bar{\mu}_j = \mu_j + Z_j F\phi , \quad (1.14)$$

where Z_j is the charge of species *j*, F is the Faraday constant and ϕ the potential of the phase in which species *j* is present. The electrochemical equilibrium expressed in equation 1.10 can be expressed in terms of the equality of the electrochemical potentials of reactants and products:

$$\bar{\mu}_A + \bar{\mu}_{e^-} \rightleftharpoons \bar{\mu}_B . \quad (1.15)$$

By combining equations 1.12 to 1.15 it is possible to derive the Nernst equation for a single electrode-solution interface:

$$\Delta\phi = \phi_M - \phi_S = \frac{\Delta\bar{\mu}^0}{F} + \frac{RT}{F}\ln\left(\frac{[A]}{[B]}\right), \quad (1.16)$$

where $\Delta\phi$ is the potential difference, ϕ_M and ϕ_S are the electrical potential of the electrode and solution respectively, R is the gas constant, *[A]* and *[B]* are the concentrations of the species involved in the equilibrium and:

$$\Delta\bar{\mu}^0 = \bar{\mu}_B^0 - \bar{\mu}_A^0 - \bar{\mu}_{e^-}^0 , \quad (1.17)$$

where the electrochemical potentials are now expressed as standard electrochemical potentials.

The Nernst equation described above is for a single electrode system. To be able to measure this potential difference in actuality, a second electrode is required, at least. The original electrode is often referred to as the working electrode (WE) and the second electrode, the reference electrode (REF). Further, Equation 1.16 assumes the species in equilibrium are ideal, which is not the case for most electrochemical experiments. It is therefore necessary to refine the definition of the potential difference measured between a WE and a REF to include contributions from the activity coefficients of the components, γ, to achieve the more experimentally applicable standard formal potential, E_f^0. If we consider the equilibrium:

$$\upsilon_A A + \upsilon_B B + \cdots e^- \rightleftarrows \upsilon_X X + \upsilon_Y Y + \cdots, \tag{1.18}$$

where υ_A etc. are stoichiometric coefficients, the equation for the potential difference inclusive of the activity coefficients of the species becomes:

$$E = E^0(A, B, \ldots/X, Y, \ldots) + \frac{RT}{F}\ln\left(\frac{\gamma_A^{\upsilon_A}\gamma_B^{\upsilon_B}\ldots[A]^{\upsilon_A}[B]^{\upsilon_B}}{\gamma_X^{\upsilon_X}\gamma_Y^{\upsilon_Y}\ldots[X]^{\upsilon_X}[Y]^{\upsilon_Y}}\right), \tag{1.19}$$

where E is now the potential difference, E^0 is the standard electrochemical potential and the activity $\alpha_j = \gamma_j[j]$. Experimentally, information on the activity coefficients of each species is not always available. It is therefore necessary to combine these activities within a new term, the formal potential, E_f^0, to achieve the experimentally applicable Nernst equation:

$$E = E_f^0(A/B) + \frac{RT}{F}\ln\left(\frac{[A][B\}}{[X][Y]}\right), \tag{1.20}$$

where,

$$E_f^0(A, B, \ldots/X, Y, \ldots) = E^0(A, B, \ldots/X, Y, \ldots) + \frac{RT}{F}\ln\left(\frac{\gamma_A^{\upsilon_A}\gamma_B^{\upsilon_B}\ldots}{\gamma_X^{\upsilon_X}\gamma_Y^{\upsilon_Y}\ldots}\right). \tag{1.21}$$

1.2 The Double-layer

Typically a potential difference exists between an electrode and the solution. This difference is distributed over a finite distance whereby the influence of electrostatic forces creates "layers" of solution species at the electrode-solution interface. The first of these layers is referred to as the compact or Stern layer whereby ions and/or molecules specifically adsorb onto the electrode surface. The distance from the electrode surface to the centre of these specifically adsorbed species can be referred to as the Inner-Helmholtz Plane, IHP, and is defined in Figure 1.1 as x_1. After the IHP, there is a layer of adsorbed solvated ions, located at x_2, which are not free to move. This layer is defined as the Outer-Helmholtz Plane, OHP. It can be observed in Figure 1.1 that the arrangement of charged species at the electrode-solution interface "screens" the potential and hence reduces the electrostatic forces the solution species experience with respect to the electrode. The IHP and OHP screen the majority of the potential with the remaining potential being screened by the diffuse layer. The diffuse layer, where solvated ions are attracted and repelled from the electrode but still experience thermal motion, is the distance from the OHP to the point at which the potential experienced by the solution phase species is effectively that of the bulk solution. The IHP, OHP and diffuse layer are collectively known as the double layer.

The thickness of the diffuse layer can be controlled through altering the concentration of electrolyte in solution. This is important when considering the electrolysis of solution based electroactive species at an electrode. The thickness of the double layer can be referred to as the Debye length, κ^{-1}, and can be estimated for a given electrolyte concentration in dilute solution by[3]:

$$\kappa^{-1} = \frac{1}{(3.29\times10^{7})Zc^{*\frac{1}{2}}}, \tag{1.22}$$

where the units of κ^{-1} are cm, Z is the charge of the ions in the electrolyte and c^* is the bulk concentration for a Z:Z electrolyte in mol dm^{-3}. The lower the electrolyte concentration, the larger the Debye length and the further the potential applied at the electrode surface extends

into the solution. The addition of sufficient electrolyte is important for the case of electron transfer kinetics; Here, compression of the double layer is necessary to prevent the electroactive species experiencing the influence of the electric field until they are within a tunnelling distance of the electrode so electron transfer can then occur under the full thermodynamic driving force of the potential applied to the electrode.

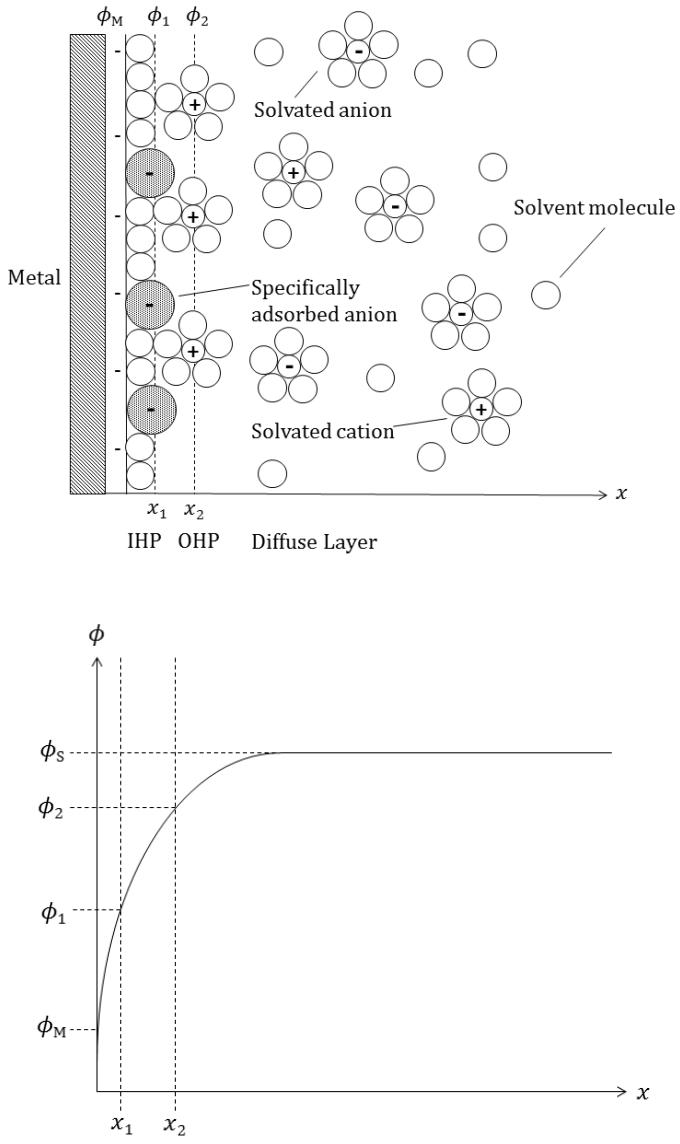


Figure 1.1 Helmholtz-Stern model of the double-layer illustrating how the potential changes through screening by the charged layers

1.3 Electrode Kinetics

Equation 1.16 states that the respective concentration of the electroactive species in equilibrium determines the potential difference at a single metal-solution interface. This is the underlying foundation of electrochemistry as the reverse is also true; that the concentration of the species and hence the direction of flow of electrons transferred at the electrode surface can be influenced by an applied potential.

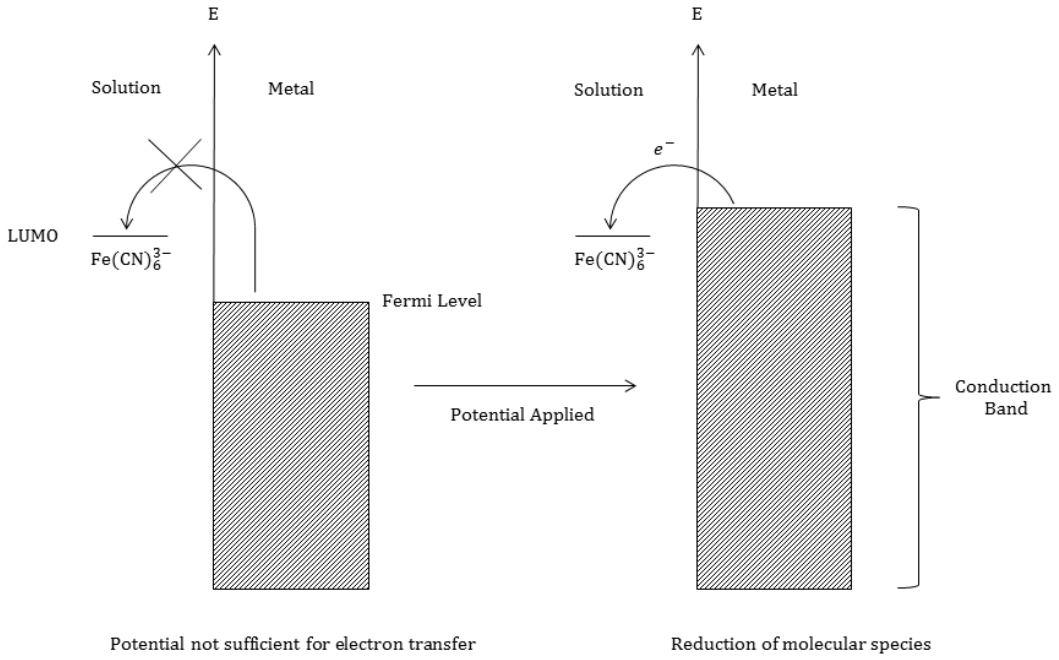


Figure 1.2 Illustration of the effect of an applied potential on the relative energies of the electrode Fermi-level and the LUMO of an electroactive species, $Fe(CN)_6^{3-}$

To understand how a potential can be applied to an electrode it is useful to consider the Fermi level model of a conductive metal. Unlike molecules with distinct molecular orbitals each with a specific energy, the overlapping of metallic orbitals creates a continuum of energy states referred to as the conduction band. Figure 1.2 illustrates how, through the application of a potential to the electrode, the energy of the Fermi level can be altered with respect to the solution phase electroactive species. In the case shown, this allows for the one electron

reduction of ferricyanide, $Fe(CN)_6^{3-}$, to ferrocyanide, $Fe(CN)_6^{4-}$. The potential applied to the electrode is controlled with respect to the REF which will be discussed later on.

By applying a potential to the electrode, the equilibrium of the redox species is disturbed and hence the system can no longer be adequately described by the Nernst equation. For electrochemical experiments it is instead useful to understand the kinetics of electrochemical processes. If we consider the ferricyanide/ferrocyanide redox couple in the vicinity of an electrode at an applied potential:

$$Fe(CN)_6^{3-}(aq) + e^-(m) \underset{k_a}{\overset{k_c}{\rightleftarrows}} Fe(CN)_6^{4-}(aq)\,, \tag{1.23}$$

the current passed at the electrode, *I*, can be expressed in terms of the flux of the electroactive species to the electrode, *J*:

$$I = FAJ\,, \tag{1.24}$$

where,

$$J = k_c[Fe(CN)_6^{3-}]_0 - k_a[Fe(CN)_6^{4-}]_0\,, \tag{1.25}$$

A is the area of the electrode, k_c is the rate constant for the reduction reaction, k_a is the rate constant for the oxidation reaction and $[j]_0$ is the concentration of species *j* at the electrode surface. Electrochemical rate constants are potential dependant. By applying a potential to the electrode the energy profile of the reaction can be altered to promote either the oxidation or reduction process (Figure 1.2). The rate constants for a single metal-solution interface can be expressed as:

$$k_c \propto exp\left[\frac{-\alpha F(\phi_M - \phi_s)}{RT}\right], \tag{1.26}$$

$$k_a \propto exp\left[\frac{\beta F(\phi_M - \phi_s)}{RT}\right], \tag{1.27}$$

$$\alpha + \beta = 1\,, \tag{1.28}$$

where α and β are the transfer coefficients for the cathodic and anodic processes respectively. As ϕ_M is made more negative with respect to ϕ_S, k_c will increase and drive the reduction of $Fe(CN)_6^{3-}$ to $Fe(CN)_6^{4-}$. As ϕ_M is made more positive with respect to ϕ_S, k_a will increase and drive the oxidation of $Fe(CN)_6^{4-}$ to $Fe(CN)_6^{3-}$. For a two electrode system, these rate constants can be expressed in terms of the potential difference and standard formal potentials:

$$k_c = k_c^0 exp\left[\frac{-\alpha F(E-E_f^0)}{RT}\right], \tag{1.29}$$

$$k_a = k_a^0 exp\left[\frac{\beta F(E-E_f^0)}{RT}\right], \tag{1.30}$$

where k^0 is the standard electrochemical rate constant. If we substitute these terms into equation 1.25 we get the Butler-Volmer expression for the flux to an electrode[4, 5]:

$$J = k_c^0 exp\left[\frac{-\alpha F(E-E_f^0)}{RT}\right][Fe(CN)_6^{3-}]_0 - k_a^0 exp\left[\frac{\beta F(E-E_f^0)}{RT}\right][Fe(CN)_6^{4-}]_0 . \tag{1.31}$$

This expression relates the flux of electroactive species, and hence the observable current, to the applied potential, the standard electrochemical rate constants and the charge transfer coefficients of the species. Note that the transfer coefficients can be found experimentally by Tafel analysis, the method for which is discussed in Section 1.6.2, and provide information on the transition state.

1.4 The Electrochemical Cell

Electrochemical cells are generally operated with either a two or three electrode configuration. Both configurations use a working electrode (WE) and a reference electrode (REF). The WE is usually a conductive, non-chemically active metallic material such as gold or platinum, or a form of carbon; glassy carbon, carbon fibre or graphite. The WE is the site of the studied electrochemical reaction and is held at a potential with respect to the REF by use of a potentiostat. The REF utilises a potential determining equilibrium in a high concentration of

electrolyte to establish and hold a fixed potential. An example is the saturated mercury-mercury chloride electrode (SCE):

$$Hg(l) + Cl^{-}(aq) \rightleftarrows \frac{1}{2}Hg_2Cl_2(s) + e^{-}(m)\,. \tag{1.32}$$

The potential for a REF is defined in terms of its relation to the standard hydrogen electrode (SHE), where $\mathrm{E}^0(H^+/\frac{1}{2}H_2) = 0$. For a SCE this is $+0.241$ V vs. SHE and remains constant through the use of a fixed concentration of electrolyte, in this case potassium chloride, and by ensuring only a small current is passed through the REF at any time. In a two electrode system the potential difference measured is a contribution of both electrode-interface potentials from the WE and REF and the IR drop between the two electrodes:

$$E = (\phi_M - \phi_S)_{WE} + IR - (\phi_M - \phi_S)_{REF}\,, \tag{1.33}$$

where $(\phi_M - \phi_S)_{WE}$ is the potential difference at the working electrode-solution interface and $(\phi_M - \phi_S)_{REF}$ is the potential difference at the reference electrode-solution interface. The contribution from IR is known as the Ohmic drop and is due to the bulk solution between the electrodes behaving as a resistor. In a two electrode system measured currents must be kept low, typically less than 10^{-9} A. If high currents are passed between the WE and RE the IR term will increase to a significant but unknown value. This will in turn lead to an unknown potential difference at the WE interface, $(\phi_M - \phi_S)_{WE}$. In addition, when current is passed through the REF the "fixed" potential, $(\phi_M - \phi_S)_{REF}$, against which the applied potential at the WE interface is defined will change. This dual affect creates an unfavourable situation where the potential being applied to the WE, $(\phi_M - \phi_S)_{WE}$, is not known and changes with time.

To circumvent this problem, a counter electrode (CE) can be introduced to create the three electrode system shown in Figure 1.3. The introduction of a third electrode allows the current to pass between the WE and CE without involvement of the REF. This allows the potential to be known with respect to the REF potential whilst passing large currents between

the WE and CE. As such a small current passes between the WE and the REF, the IR contribution in Equation 1.33 becomes negligible and the equation simplifies to:

$$E = (\phi_M - \phi_S)_{WE} - (\phi_M - \phi_S)_{REF} . \quad (1.34)$$

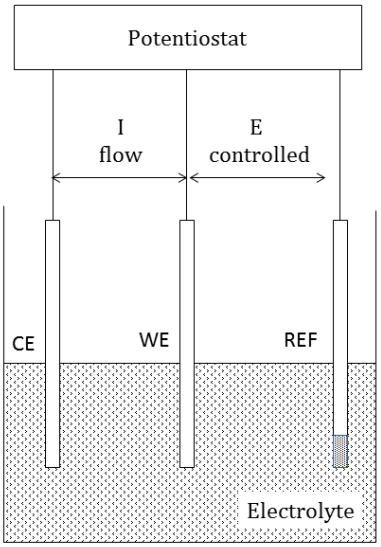


Figure 1.3 Schematic of the three electrode electrochemical cell

1.5 Mass Transport

For electron transfer to occur it is necessary for the electroactive species to be within a tunnelling distance of the electrode surface, typically $\leq$ 1 nm[6]. Equation 1.24 shows the relationship between the current and the flux of electroactive material to the electrode. The reactant flux to the electrode is therefore important in determining the voltammetry observed.

1.5.1 Diffusion

Diffusion is the transfer of mass down a concentration gradient from high to low concentration. The transfer of material by diffusion can be expressed by Adolf Fick's 1st law[7]:

$$J = -D\frac{\partial c}{\partial x}, \quad (1.35)$$

where J is the flux of material, D is the diffusion coefficient and $\frac{\partial c}{\partial x}$ is the concentration gradient at point x. The negative sign indicates that the movement of species occurs down the concentration gradient. Diffusion coefficients are generally in the range of 10^{-6} to 10^{-5} cm^2 s^{-1} for molecular species in aqueous solution. They are highly temperature sensitive as:

$$D = D_\infty exp\left(\frac{-E_a}{RT}\right), \tag{1.36}$$

where D_∞ is the hypothetical diffusion coefficient at infinite temperature, E_a is the activation energy for diffusion and T is the temperature. Diffusion coefficients are a measure of the distance in which a species travels in a given time, with smaller species having higher coefficients and hence travelling further in a given time period than larger species. The root mean square displacement of a species at a fixed temperature and a given time can be defined in terms of its diffusion coefficient as follows[8]:

$$\sqrt{\langle x^2 \rangle} = \sqrt{2Dt}, \tag{1.37}$$

where t is time. The electrochemical study of solution based species nearly always involves diffusion, and as such, control of the temperature of the system through thermostating is fundamentally important.

Equation 1.35 deals with the flux of material to an electrode down a diffusion gradient. However, as electroactive species are continuously consumed at an electrode the concentration gradient does not remain constant. It is therefore necessary to consider how the concentration changes at point x with time, t. This is expressed by Fick's 2nd law for a one-dimensional case:

$$\frac{\partial c}{\partial t} = D\frac{\partial^2 c}{\partial x^2}, \tag{1.38}$$

and for the three-dimensional case:

$$\frac{\partial c}{\partial t} = D\frac{\partial^2 c}{\partial x^2} + D\frac{\partial^2 c}{\partial y^2} + D\frac{\partial^2 c}{\partial z^2}. \tag{1.39}$$

1.5.2 Migration

In electrochemical experiments charged species are involved and their movement is influenced by electric fields. The flux to an electrode in a stationary solution can be expressed in terms of both diffusional and migrational contributions[3]:

$$J = -D\frac{\partial c}{\partial x} - Zc^*\frac{F}{RT}\left(\frac{\partial \phi}{\partial x}\right), \tag{1.40}$$

where $\frac{\partial \phi}{\partial x}$ is the electric field (or potential gradient). The first term is the familiar Fickian expression for diffusion down a concentration gradient from Equation 1.35. The second term is the contribution of migration to the flux and is a combination of the electric field, the concentration of the electrolyte and the charge of the ions.

In Section 1.2 the concept of the double layer was introduced and its effect on the potential experienced by solution species at a given distance from an electrode. In Equation 1.22 the thickness of the double layer is shown to be affected by the concentration of electrolyte. This is important when considering the transport of electroactive species to an electrode. By compressing the double layer the electric field gradient in turn is compressed. Therefore the $\frac{\partial \phi}{\partial x}$ term in Equation 1.40 is negligible until the electroactive species are in close proximity to the electrode i.e. within electron tunnelling distance of the electrode. This is beneficial in voltammetry and allows the flux of material to an electrode to be viewed as a purely diffusional problem. This is why, for simplicity of studied systems, electrolyte concentrations of typically 30 mM or more are used[9].

1.5.3 Convection

The flux to an electrode is not just affected by diffusion and migration but can also be influenced by convection. Natural convection is the movement of species due to thermal gradients in solution. Electrochemical cells are generally thermostated to minimise these thermal gradients as they can cause unpredictable changes in flux to the electrode. However, small thermal gradients cannot be completely negated and play a significant role in determining the diffusion

layer thickness during voltammetric experiments. This is explained in more detail in Section 1.61. Forced convection is caused by physical perturbation of the system, and for electrochemical experiments, can either be by movement of the electrode in solution or by flowing of the solution at, or across, an electrode. Forced convection is generally more favourable than natural convection as this allows control of the flux in the direction of the electrode surface. This allows enhanced mass transport over purely diffusional flux and, considering Equation 1.24, greater currents. This is the concept utilised in electrochemical flow cells which will be discussed in greater detail in Section 1.9. If convection and migration are supressed by using a thermostated stationary solution containing electrolyte, the total flux to the electrode can be assumed to be the diffusional flux.

1.6 Electrochemical Methods

Throughout this thesis, different amperometric techniques are used to study electrochemical systems; linear sweep voltammetry (LSV), cyclic voltammetry (CV) and chronoamperometry. These methods measure the current passed at the WE over a given time scale at either a changing or fixed potential. The importance of these techniques in the study of electrochemical systems will now be discussed.

1.6.1 Chronoamperometry

In chronoamperometry a step in potential is applied from E_1 to E_2, where typically at E_1 the potential is not sufficient for electron transfer to the studied species and E_2 allows for the electron transfer to occur and current to pass. As this electron transfer occurs, the concentration of the species undergoing electrolysis decreases in the vicinity of the electrode. This creates a concentration gradient causing diffusion of the species towards the electrode. Figure 1.4 (left) shows how this concentration gradient changes as a function of distance from the electrode and time. The consumption of material in the vicinity of the electrode and subsequent need to diffuse material to the electrode causes a decay curve to be observed in the

resultant current, shown in Figure 1.4 (right), which can be described by the Cottrell equation[10]:

$$I = \frac{nFA\sqrt{D}c^*}{\sqrt{\pi t}} \ , \tag{1.50}$$

where I is the Faradaic current , n is the number of electrons transferred, A is the area of the electrode and c^* is the concentration of the species in the bulk solution. This equation suggests that the current will continue to decay at a rate $\propto \frac{1}{\sqrt{t}}$ until the current approaches zero (Figure 1.4 (right)). In real systems the diffusion layer does not continue to infinity due to natural convection of the bulk solution. This causes mixing and limits the thickness of the diffusion layer as shown in Figure 1.5 (left), providing a source of material such that a steady state is reached as shown in Figure 1.5 (right). The name given to the distance between the electrode and the bulk solution once this steady state is reached is the Nernst diffusion layer. The thickness of the Nernst diffusion layer, δ, is dependant both on the experimental timescale and by the diffusion coefficient of the electroactive species and can be expressed as:

$$\delta = (\pi Dt)^{\frac{1}{2}}. \tag{1.51}$$

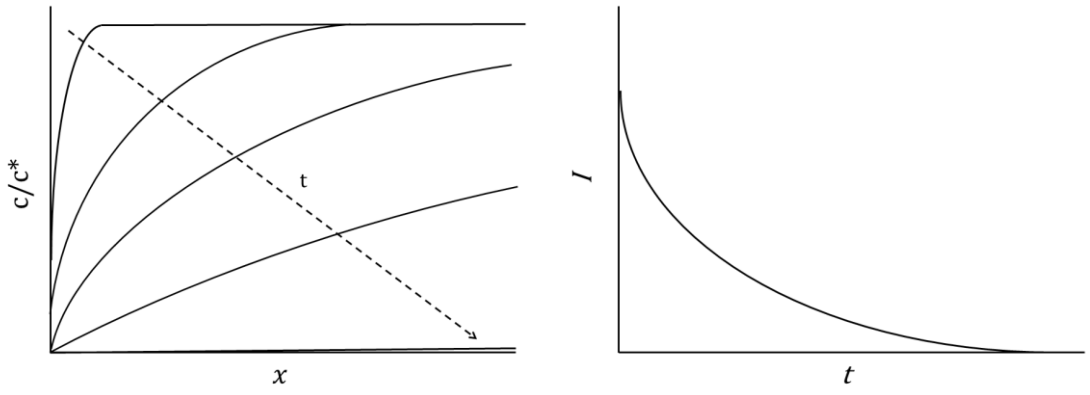


Figure 1.4 (Left) Plot illustrating the change in concentration of the electroactive species, *c*, compared to the bulk solution concentration, *c**, at distance x from a macroelectrode surface as a function of the voltammetric measurement timescale, *t*. (Right) Example of a measured current-time transient gained from chronoamperometry of a diffusional electroactive species decaying to zero current

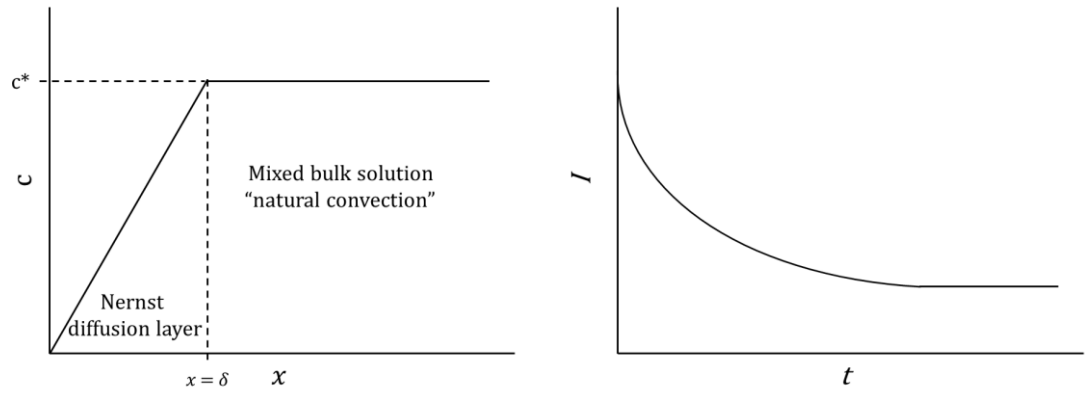


Figure 1.5 (Left) Plot of the concentration of the electroactive species, *c*, at a distance from the electrode, *x,* once steady state has been reached, defining the Nernst diffusion layer (Right) Example of a measured current-time transient gained from chronoamperometry of a diffusional electroactive species achieving steady state current on establishment of the Nernst diffusion layer

1.6.2 Linear Sweep Voltammetry, Cyclic Voltammetry and Tafel Analysis

In linear sweep voltammetry (LSV) the applied potential is swept at a given scan rate between two potentials, E_1 and E_2. When the reverse sweep is subsequently applied this is known as cyclic voltammetry (CV). The potential-time plots for both LSV and CV are shown in Figure 1.6.

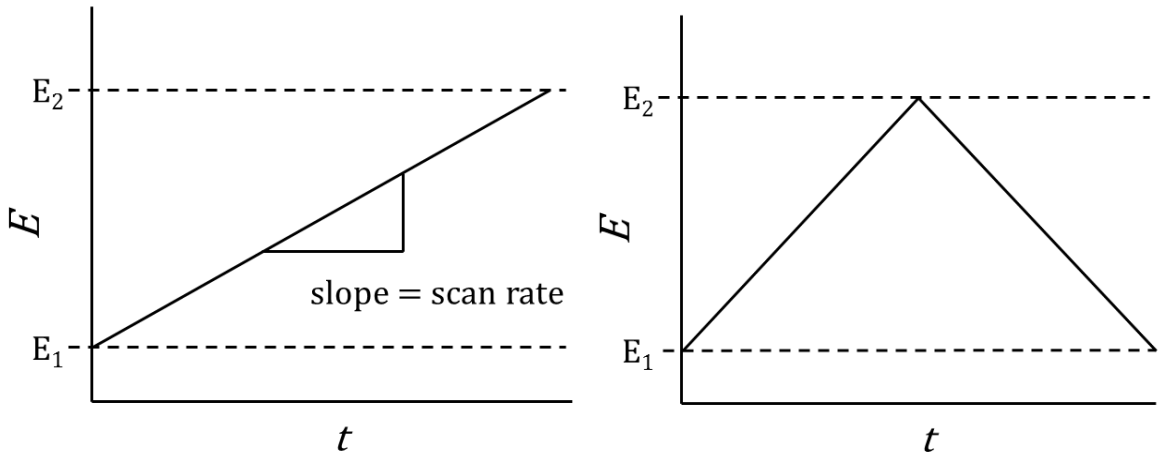


Figure 1.6 Potential-time plots for linear sweep voltammetry (left) and cyclic voltammetry (right).

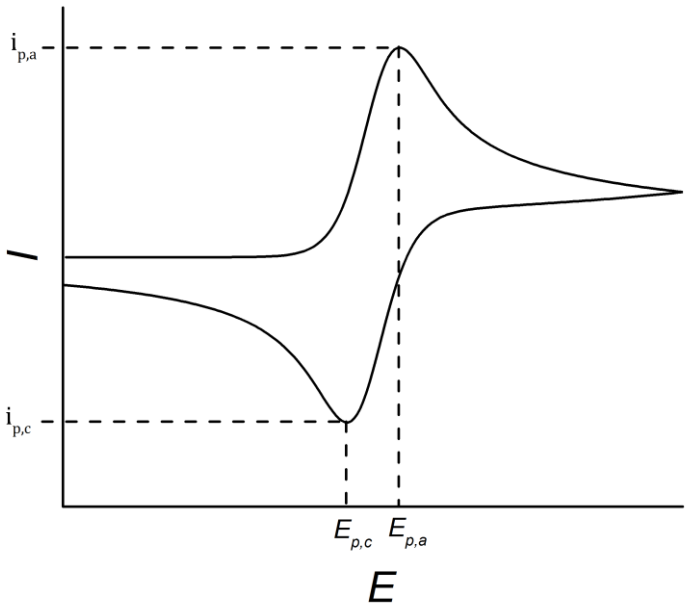


Figure 1.7 Simulated macrodisk cyclic voltammogram for a reversible redox couple

When a triangular waveform like that shown in Figure 1.6 is applied to an electrode in a solution containing a redox active species, the electrochemical process occurring at the electrode can be followed by measurement of the current as a function of the applied potential. Figure 1.7 illustrates a typical voltammogram for the CV of a reversible, diffusional species to a macroelectrode, first scanning in an oxidative direction. As the potential is scanned from E_1 to E_2, no current is passed until the potential reaches that required for oxidation of the species. This causes current to flow and be detected. In systems where migration and convection have been supressed, material is consumed at the electrode surface and is required to diffuse down a concentration gradient. The establishment of the Nernst diffusion layer (Figure 1.5) gives rise to the characteristic peak observed where $E_{p,a}$ is the peak potential for the anodic process. After establishment of the diffusion layer, the current observed decreases as material must now diffuse from the bulk into the diffusion layer and the mass transport becomes diffusion limited. This decay in current follows that for the Cottrell equation defined in Equation 1.50. The reverse

scan follows the same pattern. The material oxidised on the forward scan is now reduced and forms a peak, $E_{p,c}$, once the diffusion layer is established.

Different voltammetry can be observed for reversible and irreversible electrochemical reactions. Electrochemical processes are deemed as reversible or irreversible by comparison of the rate constant for electron transfer, k^0, derived in Section 1.3, with the mass transport rate of the species to the electrode, in this case diffusion only. Mass transport will depend on the diffusion coefficient of the species and the thickness of the diffusion layer. Equation 1.51 shows that the thickness of the diffusion layer is time dependant. In CV, the timescale of the measurement is determined by the scan rate. Therefore we can define a mass transport coefficient, m_T, in terms of the scan rate and diffusion coefficient:

$$m_T \sim \sqrt{\frac{D}{RT/_{Fv}}}, \tag{1.52}$$

where v is the scan rate. A processes can be defined as reversible if $k^0 \gg m_T$, quasi-reversible if $k^0 \sim m_T$ and irreversible if $k^0 \ll m_T$. For electrochemical processes at a macroelectrode in stationary solution, Matsuda and Ayabe introduced the parameter, Λ, as a guide for identifying whether, for a given scan rate and k^0, a process was reversible, quasi-reversible or irreversible [11-13]:

Reversible: $\Lambda \geq 15$ and $\Lambda \geq 0.3v^{\frac{1}{2}}$ cm s^{-1}

Quasi-reversible: $15 > \Lambda > 10^{-3}$ and $0.3v^{\frac{1}{2}} > \Lambda > 2 \times 10^{-5}v^{\frac{1}{2}}$ cm s^{-1}

Irreversible: $\Lambda \leq 10^{-3}$ and $\Lambda \leq 2 \times 10^{-5}v^{\frac{1}{2}}$ cm s^{-1}

where, $$\Lambda = \frac{k^0}{\left(\frac{FDv}{RT}\right)^{\frac{1}{2}}}, \tag{1.53}$$

at 298 K and assuming $\alpha \sim 0.5$. Theoretically, at fast enough scan rates all electrochemical processes can show irreversible behaviour. However this is limited by practical considerations.

Figure 1.8 shows an example voltammogram for systems with the same diffusion coefficient and scan rate but with decreasing k^0. Decreasing k^0 with respect to the scan rate causes the resultant voltammetry to proceed from reversible to quasi-reversible to irreversible behaviour. Increasing irreversibility can be shown to cause an increase in the peak-peak separation due to the reaction kinetics being outrun by diffusional mass transport.

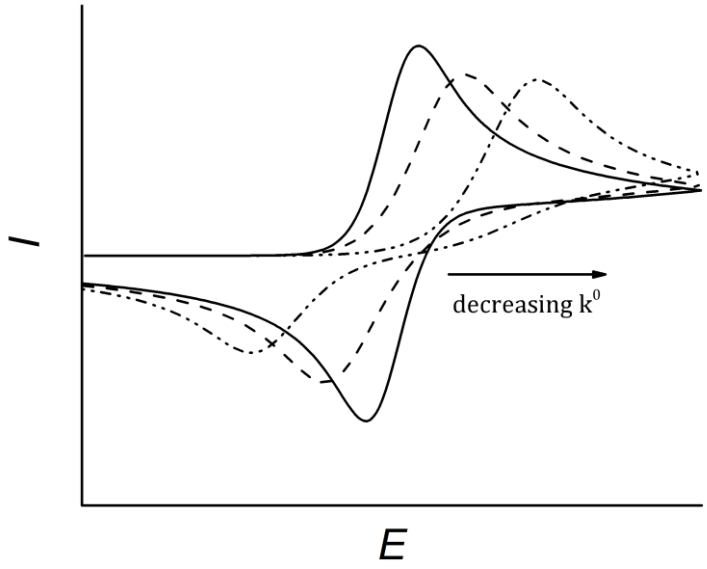


Figure 1.8 Simulation of cyclic voltammetry of $A + e^- \rightleftarrows B$ where scan rate $= 1$ V s^{-1}, $D = 1 \times 10^{-5}$ cm^2 s^{-1}, $\alpha = 0.5$, $k^0 = 0.1, 0.01, 0.001$ cm s^{-1}

Equation 1.24 shows that current passed at an electrode is related to the flux of the electroactive species to the electrode. For diffusional only systems, this flux can be influenced voltammetrically by altering the scan rate. It was mentioned previously that the faster the scan rate the thinner the diffusion layer. The thinner the diffusion layer the greater the concentration gradient and hence the greater the diffusional flux to the electrode. Figure 1.9 illustrates how the scan rate affects the observable voltammetry for a reversible process.

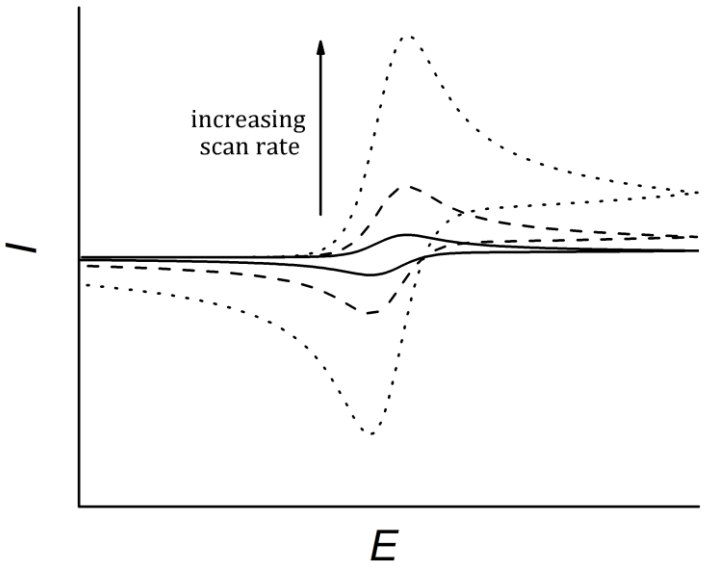


Figure 1.9 Simulation of cyclic voltammetry of A + e^- ⇄ B where D = 1 x 10^{-5} cm^2 s^{-1}, $\alpha = 0.5$, k^0 = 0.1 cm s^{-1} and scan rate = 1, 10 and 100 mV s^{-1}

It can be observed that increasing the scan rate for a reaction with fast kinetics gives a rise in the peak current whilst maintaining the same peak potential. The relationship between scan rate and peak height for a reversible system can be expressed by the Randles-Ševčik equation for a one electron and multi electron process:

n=1: $$I_p = 2.69 \times 10^5 A D^{1/2} [A] \nu^{1/2}\,, \tag{1.54}$$

n>1: $$I_p = -0.446 nFA[A]\sqrt{\frac{nF\nu D}{RT}}\,, \tag{1.55}$$

where I_p is the peak current. For both the n=1 and n>1 case I_p has a $\nu^{\frac{1}{2}}$ dependency. A scan rate study is a simple method for finding whether a process is diffusion controlled as irreversible reactions also have the same dependency with scan rate for both a one and multi electron process [14] :

n=1: $$I_p = 2.99 \times 10^5 \sqrt{\alpha} D^{\frac{1}{2}} [A] A \nu^{\frac{1}{2}}\,, \tag{1.56}$$

n>1: $$I_p = -0.496\sqrt{n' + a'_{n+1}}nFA[A]_{bulk}\sqrt{\frac{F\nu D}{RT}}\ , \tag{1.57}$$

where n' is the sum of electrons transferred before the rate determining electron transfer and a'_{n+1} is the transfer coefficient of the slow transfer step.

Transfer coefficients, as described in Section 1.3, can be experimentally determined by Tafel analysis. At extreme potentials, the Butler-Volmer expression for the flux to an electrode (see Equation 1.33), can be expressed in terms of the flux of the reacting species. For the one step, one electron reduction of A to B:

$$A + e^- \rightleftarrows B\ , \tag{1.58}$$

the redox couple becomes:

$$J_c = k_c^0 exp\left[\frac{-\alpha F\left(E-E_f^0\right)}{RT}\right][A]_0\ , \quad E \ll E_f^0\ , \tag{1.59}$$

$$J_a = k_a^0 exp\left[\frac{\beta F(E-E_f^0)}{RT}\right][B]_0\ , \quad E \gg E_f^0\ \ , \tag{1.60}$$

where J_c and J_a are the cathodic and anodic flux respectively. The reductive transfer coefficient, α, and oxidative transfer coefficient, β, can be defined as:[15]

$$\alpha = -\left(\frac{RT}{F}\right)\left(\frac{\partial \ln|J_c|}{\partial E}\right), \tag{1.61}$$

$$\beta = \left(\frac{RT}{F}\right)\left(\frac{\partial \ln|J_a|}{\partial E}\right). \tag{1.62}$$

By plotting ln(I) vs. E and measuring the gradient the transfer coefficients can be calculated and provide information on the transition state as shown in Figure 2.0.

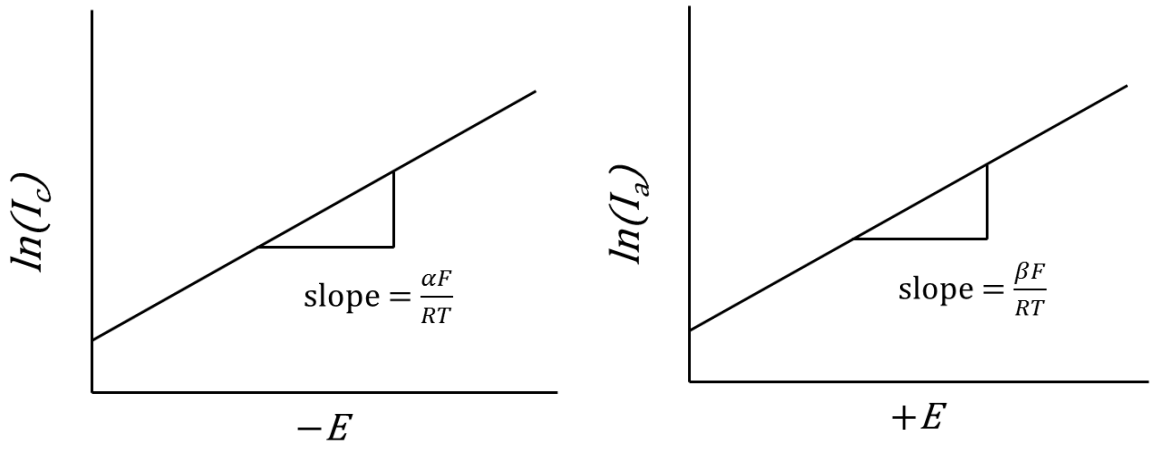


Figure 2.0 Tafel plots for the determination of the transfer coefficients α and β where n =1

Not all electrochemical processes are one step. Take the case of the two-step, 2 electron reduction:

$$A + e^- \rightleftarrows B\,,$$

$$B + e^- \rightleftarrows C\,. \tag{1.63}$$

The rate determining step will be either the 1st or 2nd electron transfer. We can define the transfer coefficients for the 1st reduction step as α_1 and α_2 for the 2nd reduction step. If the 1st reduction step is rate determining then:

$$\alpha_1 = -\left(\frac{RT}{F}\right)\left(\frac{\partial \ln|J_c|}{\partial E}\right). \tag{1.64}$$

If the 2nd step is rate determining then:

$$\alpha_2 = -\left(\frac{RT}{F}\right)\left(\frac{\partial \ln|J_c|}{\partial E}\right) - 1\,. \tag{1.65}$$

For a 2-step, 2 electron oxidation the transfer coefficients for the 1st and 2nd oxidation steps are:

$$\beta_1 = \left(\frac{RT}{F}\right)\left(\frac{\partial \ln|J_a|}{\partial E}\right), \tag{1.66}$$

$$\beta_2 = \left(\frac{RT}{F}\right)\left(\frac{\partial \ln|J_a|}{\partial E}\right) - 1. \tag{1.67}$$

Figure 2.1 shows how though a ln(I) vs. E plot the transfer coefficients can be calculated from the gradient. For multistep reactions, assuming all the transfer coefficients are ~0.5, Tafel plots indicate which step is rate determining; A calculated slope of ~0.5 will indicate the 1st step is rate determining and a slope of ~1.5 will indicate the 2nd case is rate determining.

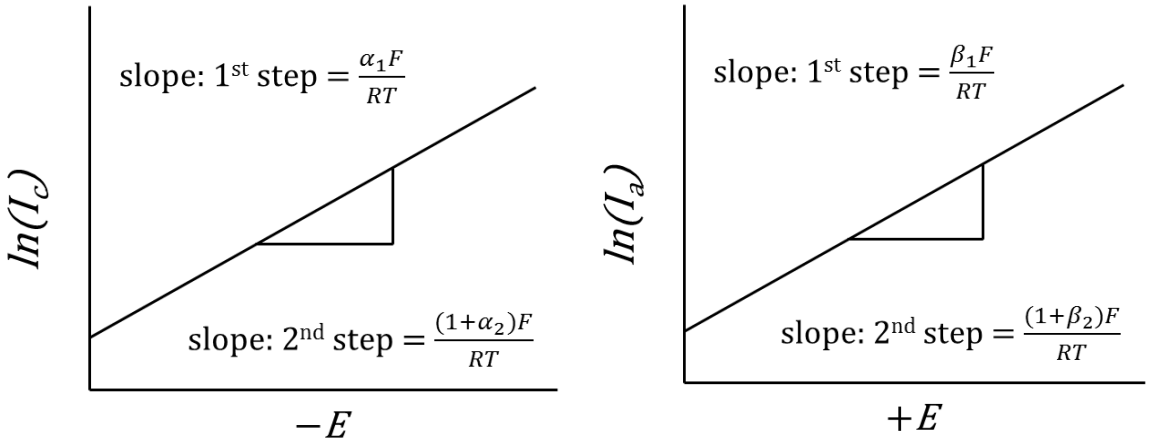


Figure 2.1 Tafel plots for the determination of the transfer coefficients for a multistep process. The gradient is provided for both cases where either the 1st or 2nd step is the rate determining step.

1.7 Electrodes: From the Macroscale to the Nanoscale

Thus far only the voltammetry measured at macroelectrodes has been considered. Electrodes of microscale geometries down to the nanoscale are often used due to their enhanced mass transport. Figure 2.2 shows the differing diffusion regimes between a macrodisk and a microdisk electrode. As illustrated, macrodisk electrodes experience a linear diffusion regime. This linear diffusion is not efficient and gives rise to the characteristic peak in current observed for the cyclic voltammetry of macroelectrode geometries.

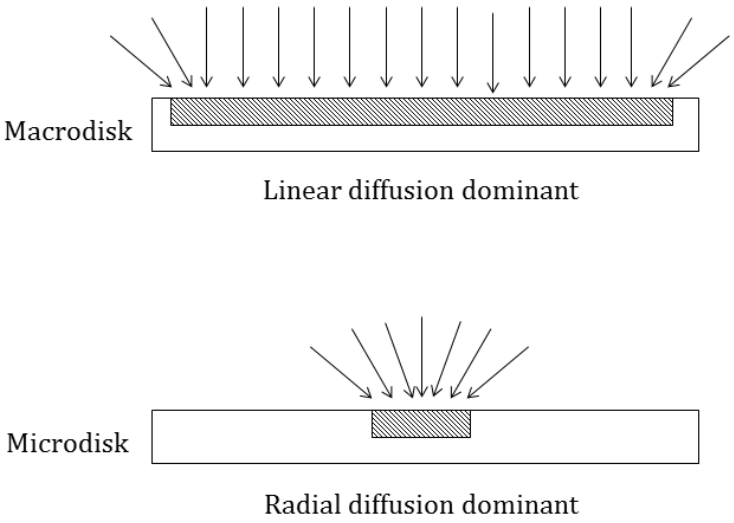


Figure 2.2 Comparison of the diffusional regimes of a macrodisk and microdisk electrode illustrating the dominance of radial diffusion at smaller electrode radius

For microelectrodes radial diffusion becomes significant allowing rapid formation of a thinner diffusion layer and greater mass transport to the electrode surface. In cyclic voltammetry this can be observed by the achievement of a steady state current at modest scan rate values as shown in Figure 2.3. The steady state current for microdisk and microhemispherical geometries can be expressed as:

$$I_{lim}(disk) = 4nr_eFDc^* , \tag{1.68}$$

$$I_{lim}(hemisphere) = 2\pi r_e nFDc^* , \tag{1.69}$$

where $I_{lim}(disk)$ and $I_{lim}(hemisphere)$ are the limiting currents for a microdisk and microhemisphere electrode respectively and r_e is the radius of the electrode. These equations also hold for diffusion to nanoelectrodes however the limiting current observed is much lower due to the smaller geometric radius. Moreover migration effects may also operate at this small scale. The low currents observed for nanoelectrodes can be a limitation for their application in

electrochemical detection. To improve the detection currents an array of electrodes can be used and this will be discussed in the next section.

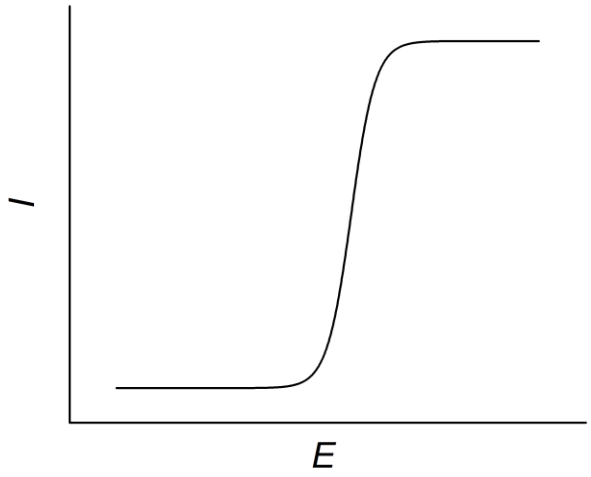


Figure 2.3 Simulated microdisk cyclic voltammogram showing steady state current

1.8 Electrode Arrays

An array of electrodes is a system comprised of several or more electrodes of the same geometry. These electrodes can be independently addressable when manufactured using complex multi-step fabrication methods[16] or integrated where the same potential is applied to all electrodes in the array[17]. Arrays of electrodes have a greater electroactive area than a single electrode, offering enhanced detection currents whilst maintaining relatively low noise. Most electrode arrays fall within two distinct categories due to the degree of order expressed in the position of the electrodes within the array; regular and random. Figure 2.4 illustrates the difference in the two; regular arrays have a high order of arrangement and random arrays have none.

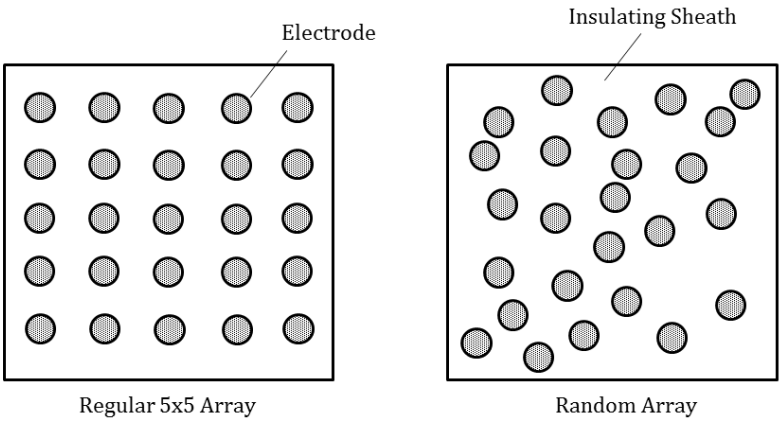


Figure 2.4 Schematic comparison of a regular and random array both consisting of 25 disk electrodes

1.8.1 Microelectrode Arrays

Microelectrode arrays consist of electrodes with diameters usually between 1 and 50 μm[18]. The diffusional characteristics and hence the observed voltammetry strongly depends on the inter-electrode spacing and the timescale of the measurements, as shown in Figure 2.5. There are four cases for diffusion to a microelectrode array[19]. When electrodes are far apart and the scan rate is very fast the diffusion layer, δ, is smaller than the radius of the electrode, r_e, and linear diffusion occurs to each microelectrode. This is case 1 and results in a peak-shaped voltammogram corresponding to the sum of the isolated linear diffusion response for the individual microelectrodes. At longer timescales (slower scan rates) $\delta \sim r_e$ and radial diffusion dominates at individual electrodes. This is case 2. The voltammetry observed is therefore that of a single microelectrode steady-state response multiplied by the number of electrodes in the array[20]. As experimental timescales lengthen and/or the electrodes are brought closer together, diffusion layers overlap and linear diffusion-like behaviour in the form of peaks in the cyclic voltammetry result. Unlike case 1, case 3 involves overlapping diffusion fields therefore the voltammetry cannot be related to an isolated electrode in the array. Case 4 is where the array experiences full linear diffusion due to the high degree of diffusion layer overlap and acts

as a macroelectrode of area equal to that of the entire geometric area of the array (electrodes and support). This occurs for closely packed electrodes at slow scan rates.

A wide number of fabrication methods have been developed for microelectrode arrays. For regular arrays the spacing is paramount and can be defined through the use of photolithographic[21, 22], screen printing[23], or patterned electrodeposition methods[24]. The electrode geometries can be planar in the case of disk electrodes or can extend above or below the insulating substrate. Regular wire arrays have found particular use for the study of neurons in biological systems as the 3D structure allows them to penetrate into living tissue, providing not only current responses but also spatial resolution of the neurons[25].

Whilst providing control of electrode geometry, these methods are complex and expensive. Random electrode arrays (RAMs), otherwise known as electrode ensembles, are easier to produce than ordered arrays with common methods including the assembly of premade microelectrodes, usually embedded in an epoxy resin[26], or electrodeposition[27]. One example is the carbon-fibre RAM developed by Fletcher *et al*[28]. Here carbon fibres of 1 cm axial length are injected into an epoxy resin. Next the resin is cut perpendicular to the orientation of the fibres providing an exposed face of randomly spaced carbon fibre microdisk electrodes.

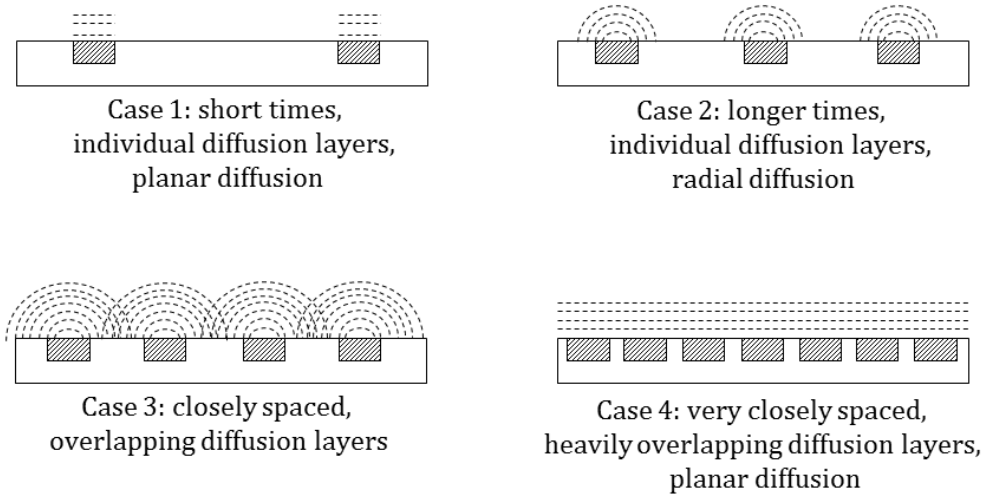


Figure 2.5 Schematic showing the four categories of diffusion to an array of microelectrodes[19]

1.8.2 Nanoelectrode Arrays

Nanoelectrode arrays follow the same principles as microelectrode arrays but are inherently more difficult to manufacture due to the fragility of the individual nanoelectrodes[29]. The first nanoelectrode array was developed by Martin *et al* [30] by platinum electrodeposition through a porous membrane. This was then immersed in molten polyethylene and polished to reveal a random array of disk electrodes. This method allowed for the radius of the electrodes to be constricted by the membrane pore size, with the smallest single electrode geometry fabricated of 100 nm diameter. This was the first nanoelectrode ensemble (NEE) reported and since templated electrodeposition has become a common method for the fabrication of NEEs [31, 32]. Alternative approaches include insulating a conducting surface and subsequently etching the insulating layer[33] and the use of nanoporous polymers to partially block an electrode surface[34]. To achieve ordered nanoelectrode arrays (NEAs) manufacturing routes have focused on improvements in templates for electrodeposition[29] as well as the use of chemical vapour deposition[35] and lithographic methods[36] to achieve the required nanoscale resolution for 2D and 3D NEAs

The above manufacturing routes for NEAs and NEEs are complex and time consuming. An alternative and effective approach is the drop-casting of nanoparticles on to a conducting surface[37]. Whilst this technique has been shown to be hindered by surface aggregation/agglomeration[38, 39] improvements have been made through the magnetic alignment of the particles during the surface modification step[40]. For nanoparticle functionalised surfaces there are four regimes for diffusion to the substrate assuming nanoparticles of the same size[41, 42]. The different cases are similar to those covered for microelectrode arrays, however here the coverage of the nanoparticles is the main factor in controlling the observable voltammetry. Figure 2.6 shows the concentration profile to a single nanoparticle on a planar surface at very fast and slower scan rates. At fast scan rates the diffusion layer can be confined to the surface of the particle resulting in planar diffusion. This is similar to case 1 for microelectrodes and results in macroelectrode like behaviour in the

voltammogram, however the scan rates needed to achieve such a condition are much higher than that for microelectrodes. At slower scan rates the diffusion layer grows from the particle resulting in convergent diffusion. As for microelectrodes, if the nanoparticle as spaced far enough apart so that their diffusion layers do not interact, case 2 is obtained i.e. steady state behaviour whereby the total current is a sum of the individual contributions of the nanoparticles. Increasing the coverage of the nanoparticles and hence decreasing the nanoparticle separation distance has the same effect as for microelectrodes with case 3 and then case 4 like behaviour resulting (Figure 2.5). It has proved complex to relate observed voltammograms to the spacing of nanoelectrode arrays with large arrays of closely packed nanoelectrodes showing the results most consistent with theory[43]. A benefit of case four nanoparticle ensembles is the modification of a large surface with a small amount of material to gain the same currents as that for the underlying substrate area. This is of particular use when the electrocatayltic material is expensive such as platinum or gold.

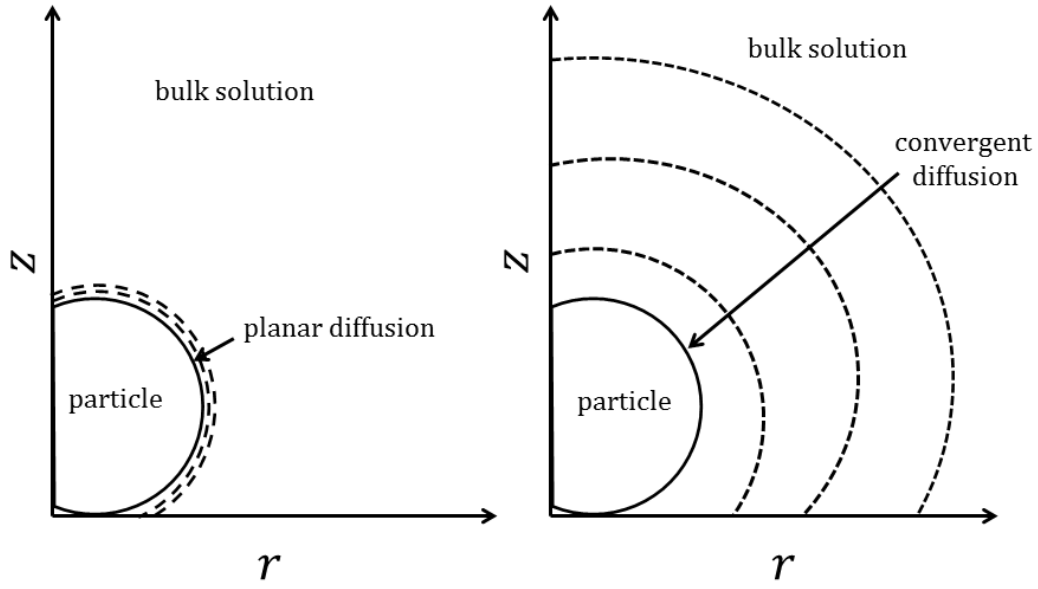


Figure 2.6 Schematic showing the concentration profile to a single spherical nanoparticle on a planar surface at a very fast scan rate (left) and a slower scan rates (right) where z and r are dimensionless cylindrical coordinates relating to the particle radius[41]. The dotted lines represent the diffusion layer to the particle.

1.9 Electrodes Under Flow: Rotating Disk and Wall-Jet Electrodes

Hitherto, the rate of mass transport has been shown to have a significant effect on the observed voltammetry of a system and the current detected. We have dealt with the increase in diffusional mass transport by the use of smaller electrode geometries and the increasing dominance of radial diffusion; however an alternative is the use of forced convection. In this section we will consider the use of flow in enhancing mass transport to an electrode.

The convective flux, J_{conv} in three dimensions can be shown to be related to the concentration of the species studied, [j], at a point with local fluid velocity, V, through a modification of Fick's 1st law[3]:

$$J_{conv} = [j]V - D\nabla[j]\,, \tag{1.70}$$

where $\nabla = \frac{\partial}{\partial x} + \frac{\partial}{\partial y} + \frac{\partial}{\partial z}$, and V has units of cm s^{-1}. The change in the concentration of j with time is:

$$\frac{\partial[j]}{\partial t} = -V\nabla[j] + D\nabla^2[j]\,, \tag{1.71}$$

and consists of both a convective and diffusional component. If an electrode is rotated in a large volume of solution it will create forced convection to the electrode surface. Figure 2.7 shows a schematic of a rotating disk electrode (RDE), whereby solution is drawn to the electrode surface and flows outwards from the rotation axis. For the same system, the diffusion layer thickness can be related to the hydrodynamic layer thickness[3, 44, 45]:

$$\delta \approx \left(\frac{D}{\upsilon}\right)^{\frac{1}{3}} \delta_H\,, \tag{1.72}$$

where,

$$\delta_H = 3.6\sqrt{\frac{\upsilon}{\omega}}, \tag{1.73}$$

υ is the kinematic viscosity, δ_H is the hydrodynamic layer thickness and ω is the rotation speed in rpm. For typical experimental values in aqueous solution of D $\sim 10^{-5}$ cm^2 s^{-1} and $\upsilon \sim 10^{-2}$ cm^2

s^{-1}, $\delta = 0.1\ \delta_H$ and it can be assumed no convection occurs in the diffusion layer. This leads to the formation of a stationary layer at the electrode surface of thickness δ.

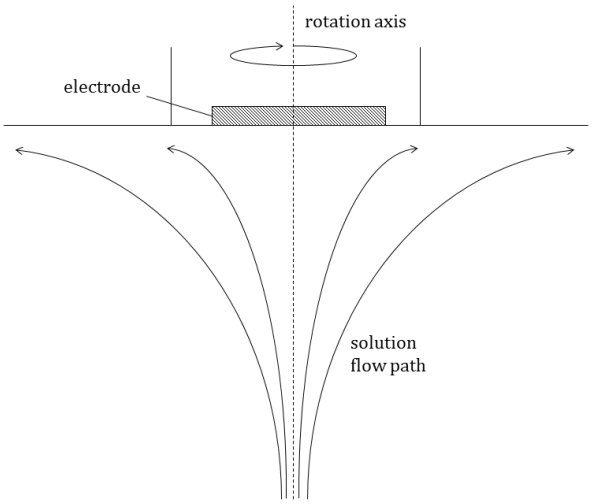


Figure 2.7 Schematic of a rotating disk electrode

For hydrodynamic voltammetry it is important to prevent turbulent flow and promote laminar flow to ensure the system can be more easily modelled. For a rotating disk electrode laminar flow is ensured by use of the Reynolds number, R_e:

$$R_e = \frac{\omega r_e^2}{\upsilon}. \tag{1.74}$$

If $R_e \leq 2 \times 10^3$ laminar flow is maintained. If $R_e > 2 \times 10^3$ then deviation from laminar flow occurs eventually leading to turbulent flow. For a macro rotating disk electrode the enhanced mass transport provided by forced convection gives rise to steady state currents instead of the conventional peak shaped voltammograms observed in diffusional only systems. The limiting current is described by the Levich equation[46]:

$$I_{lim} = 1.554nFAD^{2/3}\upsilon^{-1/6}[A]_{bulk}\omega^{1/2}. \tag{1.75}$$

By increasing the rotation speed the diffusion layer is compressed causing an increasing in mass transport to the electrode and an increase in current. As $I_{lim} \propto \omega^{1/2}$, a study of I_{lim} with varying ω allows the characterisation of new rotating disk electrode setups to ensure the correct flow profile. The maximum increase in the current possible for a given system is limited by R_e, as large electrode areas and very fast rotation velocities will induce turbulent flow.

An alternative method for utilising forced convection in voltammetry is by directing the flow of the solution through a nozzle at the electrode surface. This is called a wall-jet electrode (Figure 2.8) and provides enhanced mass transport over rotating disk electrode systems and easy incorporation into online flow detection systems[47]. The resultant flow profile for a wall-jet is an umbrella shape and, as with the rotating disk electrode, a stationary diffusion layer exists at the electrode surface. If the nozzle is much smaller than the electrode the limiting current can be related to the volumetric flow rate and the nozzle size[48]:

$$I_{lim} = 1.35nFD^{2/3}\upsilon^{-5/12}a^{-1/2}r_e^{3/4}V_f^{3/4}[A]_{bulk}\,, \tag{1.76}$$

where a is the diameter of the jet nozzle and V_f is the volumetric flow rate. The $V_f^{3/4}$ dependency of I_{lim} allows for characterisation of a wall-jet system. It is worth noting that because of the flow profile for a wall-jet the electrode is not uniformly accessible, with the outside of the electrode experiencing a lower flux than the centre. This forms a boundary layer which is indicated in Figure 2.8. The difference in flow profiles for the interior and extremities of the electrode is why the flow models for wall-jet electrodes are more complex than for RDEs.

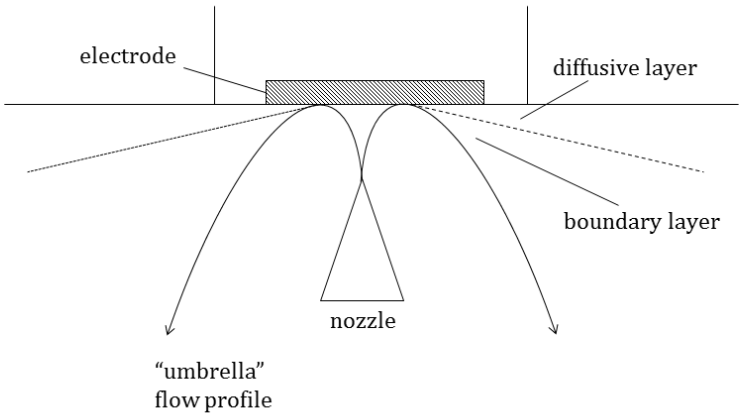


Figure 2.8 Schematic of a wall-jet electrode

This thesis deals with the study of nanoparticles by electrochemistry, in particular the nano-impact technique. To appreciate the advancements made in the work reported, it is beneficial to address both the use of nanoparticles and the current limitations of pre-existing detection and characterisation techniques. This will be discussed in the next chapter.

Chapter 2

Nanoparticles and Characterisation Techniques

This chapter introduces nanoparticle science, covering the key chemical concepts and discusses why nanoparticles are of significant interest for research. Herein, current methods applicable to this thesis for the detection, characterisation and sizing of nanoparticles are discussed, covering optical, electron microscopic and electrochemical methods. The introduction and development of the predominant focus of this thesis, namely the nano-impact technique, is also covered so as to give context to the advances made in this work.

2.1 An Introduction to Nanoparticles

A nanoparticle (NP) is defined by the European Union as a particle with at least one dimension between 1 – 100 nm[49]. NPs are a natural fixture in our environment[50, 51], for example volcanic eruptions can release ash, metal halides and metal oxides of nanoscale dimensions[52]. Also, around 50 % of aerosols in the troposphere are in the form of minerals originating from desert environments, a fifth of which are comprised of NP aggregates[53]. Typically, the term *nanoparticle* is affixed to engineered (man-made) particles[54]. Engineered NPs may differ to a naturally occurring counterpart by possessing a distinct geometry and homogeneous size for a given population as for FeO_x NPs[51]. The most popular methods for synthesising engineered NPs are seed-growth[55], sol-gel[56], solvothermal[57], ball milling and chemical vapour deposition (CVD)[58].

The driving force behind the development of engineered NPs are their special physical properties. By their nature, NPs have high surface-volume ratios; this is exceedingly beneficial for maximising cost-performance for catalytic processes[59] and environmental remediation applications[60]. Their small size also allows their incorporation into composite materials for increased performance[61] and the formation of "smart" or responsive materials[62]. Nano-

specific effects are also observed for particles of diameter <10 nm; as the NPs are of similar size to the wavelength of light they can exhibit localised surface plasmon resonance (see Section 2.2.2.) and quantum confinement effects[63] which can cause particles to fluoresce as is the case for quantum dots[64]. Due to their small size these particles can also be suspended in solution with the aid of capping/stabilising agents. Capping agents can affect the kinetics for processes such as electron transfer at the NP[65, 66] and can also affect their biocompatibility[67]. The ability of capping agents to bind to specific biological components has been utilised for assay development[68]; for example Au-NPs modified with oligonucleotides have been used for the analysis of combinatorial DNA, changing the melting point of the substrate on binding[69, 70]. The development of new NP materials has also driven the development of surface enhanced raman spectroscopy (SERS)[71].

Whilst NPs have shown themselves to be of significant importance for technological development, their rapid incorporation into all aspects of our lives has caused possible concern over their toxicity and environmental impact[72]. Evidently, there is a need to be able to characterise and detect engineered NPs both in the laboratory and in the environment. In the next section, techniques for the sizing, detection and characterisation of NPs will be discussed.

2.2 Characterisation and Detection Methods

2.2.1 Dynamic Light Scattering and Nanoparticle Tracking Analysis

Dynamic light scattering (DLS) and nanoparticle tracking analysis (NTA) utilise the diffusion of NPs to calculate their hydrodynamic radius. The hydrodynamic radius is related to the diffusion coefficient of the particle by the Stokes-Einstein equation:

$$D = \frac{k_B T}{6\pi\eta r_h}, \tag{1.78}$$

where k_B is the Boltzmann constant, η is the viscosity of the medium and r_h is the spherical hydrodynamic radius of the particle. It relates to the radius of a hard sphere that diffuses at the

same rate of the particle[73].The hydrodynamic radius differs to that of the true NP radius in aqueous solution as it has contributions from the particle core, the capping agent[74] and the hydration shell of the particle[75]. This means that the hydrodynamic radius is typically larger than that of the particle core and is illustrated schematically in Figure 2.9. The hydrodynamic radius tends towards the true radius for increasing particle size due to the reduced contribution of the surface structure to the radius in relation to the overall volume of the core particle.

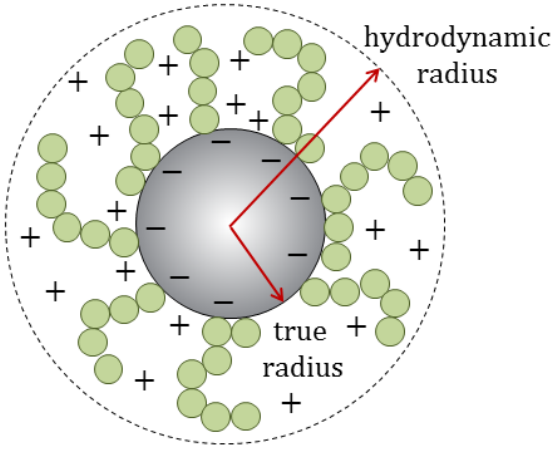


Figure 2.9 Schematic of a negatively charged nanoparticle (shaded) encased in a capping agent (green) defining the true and hydrodynamic radius

Dynamic light scattering (DLS) measures the fluctuations in the intensity of the Rayleigh scattering of bulk suspensions of particles. Figure 3.0 shows a schematic of a typical DLS set-up. Typically a Helium-Neon laser (λ_{max} = 633 nm) is directed at a suspension of NPs and the scattered light intensity is measured at different scattering angles, θ_{dls}, by a detector. The sample chamber is thermoregulated to prevent thermal oscillations during measurement as the diffusion coefficient of the particles is temperature sensitive. The scattered light intensity fluctuates with time around an average intensity value. This is due to Brownian motion of the particles which causes changes in the destructive and constructive wave interference pattern. The average scattered light intensity over the experimental timescale, $[Ɨ(q)]$, is given by[76]:

$$[Ɨ(q)] = lim_{t_k \to \infty} \frac{1}{t_k} \int_0^{t_k} Ɨ(q,t)\partial t \,, \tag{1.79}$$

where t_k is a given time, $Ⱨ(q,t)$ is the scattered light intensity at time t and the scattering vector, q, is:

$$q = \left(\frac{4\pi n}{\lambda}\right)\sin\left(\frac{\theta_{dls}}{2}\right), \tag{1.80}$$

where n is the refractive index of the solvent and λ is the wavelength of the incident light. For DLS measurements the total experimental time is assumed to give a value of $Ⱨ(q)$ that is representative of the average of the whole sample. The smaller a particle, the faster the thermal motion and hence the faster the intensity of scattered light measured fluctuates around the average value, $[Ⱨ(q)]$. The frequency of these fluctuations for a given scattering vector, q, is measured in terms of a correlation function, $c(q,\tau)$ [76]:

$$c(q,\tau) = lim_{t_k\to\infty}\frac{1}{t_k}\int_0^{t_k} Ⱨ(q,t).Ⱨ(q,t+\tau)\partial t\,. \tag{1.81}$$

The correlation function is calculated for a series of τ, where τ is the time delay between two consecutive signals. The value of $c(q,\tau)$ is at its maximum at $\tau = 0$. As the experiment progresses $c(q,\tau)$ decays as the fluctuations become less correlated. At sufficient timescales the fluctuations become statistically uncorrelated and $c(q,\tau) = [Ⱨ(q)]^2$. The decay of the correlation function, $c(q,\tau)$, occurs more rapidly for smaller particles (Figure 3.1) and can be used to calculate the average diffusion coefficient of the particles, *D*.

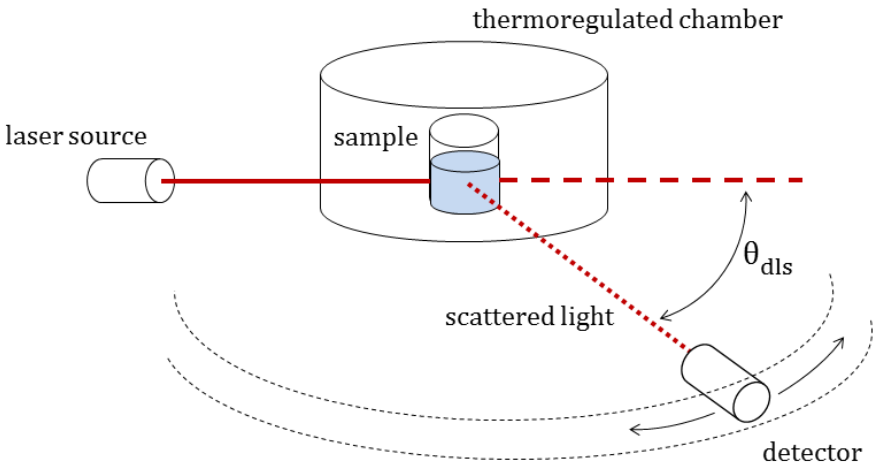


Figure 3.0 Schematic of a dynamic light scattering experiment [76]

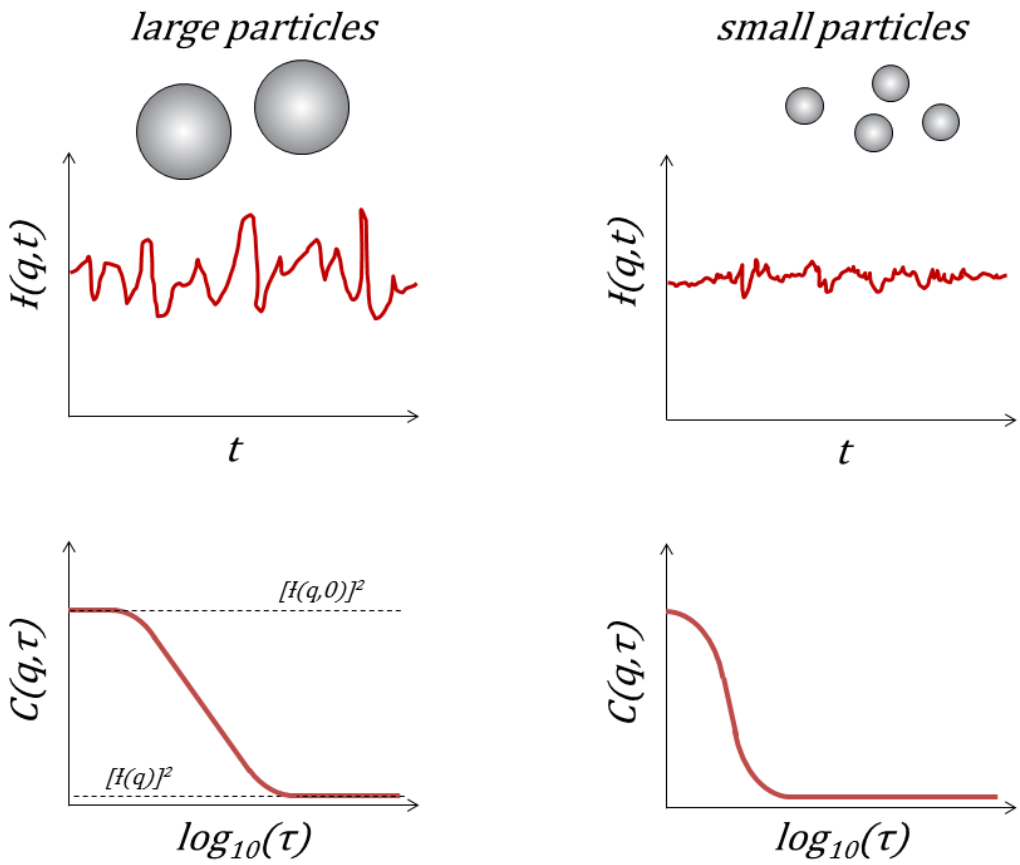


Figure 3.1 (Top) Schematic plot of the scattered light intensity, $Ɨ(q,t)$, as a function of time for large and small particles illustrating the increased frequency of signal fluctuations for smaller particles. (Bottom) Corresponding plots of the correlation function, $c(q,\tau)$, as a function of $\log_{10}(\tau)$ showing the faster rate of decay in the correlation function for smaller particles.

DLS allows for the fast sizing of particles with diameters between 0.6 nm to 10 µm and has found wide use due to its predominately automated operation[77, 78]. However, as the Rayleigh scattering of a particle is proportional to r_h^6, the calculated radius is weighted by V_p^2, where V_p is the particle volume[79]. This is particularly significant when considering particle distributions that are not monodisperse. Often the radius for a particle distribution is defined by the Z-average that is calculated through a summation of r_h for all particles detected and is the intensity weighted mean size of the particles. For a distribution with a single population maximum this is generally an accurate measure of the average r_h, however for bimodal distributions this value will be incorrect as the Z-average will lie somewhere in between the two

peak maxima. Studies have also suggested the reliability of technique for use on single particle populations with a high polydispersity is less than ideal due to the higher scattering contribution of larger particle within a given distribution [80].

Nanoparticle tracking analysis (NTA) utilises a laser to individually track suspended particles moving in suspension. Figure 3.2 shows a schematic of a typical NTA experiment. The laser is directed through the suspension of NPs and undergoes Rayleigh scattering. The scattered light is detected by a microscope coupled to a camera, which allows tracking of the Brownian motion of individual particles moving within the field of view. Each particle that is detected is therefore tracked in a two-dimensional plane over time to calculate a mean square displacement. This is related to the hydrodynamic radius of the particle by[81]:

$$\overline{(x,y)^2} = \frac{2tk_BT}{3r_h\eta} \tag{1.82}$$

where x and y are Cartesian co-ordinates and t is the time the particle is tracked.

NTA operates over a specific NP range of 10^6 to 10^9 particles mL^{-1} and allows sizing of particles from 10 to 2000 nm[82]. This range ensures there are a sufficient number of particles to detect to give a statistically valid value for the size of the particle without overloading the measurement. Unlike DLS, NTA can determine the concentration of NPs in solution. It does this by using the measured size of the particles and the number of particles detected during the experimental run-time to calculate the bulk NP concentration. However, samples may require dilution to ensure the tested suspension is within experimental ranges for particle number per unit volume. As NTA is not a bulk characterisation technique and particles are analysed individually this provides an apparent benefit over DLS for the sizing of polydisperse systems. This is because the diffusion coefficient is determined for each NP and hence reduces the bias of higher scattering of larger particles[80].

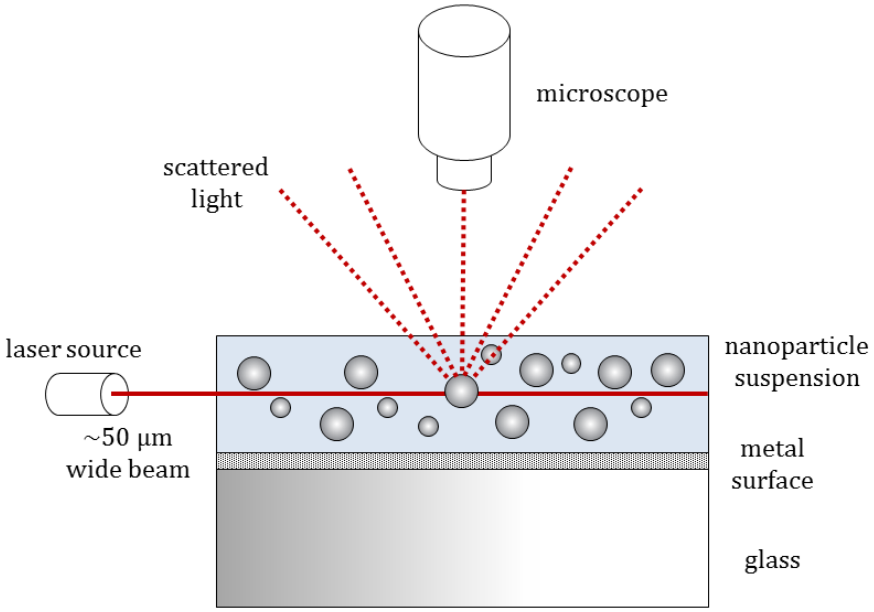


Figure 3.2 Schematic of a nanoparticle tracking analysis experiment

2.2.2 Ultraviolet-Visible Spectroscopy

Ultraviolet-visible spectroscopy (UV-Vis) comprises of a broad spectrum light source, typically a combination of a deuterium arc and tungsten lamp, to allow scanning of the incident wavelength between 190 and 1100 nm. During a measurement light is passed through both the sample and a reference solution and the relative absorbance is measured. The absorbance of a molecular species, A_{abs}, is described by the Beer-Lambert law[83]:

$$A_{abs} = \log_{10}\left(\frac{I_0}{I}\right) = \varepsilon c^* L\,, \tag{1.83}$$

where I_0 and I are the incident and transmitted intensity of the light at a given wavelength, ε is the dielectric constant and L is the path length. The use of a reference solution allows for the absorbance of the solvent to be subtracted from the unknown sample allowing the absorbance contribution from only the species of study to be obtained.

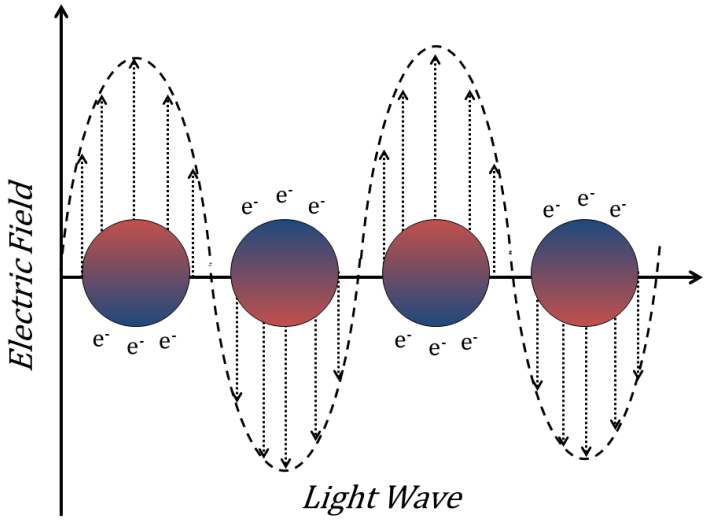


Figure 3.3 Schematic of the localised surface plasmon resonance effect for metallic nanoparticles illustrating the oscillations in the conduction band electrons at the nanoparticle surface in response to an incident light wave

When light interacts with a particle in suspension two processes can occur; absorption and scattering. The combination of these effects is referred to as the extinction[84]. Typically, for an incident wavelength range of 190 nm to 1100 nm NPs would not exhibit absorbance as the particles are too small compared to the wavelength of the light. For metallic NPs however, the absorption and scattering process are enhanced due to an effect known as localised surface plasmon resonance (LSPR)[85]. Figure 3.3 shows a schematic representation of the LSPR effect. The oscillating magnetic field of the incident light interacts with the conduction band of electrons at the particle surface. This results in a charge separation with respect to the ionic lattice forming a dipole oscillation[86]. The amplitude of this oscillation reaches a maximum value at a certain incident light frequency. This maximum is what is referred to as the LSPR and can be interpreted by Mie theory[87]. For the experimental study of particles, the LSPR can give characteristic information as it is affected by the electron density at the surface of the NP which in turn is affect by the material composition, size and shape[88].

UV-Vis spectroscopy of metallic NPs can provide information on the LSPR frequency and extinction cross-section. This can be related to the size of the particles[89] and allows

aggregation of the particles to be studied through analysis of peak broadening and/or shifting[90]. Typically the extinction maximum for a given particle material and geometry will shift to longer wavelengths for larger particles, and for aggregates/agglomerates will additionally cause an increase in the extinction cross-section.[91] Changes in particle geometry can be inferred through shifts in the extinction coefficient and the appearance of multiple LSPR maxima. This has been applied to the study of different geometries including nanorods[92], nanoprisms[93] and nanodisks[94]. It is the asymmetric geometry of these particles that gives rise to multiple LSPR signals; for example, a gold nanorod will exhibit dipole oscillations both along the longitudinal and transverse bands[95]. The oscillations along the longer axis will occur at higher wavelengths, so for a nanorod the longitudinal extinction maximum will occur nearer the IR region and the transverse extinction at lower wavelengths. UV-Vis can also be used to determine the concentration of NPs in a solution and has been reported for highly monodisperse gold NPs [96]. It is worth noting however that whilst UV-Vis is a powerful technique for the study of NPs in suspension, its use is limited to particles with strong extinction/LSPR characteristics (metallic NPs) i.e. gold[97] and silver[98].

2.2.3 Zeta Potential

The stability of NPs in suspension is important when considering their use for a given application[99]. Whether a particle will aggregate/agglomerate when added to a particular medium, or when present at a certain NP concentration, can have significant implications; for example, if used in biomedical applications NPs must remain monomeric in response to pH changes in different parts of the body so they can travel to their intended target[100].

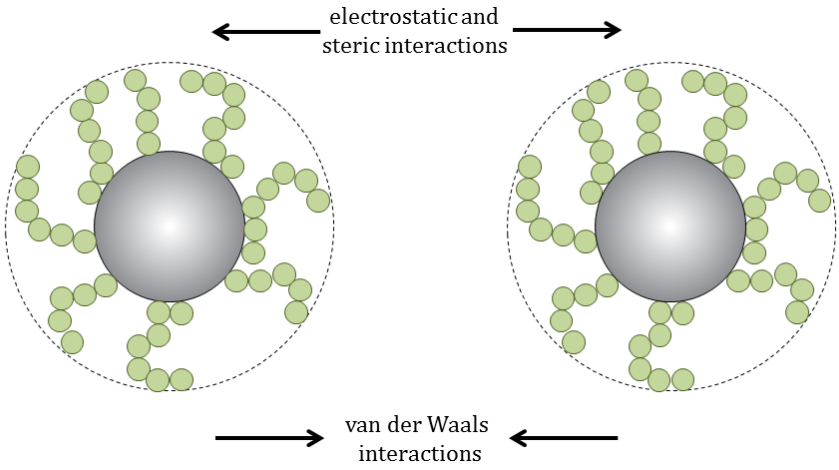


Figure 3.4 Schematic of the interactions between nanoparticles (shaded) encased in a capping agent (green)

Particles are attracted by van der Waals forces[101] and will proceed to "stick" together either irreversibly (aggregation) or reversibly (agglomeration)[102]. To maintain stability in suspension capping agents are used. Figure 3.4 illustrates the interactions between capped NPs. The attractive van der Waals interactions are negated by a combination of steric and electrostatic effects[103, 104]. Steric stabilisation is generally achieved by the use of polymers[105]. Increasing the steric bulk around the particle keeps sufficient distances between the cores preventing van der Waals interactions from dominating. This generally increases the hydrodynamic radius of a particle and can be determined by optical methods such as DLS (Section 2.2.1). However, care must be taken as increases in hydrodynamic radius does not always increase with increasing molecular weight of a polymeric capping agent[106]. Electrostatic stabilisation involves the repulsion of oppositely charged particles. The degree of electrostatic stabilisation can be measured by electrophoretic light scattering[107] and is quantified by the zeta potential of a particle, ζ. The zeta potential can be related to the electrophoretic mobility, U_e, of a particle in a given medium by:

$$U_e = \frac{2\varepsilon\zeta}{3\eta} f(\kappa a)\,, \tag{1.84}$$

where ε is the solvent dielectric constant, $f(\kappa a)$ is the Henry function and κa is the ratio of the Debye length and the NP radius. In a typical experiment a potential of $\pm$80 to 150 V is applied between two electrodes and the migration of the particles is measured by DLS. Zeta potential measurements give an approximation of the stability of the NPs with regard to agglomeration/aggregation. In general, particles with a zeta potential of $\leq \pm 10$ mV are not stable and will rapidly aggregate/agglomerate. Greater zeta potentials will give increasing stability with values $\geq \pm 30$ mV often indicating a high stability in a given medium. The zeta potential can be related to the thickness of the Debye layer of a particle by[108]:

$$\kappa = \left(\frac{e^2}{\varepsilon_0 \varepsilon k_B T}\right)^{\frac{1}{2}} (\zeta \rho + 2\psi_{salt} N_A)^{\frac{1}{2}}, \tag{1.85}$$

where ε_0 is the vacuum permittivity, ρ is the particle number density, ψ_{salt} is the ionic strength of the solvent and N_A is the Avogadro constant.

2.2.4 Electron Microscopy

Electron microscopy is a powerful technique for NP characterisation using electrons to probe the nanostructure of materials. As electrons have a shorter wavelength than light, NPs can be imaged, providing the experimentalist with information on the geometry and size of the particle[109]. The wavelength of electrons, and hence the achieved resolution, is determined by their kinetic energy as described by the de Broglie equation[110]:

$$\lambda_e = \frac{h}{\left[2m_e eV\left(1+\frac{eV}{2m_e c^2}\right)\right]^{\frac{1}{2}}}, \tag{1.86}$$

where λ_e is the wavelength of the electron, h is the Planck constant (6.626 x 10^{-34} N m s), m_e is the rest mass of an electron (9.109 x 10^{-31} Kg), eV is the kinetic energy of an electron (1.602 x 10^{-19} J) and c is the speed of light in a vacuum (2.998 x 10^8 m s^{-1}). For transmission electron microscopy (TEM) this is typically in the range of 100 to 400 keV[110], and for scanning electron microscopy (SEM) is less, usually between 2 to 40 keV[111].

All electron microscopic methods occur under vacuum. This is required to give electrons the highest mean free path possible, preventing electrons from colliding with mater before arriving at the sample. Figure 3.5 (left) shows a schematic of a TEM. During an experiment, an electron beam is generated by a filament (normally tungsten[110]). The electron beam is passed through a series of electromagnetic focusing lenses to the area of the sample under study. For a typical bright field image the TEM measures the transmitted electrons through their collision at a plate located beneath the sample. The difference in beam intensity is measured at the different pixels on the plate allowing imaging of the particle. Imaging of this type requires high electron energies, a thin sample (typically nanoscale thickness) and a high contrast (density difference) between the sample and the support.

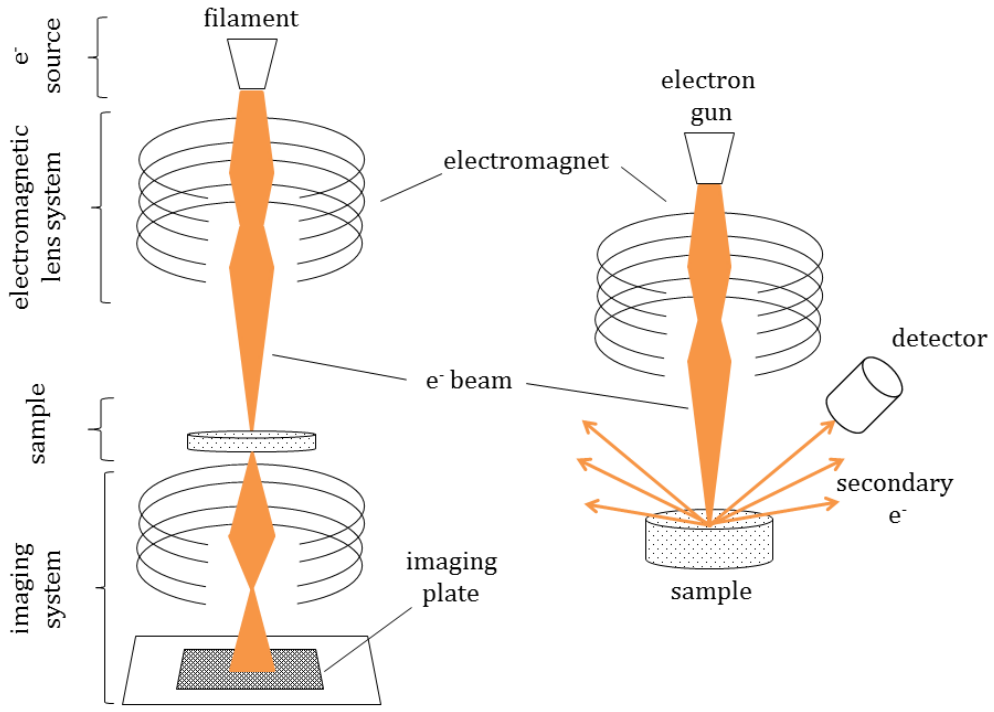


Figure 3.5 Schematic of a transmission electron microscope (Left) and a scanning electron microscope (Right).

Scanning electron microscopy (SEM) can provide topographical information for thicker samples with a penetration depth of around 1 μm[112]. Figure 3.5 (Right) shows the difference in

a SEM experiment compared to TEM. An electron beam is generated from a field emission gun[113] and is scanned across the surface of the sample. The main difference between the two measurements is that the detector is not located below the sample but above. As samples are generally thicker and electron energies are lower than TEM, the incident electrons interact more with sample. Figure 3.6 shows the tear-drop penetration profile of the beam and the different electron-sample interactions possible. The key interaction for SEM is that which produces secondary electrons; these are electrons that are ejected from the surface atoms of the sample due to inelastic scattering of incident electrons. Secondary electrons provide the highest special resolution as the interaction is limited to the top few layers of atoms which are located closely to the site of the incident beam. These electrons allow for high resolution imaging of NPs and are the electrons detected. Further information can be gained by SEM through the utilisation of other beam-sample interactions; some electrons penetrate further into the sample and are elastically scattered by atomic nuclei (back scattered electrons) and can provide composition information, often causing heaver elements to appear brighter in an SEM image than lighter elements[114]. As shown in Figure 3.6, X-rays, cathodoluminescence (CL) and electron beam induced current (EBIC) also result from electron beam irradiation of a sample and allow for more complex sample analysis[112]. For example, SEM can be coupled with energy dispersive X-ray spectroscopy (EDX) to gain the atomic composition of the material and even map this across a modified surface[115]. Through inelastic scattering of the incident electrons, core electrons can be ejected from the sample leaving behind “holes”. Electrons from higher energy shells fall in to these “holes” releasing energy in the form of X-rays. The wavelength of the X-ray corresponds to the gap between electric energy levels and therefore allows the identity of the atom to be confirmed.

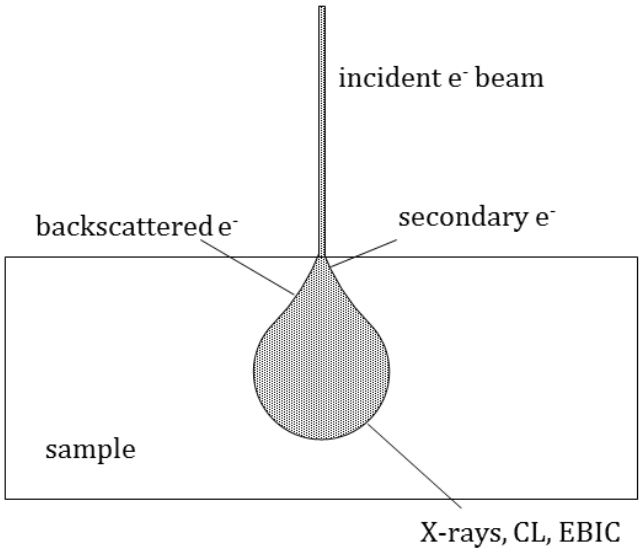


Figure 3.6 Illustration of the sample-beam interactions in scanning electron microscopy[112]

A drawback of electron microscopic techniques is the operational costs which far exceed that of optical methods. Additionally, the need to prepare dry NP samples on a suitable substrate for imaging means results are not always comparable to the solution phase, especially in terms of aggregation/agglomeration behaviour[116]. Organic materials are an added complication, requiring staining with metallics to provide a suitable electron optical contrast which can lead to artefacts[117].

2.2.5 Stripping and Dissolution Voltammetry

Electrochemical techniques are a widely employed method of studying NPs which are electroactive[118-120]. Through the oxidation or reduction of NPs deposited on an electrode surface, characteristic information can be gained through their redox potential, serving as a voltammetric "fingerprint"[121]. Electrode modification is carried out by dispersion of the target NPs in a solvent. This is then drop-casted onto the electrode surface and left to dry. Linear or cyclic voltammetry is then used to generate a current peak, the area of which corresponds to the total amount of material on the surface (assuming complete oxidation or reduction of the NPs). This is known as stripping voltammetry and has been widely applied for the characterisation of

nanomaterials[122, 123]. Studies have shown this method can be applied to calculate the relative composition of materials in an alloy[124] or core-shell particle[125]. By obtaining values for both the complete oxidation of the particle and of the surface layer formed when in alkaline solution, it is also possible to size Ni NPs and determine their concentration[126]. Coverage is important in determining the resultant voltammetry. For electrochemically reversible systems like Ag/Ag^+ higher coverage causes an increase in the overlap of diffusion layers for the formed Ag^+ leading to a higher overpotential for oxidation[127]. For irreversible systems the peak potential is thought to be independent of the size of the NPs and the coverage as the system is insensitive to the solution phase concentration of ions [128].

Whilst numerous studies have shown that stripping voltammetry can provide useful information for selected systems, quantification of NP concentrations on an electrode surface by such methods have been reported to be significantly affected by surface agglomeration/aggregation of the particles[38, 39, 129, 130]. Studies by Toh *et al.* report that the degree of surface aggregation/agglomeration of the particles is affected by the specific capping agent used[38, 39, 129, 130]. During voltammetric stripping, the particles closest to the electrode are electrolysed and particles positioned away from the electrode in the surface agglomerates/aggregates are lost to solution. This can lead to smaller stripping peaks than expected for 100 % oxidation or reduction, and an underestimation in the surface concentration of the particles.

An alternative method that avoids issues of surface agglomeration/aggregation is the voltammetric study of pre-dissolved NPs. The ions formed by dissolution can be analysed by voltammetry as discussed in Section 1.6.2 to calculate the ion concentration and hence the NP concentration (if the size of the NPs has been previously determined by other methods). This has been applied predominately to metallic NPs [131, 132], however by dissolving the NPs any size information is lost.

2.2.6 Nano-Impact Voltammetry

The electrochemical characterisation and detection of NPs discussed in Section 2.2.5 involved the analysis of an ensemble of NPs. However, recent studies have revolutionised this field with the development of electrochemical single NP detection.

The development of NP solution phase electrochemistry began with Micka[133] and his work on cobalt and nickel sulphide suspensions, and was developed more recently by Heyrovský, with his papers on TiO_2[134, 135] and SnO_2[136] ultra-small colloids. In Heyrovský's pivotal work, reduction waves were detected during the cyclic voltammograms which were attributed to the reduction of H^+ on an *ensemble* of particles colliding with an electrode. The hydrogen atoms formed were shown to go on to reduce Ti(IV) to Ti(III) in the case of the TiO_2 colloidal suspensions and reduce Sn(IV) to metallic Sn in SnO_2 colloids. This laid the groundwork for both electrocatalysis on impacting particles and their direct electrolysis. Many years later, this idea was revisited by Bard *et al*, with the first reported detection of *single* NP electrocatalysis by the *indirect-impact* method[137]. By holding a gold microelectrode at a suitable oxidative potential in a solution containing both platinum NPs and hydrazine, current-steps were detected. This was attributed to individual platinum NPs colliding with the electrode surface, enabling the electrocatalytic oxidation of hydrazine on single NPs. Figure 3.0 shows a schematic of a platinum NP colliding with an electrode under these conditions and the typical current-time response obtained. The height of these steps can be related to the size of the particles by the equation:

$$I_{step} = 4\pi\,(\ln 2) nFDc^* r_{np}\,, \tag{1.87}$$

where I_{step} is the increase in current during the step, assuming diffusion controlled electrolysis of the solution phase species to the particle. Through the analysis of multiple nanocollision steps, a size distribution was obtained and was found to agree with independent TEM analysis. As the potential dependence of the current-steps related to the potential of hydrazine oxidation on platinum, this technique demonstrated how electrochemistry could be used to both

characterise, size and detect individual NPs in solution, offering distinct advantages over stripping and dissolution voltammetry.

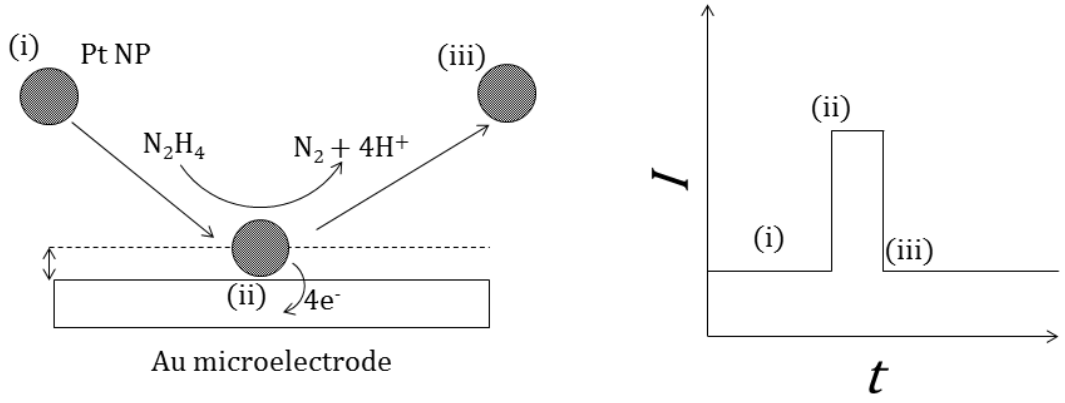


Figure 3.7 (Left) Schematic of a *indirect-impact*, showing the electrocatalytic oxidation of hydrazine on a Pt NP. (Right) Plot of a characteristic current-step observed during a current-time transient (i) NP beyond electron tunnelling distance (ii) NP within electron tunnelling distance allows electrocatalysis to occur (iii) NP leaves electrode and current drops

Despite the application of this method for the sizing and characterisation of NPs, continued research focused on the application of this technique to the electrochemical probing of surfaces[138-140]. The application of single NP voltammetry to the sizing and characterisation of NPs was not truly realised until the detection and sizing of electroactive NPs was reported without the need for a solution phase redox system. So called "*direct-impact* voltammetry" was first demonstrated by Compton *et al*, with the quantitative sizing of individual Ag NPs[141]. Figure 3.1 shows a schematic of a Ag nano-impact and the typical current-time response obtained. When a NP proceeds by Brownian motion within the tunnelling distance of the electrode, electrons are transferred from the particle to the electrode resulting in the direct oxidation of the particle itself. The total oxidation of the particle results in a characteristic spike as shown. Assuming a spherical geometry, the charge passed per current spike can be related to the radius of the NP by the equation:

$$r_{np} = \sqrt[3]{\frac{3A_rQ}{4nF\pi\rho}}, \tag{1.88}$$

where A_r is the atomic mass, Q is the charge and ρ is the bulk density of the material.

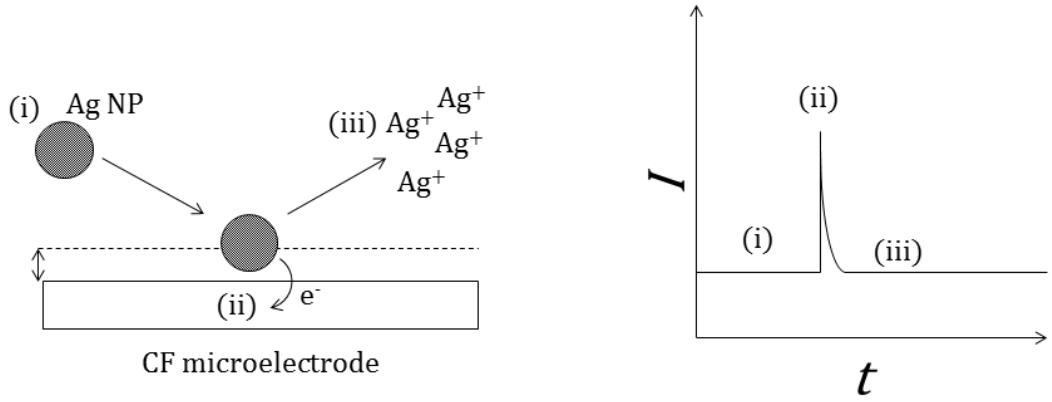


Figure 3.8 (Left) Schematic of a *direct-impact*, showing the electrochemical oxidation of a Ag NP to Ag^+ at a carbon fibre (CF) microelectrode. (Right) Plot of a characteristic current-spike observed during a current-time transient (i) NP beyond electron tunnelling distance (ii) NP within electron tunnelling distance allows oxidation to occur (iii) Complete oxidation of NP results in no current passing

Since the initial sizing of Ag NPs, a host of nanomaterials have been characterised by the *direct-impact* technique. In aqueous solution these include; metallic NPs such as copper[142] and gold[143, 144]; iron oxide[145]; organic dyes[146] and polymers[123]; and even biological systems such as bacteria and viruses[147, 148]. The *direct-impact* method has also been successfully applied to the detection and sizing of particles in non-aqueous systems by Stuart *et al,* through the quantitative sizing of buckminsterfullerence (C_{60}) in an acetonitrile/n-methyl-2-pyrrolidone mixture[149] and by Tanner *et al* through the detection of Ag NPs in room temperature ionic liquids[150]. The detection of surface functionalised NPs have also been reported, allowing the coverage of the adsorbed species to be quantified[151]. This method has been applied to great affect by Plowman *et al.* for the study of gold nano-rods[92]. In this study *direct-impacts* of 1,4-nitrothiophenol (NTP) functionalised nano-rods were carried out to quantify the coverage of NTP per particle. Knowing the packing density for the specific tag, this allowed the surface area of the NP to be determined and, in conjunction with the volumetric information gained from the

direct electrolysis of the Au nanorod, permitted determination of both the size and aspect ratio of the particle.

In *direct-impact* voltammetry, the potential required for the oxidation/reduction of a NP can be used to identify its composition. This has been reported to be of particular use in the characterisation of Au@Ag core-shell NPs[152]. Here, the stripping voltammetry of Au@Ag and pure Au NPs was compared in 20 mM HCl electrolyte. The core-shell particles were shown to undergo an oxidation process at a less positive potential to that of the pure Au NPs due to the presence of the Ag shell. Nano-impact experiments were then conducted on the core-shell particles at different potentials to obtain a plot of the average spike charge dependence with potential. The result showed spikes inherent of *direct*-impact events with two distinct potential regions; the first from 0.7 to 0.9 V vs SCE resulted in spikes attributed to the oxidation of the Ag shell; and the second from 1.2 to 1.4 V vs SCE giving spikes with a charge equal to the sum of the oxidation of the Ag shell and Au core. Assuming a spherical geometry this allowed the radius of the core and the thickness of the shell to be determined, which agreed with independent TEM analysis. The use of nano-impacts for the characterisation of bi-metallic NP compositions has also more recently been reported for the case of Ag/Au alloy particles[153].

The *direct-impact* technique, in addition to finding use in NP sizing and characterisation, has also been applied to the study of the physical properties of NPs. The study of Cu NP impacts concluded a need for an overpotential for the oxidation of NPs and allowed Butler-Volmer electron transfer coefficients to be determined from impact data[142]. Nano-impact experiments were also shown to be able to resolve the reversible and irreversible kinetics of Ag and Ni NPs respectively[154]. Solution phase aggregation behaviour of NPs has been detected by the *direct-impact method*[155] and introduced the possibility of using nano-impacts to study agglomeration/aggregation behaviour. More recent studies have also alluded to possible benefits of nano-impacts in quantifying such agglomeration/aggregation states over optical methods such as DLS and NTA[102, 116, 156].

The nano-impact technique offers significant improvements over conventional electrochemical, optical and electron microscopic techniques as it allows for the detection, characterisation and sizing of single NPs in the solution phase. The use of electrochemistry offers improvements in cost over optical and electron microscopy routes due to the inexpensive equipment required and lack of high maintenance costs, and inherently is not affected by optical clarity of the solution[157]. Previous studies have shown the benefits of using *direct-impacts* for the characterisation of particles over stripping voltammetry due to the negation of surface agglomeration/aggregation effects [38, 39, 129, 130] and have shown it can be applied to the detection of NPs in environmental media[158].

This thesis introduces new concepts to the study of NPs by the *direct-impact* method. Critically, this thesis aims to use the special chemistries of metal halide and metal oxide NPs to expand the application of nano-impacts beyond quantitative sizing towards the study of agglomeration behaviour, the tracking of chemical and photochemical conversion reactions, the mechanistic determination of NP growth during synthesis, and for the fabrication of nanoelectrode arrays. This thesis also looks at the improvement in detection limit achievable for the *direct*-impact of Ag NPs by the use of forced convection over diffusional only mass transport reported hitherto. The next chapter covers the experimental methods and techniques used throughout this thesis.

Chapter 3

Experimental Methods

This chapter details the chemical reagents and NPs used throughout the work conducted herein. The NP synthesis methods, experimental techniques and equipment applied are also covered. Other very specific experimental methods are detailed alongside the relevant works in the subsequent chapters.

3.1 Chemicals

The chemical reagents used throughout this thesis are detailed in Table 1. For Sections 4.2, 5.1 and 7.2, NPs were purchased from suppliers, as shown in Table 2. A detailed list of supplier information can be found in Table 3.

Chemical Name	Formula	Purity	Supplier	Section
Potassium nitrate	KNO_3	99.5 %	VWR	4.1
		≥99.0 %	Sigma Aldrich	6.2
Mercury(I) nitrate dihydrate	$Hg_2(NO_3)_2{\cdot}2H_2O$	99 %	Sigma Aldrich	4.1
Nitric acid	HNO_3	70 %	Sigma Aldrich	4.1
Silver nitrate	$AgNO_3$	≥99.0 %	Sigma Aldrich	4.2, 6.1, 6.2, 7.1
Hexaammineruthenium(III) chloride	$[Ru(NH_3)_6]Cl_3$	98 %	Sigma Aldrich	4.2
Potassium chloride	KCl	99 %	Sigma Aldrich	4.2, 7.2
Sodium bromide	NaBr	99 %	M&B Laboratories	4.2, 6.1, 7.1
Gelatine powder	N/A	N/A	VWR	4.2
Sodium hydroxide	NaOH	≥97 %	Sigma Aldrich	5.1
Sodium bicarbonate	$NaHCO_3$	99.7-100.3 %	Sigma Aldrich	6.1
Ascorbic acid	$C_6H_8O_6$	99+ %	Sigma Aldrich	6.1
Sodium carbonate	Na_2CO_3	99.9 %	BDH	6.1

Nanopure water	H_2O	N/A	Alfa Aesar	6.2
Sodium borohydride	$NaBH_4$	N/A	Fisher	6.2
Tri-sodium citrate	$Na_3C_6H_5O_7$	99.0 %	BDH	6.2
bis (p-sulfonatophenyl) phenylphosphine dehydrate dipotassium (BSPP)	$C_{18}H_{13}K_2O_6PS_2 \cdot 2H_2O$	97 %	Sigma Aldrich	6.2
Potassium bromide	KBr	≥99.0 %	Sigma Aldrich	7.1
Potassium phosphate monobasic	KH_2PO_4	≥99.0 %	Sigma Aldrich	7.1
Potassium phosphate dibasic	K_2HPO_4	≥98 %	Sigma Aldrich	7.1
Hydrogen Peroxide	H_2O_2	>30 % w/v	Sigma Aldrich	7.1
Potassium Ferrocyanide	$K_4Fe(CN)_6$	99.0 %	BDH	7.2

Table 1 List of chemical reagents

Material	Purity	Diameter	Concentration	Supplier	Section
Citrate-capped silver (suspension)	N/A	100	0.02 mg mL^{-1}	nano ComposiX	4.2
	N/A	50	0.02 mg mL^{-1}	nano ComposiX	7.2
Bismuth oxide (nanopowder)	+99.8 %	38	N/A	Nanophase	5.1

Table 2 List of nanoparticles purchased from suppliers

Company Name	Address
Alfa Aesar	Lancashire, United Kingdom
BASi	West Lafayette, IN, USA
Buehler	Coventry, United Kingdom
BDH	Poole, United Kingdom
Fisher	Loughborough, United Kingdom
Goodfellow Ltd	Cambridge, United Kingdom
M&B Laboratories	Sydney, Australia
nanoComposiX	San Diego, CA, USA
Nanophase	Romeoville, IL, USA
Sigma Aldrich	Dorset, United Kingdom
VWR	Soulbury, United Kingdom

Table 3 List of chemical reagent, nanoparticle and electrode suppliers

3.2 Electrochemical Instrumentation

A three-electrode system was used for all electrochemical measurements. Tables 4 and 5 outline the different working, reference and counter electrodes used in each section. Prior to experimentation, all working electrodes were polished with 1, 0.3 and 0.05 μm alumina powder (Buehler, United Kingdom). Either an Autolab PGSTAT 302N (Metrohm-Autolab, Netherlands) with an ECD module or an in-house built low noise potentiostat[159] (4 kHz bandwidth, 1 GVA^{-1} gain) were used throughout. All electrochemical experiments were performed in a thermostated Faraday cage held at 25 ^{o}C. Solutions were prepared using Millipore water of resistivity 18.2 MΩ cm at 298 K and were degassed with nitrogen before experimentation (unless otherwise stated).

An in-house Ag/AgCl reference electrode was used in Sections 4.1 and 7.2, as was constructed as follows. A Ag wire (Goodfellow Ltd., United Kingdom) was cycled by cyclic voltammetry in 0.10 M KCl to obtain a layer of AgCl. The wire was then immersed into a polyether ether ketone (PEEK) cylinder, with a polymeric frit at one end, containing 3 M KCl.

The wire was secured using Parafilm and the potential was checked against a commercial saturated saturated mercury-mercury chloride (SCE) reference electrode.

Electrode	Radius	Supplier	Section
Platinum microdisk (WE)	5.0 μm	BASi	4.1
Carbon fibre microdisk (WE)	5.5 μm	BASi	4.1
	5.6 μm	BASi	4.2
	3.5 μm	BASi	5.1, 6.1, 6.2, 7.1
Glassy carbon macrodisk (WE)	1.5 mm	CH Instruments	4.1, 4.2, 5.1, 6.1
	2.08 mm	In-house	7.2
Random array of microelectrodes (WE)	6 mm (3.5 μm per fibre)	Prof. Stephen Fletcher Loughborough University	4.1, 7.2
Platinum wire (CE)	N/A	Goodfellow Ltd.	4.1, 4.2, 5.1, 6.1, 6.2, 7.1
Graphite rod (CE)	N/A	Sigma Aldrich	7.2

Table 4 List of working and counter electrodes used

Reference Electrode	E vs. NHE	Supplier	Section
Silver-silver chloride (Ag/AgCl, 3M KCl)	+0.241 V	In-house	4.1, 7.2
Saturated mercury-mercury chloride (SCE)	+0.24 V	BASi	4.2, 7.1
Saturated mercury-mercury sulphate (MSE)	+0.64 V	BASi	4.2, 5.1, 6.1, 6.2

Table 5 List of reference electrodes used

3.3 Non-Electrochemical Methods

3.3.1 Ultraviolet-Visible Spectrometry

UV-Vis spectra were performed in section 6.1 on a U-2001 spectrometer purchased from Hitachi (Mannheim, Germany) using 10 mm UV glass cells from Hellma Analytics (Essex, UK). In section 6.2 studies were performed in 2 mm width quartz cells using a UV-1800 SHIMADZU UV spectrophotometer (Kyoto, Japan). The bulb transition was set to 300 nm with a 1 nm sampling frequency.

3.3.2 Scanning Electron Microscopy

In Section 4.2, images of the AgBr and Ag NPs were obtained using a high resolution SEM (LEO Gemini 1530, Zeiss). NP suspensions were sonicated for 5 seconds prior to drop-casting onto a TEM grid modified SEM sample holder. In Sections 5.1 and 7.1, imaging was conducted on glassy carbon sheets (Sigma Aldrich, United Kingdom) using a JeoL JSM-6500F field emission SEM at 5 and 10 keV respectively. For the EDX characterisation of the AgBr NPs and Ag nano-deposits in section 7.1, an EDAX EDX with 10 mm^2 Si-Li window was used. Image J software was used for sizing of all SEM images. Sizing distributions and images of the NPs can be found in the relevant sections. SEM images were performed in collaboration with Dr. K. Tshulik (formerly Department of Chemistry, Oxford University), Dr. K. Jurkschat, Ms J. Holter and Dr. N. Young, (Department of Materials, Oxford University, UK).

3.3.3 Transmission Electron Microscopy

A JeoL 3000F field emission gun TEM was used for imaging of the Hg_2Cl_2 NPs in Section 4.1. A Jeol 3000F 300 keV TEM was used for imaging the Ag nanoprisms in section 6.2 after drop-casting the material onto TEM carbon holey grids. Image J software was used for the sizing of all TEM images. Sizing distributions and images of the NPs can be found in the relevant sections. TEM images were performed in collaboration with Mr. C. Salter, Ms J. Holter and Dr. N. Young (Department of Materials, Oxford University, UK).

3.3.4 Nanoparticle Tracking Analysis

NPs in Sections 4.2 and 5.1 were characterised by NTA using a Malvern Nanosight LM10 (Malvern, United Kingdom) equipped with a 638 nm laser. Measurements were taken over 60 seconds at a frame rate of 30 frames per second and the data was analysed using NTA 2.3 software.

3.4 Nanoparticle Synthesis

3.4.1 Mercury(I) Chloride Nanoparticles

In Section 4.1, mercury(I) chloride NPs are synthesised for comparison with electrolytically generated particles. A solution of 0.10 M KNO_3 and 0.020 M KCl (19.5 mL) was stirred at 800 rpm in a glass beaker via use of a magnetic stirrer bar. To this, 573 µL of 10 mM $Hg_2(NO_3)_2$ in 0.5 % wt. HNO_3 was added drop wise over 7 minutes to form a white suspension. The NP suspension was sonicated before each electrochemical measurement to dis-agglomerate the particles. The NPs were imaged by TEM (Section 3.3.3) to obtain low and high magnification bright field images (Section 4.1). Large plate like crystallites were observed and attributed to KCl and KNO_3 crystal formation. Smaller particles attributed to Hg_2Cl_2 NPs were also seen in addition to the larger crystallite structures. The size range of the NPs was determined to be approx. 20 – 35 nm radius. Significant fading of the NP image was observed over 60 seconds and was attributed to deterioration of the NPs as a result of reduction by the electron beam.

3.4.2 Silver Bromide Nanoparticles

Silver bromide NPs were synthesised for use in sections 4.2, 6.1 and 7.1 and were prepared as previously reported by Johansson *et al*[160]. A 25 mL three necked flask containing 0.75 g gelatine in 10 mL water was heated to 35 ^{o}C and stirred at 350 rpm by a magnetic stirrer. To this, 5 mL of 2.0 M $AgNO_3$ and 5 mL 2.0 M NaBr were injected simultaneously and left to stir for 5 mins. The resulting suspension was transferred to a Faulken® tube and kept in dark

conditions. The set-up and storage vessel were encased in foil throughout to minimise light exposure. Sizing distributions and images of the NPs can be found in the relevant sections.

3.4.3 Silver Nanoprisms

In Section 6.2, the photochemical synthesis of silver nanoprisms is studied. The method used for the synthesis of the prisms was as previously reported[161], but with a 18 Watt fluorescent tube light source. The emission spectrum was measured using an Ocean Optics 2000 UV-Vis spectrometer (Dunedin, FL, USA) and is shown in Section 6.1.

A 250 mL conical flask containing 95 mL nanopure water, 1 mL 30 mM trisodium citrate and 2 mL 5 mM $AgNO_3$ was immersed in an ice bath and bubbled with N_2 for 30 mins. After this, 1 mL 50 mM $NaBH_4$ was added under vigorous stirring, induced by magnetic stirrer, to begin the initial reduction. Over the next 16 mins, 4 drops of the $NaBH_4$ solution were added every 2 mins to ensure $AgNO_3$ reduction reached completion. Next, 1 mL 5 mM BSPP and 0.5 mL 50 mM $NaBH_4$ were simultaneously added dropwise over 5 mins. The reaction was left vigorously stirring overnight in the dark. The next day, the photochemical conversion was initiated by positioning the flask at 135 mm from the light source described. The reaction mixture was not stirred during conversion. Samples were taken at 24 hour intervals and stored in the dark at (5.0 ± 0.2) ^{o}C.

Chapter 4

Nano-Impact Voltammetry of Metal Halide Nanoparticles

In this chapter we report how the nano-impact technique can be applied to detection and quantitative sizing of metal halide NP systems through the example of two cases; mercury(I) chloride and silver bromide.

In Section 4.1, mercury(I) chloride (Hg_2Cl_2) NPs are synthesised for the first time by two different techniques. First, particles are formed by implosion of a calomel nanolayer induced by partial electrolysis at a mercury hemisphere microelectrode. The resulting NPs are then characterised by the nano-impact method, the first time metal chloride NPs have been sized by this technique, and showing the ability to form and study NPs in situ. Second, Hg_2Cl_2 NPs are synthesised by the precipitation reaction of $Hg_2(NO_3)_2$ with KCl. The NPs are characterised on both mercury and carbon microelectrodes and their size found to agree with TEM results. This work has been published in *ChemElectroChem*[162].

In Section 4.2, two complementary studies on silver and silver bromide NPs are used to assess the large radius limit of the nano-impact method for NP sizing. Noting that by definition a NP cannot be larger than 100 nm in diameter, it is shown that the method quantitatively sizes at the largest limit, the lower limit having been previously reported as ~6 nm[159]. This work has been published in *ChemistryOpen*[163].

4.1 Metal-halide Nanoparticle Formation: Electrolytic and Chemical Synthesis of Mercury(I) Chloride Nanoparticles

4.1.1 Introduction

The development of metal halide (MX) nanoparticle synthesis methods is crucial for the continued investigation of their photocatalytic properties[164] and to provide intermediates for forming otherwise inaccessible main group NPs such as selenium and bismuth[165, 166]. Despite this, the formation of mercury halide NPs in particular mercury(I) chloride (calomel, Hg_2Cl_2) has yet to be reported. Calomel plays an important role in large scale industrial processes including the cleaning of mercury vapour from flue gas in the production of sulphuric acid and zinc[167]. In addition, Hg_2Cl_2 is known to form photochemically in the environment from elemental mercury pollutants[168]. Nanoscale mercury compounds are also well documented, the most prominent of which are elemental mercury particulates in the atmosphere[169]. The study of Hg_2Cl_2 and its ability to form nanostructures is therefore of both environmental and industrial significance, but first requires the development of a suitable synthesis method.

Mono-disperse MX NPs can be synthesised with a narrow size distribution however such methods require the use of water in oil micro-emulsions, stabilising the NPs within a reverse micellar structure[170-172]. Other methods include the controlled precipitation of metal halides in aqueous media, for example AgBr NP suspensions stabilised in solution by materials such as gelatine[160] and cucurbit[n]uril macrocycles[173]. Although the area has seen significant development there are few examples for the formation of particles of size 20-100 nm without complex multi-step chemical processes and stabilising organic coatings[174]. The use of stabilising materials has also been shown to effect the size of the NP depending on the sample preparation for analysis, with drying of the NPs resulting in significantly different structures to that in suspension[173].

A new method for the analysis of NPs in suspension is the electrolysis of individual NPs by the nano-impact technique[175, 176]. This involves the characterisation of NPs by their interaction with an electrode when colliding under Brownian motion. Depending on the NP and the presence of relevant redox species this can result in either indirect catalytic processes or direct electrolysis of the NP. These two methods were previously covered in Section 2.2.6. To date no metal halide NPs have been detected or characterised by the *direct-impact* method.

Utilisation of the nano-impact technique could allow for the formation and immediate electrochemical characterisation of NPs at an electrode surface without the need for stabilising organics or micro-emulsions. Work by Kublik *et* al. has shown that the formation of calomel on mercury electrodes can become self-limiting, preventing dissolution of mercury under oxidising potentials and inherently limiting the size of the calomel crystals formed[177]. Other studies have shown calomel crystallites can be spontaneously incorporated into mercury electrodes during the formation of mercury thin-films in the presence of millimolar concentrations of chloride[178]. With control over the size of the crystallites formed, mercury electrodes could be prepared with NPs ready for electrolytic release in to solution. Such a release mechanism has been previously demonstrated with millimetre sized Hg_2Cl_2 particles[179]. These were shown to detach from mercury electrodes when exposed to a reductive potential, resulting in milliamp size cathodic spikes in current. The partial reduction of calomel particles when an reductive overpotential is applied has previously been shown to result in the incomplete reduction of calomel particles and allows for this detachment[180]. Adaptation of this mechanism to the nanoscale would allow for a novel controlled release method for NPs and allow for in situ characterisation by the nano-impact technique.

The ease of calomel formation and the ability to eject particles from an electrode surface in to solution could allow for the development of a controlled synthesis method for fabricating Hg_2Cl_2 NPs in solution, which is the focus of the work herein. This Chapter reports the development of a novel synthesis method for metal halide NPs by the electrochemically induced

disintegration of a metal halide layer on the nanoscale to form NPs of comparable size. The resultant particles are then characterised by their individual electrolysis allowing for the formation and study of these NPs in situ. This proposed mechanism is then compared with the characterisation of chemically synthesised Hg_2Cl_2 NPs by their collision with mercury and carbon electrodes and the implications discussed.

4.1.2 Experimental

4.1.2.1 Mercury Hemisphere Preparation

Mercury hemispheres were formed by electrodepositing mercury onto platinum microdisk electrodes in a solution of 10 mM $Hg_2(NO_3)_2$ in 0.5 % wt. HNO_3 as has been previously reported in the literature[181, 182]. The deposition was conducted at -0.245 V (vs Ag wire) until a charge of 1.72 μC was passed, corresponding to the charge needed for the Faradaic reduction of Hg(I) to form a hemisphere of Hg(0) on an electrode of 10 μm diamater (approx. 30 seconds). After formation the mercury hemisphere was voltammetrically cycled in 0.10 M KNO_3 and 20 mM KCl between -0.10 V and -0.40 V (vs Ag/AgCl) at 25 mVs^{-1} until a voltammogram was obtained whereby no reductive features were observed across the potential range. The electrode was characterised electrochemically by use of 1.0 mM hexaaammineruthenium(III) chloride in 0.10 M KNO_3 before and after deposition to ensure a $\pi/2$ relationship in limiting current consistent with change in the diffusional regime from a microdisk to a hemisphere[1]:

$$I_{lim}(disk) = 4r_e nFDc^*, \tag{1.89}$$

$$I_{lim}(hemipshere) = 2\pi r_e nFDc^*, \tag{1.90}$$

where r_e is the radius of the electrode, n is the number of electrons, F is the Faraday constant, D is the diffusion coefficient of the redox species and c^* it's concentration in the bulk solution. The diffusion coefficient was taken to be 8.0 x 10^{-10} m^2 s^{-1} [183].

4.1.2.2 Nanoparticle Synthesis and Characterisation

The synthesis and imaging of mercury(I) chloride NPs is covered in Sections 3.4.1 and 3.3.2 respectively. Low and high magnification bright field images of the particle were taken with the assistance of Mr C. Salter (Department of Materials, Oxford University), and are shown in Figure 3.9. Large plate like crystallites were observed and attributed to KCl and KNO_3 crystal formation. Smaller particles attributed to Hg_2Cl_2 NPs were also seen in addition to the larger crystallite structures. Figure 4.1 (right) shows a zoomed in image of a larger crystal showing it to be an aggregate of smaller NPs. This indicates aggregation probably as a result of drying of the sample for TEM measurements. In excess of 50 NPs were counted and the size distribution determined to be approx. 20 – 35 nm radius. Significant fading of the NP image was observed over 60 seconds and was attributed to deterioration of the NPs as a result of reduction by the electron beam.

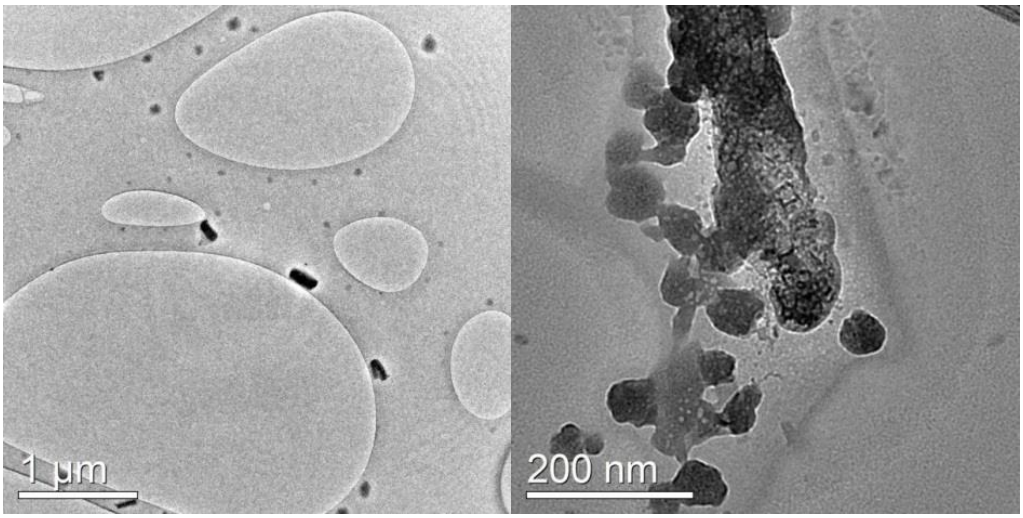


Figure 3.9 TEM images of Hg_2Cl_2 NPs synthesised by precipitation from $Hg_2(NO_3)_2$ in 0.10 M KNO_3 and 20 mM KCl at low (Left) and high (Right) magnification

Analysis of NP impacts from time-current transient measurements was carried out using Signal Counter software[184] and all histograms reported are from analysis of at least 300 impact events. Sizing of the NPs assumes the formation of spherical NPs in all cases in accordance with that found from TEM characterisation.

4.1.3 Results and Discussion

The redox chemistry of a mercury hemisphere microelectrode is first studied in chloride containing media to understand the formation and composition of a porous nanolayer of Hg_2Cl_2 at the electrode surface. Next a reductive overpotential is applied to produce cathodic spike features as a result of single NP electrolysis, observable by current time transient measurements. The origin of these features are discussed and their cause determined by the study of the effect of reductive overpotential on the frequency of the features observed. A mechanism is then proposed and supported by the direct electrolysis of Hg_2Cl_2 NPs, synthesised by chemical precipitation, on both mercury and carbon microelectrodes.

4.1.3.1 In-situ Formation and Detection of Hg_2Cl_2 NPs on a Mercury Hemisphere Microelectrode

A mercury hemisphere microelectrode of diameter 10 μm was prepared and its redox chemistry studied via cyclic voltammetry in 0.10 M KNO_3 and 3 mM KCl from -0.40 V to +0.32 V (vs Ag/AgCl) at 25 mVs^{-1}. An oxidative peak was observed at +0.28 V and a corresponding reduction peak at +0.20 V, as shown in Figure 4.0 (Top). When the voltammetric response was studied as a function of KCl concentration from 3 to 1000 mM, a shift in both oxidative and reductive peak potential resulted. Figure 4.0 (Bottom) shows the oxidative, reductive and mid peak position as a function of KCl concentration and shows the peak potential to shift by (61.5 ± 3.4) mV per decade increase in KCl, evidencing KCl involvement in the process. An increase in oxidative peak current with increasing KCl concentration was also observed (see Figure 4.1), with concentrations between 10 to 200 mM showing a sharp onset of oxidation indicative of a surface bound process. The process occurring within this range was therefore attributed to the electrochemical formation of calomel (Hg_2Cl_2) via the process[1]:

$$Hg(l) + Cl^{-}(aq) \rightarrow \frac{1}{2}Hg_2Cl_2(s) + e^{-}\,. \qquad (1.91)$$

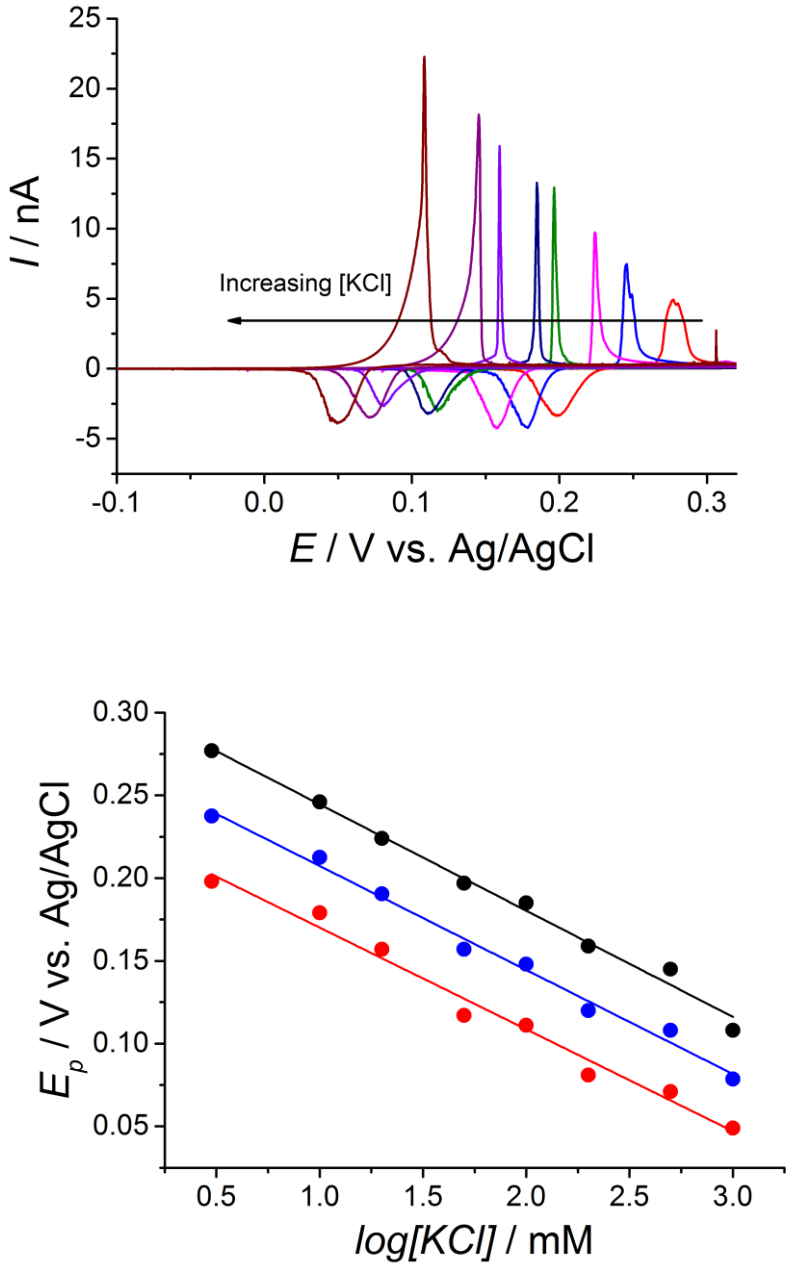


Figure 4.0 (Top) Effect of KCl concentration on the formation of calomel on a mercury hemisphere microelectrode in 0.10 M KNO_3. The potential range for cyclic voltammetry was -0.10 to + 0.32 V (vs. Ag/AgCl) at 25 mV s^{-1}. KCl concentration = 3, 10, 20, 50, 100, 200, 500 and 1000 mm. (Bottom) Peak potential as a function of KCl concentration. E_p(oxidation)(black), E_p(reduction) (red) and E_p(mid) (blue).

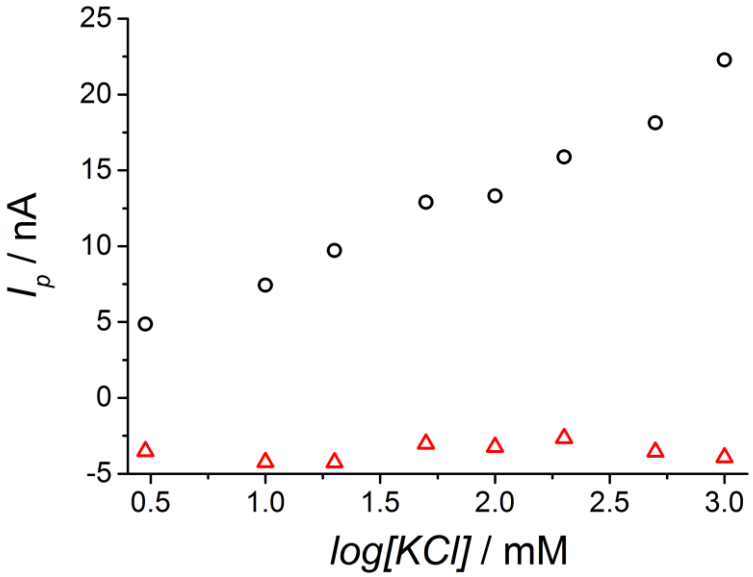


Figure 4.1 Peak current of oxidative (○) and reductive (Δ) peaks with varying [KCl]

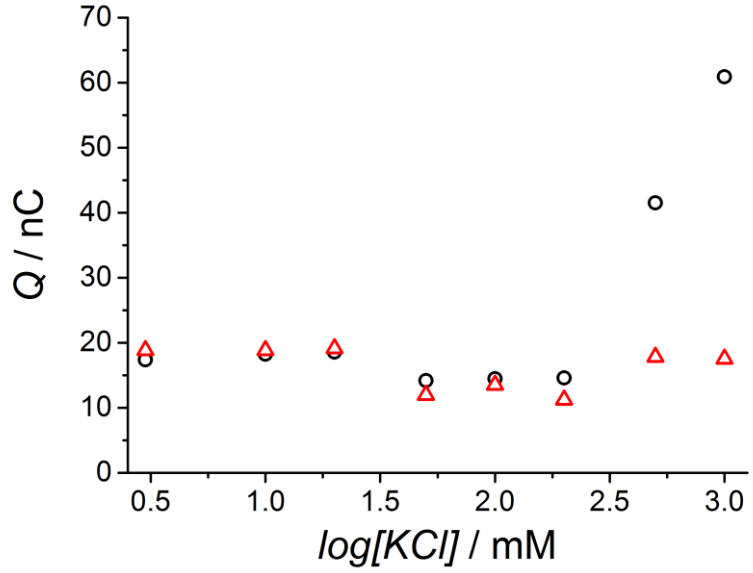


Figure 4.2 Oxidative (○)and reductive (Δ)peak current as a function of KCl concentration

As shown in Figure 4.2 the reductive peak area was found to be approximately constant at (16.8 ± 1.2) nC across the experimental range of KCl concentrations. The oxidative peak area

was found to be equal to that for the reduction for concentrations of 3 mM to 200 mM KCl, with a higher KCl concentration resulting in an oxidative charge greater than that for the reduction. As the oxidation peak area is constant below 200 mM KCl, it is inferred that in this range the amount and therefore the thickness of the calomel layer formed remains constant at approximately 37 nm (Equation 1.93). Above this range, the increase in oxidation peak area can be tentatively attributed to the oxidation of mercury to non-surface bound $Hg_2Cl_{2+x}^{x-}$ species[185]. These probably water soluble compounds would be free to diffuse in to solution and their formation explains the loss of redox active material after oxidation. A KCl concentration of 20 mM was therefore selected to next study the influence of electroreduction of the Hg_2Cl_2 layer to prevent formation of such species.

A mercury hemisphere microelectrode was electrochemically oxidised in 20 mM KCl and 0.10 M KNO_3 by linear sweep voltammetry from -0.10 V to +0.32 V (vs Ag/AgCl) at 25 mV s^{-1}. After the pre-treatment, a reductive overpotential was then applied and a current-time transient recorded. Figure 4.3 shows an example current-time transient run at -0.30 V (vs Ag/AgCl) before and after oxidation of the mercury hemisphere. Reductive features with millisecond time durations were observed only when the electrode was preconditioned via oxidation. The Faradaic electron transfer between an electrode and individual impacting NPs has been shown to give currents detected on the millisecond time scale[141]. The current spikes observed in this case therefore likely indicate the in situ formation and detection of NPs in the system.

To establish the origin of the reductive spikes, the experiment was repeated for a range of reductive overpotentials from +0.05 V to -0.70 V (vs Ag/AgCl). Between each measurement the electrode was held at a suitably reductive potential until no further features were observed to ensure the mercury hemisphere was free of calomel deposits. The cumulative frequency of impacts over the 50 second current-time transients at each potential were compared, and the

reductive spikes sized with respect to them being from the complete electrolysis of NPs, as shown in Figure 4.4. The radius of the NPs was calculated using Equation 1.92:

$$r_{np} = \sqrt[3]{\frac{3M_w Q}{4nF\pi\rho}}, \tag{1.92}$$

where M_w is the molecular weight, Q is the charge and ρ is the bulk density of the NP. A general increase in the frequency of reductive spikes was observed with increasing overpotential from +0.05 V to -0.70 V vs (Ag/AgCl), with a high degree of variability in the cumulative number of spikes seen at a given potential. The size distribution of the spikes seen across the potential range when assumed to be spherical NPs was calculated to have a modal radius of (27 ± 2) nm and an average radius of (36 ± 14) nm and the size of the NPs was not observed to be different for the different potentials analysed. The calomel layer thickness was calculated from the peak area for the oxidation of Hg before application of the reductive overpotential by Equation 1.93:

$$l = \frac{QM_w}{nF\rho 2\pi r_e^2}, \tag{1.93}$$

where l is the layer thickness and r_e is the radius of the electrode, and was found to be (47 ± 7) nm. This suggests the formation of single NPs of comparable thickness to the layer.

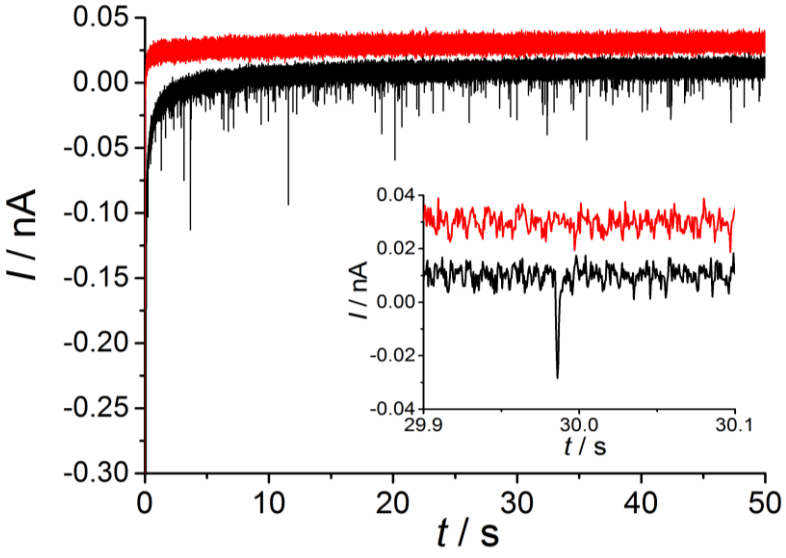


Figure 4.3 Current time transient before (red) and after (black) Hg oxidation in 0.10 M KNO_3 and 20 mM KCl at -0.30 V (vs. Ag/AgCl). Insert shows a zoomed in image of a Hg_2Cl_2 NP impact. Lines offset for clarity.

It is possible to estimate the maximum number of NPs that could be formed from a 47 nm thick calomel layer. The shell volume can be calculated to be 7.45 x 10^{-18} m^3 and the volume of a single NP of radius 36 nm to be 1.95 x 10^{-22} m^3. Therefore a maximum of 38133 NPs can be formed. The diffusion coefficient of a single Hg_2Cl_2 NP calculated using the Stokes Einstein equation (Equation 1.78) is 6.81 m^2 s^{-1}. The Nernst layer can therefore be calculated to 20 μm as $\delta = \sqrt{6Dt}$ [1] assuming a 10 s gap between the application of the potential and the beginning of measurement. Therefore, the volume occupied by the NPs upon their release from the layer can be estimated to be 3.33 x 10^{-14} m^3. The NP concentration in this volume is 1.9 x 10-6 mol m^{-3}. The maximum number of impacts expected within the 50 second current can be approximated using the integrated form of the Shoup-Szabo equation[186]:

$$N = N_A c^* r_e^3 (\tau + 1.437\tau^{1/2} + 6.57 \times 10^{-2} \ln\tau - 3.35 \times 10^{-3} \tau^{-1} + 3.43 \times 10^{-3} \tau^{-1/2} + 3.49 \times 10^{-3}\tau^{-4/2}, \quad (1.94)$$

where, $$\tau = \frac{4Dt}{r_{NP}^2},$$

and N is the number of impacts observed in a current-time transient of time, t. This equates to a maximum number of impacts occurring during the experimental timescale of 9346. This of similar magnitude to the ~500 impacts observed at -0.70 V vs Ag/AgCl, with the difference most likely due to NPs being lost to the bulk solution. The increase in frequency with increasing overpotential can be rationalised by a mechanism such as that proposed in Figure 4.5. When the mercury hemisphere is oxidised in the presence of chloride a self-limiting layer is rapidly formed due to the negligible electronic conductivity of calomel[187] and the restriction of chloride diffusion to the electrode/solution interface[177]. The formation of porous calomel structures has been previously reported in the literature[188] and explains the formation of a (47 ± 7) nm insulating layer by diffusion of chloride through the pores. The self-limiting properties of such a layer across KCl concentrations of 3 mM to 200 mM can be attributed to the time scale of the oxidation and the slow diffusion of low concentrations of chloride through the pores.

When a reductive overpotential is applied, the porosity of the layer still allows for electrolysis of the calomel at the calomel-mercury interface and results in detachment of the layer from the hemisphere due to the respective density differences, $\rho(Hg_2Cl_2)$ 7.16 g cm^{-3} [189] $< \rho(Hg)$ 13.53 g cm^{-3} [190], likely leading to a shrinking of the mercury drop relative to the Hg_2Cl_2 "shell". As electrolysis proceeds, the unsupported layer probably disintegrates resulting in the formation of a high concentration of NPs of comparative size to the layer in close proximity to the mercury hemisphere electrode. The composition of these NPs is ascribed to be entirely calomel however the presence of some elemental mercury existing on or in the NPs is possible. With increasing overpotential, it can be envisaged that reduction of the calomel at the calomel-mercury interface occurs at a faster rate thus causing a faster breakup of the layer and the formation of a greater number of NPs more suddenly. As the resultant NP size at each potential is similar, this indicates the process is not kinetically driven. The variability at each potential lends support to the process being a dynamic mechanical disintegration, facilitated by the non-homogenous structure of the rapidly formed calomel layer.

As a comparative study, Hg_2Cl_2 NPs were next chemically synthesised by a precipitation method. As reported above, suspensions of these NPs were then characterised by their direct electrolysis on both mercury and carbon microelectrodes.

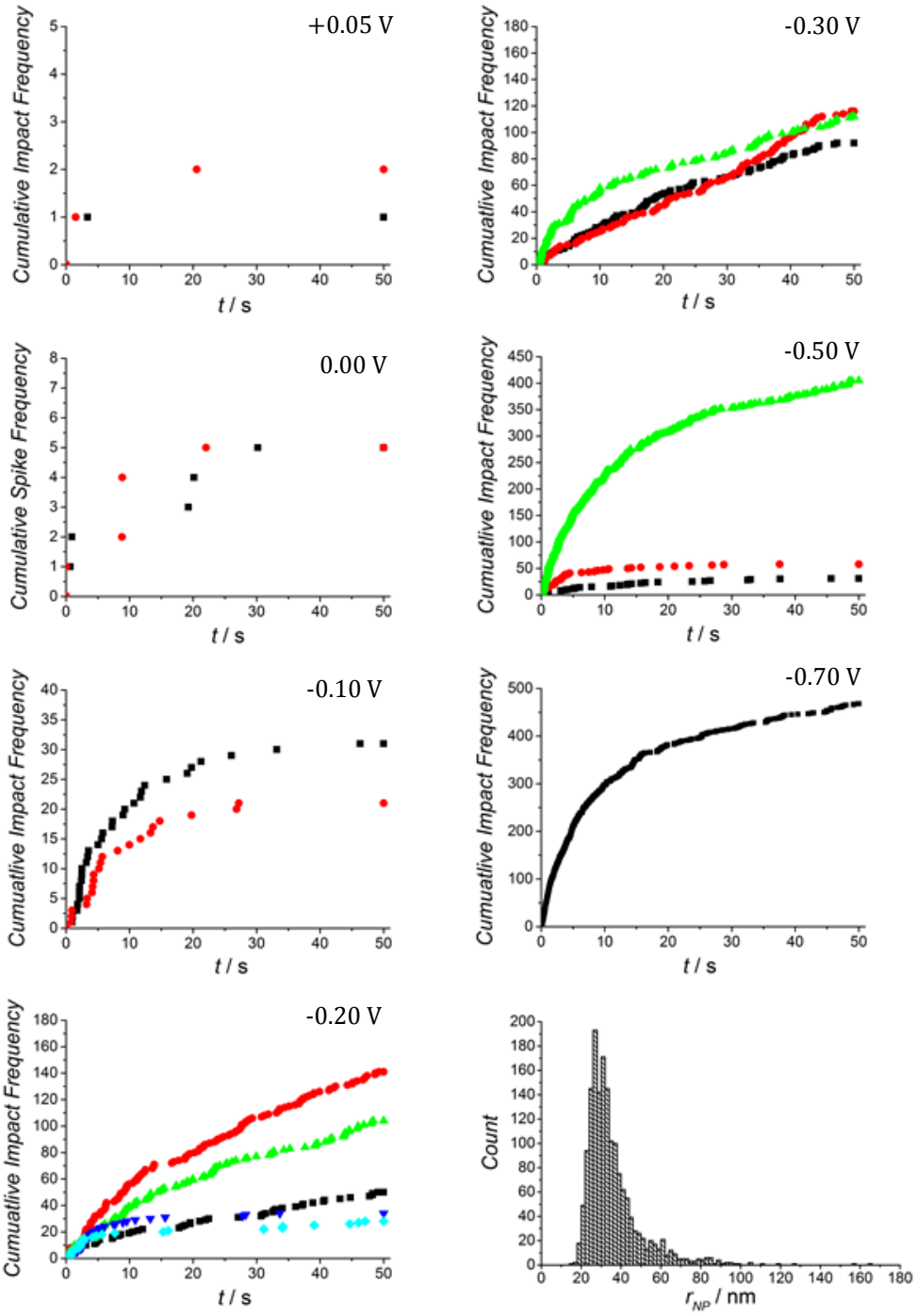


Figure 4.4 Cumulative impact frequency after Hg oxidation in 0.10 M KNO_3 and 20 mM KCl at varying reductive overpotentials (vs Ag/AgCl). Repeats at each potential are coloured accordingly. Repeats at -0.70 V showed a number of impacts above measureable limits and therefore could not be suitably analysed. Bottom right shows combined size distribution of NPs across measured potentials

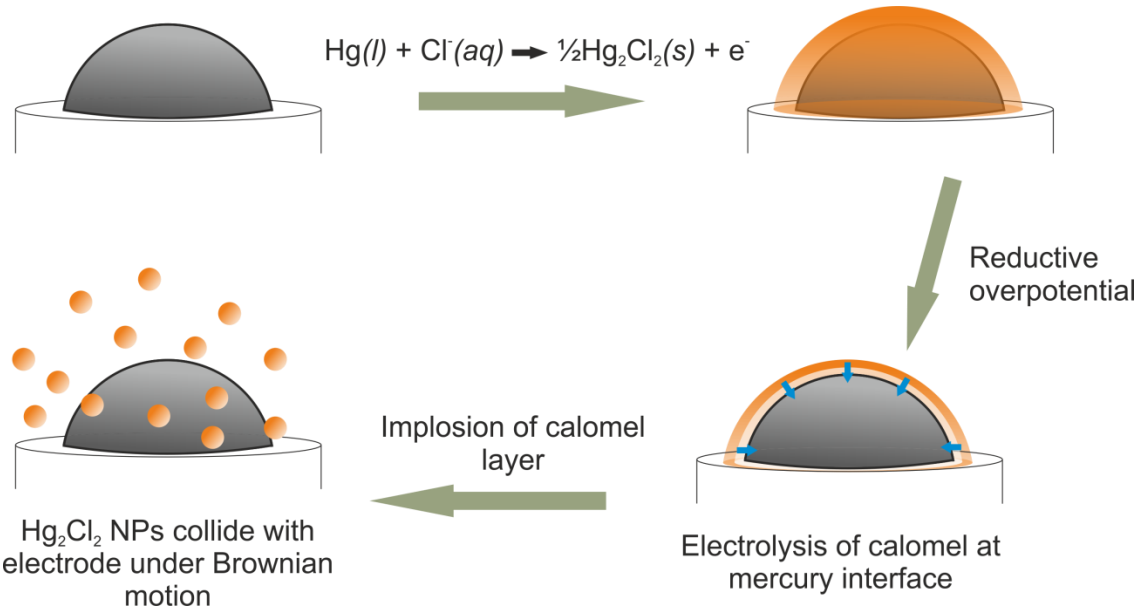


Figure 4.5 Mechanism for the formation and subsequent detection of Hg_2Cl_2 NPs on a mercury hemisphere microelectrode via the electrochemically induced disintegration of a surface bound nanoscale calomel layer

4.1.3.2 Characterisation of Chemically Synthesised Hg_2Cl_2 NPs on Mercury and Carbon Microelectrodes

A Hg_2Cl_2 NP suspension was prepared and the NPs characterised by their electrolysis on a mercury hemisphere microelectrode. These NPs were synthesised by precipitation of Hg_2Cl_2 from $Hg_2(NO_3)_2$ in a chloride containing medium, as outlined in Section 3.4.1.

To characterise the suspensions of NPs via electrolysis, a mercury hemisphere electrode was held at a potential of -0.30 V (vs Ag/AgCl) in 0.10 M KNO_3 and 20 mM KCl in the presence of Hg_2Cl_2 NPs and a current-time transient recorded. Care was taken to ensure the hemisphere was not subjected to any oxidative potential that could cause formation of calomel as previously shown. Figure 4.6 shows the resultant size distribution of the spikes recorded, with a modal radius (23 $\pm$ 2) nm and an average radius (26 $\pm$ 9) nm.

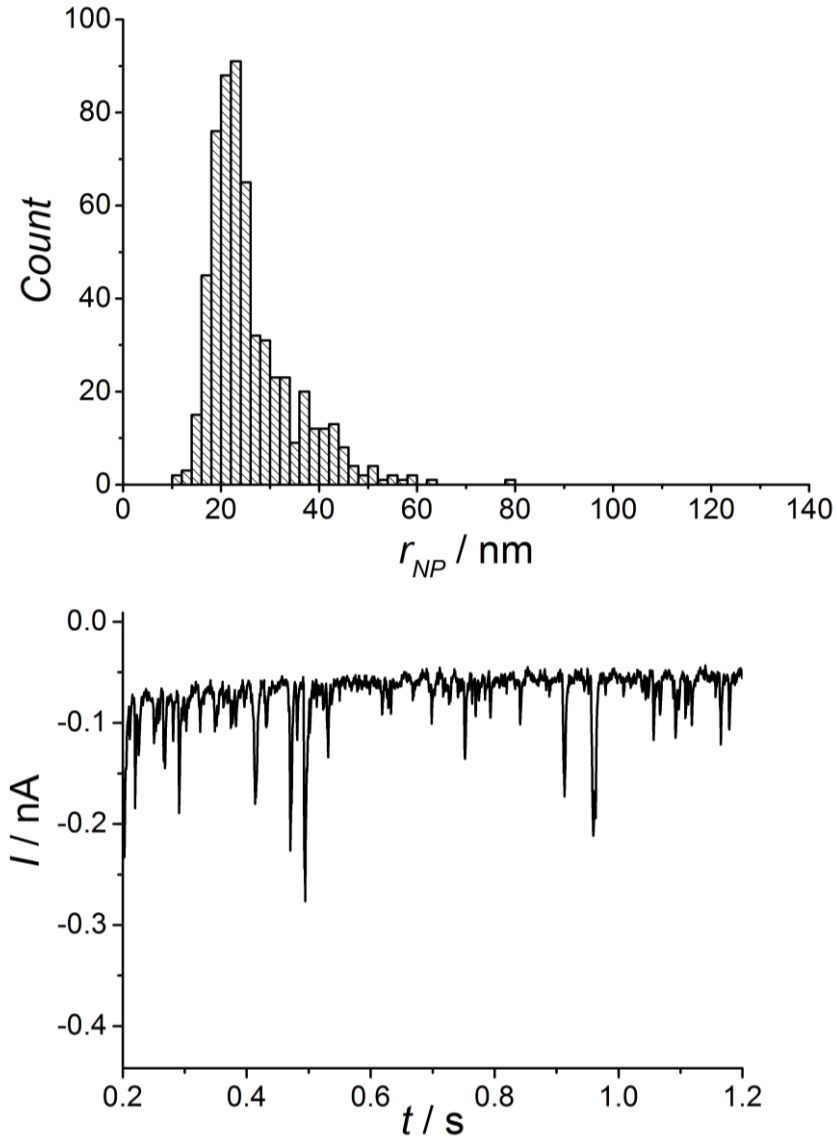


Figure 4.6 (Top) Size distribution of synthesised Hg_2Cl_2 NPs as measured on a mercury hemisphere microelectrode. (Bottom) A zoomed in image of an example current-time transient at a total Hg_2Cl_2 concentration of 5.71 μM run at -0.30 V (vs Ag/AgCl) in 0.10 M KNO_3 and 20 mM KCl.

In addition, an analogous experiment was conducted on a carbon electrode to ensure the size distribution obtained was related to electrolysis of the NPs and not to any unforeseen formation of calomel crystallites on the mercury hemisphere.

To establish the reduction potential of calomel on carbon, a glassy carbon macro electrode was modified with 3 μL of the suspension and dried under N_2. Stripping voltammetry

of the drop cast NPs was conducted in 0.10 M KNO_3 and 20 mM KCl. The stripping voltammogram can be seen in Figure 4.7 and was scanned from +0.32 V to -0.40 V (vs Ag/AgCl) at 5 mVs^{-1}. Scan 1 shows a reduction peak beginning at +0.07 V vs (Ag/AgCl) and the corresponding oxidation peak at +0.17 V, whilst scan 2 shows a shift in the reduction peak to +0.16 V (vs Ag/AgCl). This shift in reduction onset indicates a nucleation overpotential associated with the reduction of calomel nanoparticles on the carbon electrode when compared with a mercury hemisphere. This is consistent with previous studies which have shown a nucleation overpotential for Hg(I) and Hg(II) reduction on carbon[191].

When a carbon fibre microelectrode was held at a potential of -0.40 V (vs Ag/AgCl) in 0.10 M KNO_3 and 20 mM KCl in the presence of Hg_2Cl_2 NPs analysis of the resultant impacts found the modal radius to be (25 ± 2) nm with an average radius of (28 ± 10) nm as seen in Figure 4.8. These results were found to correlate with those found for the mercury hemisphere and with TEM analysis of the NP suspension. This confirms a new synthesis method for Hg_2Cl_2 NPs via precipitation of $Hg_2(NO_3)_2$ and supports the inference of the electrolysis of impacting Hg_2Cl_2 NPs on mercury hemisphere electrodes. In particular, this suggests that the spikes observed in the in-situ experiment were in fact caused by the collision of Hg_2Cl_2 NPs and their likely total electrolysis, rather than their partial reduction, and justifies the scheme proposed.

4.1.4 Conclusions

In summary, this work reports the first electrochemical synthesis of Hg_2Cl_2 NPs as well as a novel method for metal halide NP formation through the partial electrolysis and subsequent implosion of a metal halide nano-layer in aqueous media. These NPs were sized using the nano-impact method and shown to have a modal radius of (27 ± 2) nm and an average radius of (36 ± 14) nm when derived from a layer thickness of (47 ± 7) nm, and demonstrates the ability to form and study these NPs in situ. As the formation and release of Hg_2Cl_2 NPs is electrochemically controlled, the formation of such NPs in electrochemical experiments using mercury electrodes is possible and could have significant implications when used for the

sensitive characterisation of NPs. This is particularly relevant in nano-impact characterisation where mercury electrodes are already being utilised[192-194]. Herein, the chemical synthesis of calomel NPs via the precipitation of $Hg_2(NO_3)_2$ was also demonstrated. These particles were imaged by TEM and sized to have a modal radius of (23 ± 2) nm and an average radius of (26 ±9) nm when sized on a mercury hemisphere and a modal radius of (25 ± 2) nm and an average radius of (28 ± 10) nm when sized on a carbon microdisk. This is the first time metal halide NPs have been characterised by the nano-impact methodology.

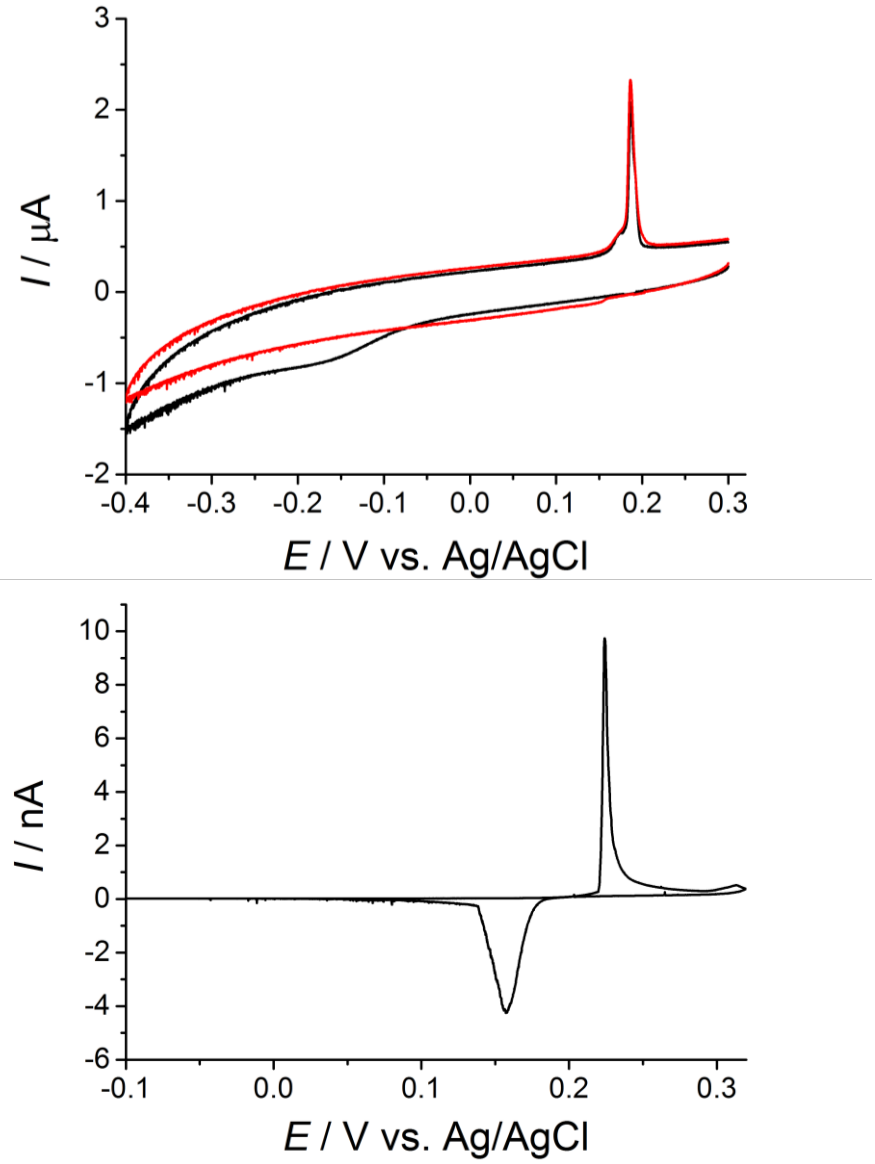


Figure 4.7 (Top) Scan 1 (black) and Scan 2 (red) of the stripping voltammetry of a 3 µL drop coast of Hg_2Cl_2 NP suspension on a GC macro electrode in 0.10 M KNO_3 and 20 mM KCl. Cyclic voltammogram potential range +0.32 V to -0.40 V (vs Ag/AgCl) at 25 mVs^{-1}. (Bottom) The oxidation and subsequent reduction of a mercury hemisphere microelectrode in the same electrolyte.

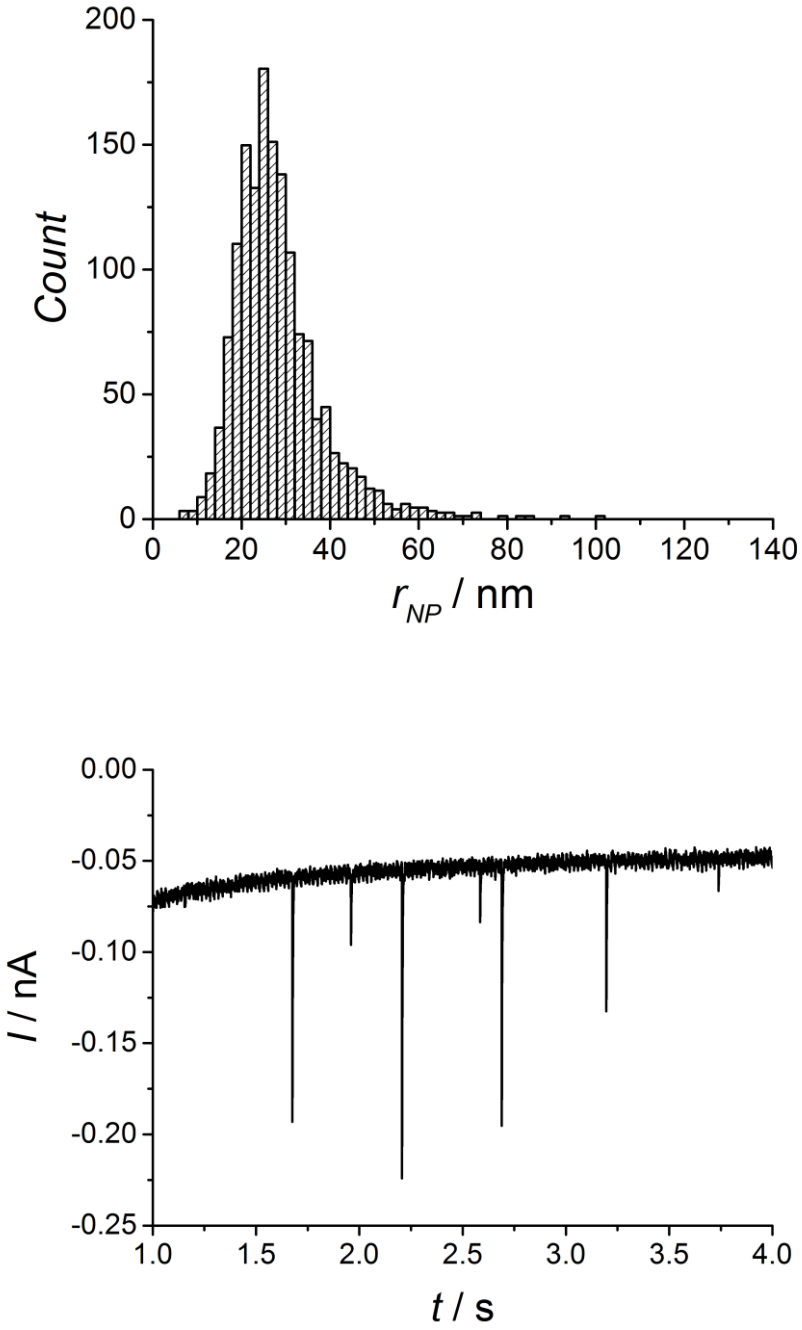


Figure 4.8 (Top) Size distribution of synthesised Hg_2Cl_2 NPs as measured on a carbon fibre microdisk electrode. (Bottom) A zoomed in image of an example current-time transient at a total Hg_2Cl_2 concentration of 0.29 mM run at -0.40 V (vs Ag/AgCl) in 0.10 M KNO_3 and 20 mM KCl

4.2 Electrochemical Nanoparticle Sizing Via Nano-Impacts: How Large a Nanoparticle Can be Measured?

4.2.1 Introduction

As discussed previously in Section 2.2, the field of NP sizing encompasses a wide array of techniques, with electron microscopy and dynamic light scattering (DLS) having become the established methods for NP quantification. These techniques however are not always applicable. Electron microscopes are ex-situ, have an inherently high cost associated with their operation and require drying of the sample which has been shown to promote particle agglomeration[173]. Optical techniques such as DLS, whilst in-situ, suffer from the inability to characterise polydisperse or optically opaque samples as well as being challenged by smaller NPs. Nanoparticle tracking analysis (NTA) is an alternative in-situ light-scattering technique which tracks individual NPs and can be accurate for sizing both monodisperse and polydisperse samples. The results strongly depend on the skill and judgement of the operator; through the use of different settings the presence of certain particles can be emphasized or ignored, leading to incorrect size distributions[195]. NTA relies on the observation of Brownian motion of the individual particles and due to variation in the mean square displacement can often lead to an overestimation of the particle size distribution width[196].

A new and rapidly developing method that addresses these issues is the electrochemical detection of NPs in solution (see Section 2.2.6). Two predominant methods in this area are by catalytic amplification of current by NPs mediating reactions at the electrode[137], or by direct quantitative electrolytic oxidation/reduction of the particle[141, 197]. Despite a large variety of NP materials having now been characterised by the *direct-impact* method[175], the limits of this technique with respect to the size of the particle still needs clarification. Recent work has sought to clarify the lower limit of detection, having achieved successful sizing of 6.3 nm diameter silver NPs by minimising background electrical noise[159]. However, the important question of how large a NP can be detected is unresolved.

As discussed in Section 2.1, NPs are by definition limited in having at least one dimension between 1-100 nm[49]. It is likely that for large enough particle sizes, complete electrochemical consumption of the particle would cease because of diffusional loss of particles from the interface before exhaustive electrolysis. Thus there is a likely upper limit to the particle size that can be measured by nano-impacts, for which this Chapter seeks to address. Current literature suggests the applicability of the direct nano-impact technique for NPs approaching 100 nm diameter with work on large organic[123, 146] and aggregated silver NPs[198]. In addition, recent work has resulted in the successful sizing of large non-aggregated metallic NPs on a RAM[199].

In this Section, we report the sizing of spherical AgBr NPs using a microdisk electrode; thus reporting the first such application of the nano-impact technique to a silver halide system and demonstrating quantitative sizing at the NP upper limit. We further report the sizing of Ag NPs via impacts building on earlier work[199] but reporting the effect of ionic strength and the need for care in this respect in so far as quantitative sizing is required. Ionic strength effects on NP systems may include aggregation/agglomeration but also, as with all dynamic electrochemical measurements, can profoundly influence the interfacial electron transfer.

4.2.2 Experimental

The synthesis of the AgBr NPs is detailed in Section 3.4.3. Scanning electron microscopy (SEM) images of the AgBr and Ag NPs were measured as outlined in Section 3.3.2 with the assistance of Dr K. Tschulik (formerly Department of Chemistry, Oxford University). Processing of these images was conducted using Image J public domain software, and found the particles to have a spherical diameter of 93 nm for AgBr and 98 nm for Ag and standard deviations of 25 nm and 8 nm respectively.

4.2.3 Results and Discussion

Synthesised AgBr and commercially available Ag NPs are first characterised by SEM; Figures 4.9 and 5.0 show the images at low and high magnification for AgBr and Ag. AgBr NPs stabilised

with gelatine are then electrochemically characterised after drop-casting on a GC macrodisk and successfully sized by the nano-impact method, showing the ability to size silver halide NPs of high polydispersity through quantitative reduction of colliding particles.

Finally, near-spherical citrate-capped silver NPs are characterised using a random array of microelectrodes (RAM) in low electrolyte concentration to demonstrate the effect of lower ionic strength on the sizing of NPs approaching the upper limit of the nanoscale. These experiments were performed by Mr. S. V. Sokolov (Deparment of Chemistry, Oxford University).

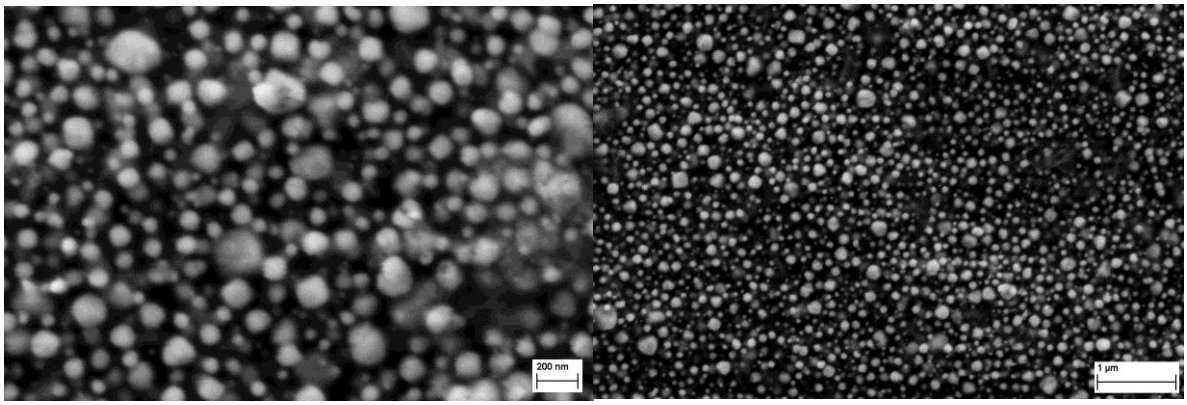


Figure 4.9 SEM images of AgBr NPs

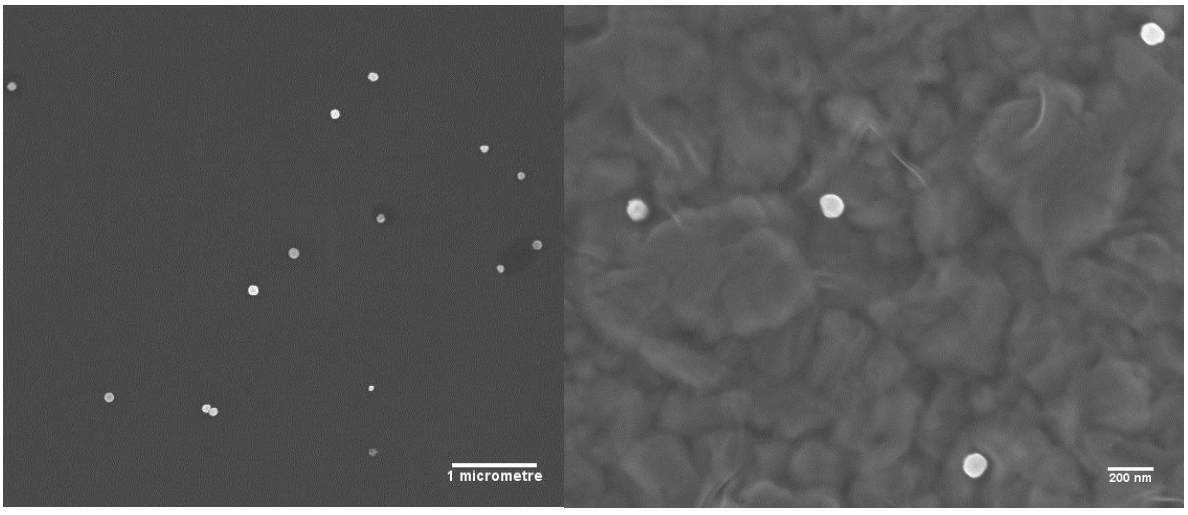


Figure 5.0 SEM images of Ag NPs showing near-spherical shape of the particles

4.2.3.1 Silver Bromide Nanoparticle Characterisation

To first establish the electrochemical behaviour of the synthesised AgBr NPs, stripping voltammetry was conducted on a GC macrodisk. Figure 5.1 shows a cyclic voltammogram (CV) of drop cast particles, scanning first reductively then oxidatively. No well-defined AgBr reduction peak is apparent, instead sharp reductive features (spikes) are observed at potentials lower than -0.75 V vs MSE. This type of voltammetric response has been previously attributed to a nucleation overpotential required for particle reduction[162] and may be associated with reduction of AgBr to Ag:

$$AgBr(s) + e^- \rightarrow Ag(s) + Br^-(aq)\,. \tag{1.95}$$

The appearance of a double oxidation peak at -0.14 V and -0.08 V on the reverse scan indicates the formation of two oxidation products, most likely AgBr and Ag^+:

$$Ag(s) \rightarrow Ag^+(aq) + e^-\,, \tag{1.96}$$

$$Ag(s) + Br^-(aq) \rightarrow AgBr(s) + e^-\,. \tag{1.97}$$

The formation of both Ag^+ and the silver halide during electrochemical silver oxidation has been previous reported and indicates successful reduction of AgBr to Ag in the scanned potential window[200, 201]. The mixture of oxidation products is most likely caused by the presence of bromide from the reduction of AgBr NPs.

As no clearly defined reduction peak was observed in the stripping voltammetry, initial impact experiments were conducted at a potential far more negative than the onset of the observed reductive features. Figure 5.2 shows the current-time transient in the absence and presence of AgBr NPs at -1.00 V vs MSE, whereby reductive features are observed only in the presence of the NPs. These spikes are indicative of direct electrolytic impacts and suggest the first successful detection of stochastic silver halide impacts.

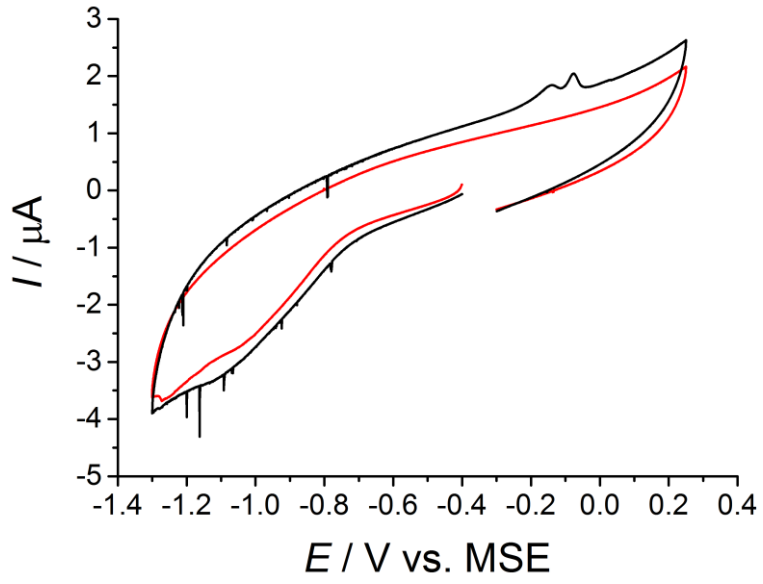


Figure 5.1 Cyclic voltammetry in 0.10 M $NaNO_3$ at 25 mVs^{-1}. (Red) Bare GC macroelectrode. (Black) GC macroelectrode drop cast with 400 pmol of AgBr suspension. The background signal is attributed to the reduction of low levels of O_2 in solution.

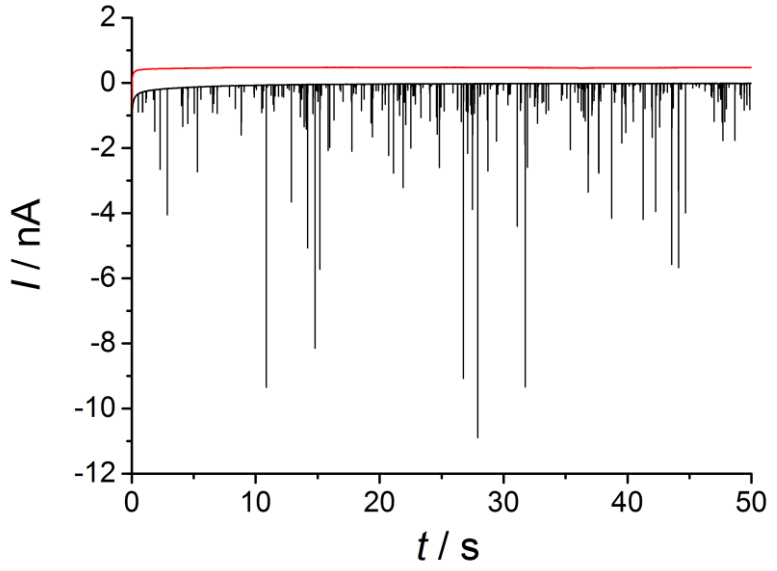


Figure 5.2 Chronoamperometry at -1.00 V vs MSE. (Red) 0.10 M $NaNO_3$ (Black) 0.10 M $NaNO_3$ and AgBr NPs (total [AgBr] = 18.8 µg mL^{-1}). Lines offset by 0.5 nA for clarity.

To investigate the effect of applied potential on the impact features the voltage was varied and the average area of the spikes calculated. Figure 5.3 shows the average spike area (charge) plotted as a function of applied potential. A clear switch on at potentials more negative

than -0.75 V is observed, with the average spike charge reaching a steady value consistent with full electrolysis of the particle. The error bars reflect the number of impacts measured for each data point which vary significantly. This onset corresponds with the earliest observable reductive features in the stripping voltammetry of the drop cast particles and indicates a significant nucleation overpotential for the reduction of impacting AgBr NPs as seen with the drop-cast particles.

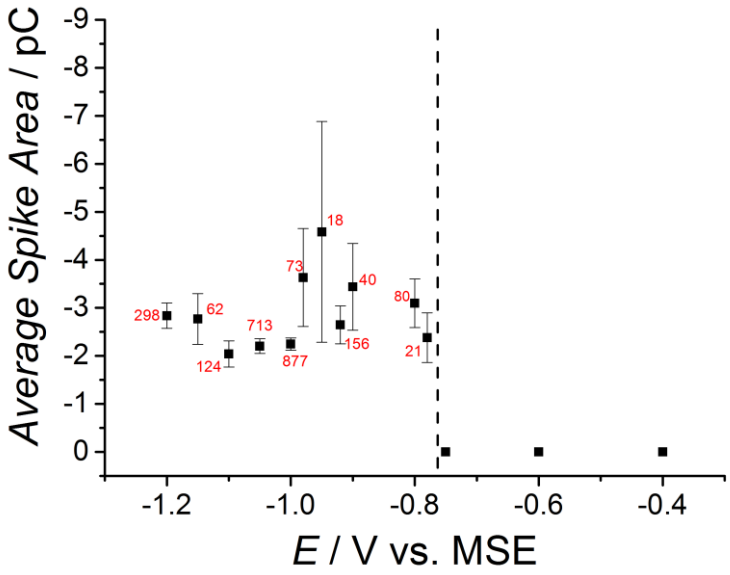


Figure 5.3 Average spike area as a function of applied potential in 0.10 M $NaNO_3$. Dotted line indicates the switch on potential for AgBr NP reduction. The numbers by each point indicate the number of spikes averaged to produce each data point.

The individual spike charges were measured across this range and a size distribution calculated using the Equation discussed in Section 2.2.6[146]:

$$D_{np} = 2\sqrt[3]{\frac{3M_wQ}{4nF\pi\rho}}, \tag{1.98}$$

where M_w is the molecular weight, Q is the charge, n is the number of electrons transferred and ρ is the NP density. Figure 5.4 shows the calculated electrochemical size distribution when compared to SEM. The sizing of the particles is in very close agreement with SEM results, with

the average diameter of the NPs found to be 92 nm and 93 nm respectively. This confirms the accurate electrochemical sizing of silver halide NPs and that the spike features observed were not due to the presence of oxygen as seen in the cyclic voltammetry. The close correlation between the size distributions shows the applicability of this technique to metal compound materials approaching the limit of the nanoscale.

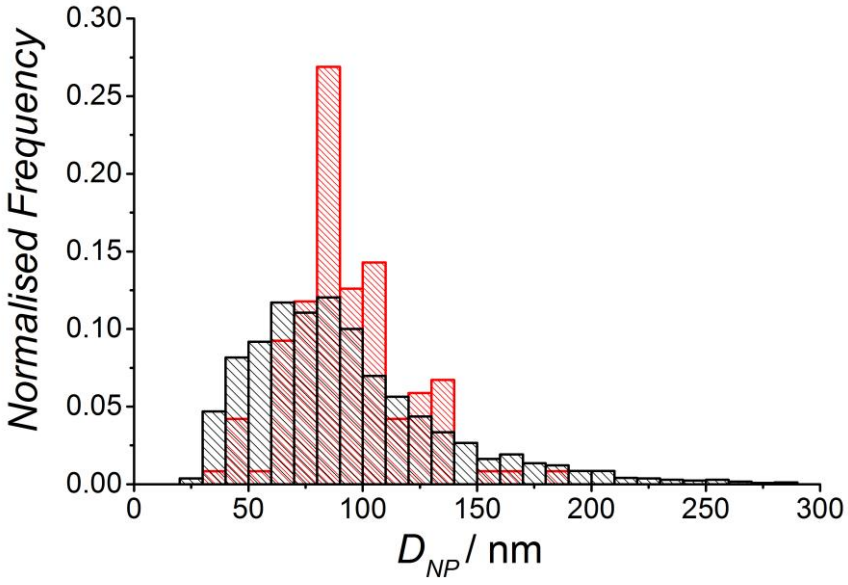


Figure 5.4 Size distribution of AgBr NPs. (Black) Electrochemical sizing summarised over potentials from -0.78 to -1.20 V vs MSE. (Red) Sizing from SEM.

4.2.3.2 Silver Nanoparticle Characterisation

Past nano-impact experiments have been conducted mostly in high ionic media and yielded excellent agreement with conventional sizing techniques[202]. Recent work on the coulometric sizing of quasi-spherical NPs has used a supporting electrolyte concentration of 0.10 M and gave good agreement between SEM imaging and coulometric sizing[199]. Lower concentrations of the supporting electrolyte have also been successfully used to characterise smaller (30 nm diameter) Ag particles[129]. In the present work we investigate the effect of reduced ionic strength on the electrochemical characterisation of large ~100 nm quasi-spherical Ag NPs via nano-impacts. An electrolyte concentration of 20 mM KCl was chosen for the experiments. A

random assembly of microelectrodes (RAM) was used during the experiments due to the higher signal to noise ratio and an increase in the number of the observable impacts resulting from an increased surface area as compared to a single microelectrode.[28].

First the electrochemical behaviour of silver NPs was determined through cyclic voltammetry of the experimental solution (1.4 mL of stock Ag NPs in 8.6 mL of 20 mM KCl) on the RAM electrode in order to determine the oxidation potential of the NPs in the lower concentration of electrolyte scanning first oxidatively then reductively. Figure 5.5 shows a cyclic voltammogram in the presence (black) and absence (red) of the NPs. No distinctive features are observed in the absence of NPs (red line). A clear oxidative peak is observed at +0.145 V vs SCE in the presence of the NPs, which is in good agreement with previous reports[199] and no further peaks were observed in the CV. The oxidation peak corresponds to formation of Ag^+ species by a one-electron oxidation:

$$Ag(s) \rightarrow Ag^+(aq) + e^-, \tag{1.99}$$

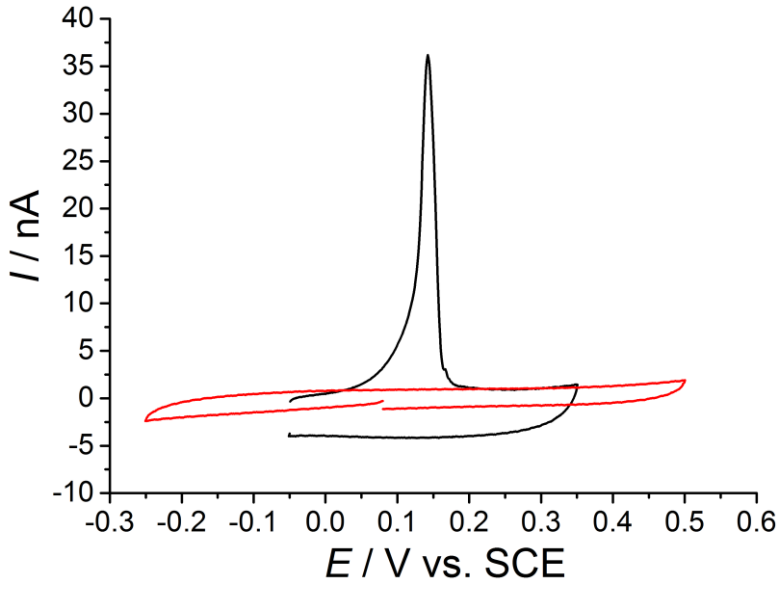


Figure 5.5 (Black) Cyclic voltammetry of Ag NPs suspended in 20mM KCl at 100 mVs^{-1} on RAM electrode. (Red) Blank

For chronoamperometry experiments a potential of +0.60 V vs SCE was chosen in order to ensure complete oxidation of the particles. The applied potential of +0.60 V is ca 400 mV in excess of the potential required for the stripping. Hence it is more than sufficient for Ag oxidation.

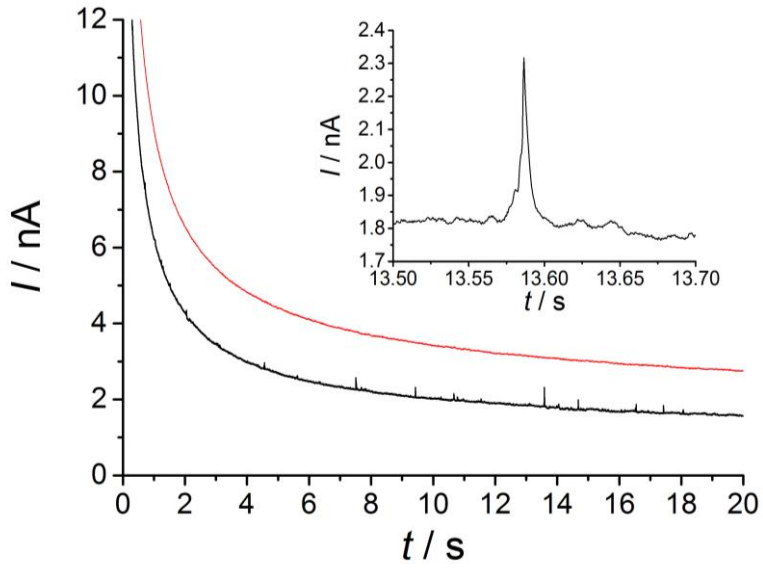


Figure 5.6 Chronoamperometry at +0.60 V vs SCE. (Red) 20 mM KCl (Black) 20mM KCl and Ag NPs (total [Ag] = 2.8 μg mL^{-1}). Lines offset by 1 nA for clarity. Inset shows zoomed-in region from 13.50-13.70 s.

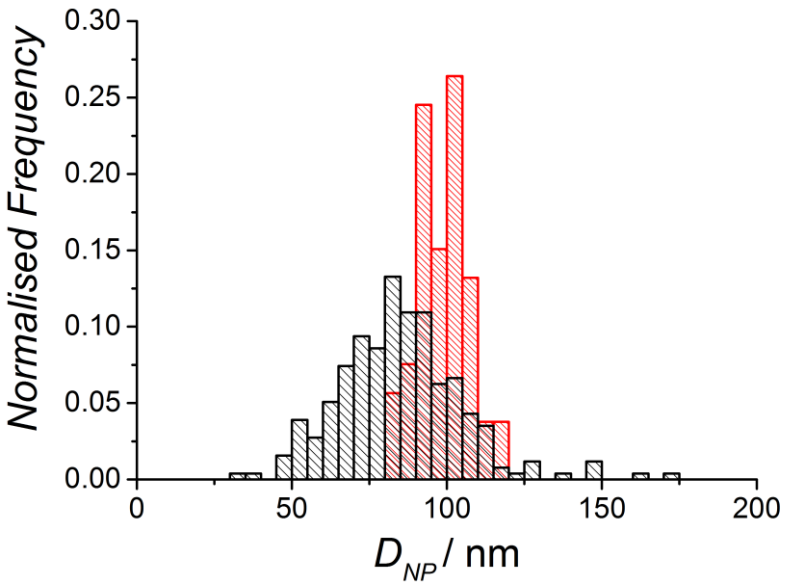


Figure 5.7 Size distribution of the Ag NPs. (Red) Electrochemical sizing from nano-impacts in 20 mM KCl (Black) Sizing from SEM.

Figure 5.6 shows the obtained current-time transient in the presence (black line) and the absence (red line) of the NPs, whereby the spikes are only observed in the presence of the Ag NPs. The spikes correspond to direct electrolytic impacts and are due to the oxidation of the colliding silver nanoparticles. The resultant spikes were analysed and the resultant size distribution was calculated using the Equation 1.97. Figure 5.7 shows the calculated electrochemical size distribution in comparison to the SEM data. The mean spherical diameter was determined from nano-impacts to be 85 nm. From the SEM images the mean spherical diameter was 100 nm. For further confirmation NTA analysis of the silver NPs was performed using a NanoSight LM10 (NanoSight, Amesbury, United Kingdom), equipped with a sample chamber with a 638 nm laser. The sample was measured for 60 s with automatic settings at 30 frames per second. The software used for capturing and data analysis was the NTA 2.3. The size distribution shown in Figure 5.8 has the mean diameter of 106 nm and standard deviation of 33 nm. The data is in good agreement with the SEM image analysis which shows a similar mean diameter, however a significantly larger standard deviation is observed (33 nm from the NTA vs 4 nm from the SEM), which may be caused by an artificial broadening[196]. The size distributions obtained from the three techniques are in close agreement but the nano-impact sizing distribution for the 20 mM KCl concentration is smaller. This discrepancy is attributed to the reduced electrolyte concentration. The apparent smaller diameter might likely be caused by incomplete dissolution of the silver nanoparticles. By contrast according to the literature excellent agreement with the SEM data was obtained for 0.10 M concentration of KCl[199]. This suggests that in order for a particle to undergo complete oxidation, potential drop across the interface must be minimized, which is only achieved for the higher concentration of the supporting electrolyte as observed for molecular electrochemistry[2].

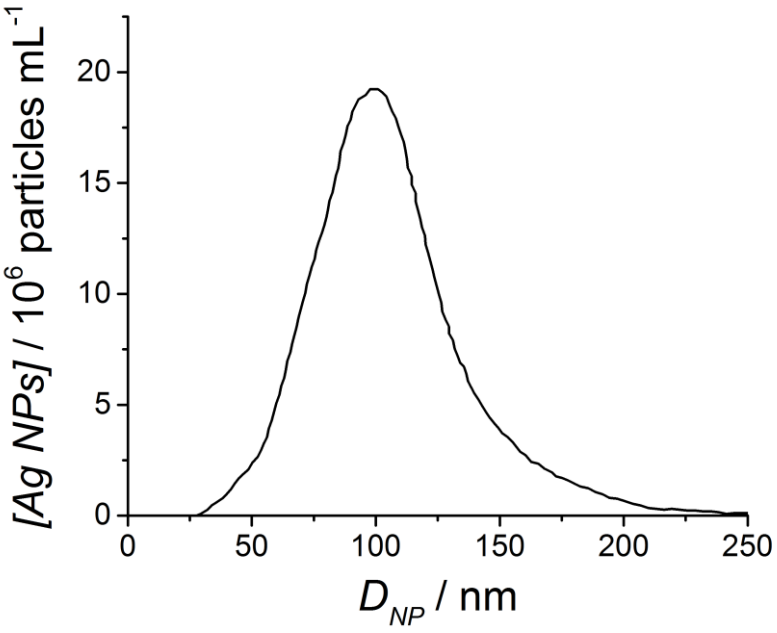


Figure 5.8 Size distribution of the Ag NPs obtained from nanoparticle tracking analysis

4.2.4 Conclusions

The successful sizing of large, high density AgBr NPs demonstrates the ability of the nano-impact technique to characterise particles across the entirety of the nanometre range. With the recent advancements herein, the technique has been shown to size particles over five orders of magnitude in charge, spanning 6 – 100 nm in diameter. However, results for the oxidation of well-studied Ag NPs, does show the choice of electrolyte can affect the reliability of the sizing obtained for large NPs. For complete dissolution, an electrolyte concentration in excess of 0.10 M should be used to ensure complete electrolysis of the studied particle. Therefore, with carefully chosen electrolyte composition, the nano-impact methodology has shown great potential for different material types and is continuing to establish itself as an alternative and effective method for the characterisation of electroactive NPs.

Chapter 5

Nano-Impact Voltammetry of Metal Oxide Nanoparticles

In the previous chapter, it was reported that the nano-impact technique can be applied to non-metallic systems with the successful quantitative sizing of both mercury(I) chloride and silver bromide. In this chapter, solutions of uncapped, weakly charged Bi_2O_3 NPs are studied in aqueous solution. Nanoparticle tracking analysis reveals the particles to be agglomerated. In contrast electrochemical detection via the nano-impacts technique shows almost exclusive detection of monomeric NPs. Comparison of the two techniques allows the conclusion to be drawn that the agglomeration/deagglomeration of the nanoparticles is *reversible*. A minimum rate constant for the deagglomeration process is estimated. This work has been published in *Chemistry: A European Journal*[203].

5.1 Bi_2O_3 Nanoparticle Clusters: *Reversible* Agglomeration Revealed by Imaging and Nano-Impact experiments

5.1.1 Introduction

As mentioned in Chapter 2, an important topic of research for suspended NPs is that of inter-particle interactions and the processes of agglomeration and aggregation[204, 205]. The relative extent of these processes in NP systems is important across the field of nanotechnology affecting NP reactivity[206, 207] and their distribution in the environment[208, 209]. The IUPAC definition of agglomeration is a *reversible* process whereby dispersed particles are held together by weak physical interactions leading to phase separation by the formation of precipitates of larger than colloidal size[210]. Aggregation is defined as an *irreversible* process in which particles are strongly bonded together to form clusters. A model for the equilibrated

reversible agglomeration of NPs has recently been derived[156] permitting the distribution of agglomerates to be predicted assuming an entropy of mixing only model. The model allows the prediction of particle size distributions for weakly interacting particles by assuming all agglomeration states are equal in energy (no significant energetic interactions between agglomerate particles). The distribution of monomers, dimers, trimers, etc., can then be numerically calculated to find the population distribution with the lowest energy configuration. The distribution is therefore determined by maximising the entropy of mixing of the system. Weakly interacting particles were also studied and found the entropy of mixing to be a contributing factor in determining the distribution even when introducing weakly repulsive forces between NPs.

Agglomerated NPs have been previously observed by nano-impacts[155] (Section 2.2.6). Citrate-capped Ag NPs impacts were measured and directly compared to NTA, with the resultant distribution for both cases showing excellent agreement, matching the size and distribution of the clusters. Here monomeric, dimeric, trimeric etc. NPs were detected in their clustered forms at the electrode and thus the agglomeration of NPs could be directly observed. This requires the kinetics of agglomeration/deagglomeration to be slow with respect to the voltammetric timescale ($\sim r_e^2/\mathrm{D}$, where r_e is the electrode radius and D is the diffusion coefficient of the NP). The *reversible but slow* nature of this agglomeration/deagglomeration behaviour was later confirmed by nano-impact experiments[102]. The addition of a magnetic field on super-paramagnetic Fe_3O_4 NPs has also been shown to promote agglomeration, with dimeric and trimeric clusters detected by nano-impacts[211]. In cases such as these, the inter-particle interactions are studied by forcing agglomeration/deagglomeration by applying external forces and then impacting the NPs. In these examples the nano-impacts method quantitatively detects dimers and trimers as well as monomers. Given that the latter diffuses to the electrode faster than the larger species this requires the rate of agglomeration/deagglomeration to be slow. It is interesting and probably technologically important to ask the question if there are cases where

the agglomeration/deagglomeration kinetics are “fast” enough to outrun experimental timescales.

The aim of this chapter is to identify such rapid agglomeration/deagglomeration processes through the comparison of NTA and nano-impact experiments of uncapped Bi_2O_3 NPs. NTA provides information on the equilibrated agglomerate size distribution, however cannot directly provide information on the speed of agglomeration/deagglomeration. If the deagglomeration rate is faster than the diffusion of the agglomerates to the electrode surface, nano-impacts may be able to resolve these effects. Due to the equilibrium inherent in agglomeration, some monomeric form must be present in suspension. Electrolysis of these monomers at the electrode surface would drive the equilibrium towards the release of monomer and hence drive rapid deagglomeration of the particle. Electrolysis of the impacting NPs would therefore act as a voltammetric perturbation of the system whilst simultaneously detecting the monomers formed. This approach accesses much faster deagglomeration kinetics than conventional sonication or bubbling methods [212, 213] and should allow resolution of rapid agglomeration/deagglomeration effects through exclusive or near exclusive detection of the monomeric form. The identity of the impacting aggregate can additionally be inferred indirectly by imaging of the nano-deposits remaining on the surface after impact [214].

5.1.2 Experimental

5.1.2.1 Equipment

Zeta-potential measurements were conducted on the bismuth oxide NPs using a Malvern Zetasiver (Malvern, United Kingdom).

5.1.2.2 Nanoparticle Characterisation

Nanoparticle tracking analysis (NTA) was used to provide solution phase characterisation of the NPs (Section 2.2.6), and was fitted to the entropy of mixing only model with assistance from Mr. S. V. Sokolov (Department of Chemistry, Oxford University). The sample preparation method

was that previously used for nano-impact experiments and was conducted with a NP concentration of 40 pM for direct comparison with electrochemical experiments. Zeta potential measurements of the Bi_2O_3 NPs was conducted in 0.10 M NaOH with a NP concentration of 40 pM to allow direct comparison with voltammetric impact experiments. Scanning electron microscopy (SEM) images of the NPs were taken by drop-cast modification of a GC sheet (Section 3.3.2). This images were taken by Ms J. Holter and Dr. N. Young (Department of Materials, Oxford University). For images of the Bi nano-deposits, nano-impact experiments were conducted with the GC sheet as the working electrode prior to imaging.

5.1.3 Results and Discussion

First, the voltammetric response of Bi_2O_3 NPs is studied by use of drop-cast modified glassy carbon (GC) macroelectrodes to establish the potentials required for nano-impact experiments. Next, nano-impact experiments are conducted at a carbon microelectrode across a range of reductive potentials and quantitative sizing achieved. Finally, the results gained from electrochemical analysis of the NPs is critically compared with results gained from NTA and SEM imaging discussed in terms of agglomeration/deagglomeration.

A GC macroelectrode was modified with 0.69 nmoles of Bi_2O_3 NPs and stripped voltammetrically in 0.10 M NaOH as seen in Figure 5.9 (top). A clear reductive peak is observed at -1.33 V vs MSE consistent with the known 3e$^-$ reduction of Bi_2O_3[215, 216]:

C1: $$Bi_2O_3 + 2OH^- \rightleftharpoons 2BiO_2^- + H_2O\,, \tag{2.00}$$

$$BiO_2^- + 2H_2O + 3e^- \rightarrow Bi + 4OH^-\,. \tag{2.01}$$

A shoulder at -1.45 V vs MSE is also apparent and is attributed to the 6e$^-$ reduction of Bi_2O_3[215, 216]:

C2: $$Bi_2O_3 + 3H_2O + 6e^- \rightarrow 2Bi + 6OH^-. \tag{2.02}$$

The presence of the C2 process may indicate a OH^- deficiency within the drop-cast layer. This might be due to the prevalence of aggregates/agglomerates forming during drying and the inhibited diffusion of the electrolyte into the clusters[163]. On the reverse scan a wide oxidation peak is observed. The process occurring here can be rationalised by considering the respective change in the oxidation and reduction peak in consecutive scans of the drop-cast NPs as seen in Figure 5.9 (bottom). Clearly the C2 process is not present after the first scan, consistent with OH^- produced during the reduction of Bi_2O_3 in the first scan and remaining in the diffusion layer of the electrode, allowing dominance of the C1 process. During the scans, the size of the oxidation peak remains approximately constant, with the only significant change being the size of the reduction peak between scan 1 and scan 2, with this ending up equating to that of the oxidation peak. This strongly indicates that the oxidation process occurring is dominated by the reverse of the $3e^-$ process C1.

Prior to nano-impact experiments the NP suspension was characterised by NTA as shown in Figure 6.0. A heavily agglomerated/aggregated system is observed, with a monomer radius of 19 nm, calculated from the peak modal value, matching the supplier specification of 19 nm. Sonication of the sample was found to have little impact on the distribution obtained indicating a fast rate of cluster formation of Bi_2O_3 NPs. Zeta potential measurements of the NPs in 0.10 M $NaNO_3$ showed the particles to have a zeta potential of -11 mV. The fitting shown in Figure 6.0. is that for the entropy of mixing only model[156] which has been shown to explain the agglomeration behaviour in capped metallic NPs. The achieved distribution in this case approximates the entropy of mixing only model with some larger particles present.

Next, nano-impact experiments were conducted on the agglomerated particles to study the agglomeration process. As there are two competing reductive processes occurring for Bi_2O_3 in the chosen electrolyte, nano-impact experiments were conducted at a range of potentials from -1.1 V to -1.70 V vs MSE.

Current-time transients were conducted at -1.70 V vs MSE with and without 40 pM NPs in 0.10 M NaOH. As seen in Figure 5.3 (top), current spikes were observed only when NPs were present indicating the reduction of Bi_2O_3 NPs. Experiments were conducted across the potential range mentioned and the size of the NPs calculated using the Equation[146]:

$$r_{np} = \sqrt[3]{\frac{3M_wQ}{4nF\pi\rho}}, \tag{2.03}$$

where r_{np} is the radius of the NP, M_w is the molecular weight of the composite material (465.96 $gmol^{-1}$), Q is the charge under the spike, n is the number of electrons involved in the reduction, F is Faraday's constant and ρ is the density of the material (9.17 g cm^{-3})[217]. Figure 6.1 (bottom) shows the resultant mean sizes of the NPs detected assuming the C1 process operates for which n=3. A clear potential dependence is observed, with no NPs being detected at potentials positive of -1.20 V vs MSE, concurrent with the stripping voltammetry in Figure 5.9. The consistent mean radius of the NPs from -1.30 V to -1.70 V vs MSE also suggests that the C2 process does not occur. This is to be expected as mass transport to an individually impacting NP is exceedingly fast[218] and would allow sufficient supply of OH^- to promote the $3e^-$ reduction.

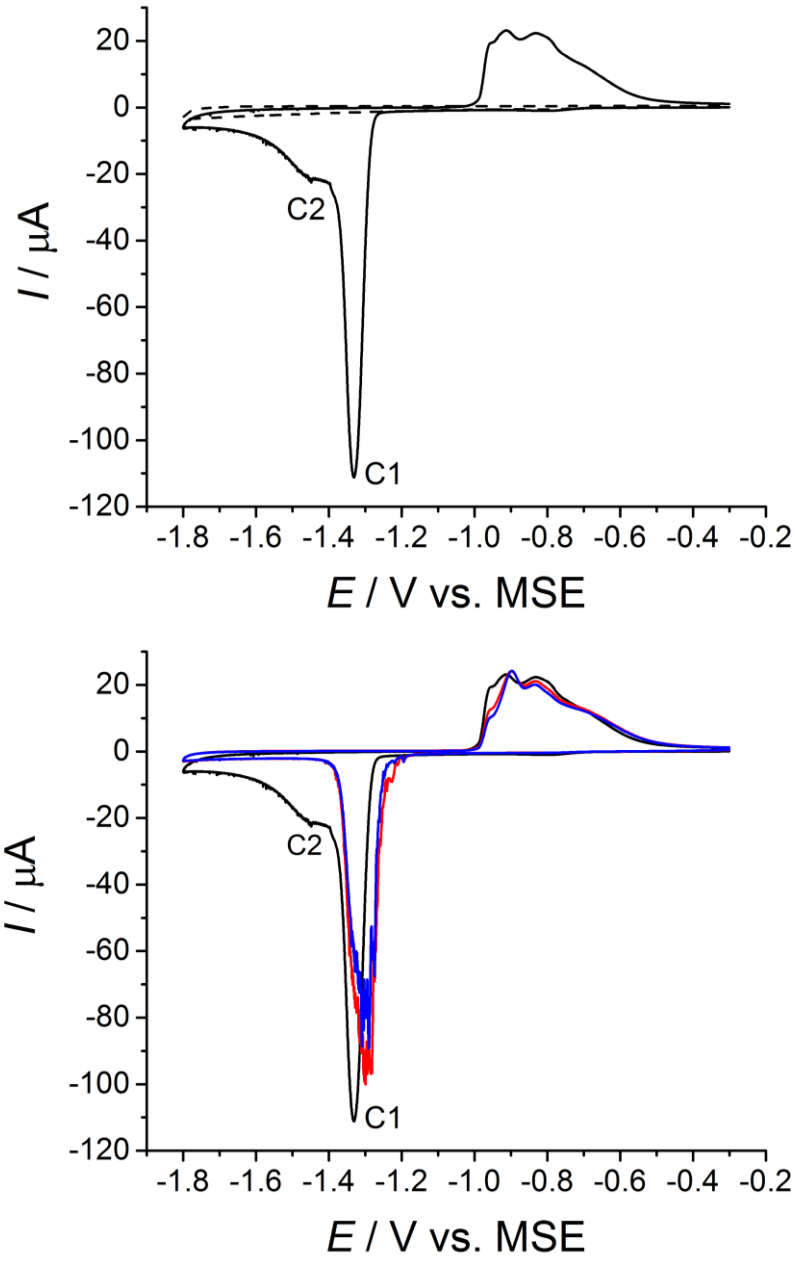


Figure 5.9 (Top) Cyclic stripping voltammetry in 0.10 M NaOH at 50mV s^{-1} (dashed line) bare GC (solid line) 0.69 nmoles of Bi_2O_3 NP modified GC. (Bottom) Consecutive scans of Bi_2O_3 modified GC (black) scan 1 (red) scan 2 (blue) scan 3.

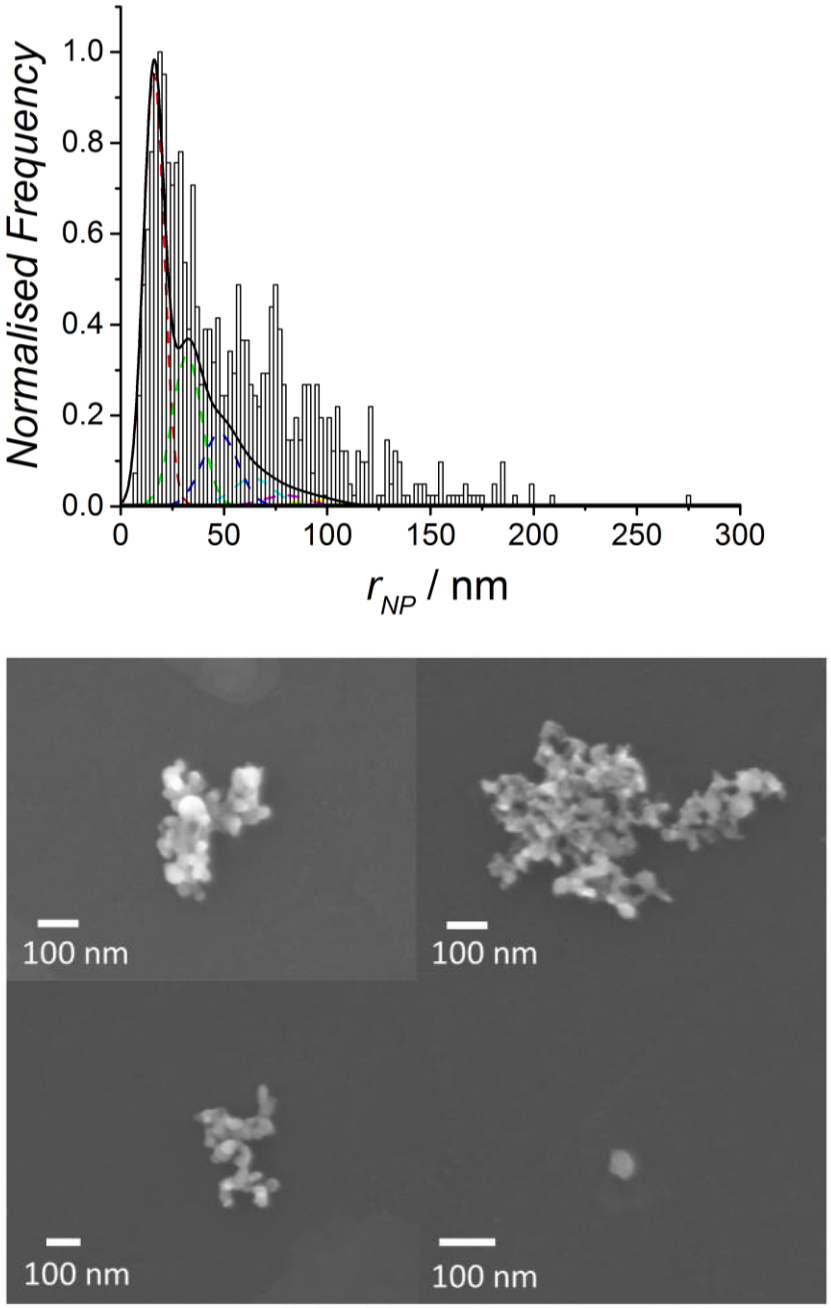


Figure 6.0 (Top) NP distribution as found from NTA, showing deviations from entropy only model[23]. (Bottom) SEM of drop-cast NPs showing Bi_2O_3 clusters and monomer.

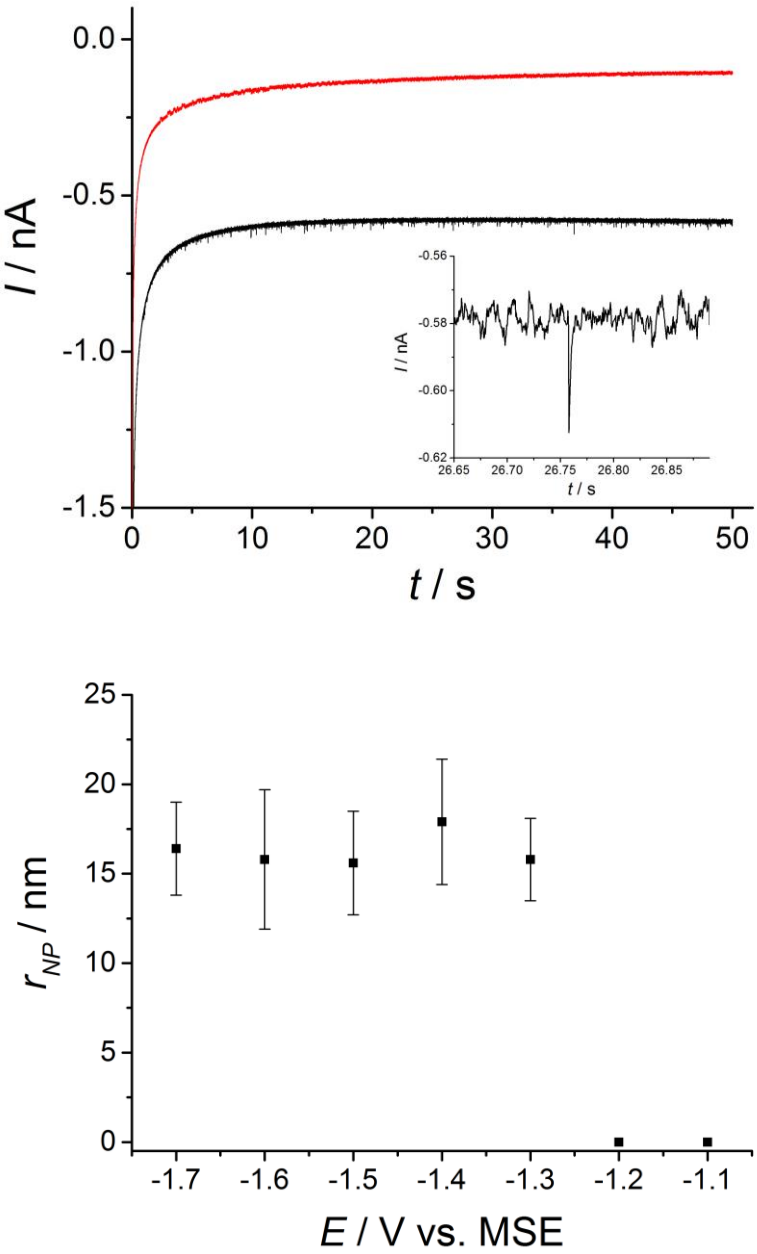


Figure 6.1 (Top) Current-time transient at a CF microelectrode held at -1.70 V vs MSE in 0.10 M NaOH (red line) No NPs (black line) 40 pM Bi_2O_3 NPs. Increase in background current on addition of NPs attributed to reduction of small amounts of solubilised bismuth hydroxide species. Insert shows a zoomed in image of an example NP impact current trace. (Bottom) Average radius of NP as a function of held potential during current-time transient.

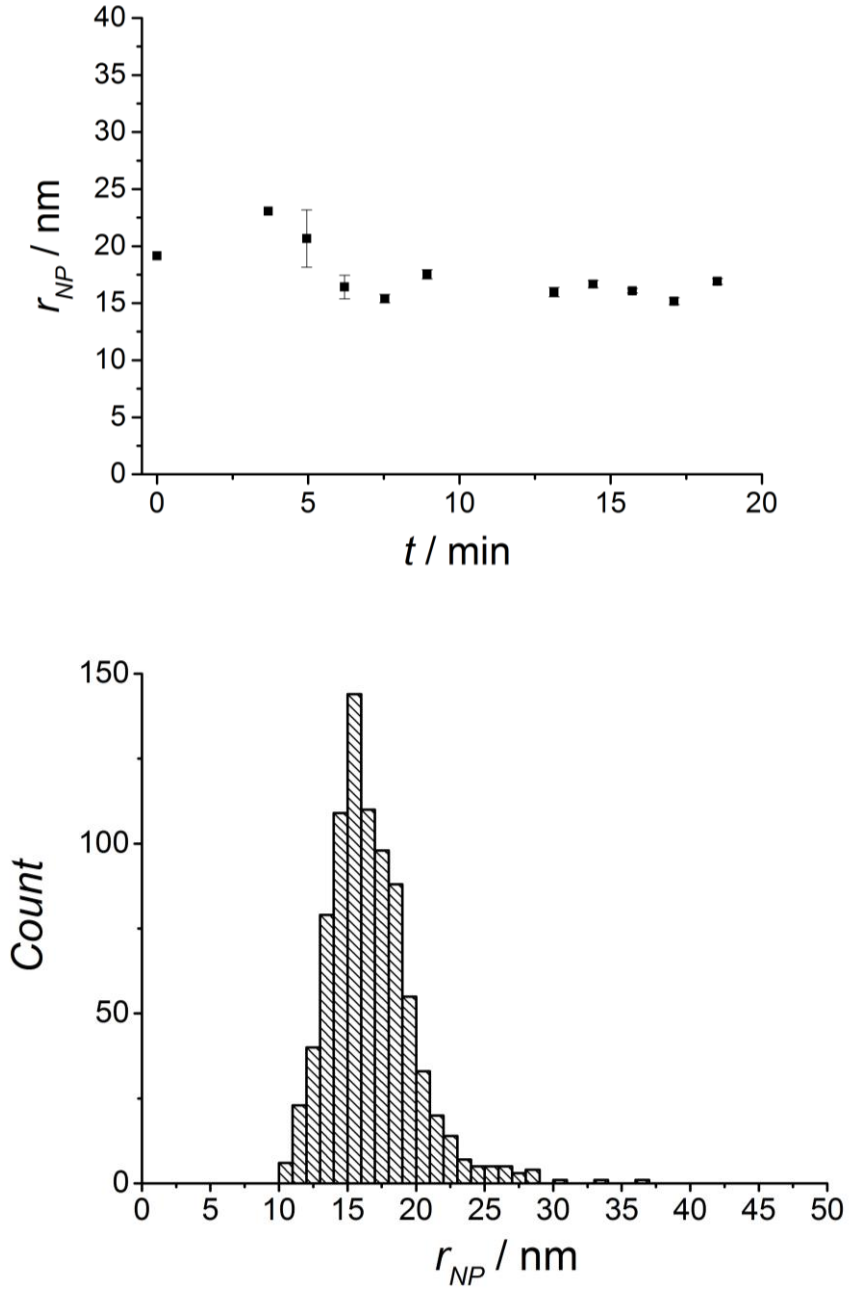


Figure 6.2 (Top) Mean radius of NP vs start time of 50 second current-time transient. (Bottom) Size distribution of Bi_2O_3 NPs summarised across potentials from -1.20 V to -1.70 V vs MSE.

As the NTA observed the presence of clusters, the size of the NPs detected by nano-impacts was studied as a function of time. Figure 6.2 (top) shows a plot of the average NP radius plotted against the start time of each 50 second current-time transient at -1.70 V vs MSE, with the first scan (T=0) occurring 2 minutes after NP addition to the electrolyte. No significant

change in the average NP radius can be observed across the 20 minute time period, with the average NP radius remaining constant at approx. 17 nm. This suggests that the NPs detected by nano-impacts are confined to monomeric NPs only, with no NP clusters detected. To achieve a NP size distribution from nano-impact experiments, the resultant radii for the 851 spikes analysed across potentials from -1.30 V to -1.70 V vs MSE were combined as seen in Figure 6.2 (bottom). The mean radius of the NPs was found to be 17 nm with a standard deviation of 3 nm showing close agreement with that of the monomer found by NTA analysis and confirming the near exclusive detection of monomeric Bi_2O_3 NPs. This difference of 2 nm radius matches that calculated for the loss of material by formation of some soluble $Bi(OH)_x^{3-x}$ species. The amount of material lost was calculated using Medusa† equilibrium software[219] at the concentrations and pH stated for nano-impacts experiments. This assumes equilibrium is reached prior to experimentation.

NTA analysis shows large proportions of clusters, which would be expected to be observed by impact voltammetry as estimated on the basis of their diffusion coefficients if they are present in the diffusion layer of the electrode[163]. This observation is seemingly in contrast to that previously reported where agglomerates were detected in their clustered form[155]. The detection of only the Bi_2O_3 monomer by electrochemical methods suggests that Bi_2O_3 clusters *reversibly* agglomerate/deagglomerate much faster than the NP systems previously studied and may explain why only monomeric NPs are detected where larger clusters are not observed even over extended time periods. Simply put the dimer, trimer and higher order agglomerated clusters which are slow diffusing dissociate within the diffusion layer so that the faster diffusing monomeric species are detected:

† Medusa software utilises a database of equilibrium constants to simulate chemical equilibrium diagrams. By inputting the species known to be present, and their phase, fraction plots can be produced as a function of pH. This method was used for the determination of the extent of dissolution of Bi_2O_3.

$$nmer \rightleftharpoons (n-1)mer + monomer$$

$$(n-1)mer \rightleftharpoons (n-2)mer + monomer$$

$$trimer \rightleftharpoons dimer + monomer$$

$$dimer \rightleftharpoons monomer + monomer$$

$$monomer + 6Ne^- + 3H_2O \rightarrow 2N_{molec}Bi^{3+} + 6OH^- \quad (2.04)$$

where N_{molec} is the number of molecules of Bi_2O_3 present in a monomeric NP.

Next, the ability of Bi_2O_3 to be reduced to Bi by voltammetric methods was exploited to allow SEM imaging of surfaces impacted by Bi_2O_3 NPs at -1.60 V vs MSE. Figure 6.3 (top) shows the resulting GC electrode is covered with nanoscale bismuth deposits. Sizing of these deposits is shown in Figure 6.3 (bottom) alongside the original NP size distribution obtained from nano-impact experiments. The mean size of the nano-deposits was found to be 14 nm with a standard deviation of 3 nm which is in good agreement with that calculated from the impact voltammetry. What is evident is the distinct lack of larger deposits resulting from the impact of NP clusters. This provides direct microscopic evidence for the "fast" *reversible* agglomeration mechanism as illustrated in Figure 6.4. "Fast" *reversible* agglomeration of Bi_2O_3 to form clusters ensures a constant source of monomeric NPs in suspension. As these clusters approach the electrode, the monomers are electrochemically reduced. This in turn drives the equilibrium towards the release of monomers for clusters approaching the electrode surface, effectively providing voltammetric perturbation of the system and immediate detection. This leads to the selective electrochemical detection of the monomeric NP component of the clusters by electrolytic induced, "fast" *reversible* deagglomeration.

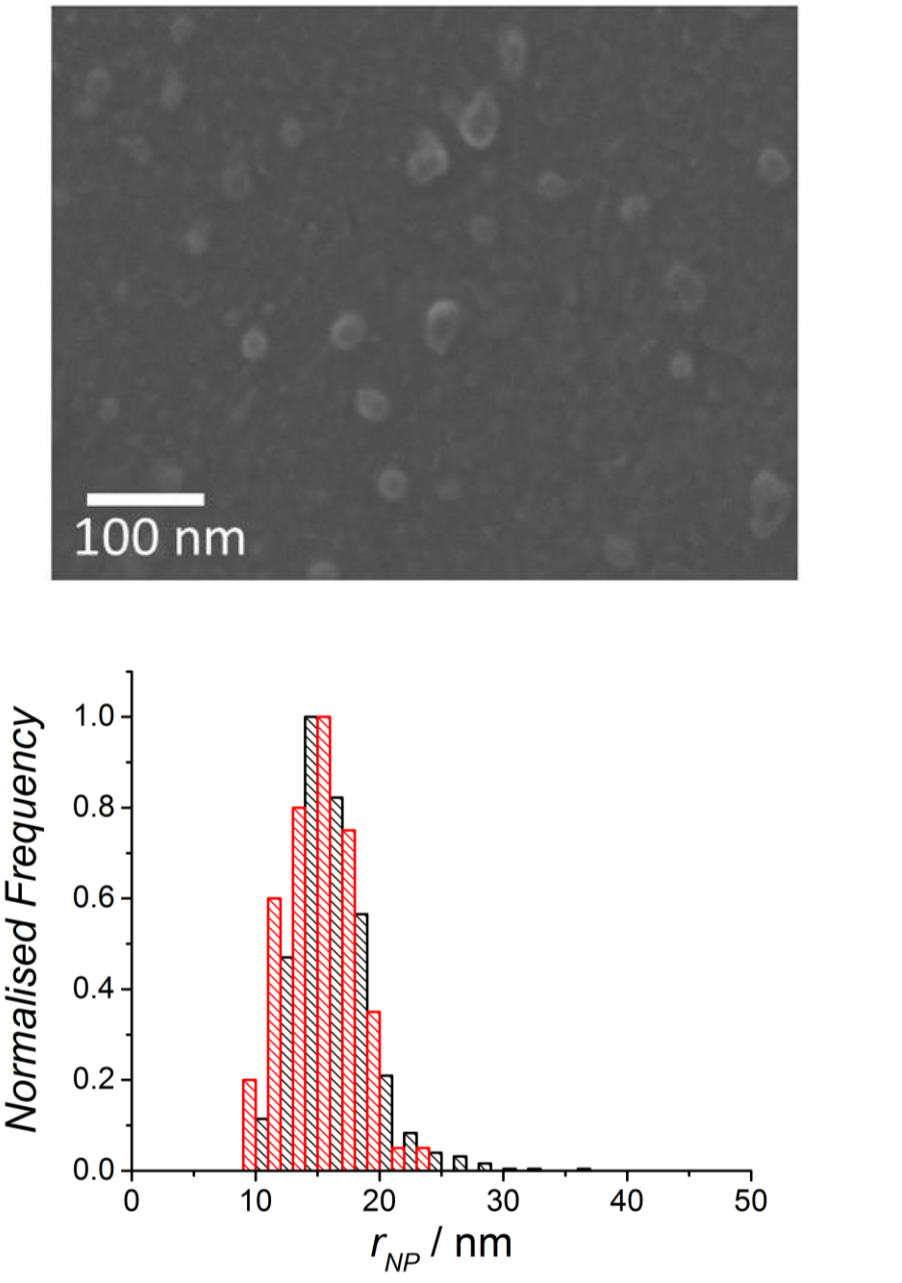


Figure 6.3 (Top) SEM image of GC surface after 5 min deposition of Bi_2O_3 NPs at -1.60 V vs MSE in 40 pM Bi_2O_3 and 0.10 M NaOH. (Bottom) Comparison of size distributions obtained from (black) NP impacts (red) SEM of nano-deposits.

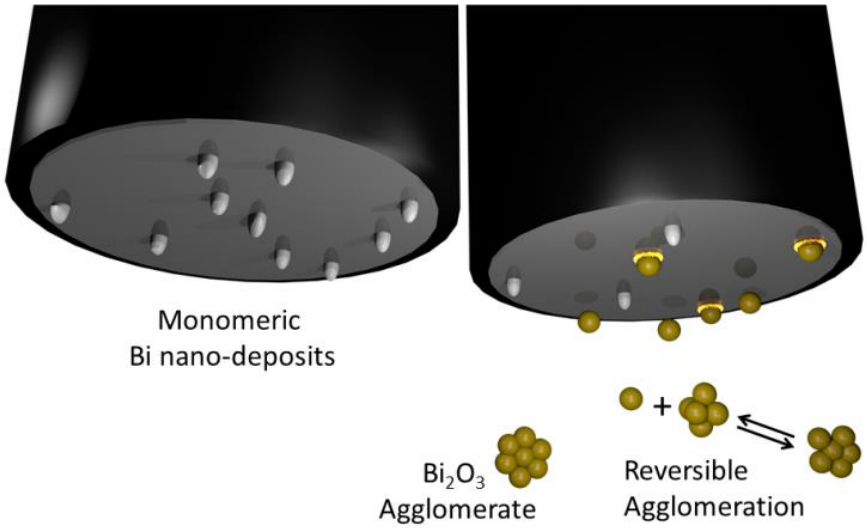


Figure 6.4 *Reversible* agglomeration of Bi_2O_3 NPs approaching the electrode, resulting in the deposition of monomeric Bi nano-deposits.

5.1.4 Conclusions

The rapid agglomeration/deagglomeration of uncapped Bi_2O_3 clusters has been confirmed by voltammetric and microscopic study. By electrolytic detection of single NPs at the electrode surface, the *reversible* nature of agglomeration has been shown to promote the release of single NPs and provide selective detection of the monomer by nano-impacts. Voltammetric studies with Ag and Fe_3O_4 NPs have previously shown only slow agglomeration of NPs[102, 155, 198, 211], observable over experimental timescales, and the detection of dimeric, trimeric and higher ordered agglomerates as well as monomers. Here, NP suspensions consisting of probably entropically agglomerated clusters have been shown to undergo rapid deagglomeration to release monomers at an active electrode surface. The electrolysis of these monomers results in the deposition of metallic Bismuth onto the electrode surface. Direct microscopic evidence of pure monomer detection is provided by imaging of the electrode by SEM. By impacting the NPs the deposits are immobilised allowing imaging without drying induced agglomeration/aggregation effects. This is the first time the rapid agglomeration behaviour of metal oxide clusters has been studied by the nano-impact technique and provides a unique and complementary mode of study in conjunction with other analytical techniques.

Chapter 6

Nano-Impact Photochemistry

As discussed previously in Section 2.2.6, the *direct-impact* method has been widely applied to NP systems allowing their electrochemical characterisation. Here we report the use of this technique in two different photochemical reactions and discuss the use of this technique for the tracking of photochemical NP conversion and NP growth.

In Section 6.1, the use of nano-impacts as a novel method for the study of photochemical reactions of individual NPs is reported. The conversion of gelatine stabilised silver bromide (AgBr) NPs to silver (Ag) NPs through photochemical reduction by ascorbic acid is studied mechanistically. Two mechanisms are proposed and investigated by monitoring the amount of electrochemically accessible AgBr against the time scale of conversion, measured through the use of the nano-impacts technique. This work is currently in press at the *Journal of Russian Electrochemistry*.

In Section 6.2, the tracking of the atom count in individual NPs during photochemical Ostwald ripening is reported. The nano-impact technique, in conjunction with UV-Vis and TEM analysis, is used to follow the photochemical formation of silver nano-prisms from spherical seed particles. A mechanism of photochemical Ostwald ripening is deduced and key growth stages are identified. This work has been published in *Nanoscale*.

6.1 Nanoparticle Photochemistry via Nano-Impacts

6.1.1 Introduction

The development of new solution-based synthesis methods for nanoparticles (NPs), especially silver (Ag), is important for the continued advancement in areas such as biology [220] and analysis [119]. Established methods for solution-based NP synthesis have revolved around the "bottom-up" approach [221], encompassing techniques such as chemical reduction [222-224] and

electrodeposition [225]. The mechanism of such solution-based processes have been thoroughly studied [226, 227] and originate with the formation of "seed" particles. With continued reaction, these "seeds" begin to nucleate, and grow by Ostwald ripening to form nanostructures, which are stabilised with a capping agent.

However, an alternative method has been developed that does not directly fit into this category – direct conversion. Zhu *et al* showed it was possible to chemically alter pre-existing titanate nanofibers, post-synthesis, through wet-chemistry phase transitions to titanium dioxide [228]. Other studies have also demonstrated the ability to alter the structure of stable spherical NPs through chemical reactions [229]. More recently however, the chemical conversion of spherical NPs was achieved whilst maintaining the spherical structure of the pre-cursor NP. This novel synthesis method has been realised through the photochemical reduction of gelatine stabilised silver bromide (AgBr) NPs to silver (Ag) NPs [230, 231]. This attractive direction for the synthesis of NPs opens new avenues for NP design. However, little is understood about the mechanism for this conversion, especially for the photochemical conversion of spherical particles.

In this section we consider two different mechanisms for the photochemical conversion of NPs, using the photochemical reduction of AgBr NPs by ascorbic acid as a model system. First, is the "core-shell" mechanism (see Figure 6.5(i)), whereby growth initiates evenly across the surface of the particle from the latent sites, forming a shell of Ag. This shell might limit the migration of Br^- and release of the halide, halting the conversion before the AgBr core could be converted [232]. Second, is the "irregular growth" mechanism (see Figure 6.5(ii)). Here the conversion propagates from random sites on the NP. This might allow the core of the particle to become converted before the process is deactivated through the complete reaction of the surface.

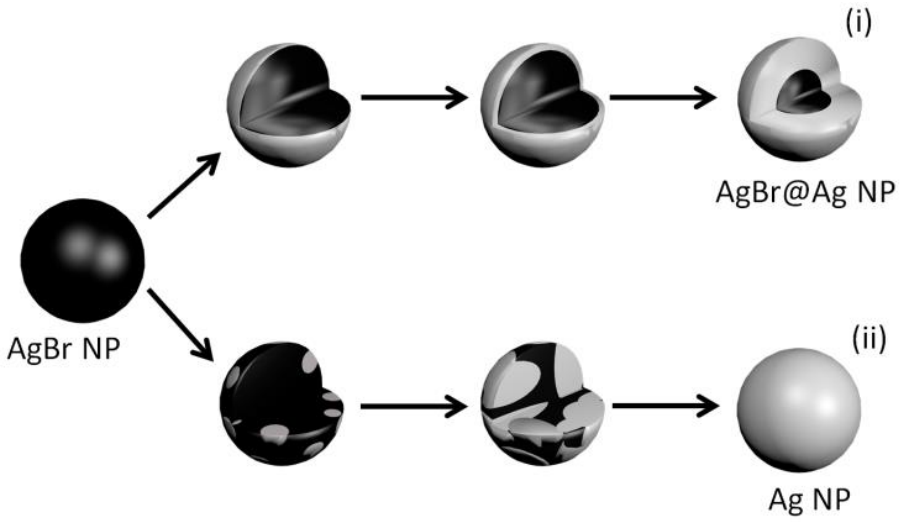


Figure 6.5 Proposed pathways for the photochemical conversion of a Ag NP by ascorbic acid. (i) "Core-shell" method whereby conversion progresses evenly across the whole surface towards the centre of the NP. (ii) "Irregular" conversion resulting in a complete Ag NP

In this chapter the possible mechanism will be electrochemically probed using the *direct-impact* technique[141] (Section 2.2.6). This technique has not previously been used to study the synthesis of particles however the method inherently lends itself to the mechanistic study of such conversions. This is because the amount of charge per NP collision provides information on the amount of electrochemically accessible redox material available in individual NPs. If a shell of Ag is formed as in mechanism (i), it can be theorised that this would provide a barrier to electrochemical reduction of the AgBr. If an irregular conversion were to occur as in mechanism (ii), AgBr would be accessible to the electrode for the duration of the conversion. By studying this electrochemical availability of AgBr during the photochemical reaction, it is therefore possible to resolve the mechanism by studying the change over the timescale of photochemical conversion. This Chapter extends the nano-impacts technique to the field of nano-photoelectrochemistry from a mechanistic perspective.

6.1.2 Experimental

6.1.2.1 Equipment

For photochemical conversion experiments, a custom made glass cell with 22 mm diameter quartz glass bottom was constructed. Illumination was provided by a F-150 halogen lamp, WPI Ltd. (Hitchin, UK) fitted with a 2 ft, 6.4 mm diameter glass fibre light guide purchased from Fiberoptics Technology, Inc. (Pomfret, USA) at 100 % illumination. The light guide was fitted with an IR dampener to minimise sample heating. The distance between the cell window and the light guide was 20 mm. The pH of the buffer used throughout was measured using a pH213 Microprocessor pH Meter from Hanna Instruments (Leighton Buzzard, United Kingdom). Calibration of the pH meter was carried out using Hamilton Duracal Buffer standards purchased from Sigma-Aldrich, United Kingdom.

6.1.2.2 Silver Bromide Nanoparticle Synthesis and Characterisation

The synthesis method for the gelatine stabilised AgBr NPs is covered in Section 3.4.3. Scanning Electron Microscopy (SEM) images were measured as outlined in Section 2.2.4, and were provided by Dr. K. Tschulik (formerly Department of Chemistry, Oxford University). Figure 6.6 shows an image of the particles which were analysed using Image J public domain software. The NPs were found to be spherical with a radius of (46 ± 1) nm with a standard deviation of 14 nm. Here and throughout this Section the error value quoted is the error of the mean.

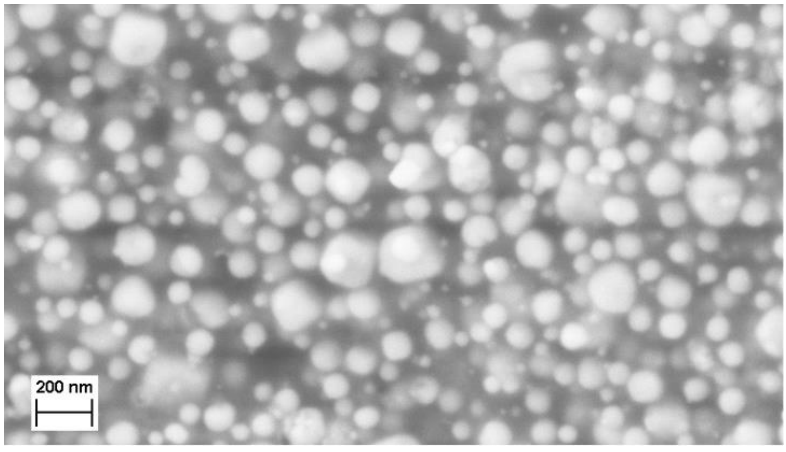


Figure 6.6 SEM image of gelatine stabilised AgBr nanoparticles.

6.1.3 Results and Discussion

Prior to nano-impact investigation the voltammetric behaviour of an ensemble of NPs drop cast on to an electrode surface was studied in the chosen electrolyte - pH10 sodium carbonate buffer. This medium was used as alkaline conditions have been shown to slow the photochemical reaction of AgBr with ascorbic acid [230], allowing the conversion to be studied over a suitable timescale for voltammetric study. Figure 6.6 shows the stripping voltammetry of 20 nmoles AgBr NPs drop cast on a GC electrode, in 0.10 M pH 10 buffer, initially scanned reductively. Reductive features, indicative of AgBr reduction can be observed after -0.75 V vs MSE:

$$AgBr(s) + e^- \rightarrow Ag(s) + Br^-(aq)\,, \tag{2.05}$$

A double oxidation peak at -0.10 V and -0.01 V vs MSE can also be seen, and can be attributed to the oxidation of Ag to AgBr and Ag^+ respectively.

$$Ag(s) \rightarrow Ag^+(aq) + e^-\,, \tag{2.06}$$

$$Ag(s) + Br^-(aq) \rightarrow AgBr(s) + e^-\,. \tag{2.07}$$

This voltammetry is in agreement with that reported previously in 0.10 M $NaNO_3$ electrolyte [163] (see Section 4.2) and implies similar or greater potentials can likely be used for quantitative nano-impact experiments.

Next, nano-impact analysis of the AgBr NPs was conducted using a suspension of AgBr NPs in 0.10 M pH 10 buffer ([AgBr] = 0.10 mM). A carbon fibre microelectrode was held at a reductive overpotential of -1.00 V vs MSE and reductive faradaic nano-impact spikes were observed, as seen in Figure 6.7.

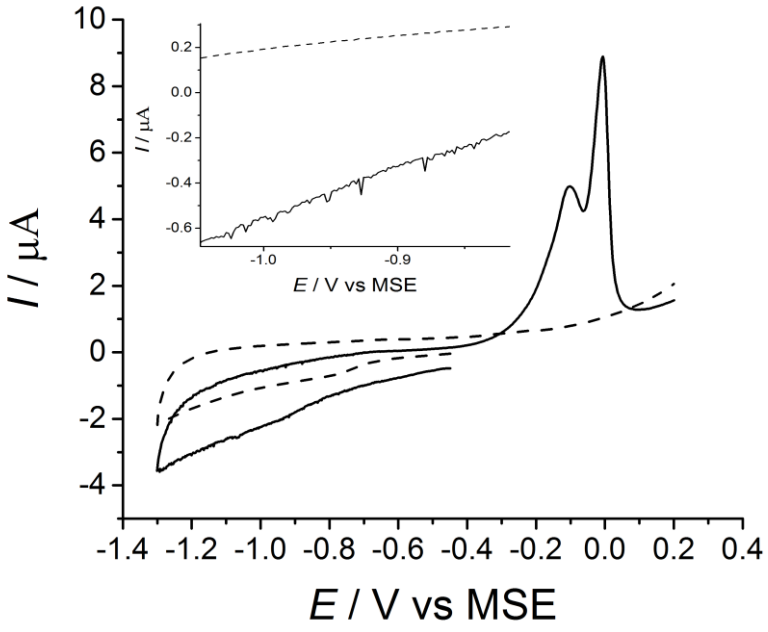


Figure 6.6 Cyclic voltammogram of a GC macro-electrode in 0.10 M pH 10 buffer at 100 mVs^{-1}. Bare GC (dashed line). GC modified by drop-casting 20 nmoles of AgBr NPs (solid line). Insert shows a zoomed in image of the voltammogram and the reductive features observed only in the presence of the drop-cast NPs.

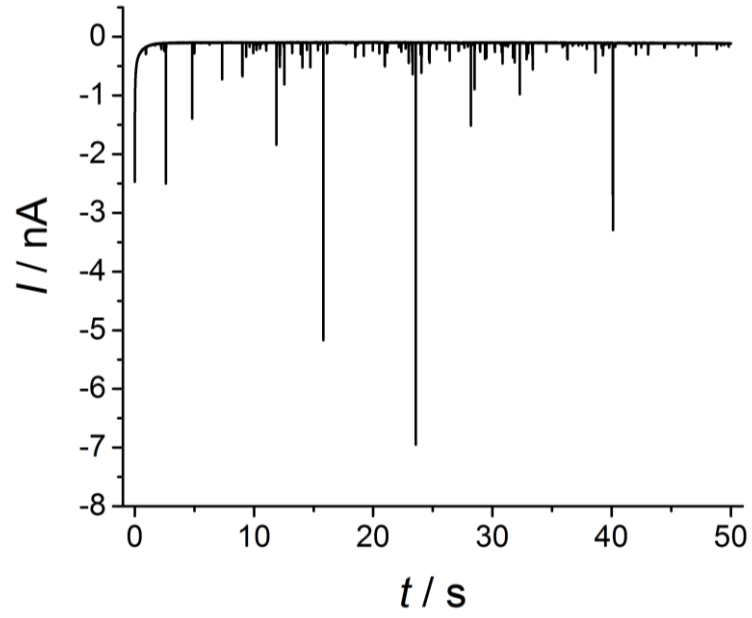


Figure 6.7 Typical current-time transient showing AgBr reductive impacts at -1.00 V vs MSE. This was conducted in 0.10 mM AgBr NP suspension and 0.10 M pH10 buffer.

These spikes were analysed noting the spherical shape of the NPs to produce a size distribution using the Equation [146] (Section 2.2.6):

$$r_{np} = \sqrt[3]{\frac{3M_w Q}{4nF\pi\rho}} \tag{2.08}$$

where r_{np} is the spherical NP radius, M_w is the molecular weight of the NP material, Q is the charge of the measured impact spike, n is the number of electrons involved in the redox process, F is Faraday's constant and ρ is the density of the NP material.

The comparison of the histogram obtained by nano-impact analysis against that measured from SEM images can be seen in Figure 6.8. The SEM image used for sizing is that shown in Figure 6.6. Strong agreement between the two particle distributions can be seen, with the mean spherical radius of the particles being (48 $\pm$ 1) nm and (46 $\pm$ 1) nm and standard deviations of 14 nm and 22 nm respectively. The close agreement between electrochemical and SEM sizing of the AgBr NPs strongly indicates that the NPs formed are pure AgBr. This is because any Ag already present in the NP would reduce the amount of AgBr available for electrochemical reduction and would lead to an underestimate of the NP size. This is further confirmed by independent UV-Vis characterisation of the NPs which can be seen in Figure 6.9. Ag NPs are well known to exhibit a characteristic peak at ~400 nm[233]. Such a peak is clearly absent from the observed UV-Vis spectrum obtained from the AgBr NPs showing the NPs formed are not Ag.

To establish the timescale of conversion of the NPs with ascorbic acid, the reaction was first investigated by UV-Vis spectrometry. A 30 mL solution of 0.3 mM ascorbic acid in 0.10 M pH 10 buffer was prepared in glass cell with quartz window. To this, 6 uL of the NP stock suspension was added and the solution bubbled with nitrogen to prevent oxidation of the ascorbic acid. The cell solution was maintained under constant illumination and samples removed every 10 mins for UV-Vis analysis. Figure 7.0 shows the UV-Vis spectrum of the NPs over a 60 min period. A clear trend can be seen with the emergence of a broad peak at 422 nm,

stabilising after 50 mins. The peak formed is indicative of the formation of large Ag NPs with a wide size distribution [233], matching that of the originating AgBr nanoparticles.

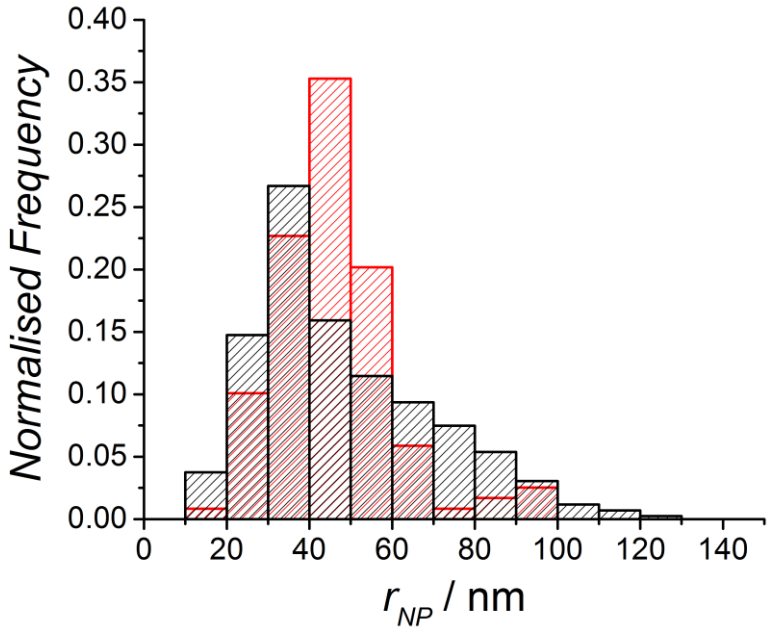


Figure 6.8 Nanoparticle size distribution comparison between SEM (red) and nanoparticle impacts (black). Normalised frequency used for ease of comparison of data sets (119 NPs analysed by SEM and 176 impacts analysed).

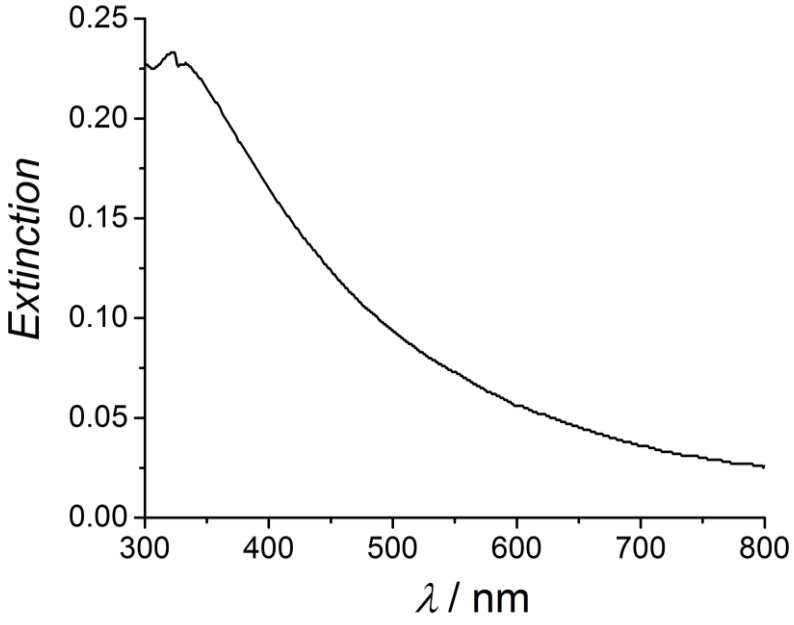


Figure 6.9 UV-Vis characterisation of AgBr NPs.

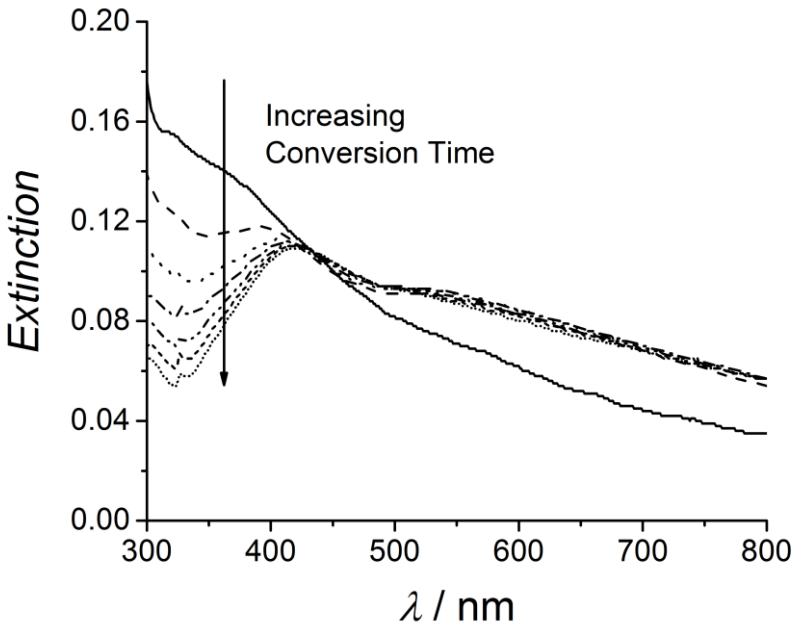


Figure 7.0 UV-Vis tracking of AgBr NP conversion over 60 minutes. Measurements taken at 10 minute intervals from 0 to 60 minutes.

Next, the photochemical conversion mechanism was probed voltammetrically by nano-impact experiments, studying both the rate of formation of Ag and the loss of AgBr. Current-time transients of 50 sec were recorded after full conversion by ascorbic acid (60 mins) at oxidative overpotentials of +0.40 V and +0.60 V vs MSE to try to detect the formed Ag NPs. No faradaic spikes were detected after full conversion despite the confirmation of suspended Ag NPs through UV-Vis spectrometry. This was attributed to reduction in size of the formed Ag NPs due to the respective density differences of AgBr and Ag. The decrease in size of the particle could occur without change to the gelatine layer thickness, and would result in an increased distance between the particle and electrode on impact when compared to that of the original AgBr NP. Additionally, hypobromite which can be formed during the synthesis process in alkaline conditions has been shown to cause gelatine cross-linking [234], which may be an additional barrier for Ag NP oxidation. The absence of impacts at overpotential of +520 mV represents a significant kinetic barrier to Ag NP oxidation under these experimental conditions. Complementary stripping voltammetry conducted on AgBr NPs converted by ascorbic acid to

detect the presence of Ag NPs resulted in interference by ascorbic acid oxidation. This was found to mask the Ag oxidation signal and meant no analysis of the change in Ag oxidation peak could be observed.

To study the loss of AgBr in the NPs during photochemical conversion, current-time transients with 50 sec duration were conducted at 10 min time intervals with the potential held at -1.00 V vs MSE. Each timed measurement was carried out individually such that illumination was constant until measurements were recorded. This was necessary as the light source contributed noise to the system and was switched off during the measurement. The results are summarised in Figure 7.1, which shows example current-time transients across the conversion time period. A trend can be seen with a reduction in spike size over the conversion timescale, with no spikes observed at 60 mins. Decreasing spike charge over time is consistent with conversion of the particles from AgBr to Ag and the loss of AgBr available for electrochemical reduction in converting particles.

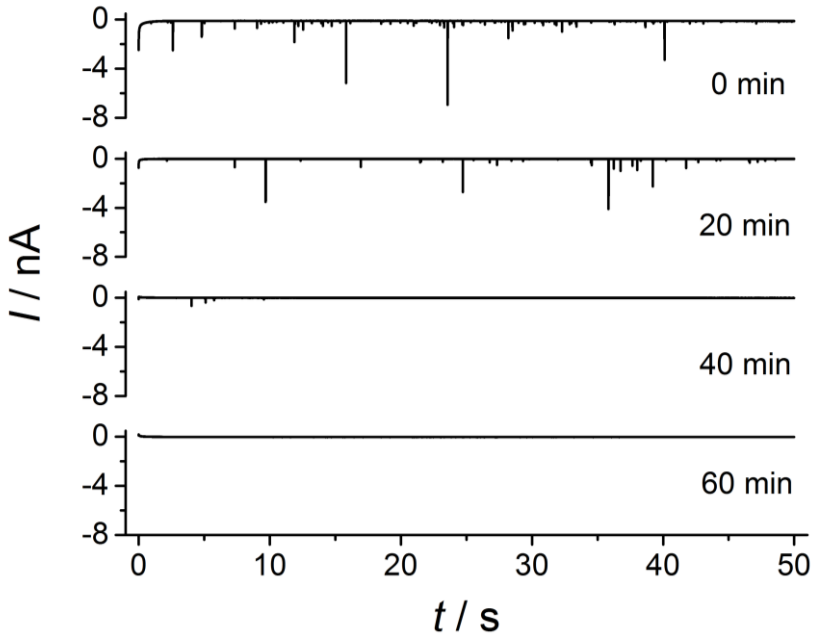


Figure 7.1 Current-time transients showing the change in AgBr reductive impacts over the time scale of conversion. This was conducted in 0.1 mM AgBr NP and 0.3 mM ascorbic acid in 0.10 M pH 10 buffer at -1.00 V vs MSE.

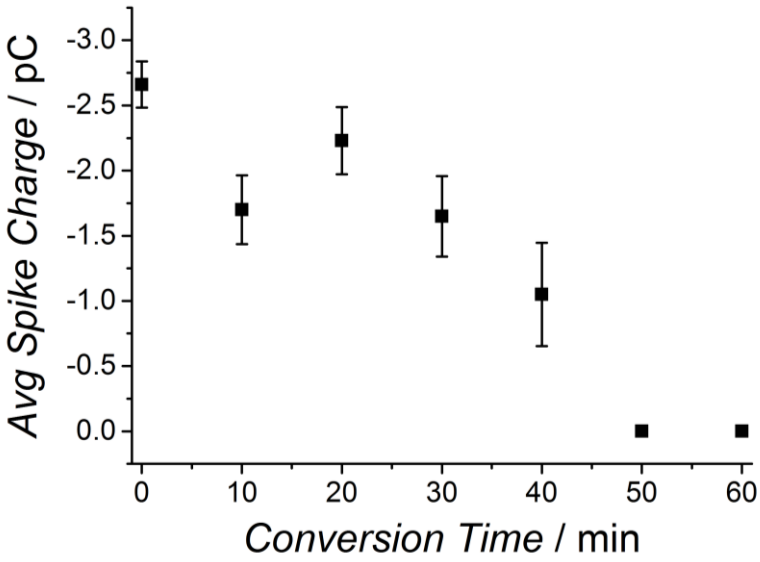


Figure 7.2 Average reductive spike charge as a function of conversion time.

The spike charges measured over the duration of conversion were analysed and plotted against conversion time to give Figure 7.2. A general trend can be clearly seen, with a decreasing value for the average spike charge over the course of conversion. This decreased until 50 mins, where no spikes are recorded. This decrease in spike charge is associated with the loss of AgBr as the conversion progresses and matches the timescale for conversion as obtained by UV-Vis spectrometry. This shows that by analysing the average spike charge, it is possible to track the conversion of NPs to its completion.

If a shell of Ag were to have formed the release of halide would have been halted due to a compact outer layer. Without a means of expelling the halide, a build-up of Br^- in the centre of the NP would promote recombination of the photochemically generated Ag^+ ions with adjacent Br^- ions to form AgBr[232]. This would result in an abrupt fall in reductive spike charge as soon as this shell developed. After 40 mins, a 60.5 % loss of NP volume can be measured which can be expressed as the conversion of more than 10 nm of the outer layer of the NP. A layer of this thickness would provide a significant barrier for Br^- release from the core. Instead, a gradual reduction in spike charge occurs, indicating that AgBr is electrochemically accessible

throughout the conversion process. This allows for expulsion of the halide and continued conversion of the NP. Therefore, this suggests that the photochemical synthesis of AgBr occurs through an irregular mechanism extending to the core of the particle before the entirety of the surface is converted.

6.1.4 Conclusions

The nano-impact technique has been shown as an informative tool for probing the synthesis mechanism of AgBr NPs to Ag through the photochemical reduction by ascorbic acid. By measuring the change in the amount of AgBr electrochemically accessible throughout the conversion timescale the reaction mechanism was found to be of an irregular nature, propagating over the NP structure. This work has expanded the use of the nano-impact technique and clearly demonstrates its use in the field of NP synthesis for both mechanistic investigation and tracking of synthesis. The use of this technique would be especially applicable for the tracking of NP conversion where identifiable UV-Vis peaks are not available, or not measurable as in opaque media [157].

6.2 In-situ Tracking of Photochemical Ostwald Ripening Through Voltammetric Atom Counting

6.2.1 Introduction

Voltammetric impact studies of solution-phase NPs are important for fundamental, commercial and environmental applications[176]. Advances in this area have led to the successful characterisation of NPs through indirect processes[137] and direct redox reactions[175] with focus on the sizing of spherical geometries (Section 2.2.6). In particular NPs colliding with an electrode held at a suitable potential are oxidised or reduced directly to provide quantitative atom count information. This technique has also been shown to provide sizing and aspect ratios of nano-rods[92] and track NP reactions[235]. In the following, the nano-impact technique is

applied to the study of NP synthesis to provide critical atom count information and new mechanistic insights.

The mechanistically informed synthesis of new NP geometries is potentially ground-breaking[236-238]. Nano-prisms of silver, synthesised by photochemical conversion of spherical seeds by Mirkin *et al.*[93, 161], are an example of a valuable NP geometry that gives rise to surprising properties[239-241] and sensing applications[242]. Mechanistic studies for nano-prism formation have revealed the basic chemistry as shown in Figure 7.3[243]. Reorganisation of Ag is rationalised by involvement of a redox cycle driven by citrate reduction of Ag^+ following O_2 indirect oxidation of Ag^0. This is *assumed* to lead to an Ostwald ripening process[244], whereby the consumption of smaller NPs provides material for growth of larger NPs. Study thus far has involved rapid conversion of seeds to prisms with either UV-Vis or ex-situ TEM used to probe key growth stages[245].

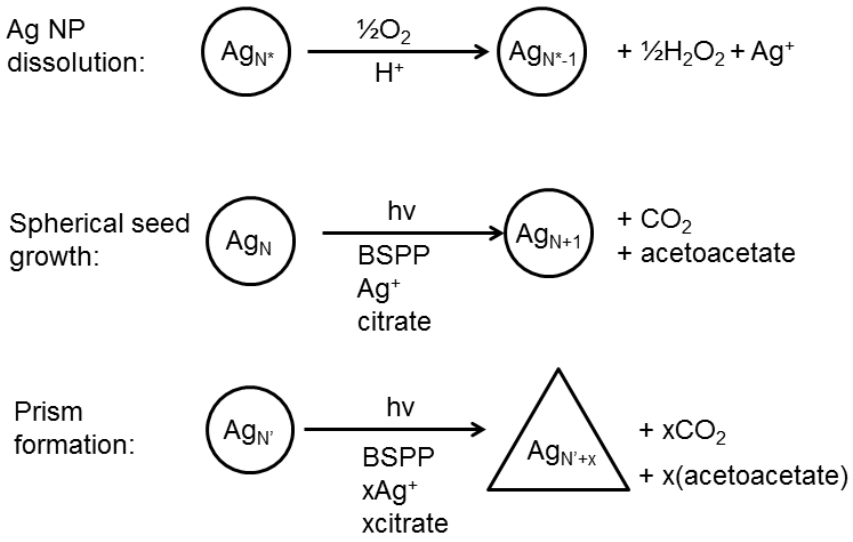


Figure 7.3 Suggested mechanism for the photochemical transformation of spherical Ag seed NPs to nano-prisms[243]. BSPP = bis (p-sulfonatophenyl) phenylphosphine. O = spherical NP. Δ = nano-prism.

Herein we report a new method using nano-impacts to track NP synthesis and provide atom counting of individual NPs in solution. The methodology outlined allows observation of

key growth stages in terms of the number of atoms gained or lost by individual particles, unaffected by potential shape bias. Importantly this method follows the growth of particles in solution without the need for extensive sample preparation.

6.2.2 Experimental

The method used for prism synthesis is covered in Section 3.4.3, but is repeated here for clarity. The method employed was as previously reported by Mirkin *et al*[161], but with a 18 Watt fluorescent tube light source. The emission spectrum was measured using an Ocean Optics 2000 UV-Vis spectrometer, and is shown in Figure 7.4.

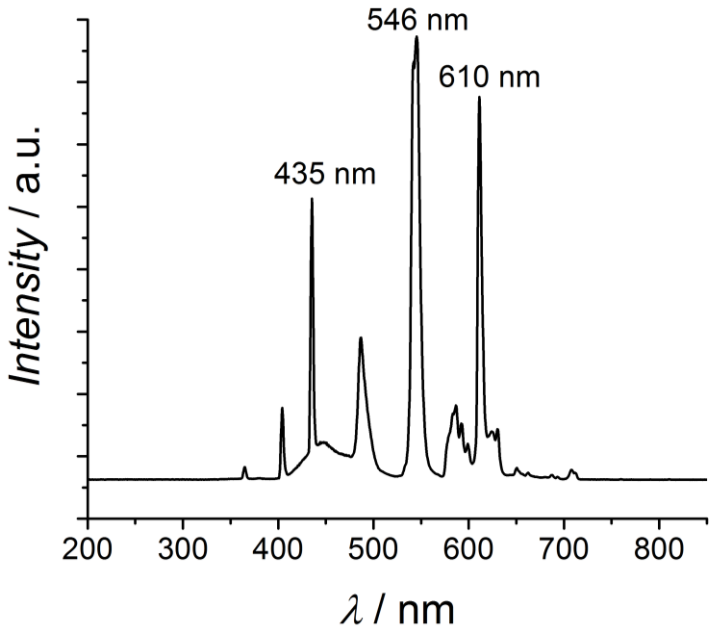


Figure 7.4 Emission spectrum of the fluorescent tube light source.

A 250 mL conical flask containing 95 mL nanopure water, 1 mL 30 mM trisodium citrate and 2 mL 5 mM $AgNO_3$ was emersed in an ice bath and bubbled with N_2 for 30 mins. After this, 1 mL 50 mM $NaBH_4$ was added under vigorous stirring, induced by magnetic stirrer, to begin the initial reduction. Over the next 16 mins, 4 drops of the $NaBH_4$ solution were added every 2 mins to ensure $AgNO_3$ reduction reached completion. Next, 1 mL 5 mM BSPP and 0.5 mL 50 mM $NaBH_4$ were simultaneously added dropwise over 5 mins. The reaction was left vigorously

stirring overnight in the dark. The next day, the photochemical conversion was initiated by positioning the flask at 135 mm from the light source described. The reaction mixture was not stirred during conversion. Samples were taken at 24 hour intervals and stored in the dark at (5.0 ± 0.2) °C.

6.2.3 Results and Discussion

Silver nano-prisms capped with citrate and bis (p-sulfonatophenyl) phenylphosphine (BSPP) were grown photochemically from spherical seed particles as reported by Mirkin *et al*[161], except for using a *much* lower intensity light source (18 W, fluorescent tube, 138 mm distance) to markedly slow the process allowing better mechanistic resolution. Figure 7.5(a) shows an image of the NP stock suspension at daily intervals for 10 days. The colour of the suspension changes from yellow to blue, indicative of a change in NP geometry[93, 161, 243].

UV-Vis can provide information on the ensemble plasmon resonance modes for NPs i.e. longitudinal and transverse, however does not provide direct information on single particles[246]. The photochemical conversion was studied by UV-Vis spectrometry as shown in Figure 7.5(b), with samples taken at daily intervals. A clear trend is apparent, with a concurrent decrease in the P1 and increase in P2 over the 10 day conversion period. P1 corresponds to the expected response for spherical seed NPs and P2 to the in-plane dipole resonance present for both nano-disk and nano-prism structures[93, 94, 161, 243]. Figure 7.5(c) shows a plot of P1 and P2 peak absorbance variance with time. An approximately sigmoidal shape is observed and indicates the main change in absorbance occurs between days 2 and 7. This period of rapid change in the P1:P2 peak absorbance ratio has previously been linked to the main growth period of the particles and indicates that under our conditions this occurs over a 5 day period. This confirms a slower rate of conversion than previously studied because of using a lower intensity light source[93, 161, 243].

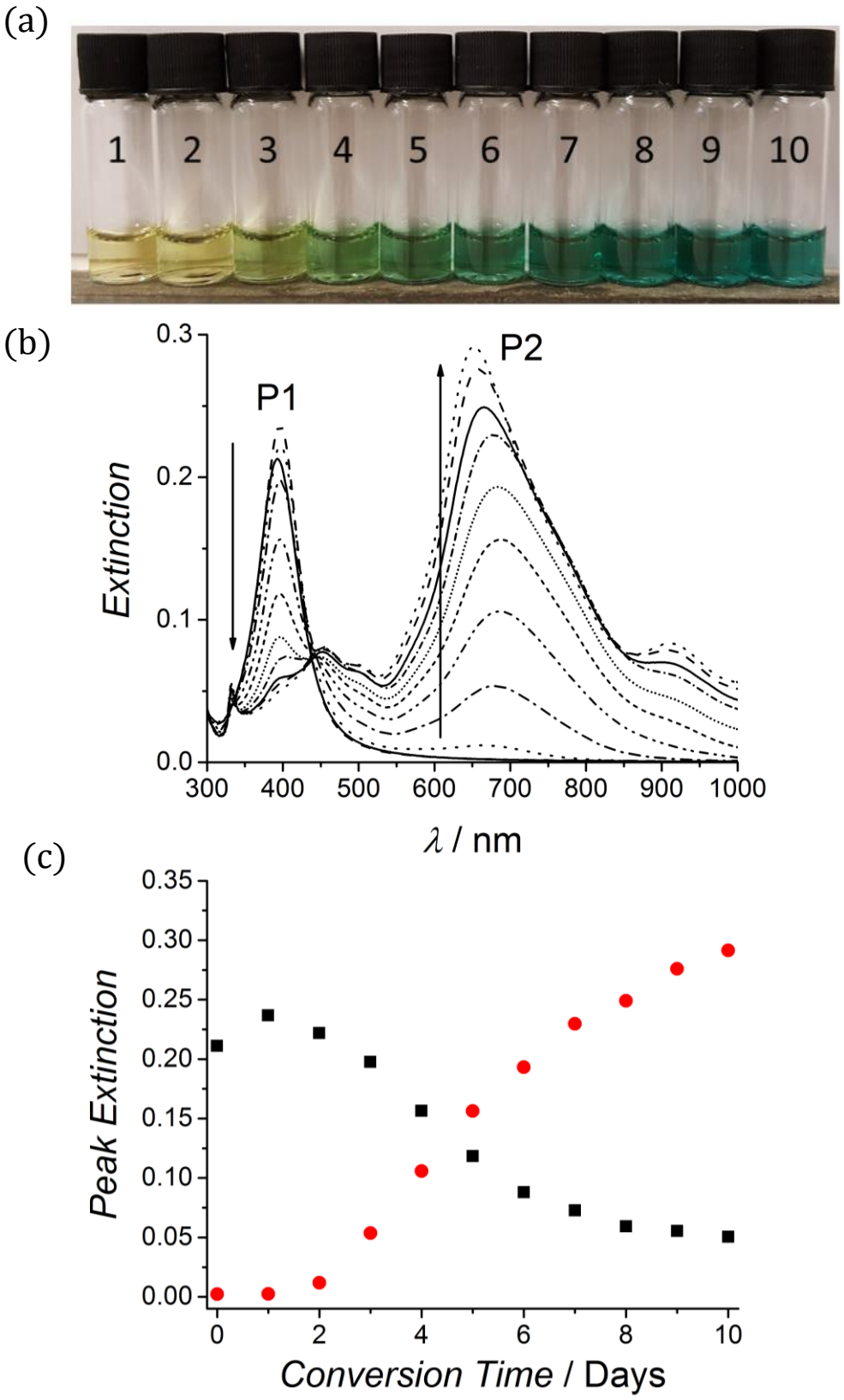


Figure 7.5 (a) Image of Ag NP suspensions showing colour change over the studied timescale of conversion. (b) UV-Vis spectra of the Ag NP suspension over the studied timescale of conversion. Direction of arrows indicates increasing time. (c) Plot of peak absorbance vs. conversion time where black is the peak at 396 nm (P1) and red corresponds to P2.

To observe geometrical transformations responsible for the UV-Vis changes detected, TEM images of the NPs were measured at intervals across the conversion period of 10 days as shown in Figure 7.6(a). These were measured by Mr. S. V Sokolov (Department of Chemistry, Oxford University), MS. J. Holter and Dr N. Young (Department of Materials, Oxford University). Care was taken to ensure a representative account of the particle distributions by taking sample images from different grid areas. Day 0 was shown to consist entirely of spherical seed particles of size (5.9 ± 2.5 nm). By day 3 all NPs observed remained spherical, but with some larger particles now present. Approximately 15 % the of analysed particles displayed planes of material extending from the core of the particle as highlighted in red in Figure 7.6(a). These planes ("rafts") appear to be thin, as evidenced by the difference in contrast compared to the originating particle, and were only found on particles with diameter >7 nm. These rafts were not observed for any other day even though identical sample preparation was employed, indicating this structure was not an artefact of the drying process. These intermediate particles have a large surface to volume ratio; hence the majority of atoms have a low coordination and may be very mobile. Such structures will have locally high surface energy and will readily transform into a lower energy, more stable structure. Similar structures have been reported previously for other silver and gold particulate systems[247]. Planes are no longer visible by day 5, where larger particles begin to form. Accurate analysis of particles on day 6 was hindered due to the irregularity of the NP geometries observed as exemplified in Figure 7.6(a). NPs of spherical geometry were still present and were all found to be below 10 nm in diameter. Days 8 and 10 showed the ultimate prismatic NPs, with some smaller spherical NP seeds still present.

To distinguish geometrical rearrangement and volumetric growth of particles over time, it is necessary to monitor the change in the number of atoms of Ag per NP. Figure 7.6 (b) shows the calculated distributions estimated from the TEM images across the conversion timescale. The distributions are split into "spherical" and "prismatic" contributions, expressed in terms of moles of Ag per NP, to allow direct comparison between different particle geometries. These were calculated using the following Equations:

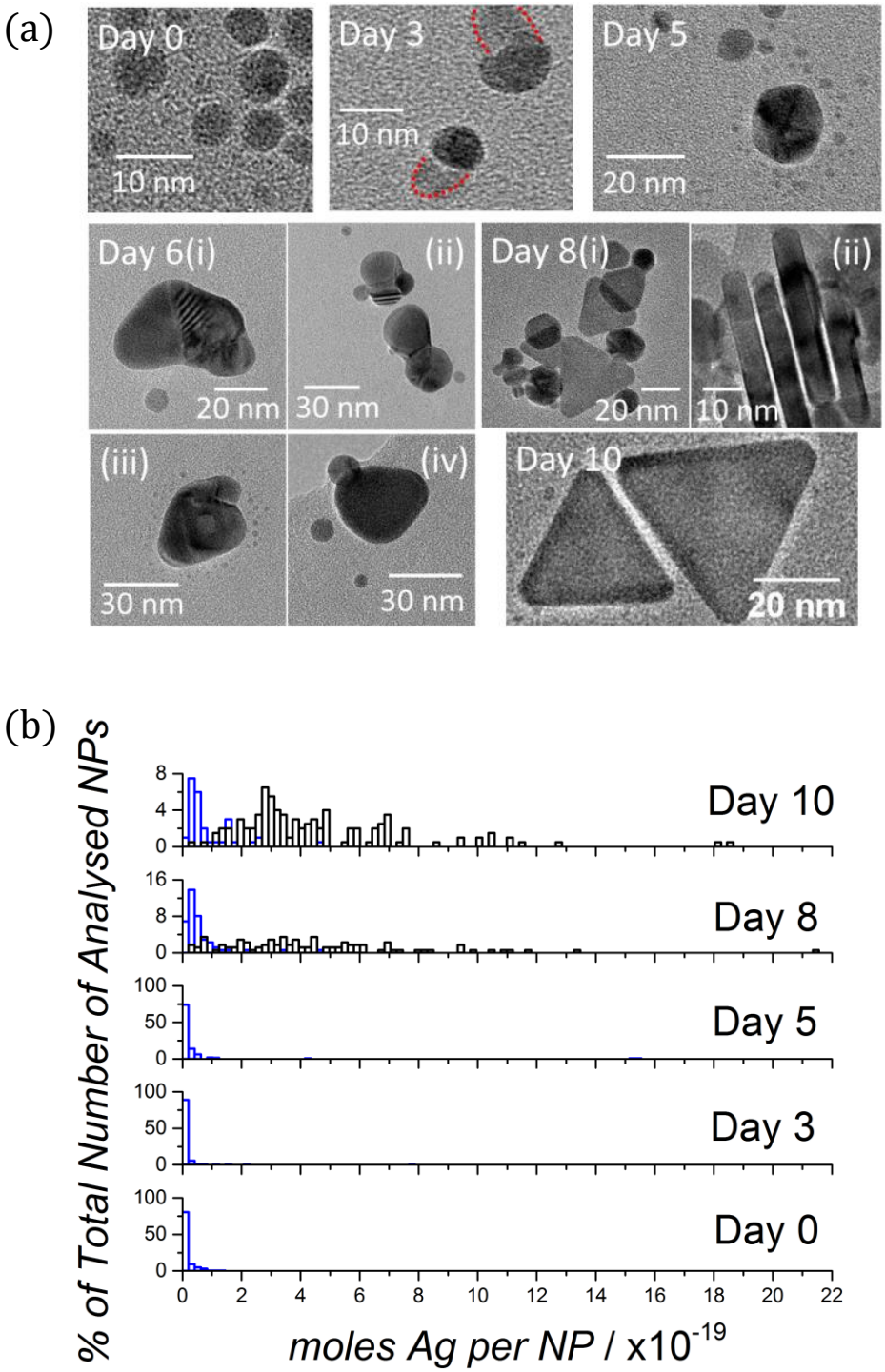


Figure 7.6 (a) Example TEM images. (b) TEM distributions for the NPs over the timescale of conversion. Blue fractions are spherical particles and black fractions are prisms. The number of particles analysed for the days 0, 3, 5, 8 and 10 were 160, 157, 158, 167 and 200 respectively.

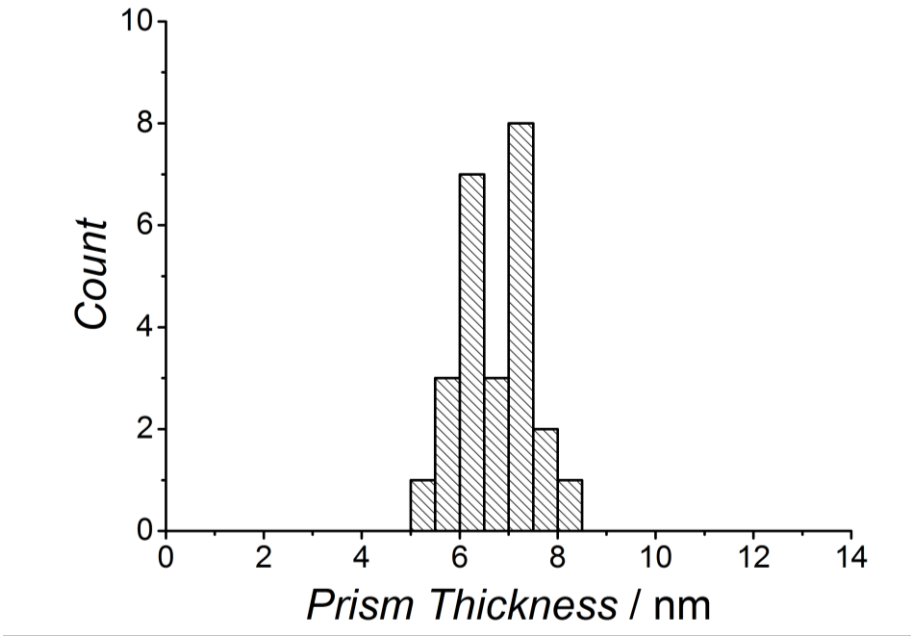


Figure 7.7 Distribution of prism thicknesses.

$$M_{\mathrm{s}} = \frac{\frac{4}{3}\pi r_e^3 p}{\mathrm{A_r}}, \tag{2.09}$$

$$M_{\mathrm{p}} = \frac{\frac{1}{4}\sqrt{3}\mathrm{d}^2\mathrm{h}_p p}{\mathrm{A_r}}, \tag{2.10}$$

where M_s and M_p are the moles of Ag per NP for spherical and prismatic NPs respectively, r_e is the radius of the spherical NP, p is the density of Ag (10.49 g cm^{-3})[190], A_r is the atomic mass of Ag, d is the edge length of the prisms and h_p is the thickness of the prism (taken perpendicular to the triangular face). This thickness was measured from TEM images of stacked prisms and was consistent for prismatic particles across the days where they appear at (6.7 ± 0.8 nm). This value was used for calculations of moles Ag per NP for all prisms. An example TEM image of the stacked prisms can be seen in Figure 7.6(a) day 8(ii) and the distribution of the prism thickness in Figure 7.7. A broadening of the distribution and a fall in the relative population of smaller particles is observed during the conversion timescale. The beginnings of ripening seem to be visible on day 3, with a slight tail in the distribution towards higher atom count. A fall in the proportion of smaller particles and slight broadening of the distribution from day 3 to 5

confirms the observation of the formation of larger particles. Note that the UV-Vis data shows a rapidly increasing signal at this period indicating a change in NP geometry. This is in contrast with TEM where only apparently spherical particles are observed. Nano-disks are known to have similar UV-Vis absorbance to nano-prisms[94] and are difficult to differentiate from spheres without electron emission loss spectroscopy (EELS) due to their similar 2-D shape when viewed from a perpendicular perspective. Therefore it can be speculated in the light of the UV-Vis spectra that nano-disks may be formed prior to prism formation. From day 5 to 8 the most significant change in distribution occurs, along with the appearance of prisms. This shows that the formation of the prismatic geometry occurs concurrently with an increase in atom count of the particle. The formation of prisms results in a decrease in the proportion of small spherical particles. By day 10 the distribution primarily consists of triangular nano-prisms. The consumption of small particles and growth of larger particles is consistent with an Ostwald ripening process. However due to the complex geometries of particles, especially at day 6, accurate sizing and volumetric information was difficult to obtain. Therefore, to complement the TEM results an in-situ study of the conversion was conducted concurrently using nano-impact analysis.

As discussed in Section 2.2.6, nano-impact voltammetry allows for analysis of NPs based only on the number of atoms in the NP[199]. As the technique is not influenced by the assumption of idealised geometries as for the TEM analysis, it may provide a more accurate description of particle growth for individual NPs. In addition, the speed and cost of use allows for samples to be measured at more frequent intervals than TEM imaging. For accurate distributions of the particles to be obtained it was necessary to minimise aggregation or agglomeration effects in electrolyte. Studies have shown prisms to be especially susceptible to inorganic anion composition, undergoing geometric reconfiguration when exposed to chloride, yet retaining their prismatic nature in nitrate[248]. The long term stability of nano-prisms in nitrate however has not been reported. Particle stability in the chosen electrolyte, 40 mM KNO_3, was ensured by UV-Vis analysis of the particles at 5 min intervals for 2 hours at 24 hour intervals. The spherical

and prismatic peaks were found to be stable under these conditions, with little broadening or reduction in height of the peaks observed due to aggregation[249]. To minimise aggregation or agglomeration during nano-impact experiments, samples of the NP stock were taken at daily intervals and diluted by 20 times in 40 mM KNO_3. The suspension was not degassed as this was found to induce aggregation or agglomeration of the prisms, noted by a loss of colour of the solution. Current-time transients were recorded at an oxidising potential of +0.40 V vs MSE. Current spikes were integrated using signal counter software[250] and Equation 3 used to calculate the moles of Ag per particle, *M*:

$$M = \frac{Q}{nF}, \tag{2.11}$$

where Q is the charge of the integrated impact spike, n is the number of electrons transferred to each Ag atom ($n = 1$) and F is the Faraday constant. An example of the current-time transient responses is in the Figure 7.8.

Figure 7.9 shows the resultant distributions from nano-impacts conducted for each day during conversion. Across the 10 day conversion period a broadening of the particle distribution is observed. This occurs concurrently with a reduction in the number of small particles detected. The most significant shift in distribution occurs from day 8 to 10. This is consistent with the TEM analysis and shows the use of nano-impacts for tracking NP growth. TEM and nano-impact distributions on the same days show agreement with the small deviations arguably attributed to the perfect geometric assumptions made in the TEM analysis and differences in diffusional flux of different sized NPs. As the resulting charge of a nano-impact event is not affected by particle shape and purely probes the atom count per NP, all stages could be analysed including day 6 where accurate sizing by TEM could not be obtained. The resultant nano-impact distribution indicates that the irregular shaped particles observed on day 6 (see Figure 7.6 (a)) do contain particles of increased atom count. However the distribution is still strongly reminiscent of the starting particles with most particles possessing less than 1×10^{-19} moles Ag per NP. Significant distribution changes only occur from day 8 to 10, which indicates

that the main growth period of the particles occurs much later on through the conversion than the geometric changes indicated by UV-Vis analysis. This highlights the surface sensitive nature of UV-Vis spectroscopy and in this case its limitations in tracking growth in these types of processes. In addition this illustrates the benefit in using the nano-impact technique to quantify growth in irregular shaped particles and the ability to track the growth of particles in the solution phase.

The slow timescale of conversion and concurrent TEM and nano-impact analysis allows us to propose the mechanism for Ostwald growth of nano-prisms as shown in Figure 8.0. Here, dissolution of small Ag seeds and growth on larger NPs occurs, with the formation of 2D planes on larger NP seeds. Next, ripening of these particles forms nano-disk intermediates which give rise to the initial changes in UV-Vis absorbance. These nano-disk-like structures then continue to grow into the prismatic structures observed at day 8 and 10. The formation of the prismatic geometry occurs with an inherent increase in atom number.

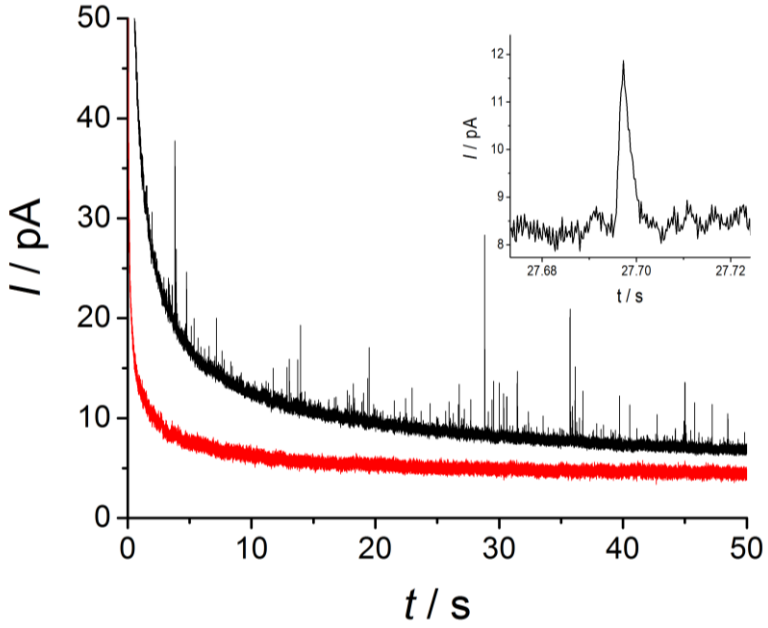


Figure 7.8 Example of typical nano-impact current-time transient response at +0.40 V vs MSE. (Black) 20 times diluted day 5 nanoparticle stock in 40 mM KNO_3. (Red) Blank 40 mM KNO_3. Insert shows zoomed in image of a single nanoparticle impact spike.

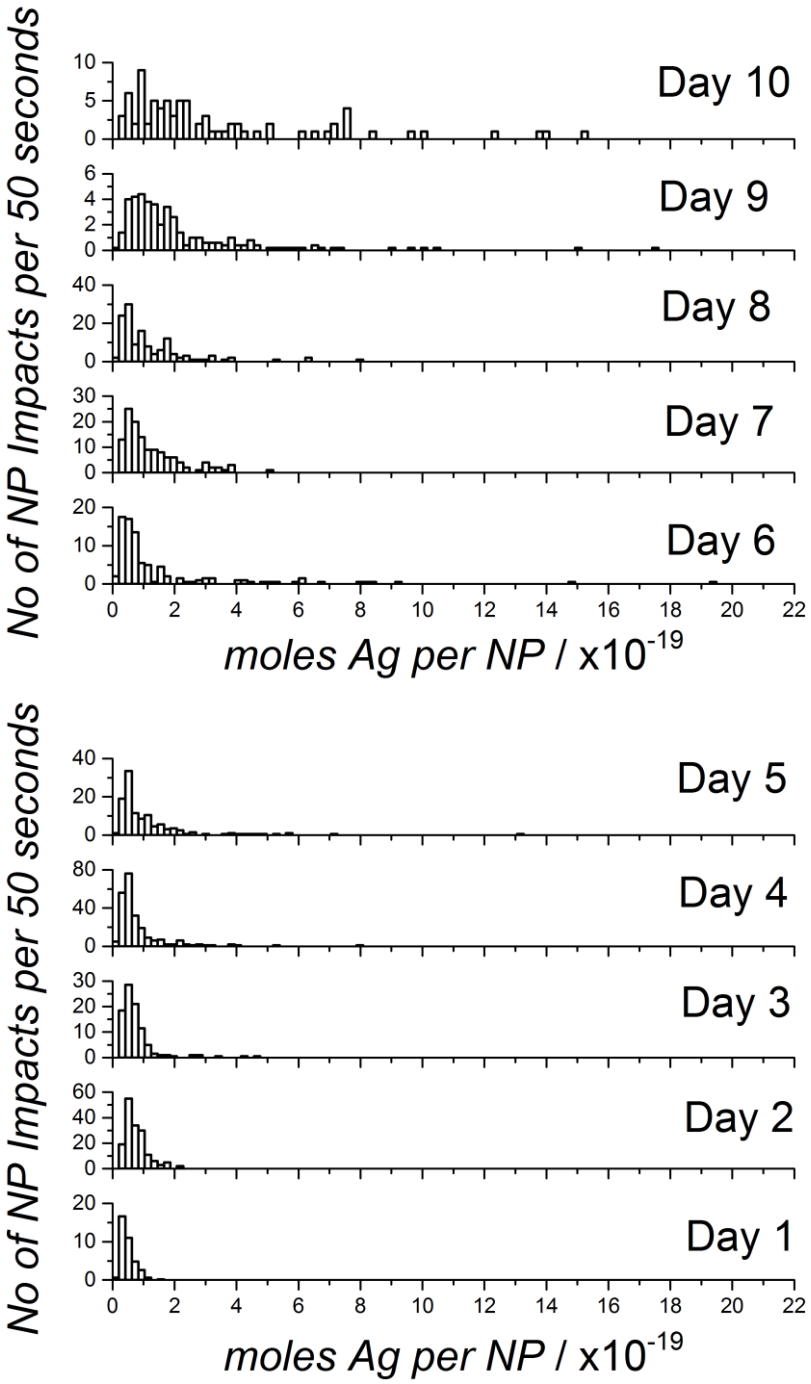


Figure 7.9 Distributions of impacted NPs at daily intervals during conversion gained by nano-impact voltammetry of the NP suspension 20 times diluted in 40 mM KNO_3 at +0.40 V vs MSE.

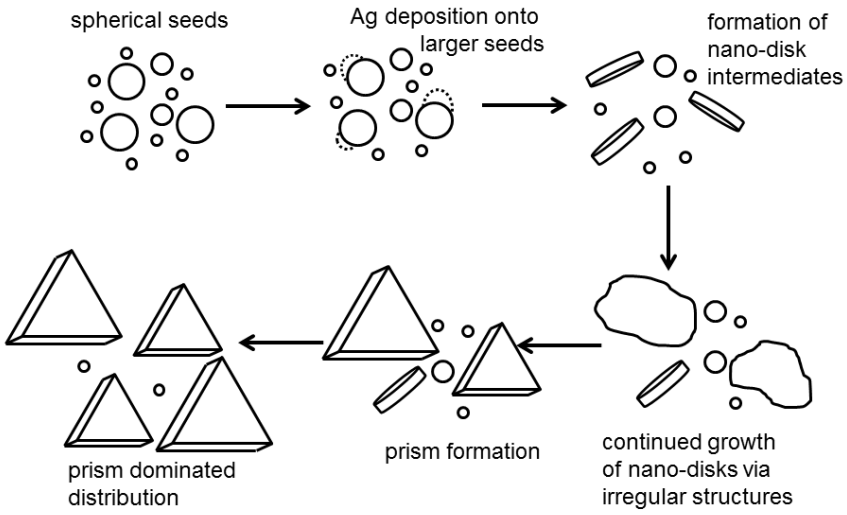


Figure 8.0 Schematic mechanism proposed for the photochemical Ostwald ripening of spherical Ag NPs to nano-prisms via nano-disk intermediates

6.2.4 Conclusions

In summary, the nano-impacts technique has been shown to track NP growth by Ostwald ripening, providing atom counting information of individual NPs in solution. This is found to correlate with TEM imaging and newly indicates the role of a nano-disk geometry in the conversion of spherical NPs to nano-prisms. With accurate volumetric information gained from nano-impact analysis, it can be inferred that geometric changes to the particles occurs prior to growth. The direct volumetric information gained from nano-impact analysis also facilliates the quantifaction of growth during irregular-shaped stages which troubles TEM analysis. As the atom count information gained by nano-impacts is not affected by the shape of the particles it provides a complemetary method for following growth in such systems where UV-Vis spectroscopy is relatively insensitive to some geometric changes. In addition this provides benefits over dynamic light scattering and nanoparticle tracking analysis techniques that rely on spherical assumptions. This method of following particle growth by nano-impact voltammetry is broadly applicable and is a low cost and fast method for following NP synthesis in solution whilst also providing mechanistic insights, statistical information and population distributions.

Chapter 7

Nano-Impact Voltammetry and Electrode Arrays

In this chapter, the interplay of nano-impacts and electrode arrays is studied. In Section 7.1 the fabrication of functional nanoelectrode arrays by the electrolysis of AgBr NPs impacting on a glassy carbon electrode from suspension in aqueous solution is reported. This builds on the nano-impact deposition of bismuth oxide NPs onto electrode substrates as developed in Section 5.1. The impacted NPs result in Ag NP deposits of similar size to the originating NP, with the coverage of these arrays easily controlled by the time of the deposition step. The NPs constituting the array are deposited randomly across the surface with little aggregation or agglomeration. The fabricated arrays are themselves electrochemically active, mediating the reduction of hydrogen peroxide, H_2O_2. This work has been published in *Nanoscale*[214].

In Section 7.2, the femtomolar detection of silver NPs by *direct-impact* voltammetry is reported. This is achieved through the use of a random array of microelectrodes (RAM) integrated into a purpose built flow cell, allowing combined diffusion and convection to the electrode surface. A coupled RAM-flow cell system is implemented and is shown to give reproducible wall-jet type flow characteristics using potassium ferrocyanide as a molecular redox species. The calibrated flow system is then used to detect and quantitatively size silver NPs at femtomolar concentrations. Under flow conditions, it is found the NP impact frequency increases linearly with the volumetric flow rate. The resulting limit of detection is more than 2 orders of magnitude smaller than the previous detection limit for *direct-impact* voltammetry of 900 fM (Ellison, J.; *et al. Sens. Actuators, B* **2014**, *200*, 47), and over 30 times smaller than the previous detection limit for *indirect-impact* voltammetry of 83 fM (Alligrant, T. M.; *et al. Langmuir* **2014**, *30*, 13462). This work has been published in *Analytical Chemistry*[251].

7.1 Nanoelectrode Array Formation by Electrolytic Nanoparticle Impacts

7.1.1 Introduction

The miniaturisation of electrodes has progressed over recent decades, with the development of microelectrodes[252] and more recently nanoelectrodes[253] bringing the benefits of increased mass transport and lower background currents to the field of electrochemical analysis. Arrays of electrodes, including those of nanoelectrodes, have continued this trend allowing enhanced detection limits of molecular species and maximisation of signal from minimal use of costly electrode materials[18, 29, 254, 255].

As discussed in Section 1.8.2, nanoelectrode ensembles (NEEs) or random arrays have been produced by a multitude of methods including template synthesis[30, 256, 257], colloidal NP assembly[258], etching[33] and electrodeposition[259-262]. These types of array are usually faster and easier to produce than the more ordered arrays, which can be fabricated by lithography[263] and the use of highly ordered block copolymers to give well defined inter-electrode spacing[34]. This inter-particle distance is crucial in dictating the diffusional regime to the electrodes and hence the observed voltammetry[1, 264, 265]. In random arrays, the case of NPs being diffusionally independent is uncommon, with most involving the at least partial overlapping of diffusion layers across the substrate. If the electrodes are close enough, this overlapping of diffusion layers gives rise to planar diffusion to the entirety of the modified electrode surface[264, 265]. This allows for macroelectrode responses to be gained from a far smaller amount of the often more costly electrocatalytic material but the advantages of maintained mass transport are lost.

One popular method for functionalising electrodes with nanomaterials for electroanalytical applications is by electrodeposition[261, 262, 266]. The reduction of metallic ions results in nucleation sites on the substrate, leading to continued electrodeposition and growth into nanostructures. The size and geometry of NPs formed by this method can be very difficult to control, with aggregation of NPs probable[267]. Modification of an electrode with pre-synthesised NPs navigates around this issue, allowing control over the geometry and size of the

NPs constituting the array. Modification involves the drop-casting of suspended nanomaterial onto the underlying electrode. Controlling the arrangement of the NPs however is challenging and normally results in aggregated clusters forming during drying[38, 268]. Therefore, a way to control the coverage of such arrays without being limited by aggregation would greatly increase the application potential of NP modified surfaces.

In Section 4.2, the nano-impact study of silver bromide, AgBr, NPs has shown it is possible to electrochemically reduce single NPs up to 100 nm in diameter at an electrode[163]. An interesting possibility is that reduction of silver halides might result in the formation of Ag deposits on an electrode surface resulting in a functional nanoelectrode array. The bulk electrolysis of silver chloride, AgCl, *micro*particles has been previously reported by the electrochemical reduction of AgCl powder. This powder was compacted into a quartz tube with Pt working and counter electrodes at either end and electrochemically reduced over a time scale of approximately 2 hours. This resulted in Ag particles with similar geometry to that of the originating particles however with a smaller radius, reflecting the difference in density between the two materials[269].

In this chapter we build on this observation and demonstrate the ability to fabricate random ensembles of Ag nanoelectrodes from the complete electrolysis of impacting AgBr NPs. The coverage of these nanoelectrode arrays is shown to directly correlate with the length of time the electrode is exposed to nano-impacts and the nano-deposits shown to electrocatalyse the reduction of hydrogen peroxide, H_2O_2.

7.1.2 Experimental

7.1.2.1 Chemicals

The concentration of hydrogen peroxide was checked by UV-Vis spectroscopy and was found to be 8.4 M. This concentration value was used for the calculations herein.

7.1.2.2 Nanoparticle and Nanoelectrode Array Characterisation

The synthesis of the AgBr NPs is covered in Section 3.4.3. Images of both the synthesised NPs and fabricated nanoelectrode arrays were measured using a SEM as outlined in Section 3.3.2 with the assistance of Ms J. Holter and Dr N Young (Department of Materials, Oxford University). Sizing of the AgBr NPs was carried out using ImageJ software, and the resulting distribution shown in Figure 8.1. The particles were found to be near-spherical with an average spherical radius of 53.2 nm with a standard deviation of 22.4 nm. In addition to imaging, energy-dispersive X-ray spectroscopy (EDX) analysis was conducted on the synthesised AgBr NPs and formed nano-deposits as outlined, also outlined in Section 3.3.2. This was also performed with assistance from Ms J. Holter and Dr N Young.

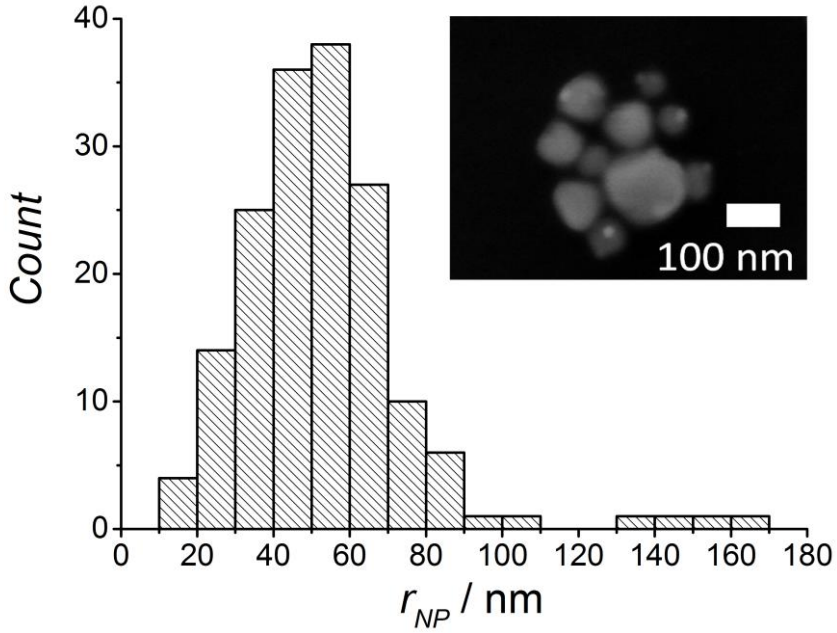


Figure 8.1 AgBr NP sizing by SEM. Insert shows an example SEM image of the NPs.

7.1.3 Results and Discussion

In the following, stripping voltammetry of a AgBr NP modified GC electrode is first conducted to determine the required potentials for reductive AgBr impacts. Next, the deposition of Ag by the

electrolysis of impacting AgBr NPs is determined by voltammetric stripping of the formed Ag deposits over different nano-impact time scales. Next, characterisation of the nanoelectrode arrays is achieved through electron microscope imaging, and finally, the electrocatalysis of H_2O_2 on the nanoelectrode arrays is used to determine the diffusional behaviour to the array.

7.1.3.1 Stripping Voltammetry of Immobilised AgBr Nanoparticles

To establish the likely potentials required for the reduction of impacting AgBr NPs, cyclic stripping voltammetry was conducted on a drop-cast sample of AgBr NPs on a GC macroelectrode in 0.10 M KBr. The resultant voltammetry can be seen in Figure 8.2. Rather than a well-defined reduction peak, reductive features inherent of a nucleation overpotential for NP reduction[136, 162] are clearly observed initiating at a potential of -0.39 V vs SCE. This agrees with that found previously for AgBr NP reduction on GC macroelectrodes in Chapter 4.2[163] and is attributed to the reduction of AgBr to Ag and Br^-:

$$AgBr(s) + e^- \rightarrow Ag(s) + Br^-(aq)\,. \qquad (2.12)$$

On the reverse scan, a sharp oxidation peak at -0.04 V vs SCE emerges. This is approximately a $+400$ mV shift in the peak potential with that reported for the oxidation of Ag in non-bromide containing electrolytes such as $NaNO_3$[163] (Chapter 4.2) and confirms the role of bromide in the oxidation process. The oxidation reaction is therefore primarily attributed to the oxidation of Ag to AgBr:

$$Ag(s) + Br^-(aq) \rightarrow AgBr(s) + e^-\,. \qquad (2.13)$$

The shoulder observed on the oxidation peak is likely due to the formation of some Ag^+. Quantitative sizing of AgBr NPs of similar size has been previously reported by the nano-impacts technique (Chapter 4.2)[163], where total electrolysis of the NP is shown to occur at potentials equal to, or negative of, the onset potential of AgBr reduction. Therefore, for the nano-impacts reported herein, a potential of -0.80 V vs SCE was chosen to ensure the complete electrolysis of the impacting NPs.

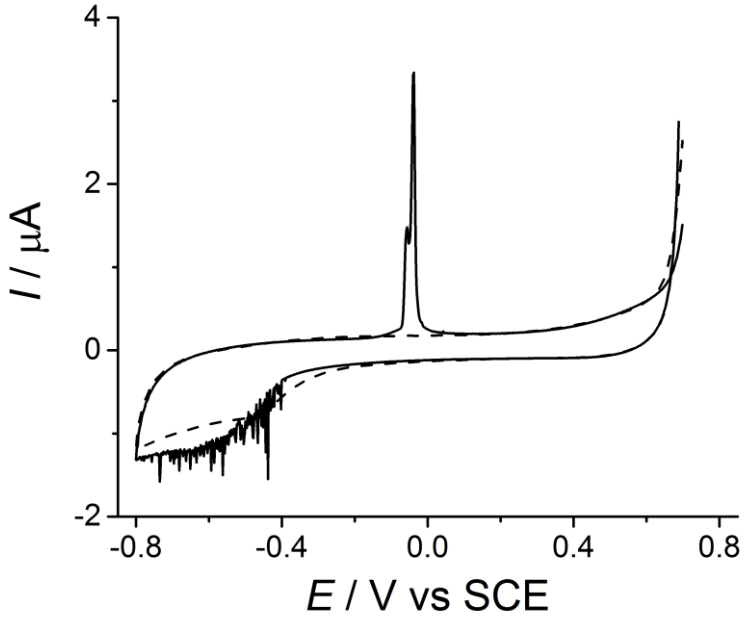


Figure 8.2 Cyclic voltammetry in 100 mM KBr at 100mVs^{-1}. Bare GC (dashed line). GC modified with 0.50 nmoles AgBr drop-cast (solid line).

7.1.3.2 Electrolytic Deposition of Ag by the Electrolysis of Impacting AgBr Nanoparticles

The complete electrolysis of impacting silver halide NPs such as AgBr to metallic Ag is likely to result in the deposition of NPs of Ag on to the electrode surface. To quantify the amount of Ag deposited by nano-impacts, stripping voltammetry of the deposits was conducted. A GC macroelectrode was immersed in a solution of 0.10 M KBr containing NPs, such that the total AgBr concentration in solution was 0.25 mM, and the potential held at -0.80 V vs SCE for different times. After deposition, the electrode was transferred to a fresh solution of 0.10 M KBr for voltammetric stripping of any deposited Ag at a scan rate of 50 mVs^{-1}. Figure 8.3 shows the resultant voltammetry for deposition times of 50 s, 1000 s, 1 h, 2 h, 3 h, 4 h and 5 h, scanning from -0.15 V to +0.70 V vs SCE. A starting potential of -0.15 V was used as this fell within the apparent electrochemically inert region between -0.39 V and -0.15 V vs SCE observable from the drop-cast voltammetry in Figure 8.2. The presence of Ag at the electrode surface is confirmed by the presence of a Ag oxidation peak at a potential of -0.01 V vs SCE. This is shifted by +30 mV to

that of the stripping voltammetry of the AgBr NP modified GC electrode as observed in Figure 8.2, where the Ag oxidation peak was found to occur at -0.04 V vs SCE. Such shifts in potential have previously been attributed to changes in surface coverage of the NPs on the electrode surface when studied by drop-casting experiments [38, 39]. However, Figure 8.3 clearly shows that there is no significant change in the peak potential for different coverages of NP. This highlights a distinct difference between stripping voltammetry of drop-cast NPs and NPs deposited by nano-impacts and likely indicates that the NPs deposited result in non-aggregated Ag deposits. Figure 8.4 shows the resulting charge densities for the stripping of Ag deposits over the different deposition times and the percentage coverage of the NPs on the electrode surface calculated assuming simple, regular 2D hexagonal close-packing[270]. A clear linear increase in the amount of Ag deposited as a function of deposition time is observed with coverage in the range of 0.19 % to 3.5 %.

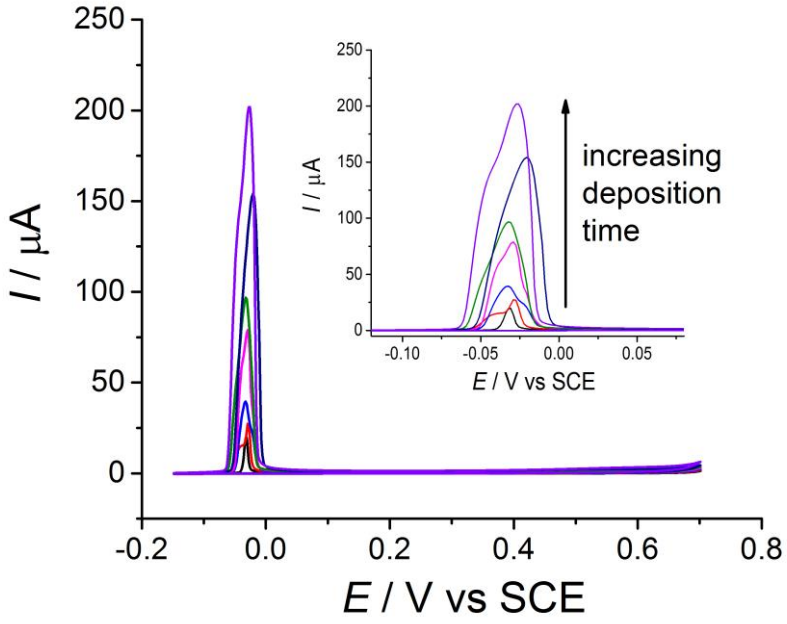


Figure 8.3 Ag stripping voltammetry with increasing AgBr NP impact deposition times at -0.80 V vs SCE. The stripping voltammetry was conducted in 0.10 M KBr at 50 mVs^{-1} after deposition times of 50 s, 1000s, 1 h, 2 h, 3 h, 4 h, 5h.

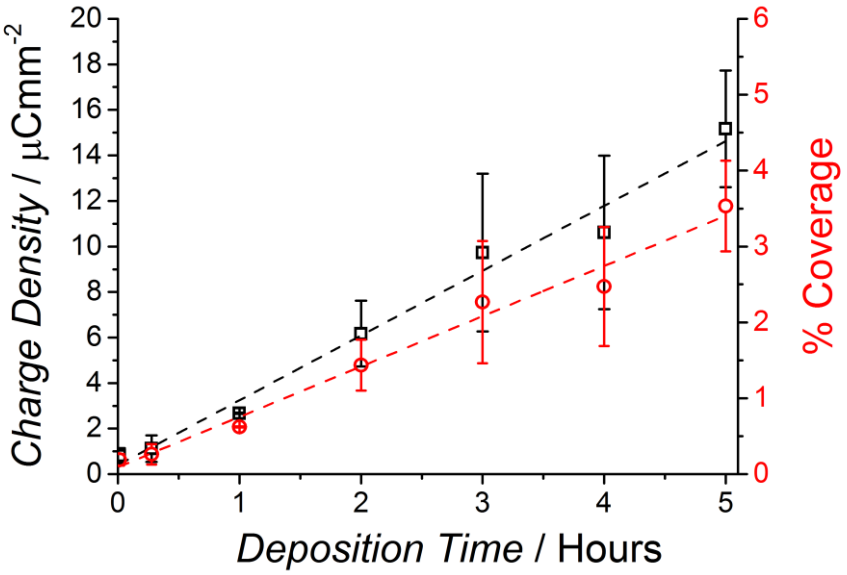


Figure 8.4 Ag stripping charge density and % coverage plotted against deposition time. Stripping voltammetry conducted in 0.10 M KBr. AgBr NP impact deposition conducted with 0.25 mM AgBr in 0.10 M KBr at -0.80 V vs SCE. Coverage calculated assuming 2D hexagonal close-packing[270].

Next, SEM images were taken of two GC surfaces after exposure to nano-impacts for times of 1000 s and 2 h so that the structure of the deposited Ag could be observed. Figure 8.5 shows example SEM images of the two GC surfaces. In both cases, the electrolysed particles can be seen to give rise to randomly arranged, approximately circular structures of similar size. The size of the nano-deposits was analysed by SEM, see Figure 8.6, and found to have an average radius of (37.9 ± 14.0) nm, slightly smaller than the originating AgBr NPs of radius (53.2 ± 22.4) nm. This is expected due to the higher density of Ag compared to AgBr and indicates that each deposit is formed by the electrolysis of an individual impacting NP. Of particular interest is the arrangement of the particles on the surface of the GC. Little aggregation or agglomeration of the particles is observed – instead the NPs are randomly distributed across the surface. This is in contrast to reports for drop-casting which results in aggregation of the surface NPs[38, 271] and suggests that the impacting AgBr particle is reduced to an immobilised, nano-sized Ag deposit at the point of impact. The percentage coverage of the electrode surface by the Ag NPs at 1000 s

and 2 hours was calculated by analysis of the SEM images using Image J software. This was found to be approximately 0.4 % and 0.9 % respectively and in good agreement with the calculated values from the stripping voltammetry of (0.26 ± 0.14) % and (1.44 ± 0.34) %.

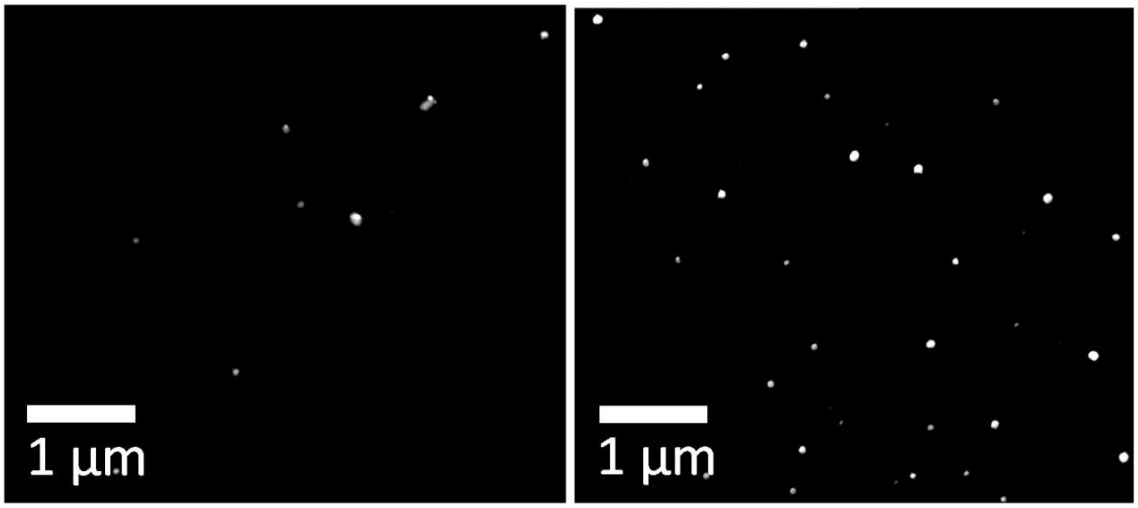


Figure 8.5 SEM images of GC electrodes after AgBr NP impact deposition. 1000 seconds (top). 2 hours (bottom). AgBr NP impact deposition conducted with 0.25 mM AgBr in 0.10 M KBr at -0.80 V vs SCE.

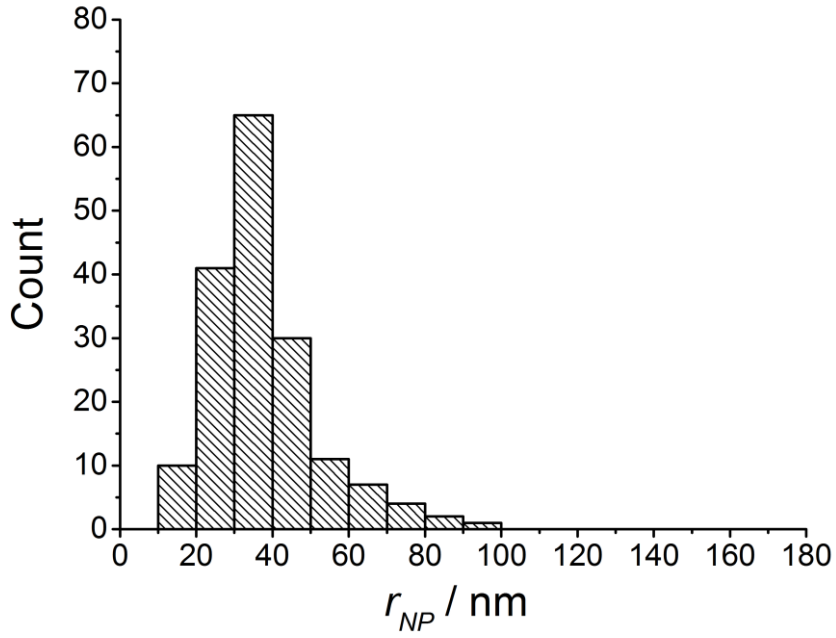


Figure 8.6 Ag nano-deposit sizing by SEM.

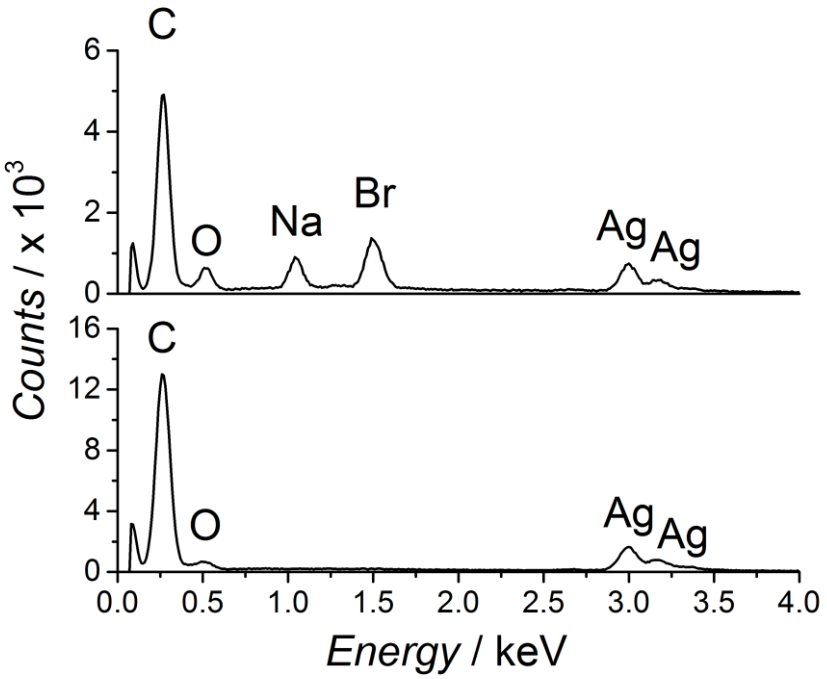


Figure 8.7 Example EDX spectra of nanoparticles. AgBr NPs (top). Ag deposits constituting the nanoelectrode array (bottom). The peak for sodium in the top spectrum is observed due to presence of residual $NaNO_3$ from the synthesis of the AgBr NPs.

In addition to SEM imaging, EDX analysis was conducted on the NPs before and after electrolysis by nano-impacts. Figure 8.7 shows example EDX spectra obtained. The absence of the bromide peak for the particles after deposition suggests complete electrolysis of the NPs and the formation of Ag deposits.

7.1.3.3 Characterisation of Ag Nanoelectrode Array by Electrocatalysis of H_2O_2

Next, the fabricated nanoelectrode arrays were tested to show whether the formed Ag deposits were electrochemically active. The electrocatalytic reduction of H_2O_2 on Ag macroelectrodes has been shown to give rise to a reduction wave at -0.4 V vs SCE, associated with the two electron reduction of H_2O_2 by the process[272]:

$$H_2O_2(aq) + e^- \rightarrow OH(ads) + OH^-(aq)\,, \tag{2.14}$$

$$OH(ads) + e^- \rightarrow OH^-(aq)\,, \tag{2.15}$$

$$2OH^- + 2H^+ \rightarrow 2H_2O\,. \tag{2.16}$$

For voltammetric characterisation of the arrays, the electrocatalytic reduction of 1 mM H_2O_2 in 50 mM pH 7.4 phosphate buffer was conducted on a GC electrode before and after exposure to nano-impacts of AgBr NPs for a time of 1000 s. The resultant voltammetry can be observed in Figure 8.8. An irreversible reductive wave at -0.63 V vs SCE is observed only after deposition of the NPs. This is an overpotential characteristic of the electrocatalysis of H_2O_2 on Ag nanoelectrode arrays[266, 271]. For Ag nanoelectrode arrays with a high coverage of Ag, a characteristic shoulder emerges at -0.7 V vs SCE due to oxygen reduction on the underlying GC electrode. This is due to the rate of the Ag-catalysed decomposition of H_2O_2 being sufficient for detection by voltammetry[271]. The absence of this oxygen reduction peak for the array tested here indicates a low surface area of Ag on the electrode and agrees with the voltammetric stripping and SEM observations of a low coverage of Ag NPs on the GC surface.

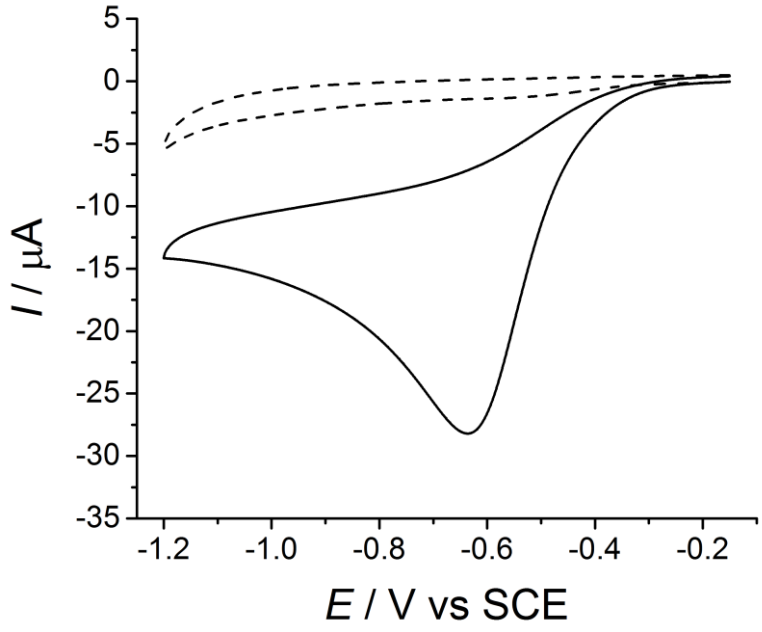


Figure 8.8 Cyclic voltammetry of 1 mM H_2O_2 in 50 mM pH 7.4 phosphate buffer at 50 mVs^{-1}. Bare GC electrode (dashed line). Ag NP array formed by 1000 s AgBr NP impact deposition on a GC electrode in 0.10 M KBr at -0.80 V vs SCE (solid line).

Figure 8.9 shows the voltammetry observed at the array with varying scan rates of 5, 50, 100, 200, 500 and 1000 mVs^{-1} as well as the resultant peak currents plotted against the square root of scan rate. A clear linear increase in the peak current with the square root of scan rate is observed, as expected of a diffusion controlled process. The cathodic transfer coefficient α is defined by the following Equation[15] (Section 1.6.2):

$$\alpha = -\left(\frac{RT}{F}\right)\left(\frac{\partial ln\,|j_c|}{\partial E}\right), \tag{2.17}$$

where R is the gas constant, T is the temperature, F is Faraday's constant, j_c is the cathodic current density and E the applied potential. This was calculated to be (0.33 ± 0.08), showing good agreement with previously reported values for the mechanism for H_2O_2 reduction outlined in Equations 2.14-2.16 of ≈ 0.25[271]. The diffusion coefficient of H_2O_2 was also calculated using the Randles-Ševčík equation for a fully irreversible process as previously discussed in Section 1.6.2[1]:

$$I_p = -0.496\sqrt{n' + \alpha'_{n+1}}\, nFA[A]_{bulk}\sqrt{\frac{F\nu D}{RT}}, \tag{2.18}$$

where I_p is the peak current, n' is the sum of electrons transferred before the rate determining electron transfer, α'_{n+1} is the transfer coefficient of the slow transfer step, n is the overall number of electrons transferred in the reaction, $[A]_{bulk}$ is the concentration of the electroactive species in solution, A is the area of the GC macroelectrode, ν is the scan rate and D is the diffusion coefficient. From the gradient of the peak current plotted against the square root of scan rate the diffusion coefficient was calculated to be 1.75×10^5 $cm^2\ s^{-1}$. This is in agreement with previously reported values of $\approx 1 \times 10^5$ $cm^2\ s^{-1}$ [266, 273, 274] and demonstrates that the reduction of H_2O_2 on the nanoelectrode array behaves as a diffusionally controlled irreversible reduction. Therefore, it can be determined that the separation of Ag deposits is small enough to result in overlapping diffusion fields and linear diffusion of the reacting species to the entirety of the underlying electrode as expected for a random array of nanoelectrodes.

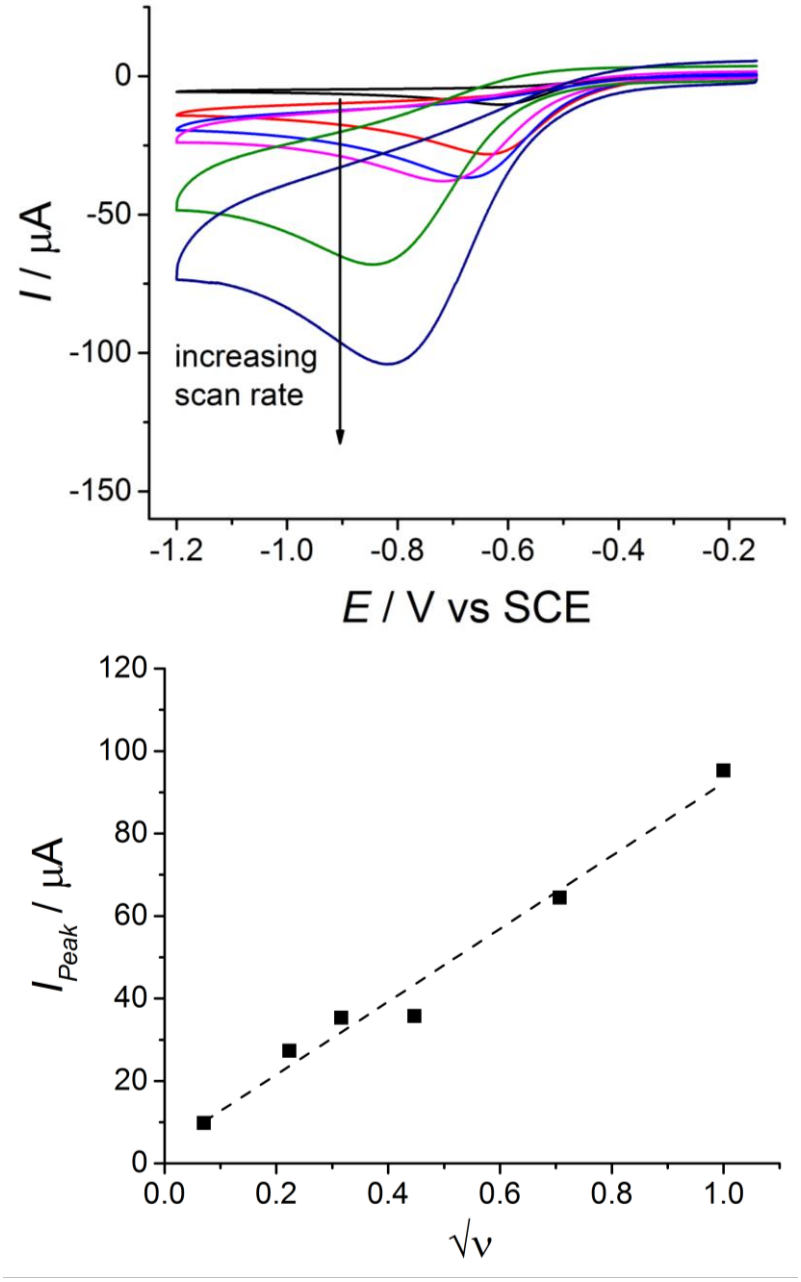


Figure 8.9 Scan rate study of Ag NP array (1000 second deposition time) in 1 mM H_2O_2 and 50 mM pH 7.4 phosphate buffer at 5, 50, 100, 200, 500 and 1000 mVs^{-1} (top). Plot of peak current against the square root of scan rate (bottom). Calculated $\alpha_c = (0.33 \pm 0.08)$. Calculated H_2O_2 diffusion coefficient = 1.75 x 10^{-5} cm^2s^{-1}.

7.1.4 Conclusions

The fabrication of Ag nanoelectrode arrays has been realised through the electrolysis of impacting AgBr NPs. The AgBr NPs are found to reduce on impact, leaving randomly distributed Ag nanoparticle deposits on the electrode surface. The resulting Ag nanoelectrode arrays are shown to be electrocatalytically active for the reduction of H_2O_2, behaving as a random array of nanoelectrodes with overlapping diffusion fields. The nanoelectrode arrays fabricated by nano-impact deposition are found to show little aggregation of the NPs. Such a dispersion of single NPs is difficult to achieve by conventional drop-casting methods. This clearly shows that by using the nano-impact method for the fabrication of arrays, greater control over the nanoelectrode array structure can be achieved and demonstrates the use of the nano-impact technique for electrode array fabrication.

7.2 Femtomolar Detection of Silver Nanoparticles by Flow-Enhanced Direct-Impact Voltammetry at a Microelectrode Array

7.2.1 Introduction

As previously discussed in Section 2.1, there is considerable interest in NPs from both fundamental and application perspectives[220]. Current methods for the detection and characterization of NPs are varied (see Section 2.2) but primarily consist of optical techniques such as UV-Vis spectroscopy, dynamic light scattering (DLS) or NP tracking analysis (NTA). UV-Vis spectroscopy allows for the detection of monodisperse NP samples yet is limited by inaccuracies in measuring polydisperse systems[275]. This is a characteristic shared by DLS which is significantly influenced by the scattering of larger particles and has been reported to have inaccuracies in population distributions of up to several orders in magnitude when dealing with polydisperse systems[275]. NTA is less affected by polydispersity and can operate with samples consisting of 10^7 to 10^9 particles per mL equivalent to a lower limit of detection of 16.6

fM [195]. However, a common feature shared by all optical detection methods is their cost and inability to analyse samples of poor optical clarity[157]. Electrochemical detection is a potentially cheap and simple method for the detection and characterization of electroactive NPs that is indifferent to optical clarity but has previously largely relied on bulk drop-cast studies[122]. This was discussed in Section 2.2.5. Unfortunately, such methods cannot provide key information on the size distribution of the particles and have been shown to suffer from incomplete stripping due to surface agglomeration/aggregation[38, 39, 129, 130]. This is a significant drawback and indicates the need for the continued development of new detection methods for NPs that provide both low detection limits and reliable particle size distributions.

Recent advancements in electrochemical NP sensing has seen the detection of single NPs by the "nano-impacts" technique. This was discussed in detail in Section 2.2.6. An example case of the *direct-impact* method is the electro-oxidation of an impacting silver NP:

$$xAg(nanoparticle) \rightarrow xAg^{+} + xe^{-}\,. \qquad (2.19)$$

Silver NPs are an excellent model system for *direct*-impacts and have been utilised for proof of concept works including shape determination, hindered diffusion effects and agglomeration/aggregation processes[102, 199, 276].

The *direct-impact* technique has hitherto been conducted in stationary systems, relying on diffusional mass transport of particles to the micro-disk electrode surface. Under these conditions the use of micro-wire electrodes is thought to be optimal and has been shown to achieve a detection limit of 900 fM[277]. Crooks and co-workers have developed an alternative *indirect* approach to detecting Ag NPs through functionalisation of magnetic microbeads with multiple NPs and enhancing the collision rate of the functionalized beads with an ultramicroelectrode. The reported silver detection limit was 61 fM[278]. For real-world applications sensors require low operating costs, simplicity of operation and fast response. Indirect and magnetically guided bead/particle impacts[278, 279] while interesting from research

point of view challenge these requirements and an alternative is warranted. In the present work we focus on direct impact electrochemistry.

As discussed in Section 1.9, forced convection provides an additional and efficient way of increasing mass transport to an electrode surface by decreasing the diffusion layer thickness[2, 280]. Traditionally rotating disk electrodes (RDEs) have been employed by electrochemists due to the distinct advantages of laminar flow and well-established theory, which allows in-depth analysis of interfacial kinetics[46, 281, 282]. However, flow cells have distinct advantages in that they are all-sealed units that are less prone to turbulence, and are readily adapted to colloidal systems[283]. Flow cells have found applications in both research and industry due to their on-line detection capabilities, with examples including heavy metal detection[284] and biological redox processes[285]. Recent work has also exploited enhanced mass transport by flow for the detection of NPs by the *indirect-impact* method and has achieved detection limits of 83 fM[286].

As well as introducing convection, another clear avenue for enhancing detection limits for *direct-impacts* is the use of larger electrode areas. To date, the majority of impact studies have used single microelectrodes due to their enhanced radial diffusion, high signal-noise and their lack of moving parts. However, the use of microelectrodes comes with limitations. They are known to have a high degree of fragility making them unsuitable in some applications[1] and they often require extensive shielding to optimize the signal-noise ratio[287]. Larger electrode areas have already shown to give enhanced detection limits by use of the micro-wire electrode[277] but are not easily integrated into a flow regime. An alternative is therefore sought which provides an inherently high signal-noise ratio whilst measuring the collision frequency under flow to allow low limits of detection. Arrays of gold microelectrodes with 25 μm for the smaller diameter and 30-180 μm for the larger diameter have been adapted from conventional electronic integrated circuit chips[288, 289]. However, these are rather large, and smaller carbon electrodes are preferred for the present purpose. For this reason, we use the random array of

microelectrodes (RAM) approach pioneered by S. Fletcher and M. Horne[28]. These RAMs consists of hundreds of carbon fibres connected in parallel to a current collector. This arrangement provides current amplification proportional to the number of active fibres, whilst maintaining radial diffusion. RAMs can also be re-polished to provide a clean and reproducible surface, facilitating ease of use and maximising applicability to real systems.

The ultimate limit of detection in impact electrochemistry is a single entity; however, the technique suffers because the time it takes the entity to reach the probe by random walk alone can be tens of thousands of seconds for extremely dilute samples[276]. Here, we describe a method to increase the rate with which entities collide with an electrode by invoking convective mass transfer using a flow cell, allowing for the analysis of femtomolar levels of Ag NPs. The flow response of the system is first characterised by the molecular redox species potassium ferrocyanide. This is then extended to the concurrent detection and sizing of citrate-capped silver NPs at femtomolar concentrations with the effect of volumetric flow rate on the frequency of impacts reported.

7.2.2 Experimental

7.2.2.1 Characterisation of Electrodes

Two RAMs[28] were used as working electrodes for experiments, consisting of ~7 μm diameter carbon fibres insulated with cured epoxy resin and having an average electrode separation of 70 μm. Where different RAMs were used in various experiments the results have been normalized by the number of active fibres for each RAM to allow direct comparison. The number of active fibres varies between RAMs due to the manufacturing process and was calculated as follows. Cyclic voltammetry of the RAMs was conducted under stationary conditions in 1 mM $K_4Fe(CN)_6$ and 0.10 M KCl at 100 mVs^{-1} and is reported in Figure 9.0. The limiting current obtained can be related to the number of active fibres, N_{fib}, assuming a 7 μm fibre diameter and micro-disk geometry:

$$N_{fib} = \frac{I_{lim}}{4r_e nFDc^*}, \tag{2.20}$$

where I_{lim}, is the limiting current, r_e, is the radius of the fibre, D is the diffusion coefficient and c^* is the concentration of $K_4Fe(CN_6)$. Using this equation the RAMs were found to have 663 and 436 functional fibres respectively.

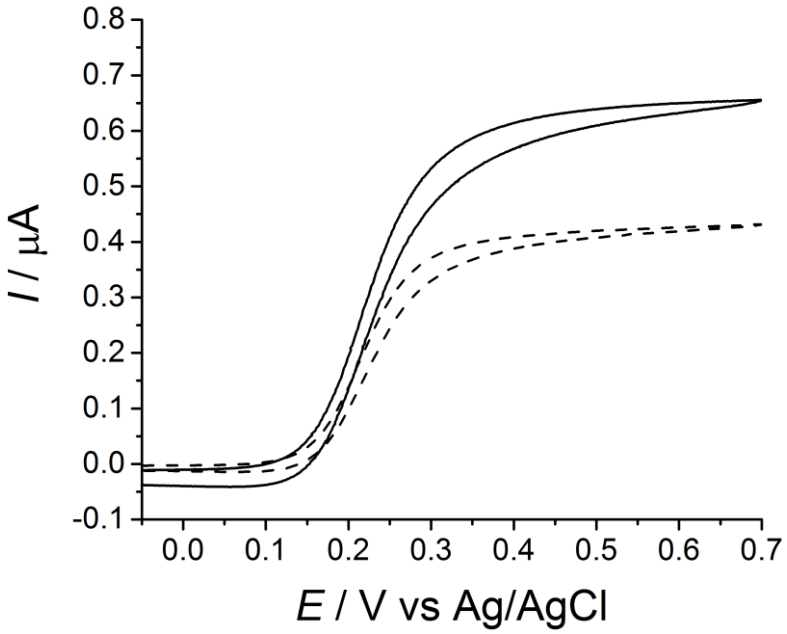


Figure 9.0 Characterisation of the two RAMs used for experiments in 1mM $K_4Fe(CN)_6$ and 0.10 M KCl at 100 mVs^{-1}

7.2.2.2 Flow Cell

The flow cell was designed and built in-house. It allows the interchange of working electrodes, with a washer allowing control over the inlet-working electrode distance. A schematic design is shown in Figure 9.1, and full schematics in Figure 9.2. Figure 9.1 shows the demountable flow cell system which is built from three separate sections which are bolted together. The three main cell components were manufactured from polyether ether ketone (PEEK), with Delrin® used for the reference and working electrode holder. During operation, solution is flowed through the cell using a computer controlled Fusion 100 Chemyx syringe pump (USA) and is injected onto the electrode surface through a 0.5 mm diameter inlet hole. The inlet-electrode

distance can be altered by using different washer thicknesses, however was maintained at 2 mm for all experiments conducted herein. The flow is then strained by the central component through 8 pores of 0.5 mm diameter before passing into a pressure-equalizing well containing the counter and reference electrodes. The positioning of the electrodes in this cell ensures that the electroactive solution components cannot be affected by the counter electrode before reaching the working electrode.

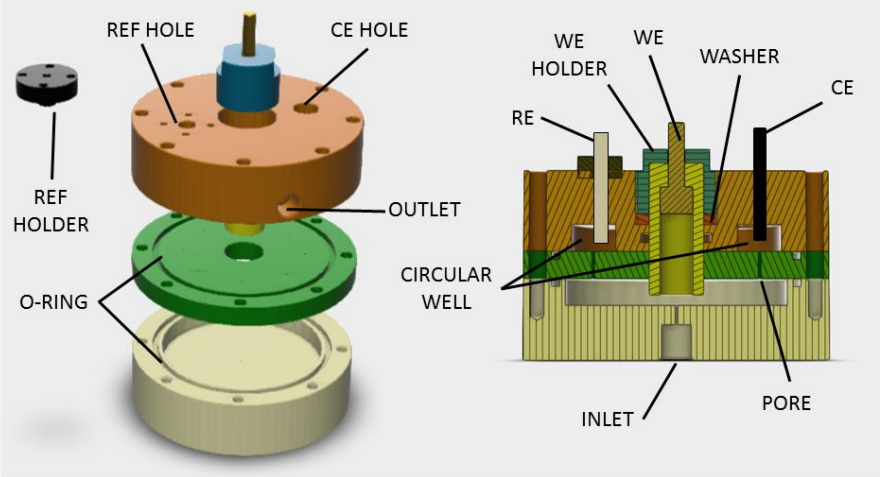


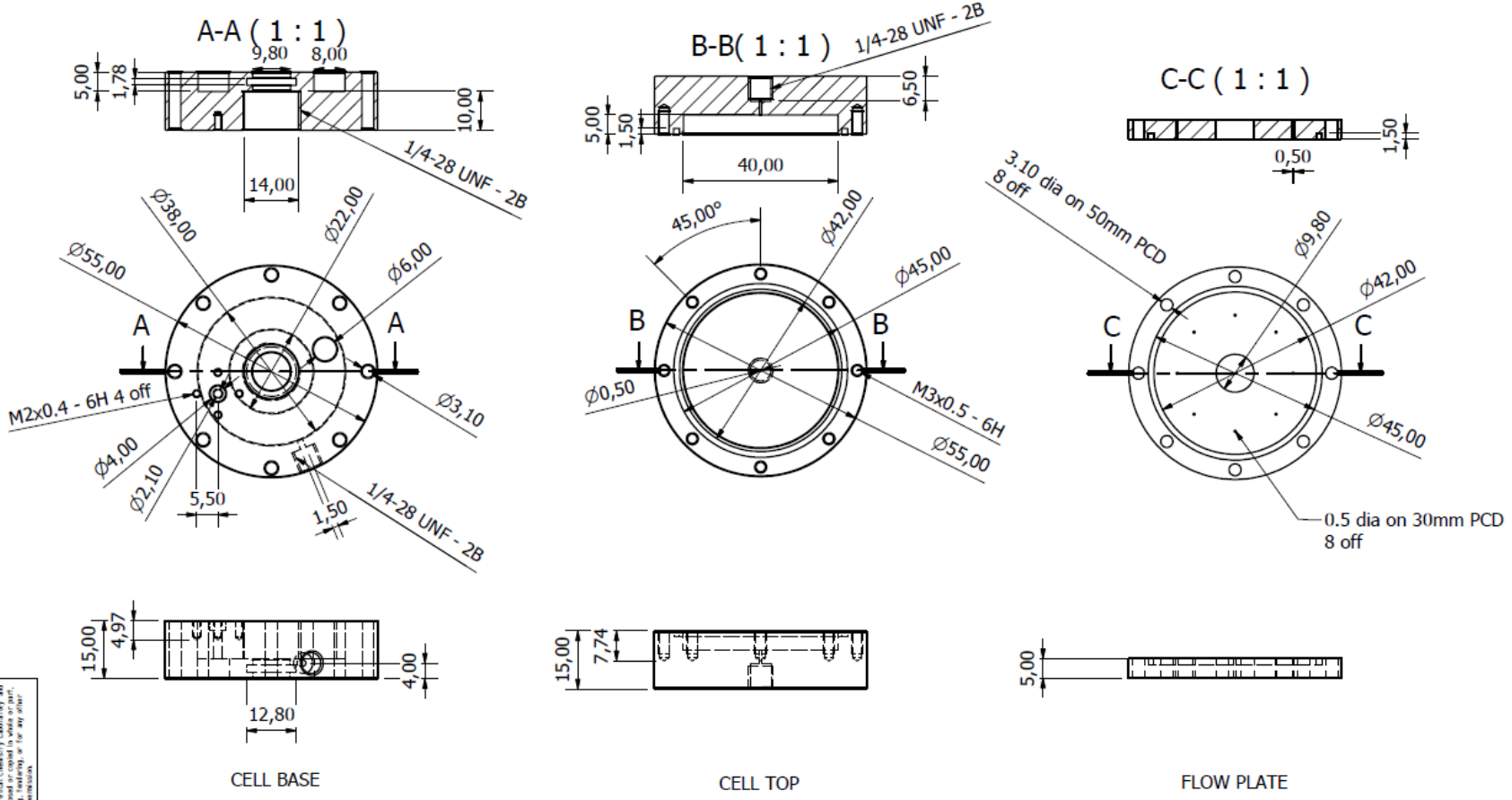
Figure 9.1 Expanded and cross-sectional views of the home-built flow cell.

7.2.2.3 Initial Flow Cell Characterization using a Glassy Carbon Macroelectrode.

Initial characterization of the flow was carried out using a GC macroelectrode. Linear sweep voltammetry was conducted in 1 mM $K_4Fe(CN)_6$ and 0.10 M KCl from -0.05 V to +0.70 V vs Ag/AgCl over a range of volumetric flow rates. The results are reported in Figure 9.3. Steady state limiting current values, I_{lim}, were obtained and plotted as $\log_{10}(I_{lim})$ vs. $\log_{10}(\textit{flow rate})$, as shown in Figure 9.4 to obtain a slope of (0.74 ± 0.08). This is in excellent agreement with the Levich Equation for a wall jet (see Section 1.9) with $I_{lim} \propto V_f^{\frac{3}{4}}$ [48]:

$$I_{lim} = 1.35nFD^{\frac{2}{3}}\upsilon^{-\frac{5}{12}}a^{-\frac{1}{2}}r_e^{\frac{3}{4}}V_f^{\frac{3}{4}}c^*, \qquad (2.21)$$

where υ is the kinematic viscosity, α is the diameter of the jet nozzle and V_f is the volumetric flow rate.



This drawing and any information or description shall not be loaned, disclosed or copied in whole or part, or used for manufacturing purposes, or for any other purpose without written permission.

Revision	Date	Issue

Dimensions in millimetres unless otherwise stated

Remove all burrs and sharp edges

Job Title: Radial Flow Cell

Part Description:BASE, FLOW PLATE & TOP

Material: PEEK | Qty:ONE EACH

Finish:N/A

Research Worker:Tom Bartlett | Group:RGC

PTCL WORKSHOP

Tolerances (unless otherwise stated)
Dim'n 0 ± 1mm
Dim'n 0.0 ± 0.1mm
Dim'n 0.00 ± 0.05mm
Angle ± 0° 30'
Surface Finish 1.6u

0 50 millimetres full scale 50

SCALE | A3

Date: 11/5/16 | Drawn By: PF

File:

Contact: peter.fair@chem.ox.ac.uk

Path: WS12_Z:\Pete\

Mechanical Workshop
Physical & Theoretical Chemistry Dept
Oxford University
South Parks Road
Oxford. OX1 3QZ.
Tel. 01865 275441, Fax 01865 275410

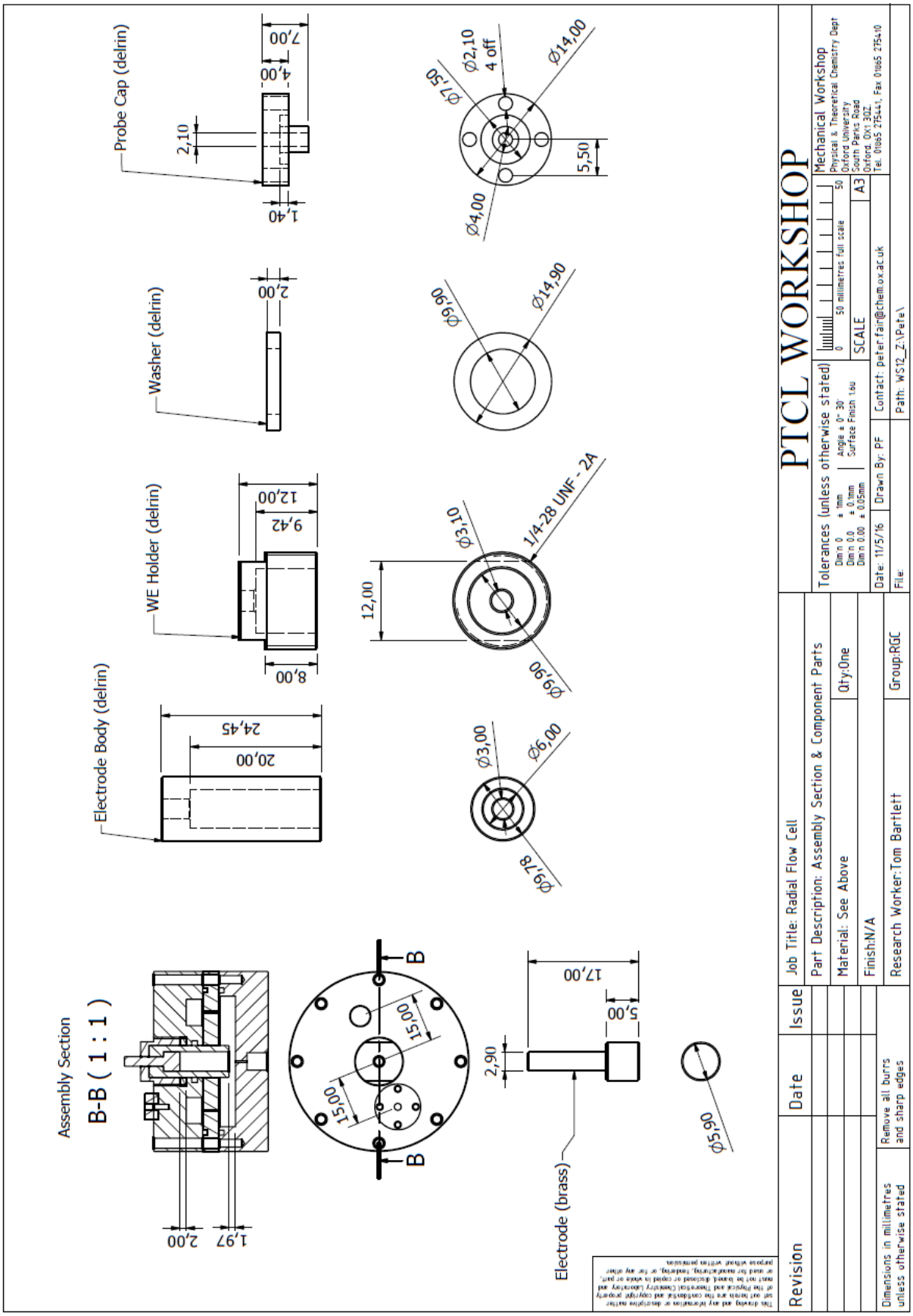


Figure 9.2 Schematic drawings of the flow cell and components

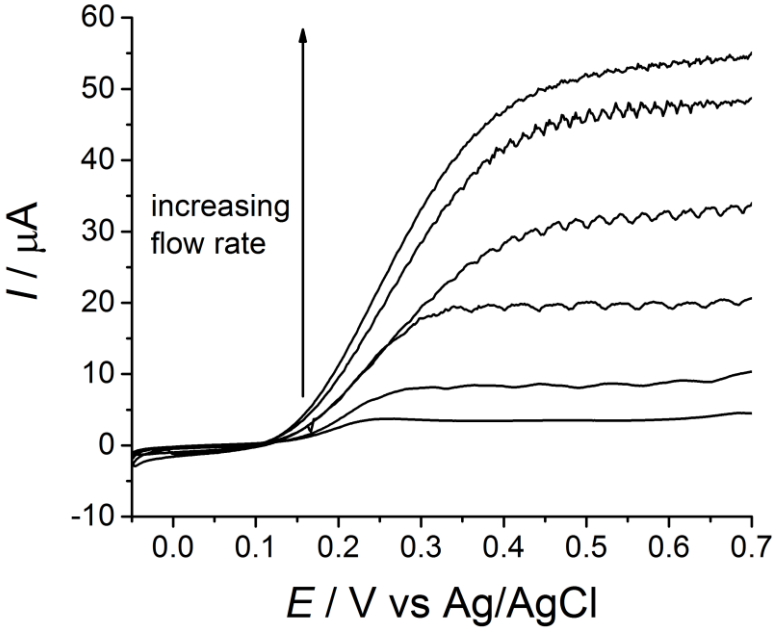
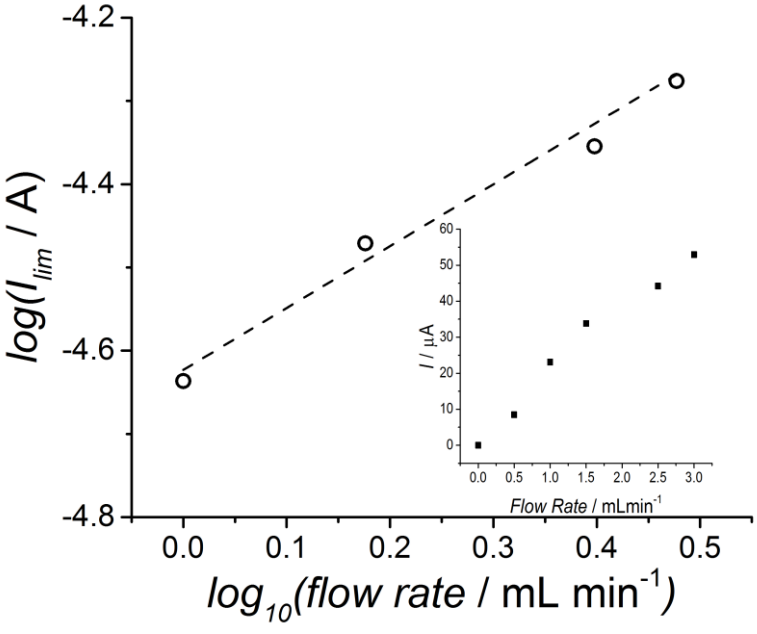


Figure 9.3 Flow dependence of GC macroelectrode in 1mM $K_4Fe(CN)_6$ and 0.10 M KCl at 1 mV s^{-1} at 0, 0.5, 1.0, 1.5, 2.5, 3.0 mL min^{-1}



Figuire 9.4 Log/log plot of I_{lim} vs *volumetric flow rate* for a GC macroelectrode in 1 mM $K_4Fe(CN)_6$ and 0.10 M KCl at 1 mV s^{-1}. Fitting shows a slope of (0.74 $\pm$ 0.08) for flows of 1 to 3 mL min^{-1} concurrent with wall-jet behaviour at flow rates greater than 1 mL min^{-1}

7.2.3 Results and Discussion

Prior to nano-impact detection the effects of flow on the steady state response for molecular species was first studied. This provided an estimate of the possible increase in detectivity achievable by this system. Linear sweep voltammetry was conducted in 1 mM $K_4Fe(CN)_6$ and 0.10 M KCl from -0.05 V to +0.70 V vs Ag/AgCl at 100 mVs^{-1} with a RAM across a range of flow rates. Figure 9.5 shows example voltammograms obtained at 0, 6, 20, 35 and 50 mL min^{-1}. The RAM is found to give a steady state response under stationary and flow conditions confirming the diffusional independence of the individual micro-fibers in the RAM. As the volumetric flow increases the steady state response is maintained along with an increase of the I_{lim}. Figure 9.6 shows a plot of $\log_{10}(I_{lim})$ vs $\log_{10}(\textit{flow rate})$ for a range of flows from 0 to 50 mL min^{-1}. A clear trend is observed with a slope of (0.41 ± 0.01). The dependence of the transport limited current at the RAM with flow rate is less than that observed for the GC macroelectrode. This reflects the changed electrode geometry[290] and that the RAM is comprised of many microelectrodes each of which has a lower sensitivity to flow compared to a macroelectrode. The increase in I_{lim} from a diffusional-only regime to the maximum volumetric flow rate used of 50 mL min^{-1} was found to be from 0.63 µA to 2.90 µA, equivalent to an enhancement of signal of almost 5 times.

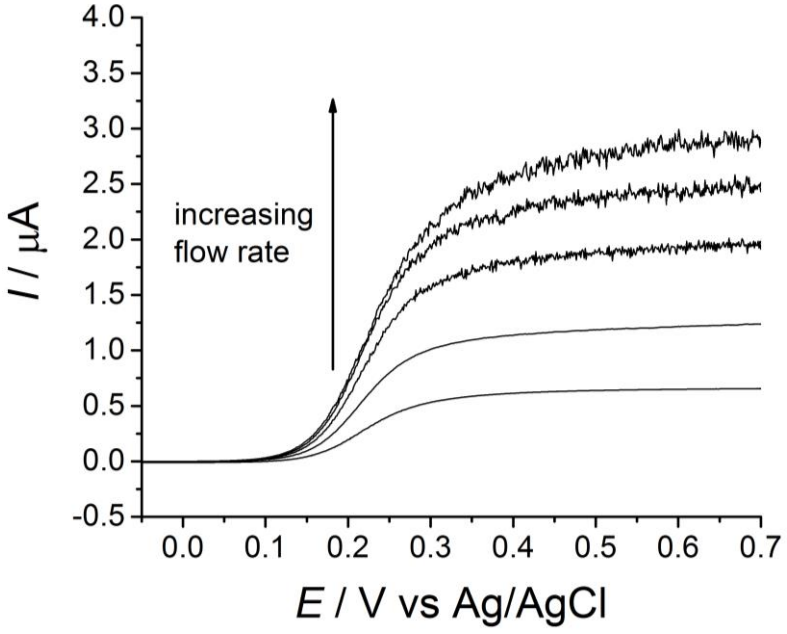


Figure 9.5. Flow dependence of RAM in 1 mM $K_4Fe(CN)_6$ and 0.10 M KCl at 100 mVs^{-1} at 0, 6, 20, 35, 50 mL min^{-1}

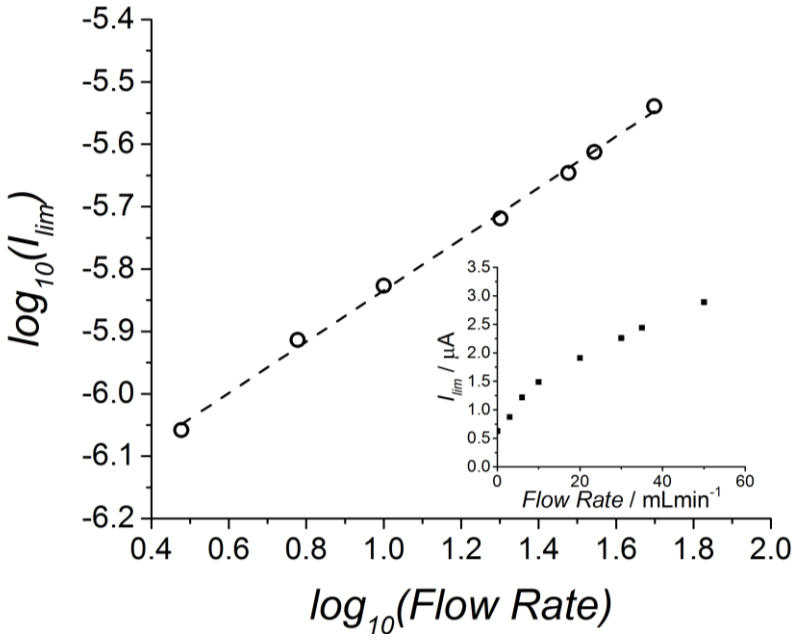


Figure 9.6. Log/log plot of I_{lim} vs. *volumetric flow rate* for a RAM in 1 mM $K_4Fe(CN)_6$ and 0.10 M KCl at 100 mVs^{-1} with a slope of (0.41 ± 0.01). Inset shows the I_{lim} vs. *volumetric flow rate*.

Next, the flow dependence of silver NP impacts was conducted using the RAM-flow cell. Figure 9.7 shows twenty-second-duration current-time transients at +0.60 V vs Ag/AgCl at a NP concentration of 6.2 fM in 40 mM KCl across the experimental flow range of 0 to 50 mL min^{-1}. This potential was chosen as it is suitable for the complete oxidation of silver NPs up to 100 nm in diameter[163]. No impacts were observed under stationary flow due to the low concentration. When the NP suspension was flowed at 10 mL min^{-1} current spikes were detected indicative of silver NP oxidation. The frequency of spikes was observed to increase with increasing volumetric flow rate. The noise of the system was not significantly affected by flow rate and remained below 100 pA even at the highest flow rate of 50 mL min^{-1} allowing clear, unambiguous detection of the current spikes. The background current is likely due to surface oxidation of the RAM electrodes and/or residual citrate used for capping the particles. In order to validate that the current spikes observed were due to *direct-impact* voltammetry of the silver NPs, these were analysed using Equation 2.20 to obtain the size distribution. This is shown in Figure 9.8 4 alongside DLS characterisation of the particles. The size of the particles determined

by voltammetry and DLS was found to be (57.0 $\pm$ 1.5 nm) and 58 nm respectively confirming quantitative sizing of the particles alongside detection at a Ag NP concentration of 6.2 fM.

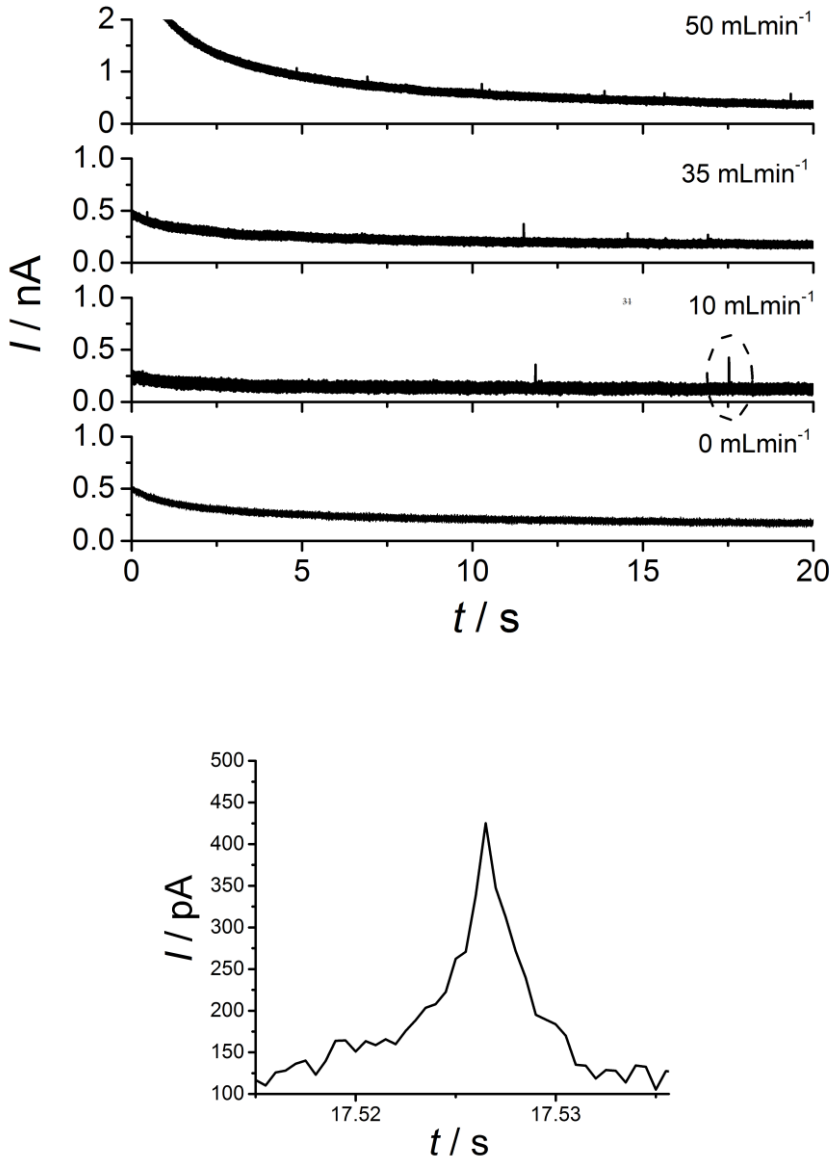


Figure 9.7 Example current-time transients recorded at varying flow rates showing nano-impact spikes. Current-time transients were conducted at +0.60 V vs Ag/AgCl at a silver NP concentration of 6.2 fM in 40 mM KCl. Inset shows a zoomed in image of a current spike at 10 mL min^{-1} (circled). The background consists mainly of capacitively coupled mains interference (50 Hz in the UK).

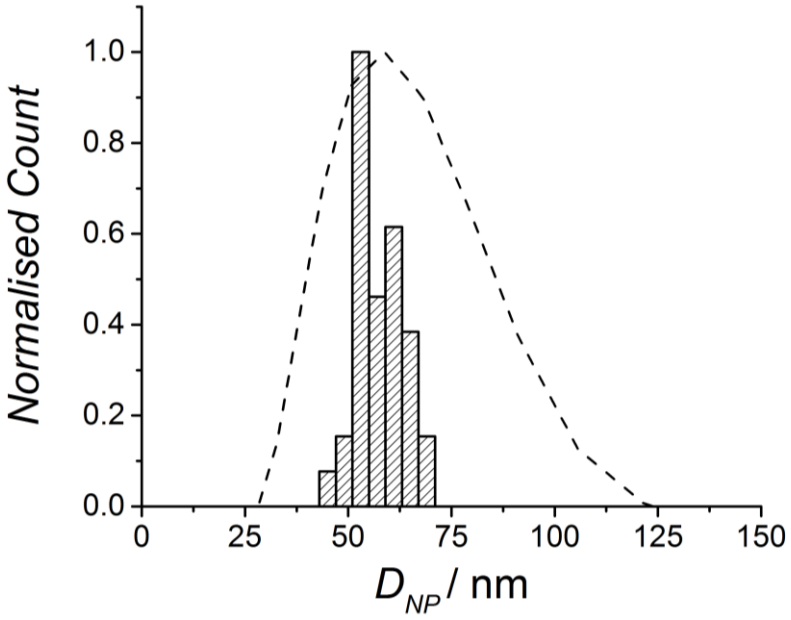


Figure 9.8 Probability density of Ag NPs by DLS and nano-impacts. Impact distribution was gained by integration of current spikes across all measured flow rates.

Finally a lower concentration of 2.5 fM NPs was studied under the same conditions. Figure 9.9 shows the change in impact frequency with flow rate for this concentration and 6.2 fM. No impacts were observed at a Ag NP concentration of 2.5 fM with volumetric flow rates up to 20 mL min^{-1}. It can be seen that for the lower concentration, high flow rates are required to detect particle impacts and stresses the benefits of flow over diffusional only mass transport for NP impact voltammetry. At higher flows however NP impacts were detected. This is the lowest concentration of NPs ever used in a successful nano-impact experiment, with an enhancement in experimental detectivity by two orders of magnitude over earlier attempts[277] and by one order of magnitude for *indirect-impacts*[286]. Hitherto, the lowest reported experimentally detected concentration of NPs by *direct-impacts* is 900 fM using a carbon fiber micro-wire electrode[277]. Non-specific adsorption is inherent in NP chemistry and can have an effect on the concentration of NPs in suspension. As a result a lower frequency of impacts may be observed leading to errors in concentration estimates. In addition care must be taken to minimize agglomeration/aggregation during nano-impact experiments. Readers interested in

experimental aspects of the electrochemistry of the particles are directed to work of Tschulik et al[202].

Figure 10.0 shows the log/log plot for the nano-impact results obtained at 6.2 fM silver NP concentration. The gradient of the fitting was found to be (0.83 ± 0.07). This differs for that found for the study of molecular species at the RAM however fits with that expected for a wall-jet system. This may suggest that nano-impacts are less sensitive to the nature of the electrode surface than molecular species and hence experience the RAM as if it were a macroelectrode. This is advantageous as this means the frequency enhancement provided by the wall-jet system is maximised for nano-impact detection.

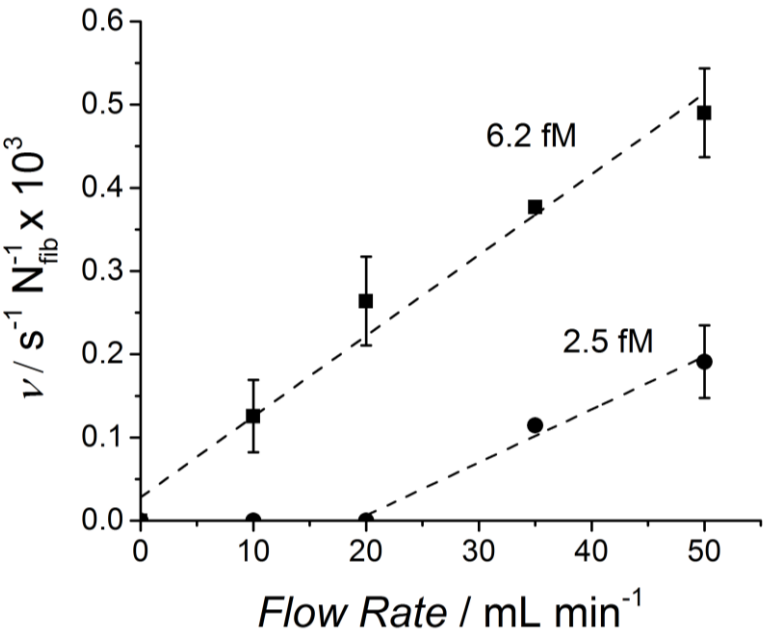


Figure 9.9 Nano-impact frequency at RAMs at varying volumetric flow rates at a silver NP concentration of 6.2 fM and 2.5 fM. Current-time transients were conducted at +0.60 V vs Ag/AgCl in 40 mM KCl.

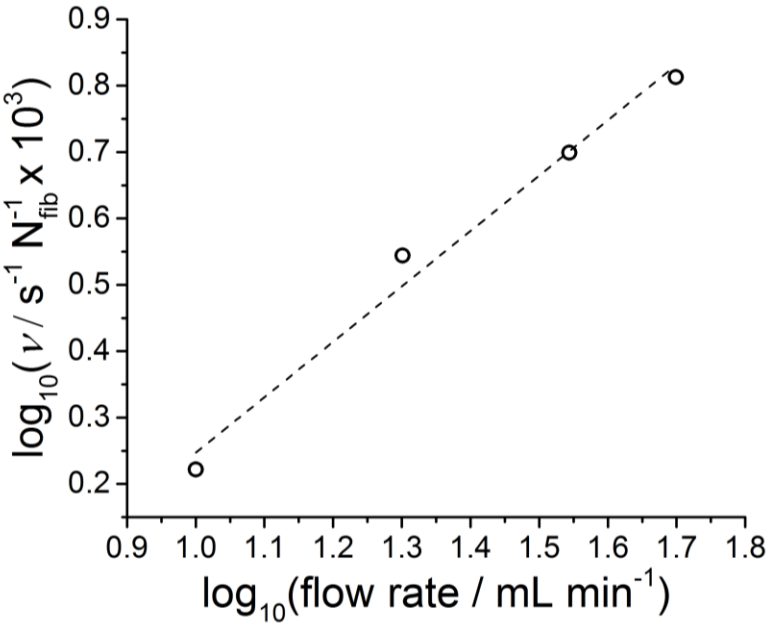


Figure 10.0 Log/log plot of *impact frequency* vs. *volumetric flow rate* for a RAM in 6.2 fM silver NPs and 0.40 M KCl with a slope of (0.83 ± 0.07).

7.2.4 Conclusions

Femtomolar NP concentrations have been detected for the first time by *direct-impact* voltammetry due to enhancement of mass transport by flow. The method detailed herein allows determination of the presence of NPs and their concurrent sizing. We have demonstrated that the frequency of impacts increases monotonically with an increase in concentration. The actual frequency is likely to be affected by non-specific adsorption and agglomeration as discussed in previous works[279, 286, 291]. This is an improvement of over two orders of magnitude in the detection limit for that previously reported[292]. This extremely sensitive detection is a direct result of combining flow with a RAM electrode, increasing the signal-noise ratio. The presented method can be adjusted for sizing smaller NPs by choosing different array geometries in order to have suitable noise characteristics. This is of significant importance for the field of analytical NP detection and is a proof of principle for NP detection by *direct-impact* voltammetry under flow conditions. Further applications of the developed methodology may include applications to biological systems with the aim of development of point of care sensors for viruses and bacteria through simple yet highly efficient methods.

Conclusions and Future Work

This thesis has investigated new concepts in the study of nanoparticles (NPs) by nano-impact voltammetry, with the investigation of new materials allowing significant applications of the technique to be developed. The electrolytic synthesis of mercury(I) chloride NPs through the electrolytic implosion of metal halide nanoscale layer on a mercury hemisphere microelectrode was reported due to the in-situ detection of the generated particles by the nano-impact method. The sizing of silver bromide was shown to be quantitative for sizes up to 100 nm in diameter and was further emphasised through the comparative study of silver NPs of similar dimensions. The study of bismuth oxide provided a model system for the investigation of reversible agglomeration. By utilising the formation of bismuth metal deposits on a glassy carbon substrate through the electrolysis of impacting bismuth oxide NPs, ex-situ imaging of the surface could be used to study the site of impact. This methodology could not have previously been obtained for the study of metallic NPs as they are destroyed during electrolysis. This new methodology provided both nano-impact and electron microscopic evidence for the electrolytic induced deagglomeration of particles.

The successful study of silver bromide particles by the nano-impact technique allowed the investigation of photochemical properties through the light driven reduction of silver bromide NPs by ascorbic acid. The nano-impact technique was shown to be able to probe the accessibility of silver bromide during the conversion process, providing key mechanistic insights over UV-Vis spectroscopy alone. In addition to the nano-impact study of new materials, new advancements have been made in the study of silver NPs. Building on the study of the photochemical conversion of silver bromide NPs to silver, the photochemical Ostwald ripening of silver nanoseeds to nanoprisms was investigated through a combination of UV-Vis, TEM and nano-impact voltammetry. Nano-impacts was shown to be of pivotal importance as it allowed the tracking of growth in the particles through quantification of their atom count even for stages possessing irregular shaped geometries.

The electrolysis of silver bromide to silver upon impacting at an electrode was exploited for the successful formation of a random array of silver nanoelectrodes. The almost entirely monomeric deposits, as measured by SEM, are further evidence for the deagglomeration effect also shown for the uncapped bismuth oxide NPs.

Finally, femtomolar concentrations of silver NPs were detected by use of a random array of microelectrodes (RAM) coupled flow cell. The high electrode area and low background noise provided by the RAM, along with mass transport enhancement by application of hydrodynamic flow was shown to significantly enhance the limit of detection for NPs by the nano-impact technique.

The work herein stimulates interesting pathways for future research. One area of possible development is the use of nano-impacts for the formation of nanoelectrode arrays. Future work could include the synthesis of alternative metal halides such as gold and platinum. Due to the dissociation of these compounds in aqueous solution this would most likely require the development of methods for the synthesis and nano-impact deposition of such materials in non-aqueous solution. This could lead to the high through-put manufacture of nanoelectrode arrays and functionalised surfaces. The significant developments in detection for the nano-impact technique demonstrated through use of a RAM coupled flow cell also indicate the possible application of nano-impacts in environmental and industrial NP detection. This would require further study and testing such sensing systems in the field.

Bibliography

[1] R. G. Compton, C. E. Banks, *Understanding Voltammetry*, 2nd ed., Imperial College Press, **2011**.

[2] A. J. Bard, L. R. Faulkner, *Electrochemical Methods*, second ed., John Wiley @ Sons, **2001**.

[3] C. M. A. Brett, M. O. Brett, *Electrochemistry: Principles, Methods and Applications*, Oxford University Press, Oxford, **1993**.

[4] J. A. V. Butler, *Trans. Faraday Soc.* **1924**, *19*, 729-733.

[5] T. Erdey-Grúz, M. Volmer, *Z. Physik. Chem.* **1930**, *150*, 203-213.

[6] R. F. Khairutdinov, K. I. Zamaraev, V. P. Zhadanov, *Electron Tunneling in Chemistry: Chemical Reactions Over Large Distances, Vol. 30*, Elsevier Science, Amsterdam, The Netherlands, **1989**.

[7] A. Fick, *J. Membr. Sci.* **1995**, *100*, 33-38.

[8] A. Einstein, *Investigation on the Theory of the Brownian Movement*, Dover Books, New York, **1926**.

[9] E. J. F. Dickinson, J. G. Limon-Petersen, N. V. Rees, R. G. Compton, *J. Phys. Chem. C.* **2009**, *113*, 11157-11171.

[10] F. G. Cottrell, *Z. Phys. Chem.* **1903**, *42*, 385.

[11] H. Matsuda, Y. Ayabe, *Bull. Chem. Soc. Japan* **1955**, *28*, 422.

[12] H. Matsuda, Y. Ayabe, *Bull. Chem. Soc. Japan* **1956**, *29*, 132.

[13] H. Matsuda, Y. Ayabe, *Z. Elektrochem* **1959**, *64*, 1164.

[14] J. E. B. Randles, *Discuss. Faraday Soc.* **1947**, *1*, 11.

[15] R. Guidelli, R. G. Compton, J. M. Feliu, E. Gileadi, J. Lipkowski, W. Schmickler, S. Trasatti, *Pure Appl. Chem.* **2014**, *86*.

[16] J. Wang, R. Trouillon, Y. Lin, M. I. Svensson, A. G. Ewing, *Anal. Chem.* **2013**, *85*, 5600-5608.

[17] D. P. Valencia, A. P. R. de Souza, V. R. Gonçales, J. L. S. Antonio, S. I. Cordoba de Torresi, M. Bertotti, *Electrochem. Commun.* **2014**, *38*, 32-35.

[18] X. J. Huang, A. M. O'Mahony, R. G. Compton, *Small* **2009**, *5*, 776-788.

[19] T. J. Davies, C. E. Banks, R. G. Compton, *J. Solid State Electrochem.* **2005**, *9*, 797-808.

[20] P. Tomcik, *Sensors* **2013**, *13*, 13659-13684.

[21] A. Tsigara, A. Benkhial, S. Warren, F. Akkari, J. Wright, F. Frehill, E. Dempsey, *Thin Solid Films* **2013**, *537*, 269-274.

[22] A. Gholizadeh, S. Shahrokhian, A. Iraji zad, S. Mohajerzadeh, M. Vosoughi, S. Darbari, J. Koohsorkhi, M. Mehran, *Anal. Chem.* **2012**, *84*, 5932-5938.

[23] F. Tan, J. P. Metters, C. E. Banks, *Sens. Actuators, B* **2013**, *181*, 454-462.

[24] L. Soleymani, Z. Fang, X. Sun, H. Yang, B. J. Taft, E. H. Sargent, S. O. Kelley, *Angew. Chem., Int. Ed. Engl.* **2009**, *48*, 8457-8460.

[25] M. A. Nicolelis, D. Dimitrov, J. M. Carmena, R. Crist, G. Lehew, J. D. Kralik, S. P. Wise, *Proc. Natl. Acad. Sci. U. S. A.* **2003**, *100*, 11041-11046.

[26] S. Brinić, N. Vladislavić, M. Buzuk, M. Bralić, M. Šolić, *J. Electroanal. Chem.* **2013**, *705*, 86-90.

[27] I. Taurino, A. Magrez, F. Matteini, L. Forro, G. De Micheli, S. Carrara, *Nanoscale* **2013**, *5*, 12448-12455.

[28] S. Fletcher, M. D. Horne, *Electrochem. Commun.* **1999**, *1*, 502-512.

[29] D. W. Arrigan, *Analyst* **2004**, *129*, 1157-1165.

[30] R. M. Penner, C. R. Martin, *Anal. Chem.* **1987**, *59*, 2625-2630.

[31] L. Liu, N. Q. Jia, Q. Zhou, M. M. Yan, Z. Y. Jiang, *Mater. Sci. Eng., Proc. Conf.* **2007**, *27*, 57-60.

[32] Y. Bahari Mollamahalle, M. Ghorbani, A. Dolati, *Electrochim. Acta* **2012**, *75*, 157-163.

[33] W. S. Baker, R. M. Crooks, *J. Phys. Chem. B* **1998**, *102*, 10041-10046.

[34] E. Jeoung, T. H. Galow, J. Schotter, M. Bal, A. Ursache, M. T. Tuominen, C. M. Stafford, T. P. Russell, V. M. Rotello, *Langmuir* **2001**, *17*, 6396-6398.

[35] Y. Tu, Y. Lin, W. Yantasee, Z. Ren, *Electroanal.* **2005**, *17*, 79-84.

[36] A. Valsesia, P. Lisboa, P. Colpo, F. Rossi, *Anal. Chem.* **2006**, *78*, 7588-7591.

[37] H. He, S. P. Berglund, A. J. E. Rettie, W. D. Chemelewski, P. Xiao, Y. Zhang, C. B. Mullins, *J. Mater. Chem. A.* **2014**, *2*, 9371.

[38] H. S. Toh, C. Batchelor-McAuley, K. Tschulik, M. Uhlemann, A. Crossley, R. G. Compton, *Nanoscale* **2013**, *5*, 4884-4893.

[39] S. J. Cloake, H. S. Toh, P. T. Lee, C. Salter, C. Johnston, R. G. Compton, *ChemistryOpen* **2015**, *4*, 22-26.

[40] S. Disch, E. Wetterskog, R. P. Hermann, D. Korolkov, P. Busch, P. Boesecke, O. Lyon, U. Vainio, G. Salazar-Alvarez, L. Bergstrom, T. Bruckel, *Nanoscale* **2013**, *5*, 3969-3975.

[41] I. Streeter, R. Baron, R. G. Compton, *J. Phys. Chem. C.* **2007**, *111*, 17008-17014.

[42] I. Streeter, R. G. Compton, *J. Phys. Chem. C.* **2007**, *111*, 18049-18054.

[43] N. Godino, X. Borrisé, F. X. Muñoz, F. J. del Campo, R. G. Compton, *J. Phys. Chem. C.* **2009**, *113*, 11119-11125.

[44] T. V. Kármán, *Z. Angew. Math. Mech.* **1921**, *1*, 233-252.

[45] W. G. Cochran, S. Goldstein, *Math. Proc. Cambridge Philos. Soc.* **2008**, *30*, 365.

[46] J. Koutecky, B. G. Levich, *Zh. Fiz. Khim.* **1958**, *32*, 1565-1575.

[47] B. Soucaze-Guillous, W. Kutner, *Electroanal.* **1997**, *9*, 32-39.

[48] W. J. Albery, C. M. A. Brett, *J. Electroanal. Chem. Interfacial Electrochem.* **1983**, *148*, 201-210.

[49] SCENIHR, Opinion on the Scientific Basis for the Definition of the Term "Nanomaterial", European Union, **2010**.

[50] V. K. Sharma, J. Filip, R. Zboril, R. S. Varma, *Chem. Soc. Rev.* **2015**, *44*, 8410-8423.

[51] S. Wagner, A. Gondikas, E. Neubauer, T. Hofmann, F. von der Kammer, *Angew. Chem., Int. Ed. Engl.* **2014**, *53*, 12398-12419.

[52] N. Strambeanu, L. Demetrovici, D. Dragos, *Nanoparticles' Promises and Risks*, Springer, Switzerland, **2015**.

[53] Z. Shi, *J. Geophys. Res.* **2005**, *110*.

[54] S. Foss Hansen, B. H. Larsen, S. I. Olsen, A. Baun, *Nanotoxicology* **2009**, *1*, 243-250.

[55] P. Zhao, N. Li, D. Astruc, *Coord. Chem. Rev.* **2013**, *257*, 638-665.

[56] B. G. Trewyn, Slowing, II, S. Giri, H. T. Chen, V. S. Lin, *Acc. Chem. Res.* **2007**, *40*, 846-853.

[57] S. Baruah, J. Dutta, *Sci. Technol. Adv. Mater.* **2011**, *12*, 013004.

[58] Z. Z. Fang, X. Wang, T. Ryu, K. S. Hwang, H. Y. Sohn, *Int. J. Refract. Met. Hard Mater.* **2009**, *27*, 288-299.

[59] J. Chen, B. Lim, E. P. Lee, Y. Xia, *Nano Today* **2009**, *4*, 81-95.

[60] X.-q. Li, D. W. Elliott, W.-x. Zhang, *Crit. Rev. Solid State Mater. Sci.* **2006**, *31*, 111-122.

[61] A. C. Balazs, T. Emrick, T. P. Russell, *Science* **2006**, *314*, 1107-1110.

[62] P. H. C. Camargo, K. G. Satyanarayana, F. Wypych, *Mater. Res. (Sao Carlos, Braz.)* **2009**, *12*, 1-39.

[63] K. A. Willets, R. P. Van Duyne, *Annu. Rev. Phys. Chem.* **2007**, *58*, 267-297.

[64] U. Resch-Genger, M. Grabolle, S. Cavaliere-Jaricot, R. Nitschke, T. Nann, *Nat. Methods* **2008**, *5*, 763-775.

[65] Y. Zhang, Y. Chen, P. Westerhoff, J. Crittenden, *Water Res.* **2009**, *43*, 4249-4257.

[66] E. E. L. Tanner, K. Tschulik, R. Tahany, K. Jurkschat, C. Batchelor-McAuley, R. G. Compton, *J. Phys. Chem. C.* **2015**, *119*, 18808-18815.

[67] Z. Li, K. Greden, P. J. Alvarez, K. B. Gregory, G. V. Lowry, *Environ. Sci. Technol.* **2010**, *44*, 3462-3467.

[68] J. Henry, A. Anand, M. Chowdhury, G. Cote, R. Moreira, T. Good, *Anal. Biochem.* **2004**, *334*, 1-8.

[69] J. J. Storhoff, R. Elghanian, R. C. Mucic, C. A. Mirkin, R. L. Letsinger, *J. Am. Chem. Soc.* **1998**, *120*, 1959-1964.

[70] T. A. Taton, *Science* **2000**, *289*, 1757-1760.

[71] P. L. Stiles, J. A. Dieringer, N. C. Shah, R. P. Van Duyne, *Annu. Rev. Anal. Chem.* **2008**, *1*, 601-626.

[72] A. Nel, T. Xia, L. Madler, N. Li, *Science* **2006**, *311*, 622-627.

[73] *Nanoparticles in Translational Science and Medicine, Vol. 104*, Elsevier, London, UK, **2011**.

[74] M. J. Mulvihill, S. E. Habas, I. Jen-La Plante, J. Wan, T. Mokari, *Chem. Mater.* **2010**, *22*, 5251-5257.

[75] S. Hirn, M. Semmler-Behnke, C. Schleh, A. Wenk, J. Lipka, M. Schaffler, S. Takenaka, W. Moller, G. Schmid, U. Simon, W. G. Kreyling, *Eur. J. Pharm. Biopharm.* **2011**, *77*, 407-416.

[76] J. Lim, S. P. Yeap, H. X. Che, S. C. Low, *Nanoscale Res. Lett.* **2013**, *8*, 381.

[77] Malvern.com, Zetasizer Nano S, **2016**, http://www.malvern.com/en/products/product-range/zetasizer-range/zetasizer-nano-range/zetasizer-nano-s/default.aspx

[78] M. Kaszuba, D. McKnight, M. T. Connah, F. K. McNeil-Watson, U. Nobbmann, *J. Nanopart. Res.* **2007**, *10*, 823-829.

[79] H. C. van de Hulst, *Light Scattering by Small Particles*, Dover Publications, New York, **1957**.

[80] V. Filipe, A. Hawe, W. Jiskoot, *Pharm. Res.* **2010**, *27*, 796-810.

[81] A. Malloy, B. Carr, *Part. Part. Syst. Charact.* **2006**, *23*, 197-204.

[82] Malvern.com, Nanoparticle Tracking Analysis, **2016**, http://www.malvern.com/en/products/technology/nanoparticle-tracking-analysis/

[83] D. F. Swinehart, *J. Chem. Educ.* **1962**, *39*, 333.

[84] L. B. Scaffardi, N. Pellegri, O. d. Sanctis, J. O. Tocho, *Nanotechnology* **2005**, *16*, 158-163.

[85] X. Huang, M. A. El-Sayed, *J. Adv. Res.* **2010**, *1*, 13-28.

[86] *UV-Vis and Photoluminescence Spectroscopy for Nanomaterials Characterization*, Springer, New York, **2013**.

[87] G. Mie, *Ann. Phys.* **1908**, *25*, 377-445.

[88] Y. A. Akimov, *Plasmonics* **2012**, *7*, 495-500.

[89] P. K. Jain, K. S. Lee, I. H. El-Sayed, M. A. El-Sayed, *J. Phys. Chem. B.* **2006**, *110*, 7238-7248.

[90] R. Kanjanawarut, B. Yuan, S. XiaoDi, *Nucleic Acid Ther.* **2013**, *23*, 273-280.

[91] E. Ringe, J. M. McMahon, K. Sohn, C. Cobley, Y. Xia, J. Huang, G. C. Schatz, L. D. Marks, R. P. Van Duyne, *J. Phys. Chem. C.* **2010**, *114*, 12511-12516.

[92] B. J. Plowman, N. P. Young, C. Batchelor-McAuley, R. G. Compton, *Angew. Chem., Int. Ed. Engl.* **2016**, *55*, 7002-7005.

[93] R. Jin, Y. Cao, C. A. Mirkin, K. L. Kelly, G. C. Schatz, J. G. Zheng, *Science* **2001**, *294*, 1901-1903.

[94] P. Sarkar, D. K. Bhui, H. Bar, G. P. Sahoo, S. Samanta, S. Pyne, A. Misra, *Nanoscale Res. Lett.* **2010**, *5*, 1611-1618.

[95] H. Chen, L. Shao, Q. Li, J. Wang, *Chem. Soc. Rev.* **2013**, *42*, 2679-2724.

[96] W. Haiss, N. T. Thanh, J. Aveyard, D. G. Fernig, *Anal. Chem.* **2007**, *79*, 4215-4221.

[97] X. Liu, M. Atwater, J. Wang, Q. Huo, *Colloids Surf., B* **2007**, *58*, 3-7.

[98] S. He, J. Yao, P. Jiang, D. Shi, H. Zhang, S. Xie, S. Pang, H. Gao, *Langmuir* **2001**, *17*, 1571-1575.

[99] D. Li, R. B. Kaner, *J. Am. Chem. Soc.* **2006**, *128*, 968-975.

[100] A. M. Alkilany, C. J. Murphy, *J. Nanopart. Res.* **2010**, *12*, 2313-2333.

[101] H. C. Hamaker, *Physica* **1937**, *4*, 1058-1072.

[102] S. V. Sokolov, K. Tschulik, C. Batchelor-McAuley, K. Jurkschat, R. G. Compton, *Anal. Chem.* **2015**, *87*, 10033-10039.

[103] T. Sakura, T. Takahashi, K. Kataoka, Y. Nagasaki, *Colloid Polym. Sci.* **2005**, *284*, 97-101.

[104] R. A. Sperling, W. J. Parak, *Philos. Trans. R. Soc., A* **2010**, *368*, 1333-1383.

[105] N. T. K. Thanh, L. A. W. Green, *Nano Today* **2010**, *5*, 213-230.

[106] A. Nelson, T. Cosgrove, *Langmuir* **2004**, *20*, 10382-10388.

[107] J. D. Clogston, A. K. Patri, *Methods Mol. Biol.* **2011**, *697*, 63-70.

[108] Y. Zeng, S. Grandner, C. L. P. Oliveira, A. F. Thünemann, O. Paris, J. S. Pedersen, S. H. L. Klapp, R. von Klitzing, *Soft Matter* **2011**, *7*, 10899.

[109] A. Carlsson, A. Puig-Molina, T. V. Janssens, *J. Phys. Chem. B.* **2006**, *110*, 5286-5293.

[110] D. B. Williams, C. B. Carter, Springer, New York, **2009**.

[111] C. E. Lyman, D. E. Newbury, J. Goldstein, D. B. Williams, A. D. Romig, J. Armstrong, P. Echlin, C. Fiori, D. C. Joy, E. Lifshin, K.-R. Peters, *Scanning Electron Microscopy, X-Ray Microanalysis and Analytical Electron Microscopy: A Laboratory Workbook*, Plenum Press, New York and London, **1990**.

[112] K. D. Vernon-Parry, *III-Vs Review* **2000**, *13*, 40-44.

[113] F. Houdellier, L. de Knoop, C. Gatel, A. Masseboeuf, S. Mamishin, Y. Taniguchi, M. Delmas, M. Monthioux, M. J. Hytch, E. Snoeck, *Ultramicroscopy* **2015**, *151*, 107-115.

[114] Anderson Materials Evaluation, SEM Illustriative Example: Secondary Electron and Backscatter Electron Images, **2016**, http://www.andersonmaterials.com/sem/sem-secondary-backscatter-images.html

[115] D. E. Newbury, N. W. M. Ritchie, *J. Anal. At. Spectrom.* **2013**, *28*, 973.

[116] K. Shimizu, S. V. Sokolov, R. G. Compton, *Colloids Interface Sci. Commun.* **2016**, *13*, 19-22.

[117] R. Henderson, *Q. Rev. Biophys.* **2009**, *28*, 171.

[118] S. E. Kleijn, S. C. Lai, M. T. Koper, P. R. Unwin, *Angew. Chem., Int. Ed. Engl.* **2014**, *53*, 3558-3586.

[119] F. W. Campbell, R. G. Compton, *Anal. Bioanal. Chem.* **2009**, *396*, 241-259.

[120] F. J. Vidal-Iglesias, R. M. Arán-Ais, J. Solla-Gullón, E. Herrero, J. M. Feliu, *ACS Catal.* **2012**, *2*, 901-910.

[121] N. A. Kolpakova, Y. A. Oskina, E. N. Dyachenko, A. Y. Pshenichkin, *Procedia Chem.* **2015**, *15*, 335-341.

[122] S. E. Ward Jones, F. W. Campbell, R. Baron, L. Xiao, R. G. Compton, *J. Phys. Chem. C* **2008**, *112*, 17820-17827.

[123] X. F. Zhou, W. Cheng, C. Batchelor-Mcauley, K. Tschulik, R. G. Compton, *Electroanalysis* **2014**, *26*, 248-253.

[124] B. J. Plowman, B. Sidhureddy, S. V. Sokolov, N. P. Young, A. Chen, R. G. Compton, *ChemElectroChem* **2016**.

[125] J. Ghilane, F. R. Fan, A. J. Bard, N. Dunwoody, *Nano Lett* **2007**, *7*, 1406-1412.

[126] M. Giovanni, A. Ambrosi, M. Pumera, *Chem. Asian. J* **2012**, *7*, 702-706.

[127] A. Henglein, *J. Phys. Chem.* **1993**, *97*, 5457-5471.

[128] S. E. Ward Jones, F. G. Chevallier, C. A. Paddon, R. G. Compton, *Anal Chem* **2007**, *79*, 4110-4119.

[129] H. S. Toh, K. Jurkschat, R. G. Compton, *Chem. - Eur. J.* **2015**, *21*, 2998-3004.

[130] H. S. Toh, C. Batchelor-McAuley, K. Tschulik, R. G. Compton, *Sci. China: Chem.* **2014**, *57*, 1199-1210.

[131] T. Romih, S. B. Hočevar, A. Jemec, D. Drobne, *Electrochim. Acta* **2016**, *188*, 393-397.

[132] F. Zhou, M. Lu, W. Wang, Z. P. Bian, J. R. Zhang, J. J. Zhu, *Clin. Chem.* **2010**, *56*, 1701-1707.

[133] K. Micka, *Collect. Czech. Chem. Commun.* **1957**, *22*, 1400-1410.

[134] M. Heyrovský, J. Jirkovský, M. Štruplová-Bartáčková, *Langmuir* **1995**, *11*, 4300-4308.

[135] M. Heyrovský, J. Jirkovský, M. Štruplová-Bartáčková, *Langmuir* **1995**, *11*, 4309-4312.

[136] M. Heyrovský, J. Jirkovský, B. R. Müller, *Langmuir* **1995**, *11*, 4293-4299.

[137] X. Xiao, A. J. Bard, *J. Am. Chem. Soc.* **2007**, *129*, 9610-9612.

[138] H. S. Ahn, A. J. Bard, *Angew. Chem., Int. Ed. Engl.* **2015**, *54*, 13753-13757.

[139] X. Xiao, S. Pan, J. S. Jang, F. R. F. Fan, A. J. Bard, *J. Phys. Chem. C.* **2009**, *113*, 14978-14982.

[140] H. Zhou, F. R. F. Fan, A. J. Bard, *J. Phys. Chem. Lett.* **2010**, *1*, 2671-2674.

[141] Y. G. Zhou, N. V. Rees, R. G. Compton, *Angew. Chem., Int. Ed. Engl.* **2011**, *50*, 4219-4221.

[142] B. Haddou, N. V. Rees, R. G. Compton, *Phys. Chem. Chem. Phys.* **2012**, *14*, 13612-13617.

[143] D. Qiu, S. Wang, Y. Zheng, Z. Deng, *Nanotechnology* **2013**, *24*, 505707.

[144] Y. G. Zhou, N. V. Rees, J. Pillay, R. Tshikhudo, S. Vilakazi, R. G. Compton, *Chem. Commun.* **2012**, *48*, 224-226.

[145] K. Tschulik, B. Haddou, D. Omanović, N. V. Rees, R. G. Compton, *Nano Res.* **2013**, *6*, 836-841.

[146] W. Cheng, X. F. Zhou, R. G. Compton, *Angew. Chem., Int. Ed. Engl.* **2013**, *52*, 12980-12982.

[147] L. Sepunaru, K. Tschulik, C. Batchelor-McAuley, R. Gavish, R. G. Compton, *Biomater. Sci.* **2015**, *3*, 816-820.

[148] L. Sepunaru, B. J. Plowman, S. V. Sokolov, N. P. Young, R. G. Compton, *Chem. Sci.* **2016**.

[149] E. J. Stuart, K. Tschulik, C. Batchelor-McAuley, R. G. Compton, *ACS Nano* **2014**, *8*, 7648-7654.

[150] E. E. L. Tanner, C. Batchelor-McAuley, R. G. Compton, *J. Phys. Chem. C.* **2016**, *120*, 1959-1965.

[151] Y. G. Zhou, N. V. Rees, R. G. Compton, *Chem. Commun.* **2012**, *48*, 2510-2512.

[152] L. R. Holt, B. J. Plowman, N. P. Young, K. Tschulik, R. G. Compton, *Angew. Chem., Int. Ed. Engl.* **2016**, *55*, 397-400.

[153] E. N. Saw, V. Grasmik, C. Rurainsky, M. Epple, K. Tschulik, *Faraday Discuss.* **2016**.

[154] Y. G. Zhou, B. Haddou, N. V. Rees, R. G. Compton, *Phys. Chem. Chem. Phys.* **2012**, *14*, 14354-14357.

[155] J. Ellison, K. Tschulik, E. J. Stuart, K. Jurkschat, D. Omanovic, M. Uhlemann, A. Crossley, R. G. Compton, *ChemistryOpen* **2013**, *2*, 69-75.

[156] S. V. Sokolov, E. Kätelhön, R. G. Compton, *J. Phys. Chem. C.* **2015**, *119*, 25093-25099.

[157] H. S. Toh, R. G. Compton, *ChemistryOpen* **2015**, *4*, 261-263.

[158] E. J. E. Stuart, N. V. Rees, J. T. Cullen, R. G. Compton, *Nanoscale* **2013**, *5*, 174-177.

[159] C. Batchelor-McAuley, J. Ellison, K. Tschulik, P. L. Hurst, R. Boldt, R. G. Compton, *Analyst* **2015**, *140*, 5048-5054.

[160] K. P. Johansson, A. P. Marchetti, G. L. McLendon, *J. Phys. Chem.* **1992**, *96*, 2873-2879.

[161] R. Jin, Y. C. Cao, E. Hao, G. S. Metraux, G. C. Schatz, C. A. Mirkin, *Nature* **2003**, *425*, 487-490.

[162] T. R. Bartlett, C. Batchelor-McAuley, K. Tschulik, K. Jurkschat, R. G. Compton, *ChemElectroChem* **2015**, *2*, 522-528.

[163] T. R. Bartlett, S. V. Sokolov, R. G. Compton, *ChemistryOpen* **2015**, *4*, 600-605.

[164] P. Wang, B. Huang, X. Qin, X. Zhang, Y. Dai, J. Wei, M. H. Whangbo, *Angew. Chem., Int. Ed. Engl.* **2008**, *47*, 7931-7933.

[165] A. Luz, C. Feldmann, *J. Mater. Chem.* **2009**, *19*, 8107.

[166] A. Luz, A. Malek-Luz, C. Feldmann, *Chem. Mater.* **2013**, *25*, 202-209.

[167] S. Fugleberg, in *The Finnish Environment*, 315 ed. (Ed.: M. Riekkola-Vanhanen), Finnish Environmental Institute, **1999**, pp. 13-14.

[168] G.-R. Sheu, R. Mason, *J. Atmos. Chem.* **2004**, *48*, 107-130.

[169] P.-R. Kim, Y.-J. Han, T. M. Holsen, S.-M. Yi, *Atmos. Environ.* **2012**, *61*, 94-102.

[170] M. Husein, E. Rodil, J. H. Vera, *J. Colloid Interface Sci.* **2004**, *273*, 426-434.

[171] M. Husein, E. Rodil, J. Vera, *Langmuir* **2003**, *19*, 8467-8474.

[172] C. Ravikumar, S. K. Singh, R. Bandyopadhyaya, *J. Phys. Chem. C* **2010**, *114*, 8806-8813.

[173] G. Loget, T. C. Lee, R. W. Taylor, S. Mahajan, O. Nicoletti, S. T. Jones, R. J. Coulston, V. Lapeyre, P. Garrigue, P. A. Midgley, O. A. Scherman, J. J. Baumberg, A. Kuhn, *Small* **2012**, *8*, 2698-2703.

[174] M. Ray, S. Paria, *Ind. Eng. Chem. Res.* **2011**, *50*, 11601-11607.

[175] N. V. Rees, *Electrochem. Commun.* **2014**, *43*, 83-86.

[176] M. Pumera, *ACS Nano* **2014**, *8*, 7555-7558.

[177] W. Kemula, Z. Galus, Z. Kublik, *Nature* **1958**, *182*, 1228-1229.

[178] M. A. Nolan, S. P. Kounaves, *Anal. Chem.* **1999**, *71*, 1176-1182.

[179] D. Jagner, E. Sahlin, L. Renman, *Anal. Chem.* **1996**, *68*, 1616-1622.

[180] R. Bilewicz, Z. Stojek, Z. Kublik, *J. Electroanal. Chem. Interfacial Electrochem.* **1979**, *96*, 29-44.

[181] E. I. Rogers, B. Šljukic, C. Hardacre, R. G. Compton, *J. Chem. Eng. Data* **2009**, *54*, 2049-2053.

[182] K. R. Wehmeyer, R. M. Wightman, *Anal. Chem.* **1985**, *57*, 1989-1993.

[183] Y. Wang, J. G. Limon-Petersen, R. G. Compton, *J. Electroanal. Chem.* **2011**, *652*, 13-17.

[184] E. J. E. Stuart, K. Tschulik, D. Omanović, J. T. Cullen, K. Jurkschat, A. Crossley, R. G. Compton, *Nanotechnology* **2013**, *24*.

[185] A. B. Garrett, M. V. Noble, S. Miller, *J. Chem. Educ.* **1942**, *19*, 485.

[186] E. J. E. Stuart, Y. G. Zhou, N. V. Rees, R. G. Compton, *RSC Adv.* **2012**, *2*, 6879-6884.

[187] Dissanayake, *Solid State Physics-2: Proceedings*, Nova Biomedical, **1991**.

[188] E. H. Boult, H. R. Thirsk, *Trans. Faraday Soc.* **1954**, *50*, 404-412.

[189] N. J. Calos, C. H. L. Kennard, R. L. Davis, *Zeitschrift für Kristallographie* **1989**, *187*, 305-307.

[190] *Handbook of Chemistry and Physics*, 55 ed., CRC Press, **1974**.

[191] A. Serruya, J. Mostany, B. R. Scharifker, *J. Electroanal. Chem.* **1999**, *464*, 39-47.

[192] R. Dasari, D. A. Robinson, K. J. Stevenson, *J. Am. Chem. Soc.* **2013**, *135*, 570-573.

[193] R. Dasari, B. Walther, D. A. Robinson, K. J. Stevenson, *Langmuir* **2013**, *29*, 15100-15106.

[194] R. Dasari, K. Tai, D. A. Robinson, K. J. Stevenson, *ACS Nano* **2014**, *8*, 4539-4546.

[195] V. Filipe, A. Hawe, W. Jiskoot, *Pharm. Res.* **2010**, *27*, 796-810.

[196] C. Finder, M. Wohlgemuth, C. Mayer, *Part. Part. Syst. Charact.* **2004**, *21*, 372-378.

[197] Y. G. Zhou, N. V. Rees, R. G. Compton, *Chem. Phys. Lett.* **2011**, *514*, 291-293.

[198] N. V. Rees, Y. G. Zhou, R. G. Compton, *ChemPhyChem* **2011**, *12*, 1645-1647.

[199] S. S. Sokolov, C. Batchelor-McAuley, K. Tschulik, S. Fletcher, R. G. Compton, *Chem. - Eur. J.* **2015**, *21*, 10741-10746.

[200] A. G. Brolo, S. D. Sharma, *Electrochim. Acta* **2003**, *48*, 1375-1384.

[201] H. S. Toh, C. Batchelor-McAuley, K. Tschulik, R. G. Compton, *Analyst* **2013**, *138*, 4292-4297.

[202] K. Tschulik, C. Batchelor-McAuley, H. S. Toh, E. J. Stuart, R. G. Compton, *Phys. Chem. Chem. Phys.* **2014**, *16*, 616-623.

[203] T. R. Bartlett, S. V. Sokolov, J. Holter, N. Young, R. G. Compton, *Chem. - Eur. J.* **2016**, *22*, 7408-7414.

[204] L. V. Stebounova, E. Guio, V. H. Grassian, *J. Nanopart. Res.* **2010**, *13*, 233-244.

[205] D. J. Srolovitz, M. G. Goldiner, *JOM* **1995**, *47*, 31-36.

[206] C. Levard, E. M. Hotze, G. V. Lowry, G. E. Brown, Jr., *Environ. Sci. Technol.* **2012**, *46*, 6900-6914.

[207] P. J. Vikesland, A. M. Heathcock, R. L. Rebodos, K. E. Makus, *Environ. Sci. Technol.* **2007**, *41*, 5277-5283.

[208] S. Elzey, V. H. Grassian, *J. Nanopart. Res.* **2009**, *12*, 1945-1958.

[209] E. M. Hotze, T. Phenrat, G. V. Lowry, *J. Environ. Qual.* **2010**, *39*, 1909.

[210] J. V. Alemán, A. V. Chadwick, J. He, M. Hess, K. Horie, R. G. Jones, P. Kratochvíl, I. Meisel, I. Mita, G. Moad, S. Penczek, R. F. T. Stepto, *Pure Appl. Chem.* **2007**, *79*.

[211] K. Tschulik, R. G. Compton, *Phys. Chem. Chem. Phys.* **2014**, *16*, 13909-13913.

[212] D. Zhou, S. W. Bennett, A. A. Keller, *PLoS One* **2012**, *7*, e37363.

[213] A. Teleki, R. Wengeler, L. Wengeler, H. Nirschl, S. E. Pratsinis, *Powder Technol.* **2008**, *181*, 292-300.

[214] T. R. Bartlett, J. Holter, N. Young, R. G. Compton, *Nanoscale* **2016**.

[215] A. M. Espinosa, M. T. San José, M. L. Tascón, M. D. Vászquez, P. Sánchez Batanero, *Electrochim. Acta* **1991**, *36*, 1561-1571.

[216] G. H. Hwang, W. K. Han, S. J. Kim, S. J. Hong, J. S. Park, H. J. Park, S. G. Kang, *J Ceram Process Res* **2009**, *10*, 190-194.

[217] S. K. Blower, C. Greaves, *Acta Crystallogr., Sect. C: Cryst. Struct. Commun.* **1988**, *44*, 587-589.

[218] J. M. Kahk, N. V. Rees, J. Pillay, R. Tshikhudo, S. Vilakazi, R. G. Compton, *Nano Today* **2012**, *7*, 174-179.

[219] I. Puigdomenech, MEDUSA, avaliable from: https://www.kth.se/en/che/medusa/downloads-1.3865254

[220] M. Murphy, K. Ting, X. Zhang, C. Soo, Z. Zheng, *Am. J. Nanomater.* **2015**, *2015*, 1-12.

[221] N. L. Pacioni, C. D. Borsarelli, V. Rey, A. V. Veglia, *Synthetic Routes for the Preparation of Silver Nanoparticles*, Springer International Publishing, Switzerland, **2015**.

[222] C. B. Murray, C. R. Kagan, M. G. Bawendi, *Annu. Rev. Mater. Sci.* **2000**, *30*, 545-610.

[223] H. Hiramatsu, F. E. Osterloh, *Chem. Mater.* **2004**, *16*, 2509-2511.

[224] J. Eastoe, M. J. Hollamby, L. Hudson, *Adv. Colloid Interface Sci.* **2006**, *128-130*, 5-15.

[225] A. A. Isse, S. Gottardello, C. Maccato, A. Gennaro, *Electrochem. Commun.* **2006**, *8*, 1707-1712.

[226] V. K. LaMer, R. H. Dinegar, *J. Am. Chem. Soc.* **1950**, *72*, 4847-4854.

[227] Y. De Smet, L. Deriemaeker, R. Finsy, *Langmuir* **1997**, *13*, 6884-6888.

[228] H. Y. Zhu, Y. Lan, X. P. Gao, S. P. Ringer, Z. F. Zheng, D. Y. Song, J. C. Zhao, *J. Am. Chem. Soc.* **2005**, *127*, 6730-6736.

[229] Z. Tang, Y. Wang, K. Sun, N. A. Kotov, *Adv. Mater.* **2005**, *17*, 358-363.

[230] A. Król-Gracz, E. Michalak, P. M. Nowak, A. Dyonizy, *Cent. Eur. J. Chem.* **2011**, *9*, 982-989.

[231] A. Król-Gracz, P. Nowak, E. Michalak, A. Dyonizy, *Acta Phys. Pol., A* **2012**, *121*, 196.

[232] T. B. Brill, Plenum Press, New York, **1980**, p. 258.

[233] D. Paramelle, A. Sadovoy, S. Gorelik, P. Free, J. Hobley, D. G. Fernig, *Analyst* **2014**, *139*, 4855.

[234] A. W. Kenchington, *Biochem. J.* **1957**, *68*, 458-468.

[235] T. R. Bartlett, R. G. Compton, *Russ. J. Electrochem.* **2016**.

[236] J. J. Mock, M. Barbic, D. R. Smith, D. A. Schultz, S. Schultz, *J. Chem. Phys.* **2002**, *116*, 6755.

[237] K. L. Kelly, E. Coronado, L. L. Zhao, G. C. Schatz, *J. Phys. Chem. B.* **2003**, *107*, 668-677.

[238] A. Albanese, P. S. Tang, W. C. Chan, *Annu. Rev. Biomed. Eng.* **2012**, *14*, 1-16.

[239] A. K. Singh, D. Senapati, A. Neely, G. Kolawole, C. Hawker, P. C. Ray, *Chem. Phys. Lett.* **2009**, *481*, 94-98.

[240] J. Nelayah, M. Kociak, O. Stephan, N. Geuquet, L. Henrard, F. J. Garcia de Abajo, I. Pastoriza-Santos, L. M. Liz-Marzan, C. Colliex, *Nano Lett.* **2010**, *10*, 902-907.

[241] N. L. Gruenke, M. F. Cardinal, M. O. McAnally, R. R. Frontiera, G. C. Schatz, R. P. Van Duyne, *Chem. Soc. Rev.* **2016**.

[242] M. M. Shahjamali, M. Salvador, M. Bosman, D. S. Ginger, C. Xue, *J. Phys. Chem. C.* **2014**, *118*, 12459-12468.

[243] C. Xue, G. S. Metraux, J. E. Millstone, C. A. Mirkin, *J. Am. Chem. Soc.* **2008**, *130*, 8337-8344.

[244] W. Z. Ostwald, *Phys. Chem.* **1901**, *37*, 385.

[245] C. Xue, J. E. Millstone, S. Li, C. A. Mirkin, *Angew. Chem., Int. Ed. Engl.* **2007**, *46*, 8436-8439.

[246] X. Xu, M. B. Cortie, *Adv. Funct. Mater* **2006**, *16*, 2170-2176.

[247] A. I. Kirkland, D. A. Jefferson, D. G. Duff, P. P. Edwards, I. Gameson, B. F. G. Johnson, D. J. Smith, *Proc. R. Soc. A* **1993**, *440*, 589-609.

[248] X. C. Jiang, A. B. Yu, *Langmuir* **2008**, *24*, 4300-4309.

[249] S. Botasini, E. Méndez, *J. Nanopart. Res.* **2013**, *15*, 1526.

[250] W. Cheng, R. G. Compton, *Angew. Chem., Int. Ed. Engl.* **2014**, *53*, 13928-13930.

[251] S. V. Sokolov, T. R. Bartlett, P. Fair, S. Fletcher, R. G. Compton, *Anal. Chem.* **2016**.

[252] D. H. Hubel, *Science* **1957**, *125*, 549-550.

[253] R. B. Morris, D. J. Franta, H. S. White, *J. Phys. Chem.* **1987**, *91*, 3559-3564.

[254] R. G. Compton, G. G. Wildgoose, N. V. Rees, I. Streeter, R. Baron, *Chem. Phys. Lett.* **2008**, *459*, 1-17.

[255] M. Ongaro, P. Ugo, *Anal. Bioanal. Chem.* **2013**, *405*, 3715-3729.

[256] V. P. Menon, C. R. Martin, *Anal. Chem.* **1995**, *67*, 1920-1928.

[257] U. Hasse, F. Scholz, *J. Solid State Electrochem.* **2005**, *10*, 380-382.

[258] W. Cheng, S. Dong, E. Wang, *Anal. Chem.* **2002**, *74*, 3599-3604.

[259] X. Dai, R. G. Compton, *Electroanalysis* **2005**, *17*, 1325-1330.

[260] C. Batchelor-McAuley, C. E. Banks, A. O. Simm, T. G. Jones, R. G. Compton, *Analyst* **2006**, *131*, 106-110.

[261] X. Dai, R. G. Compton, *Analyst* **2006**, *131*, 516.

[262] K. E. Toghill, G. G. Wildgoose, A. Moshar, C. Mulcahy, R. G. Compton, *Electroanalysis* **2008**, *20*, 1731-1737.

[263] O. Ordeig, C. E. Banks, T. J. Davies, F. J. d. Campo, F. X. Muñoz, R. G. Compton, *Anal. Sci.* **2006**, *22*, 679-683.

[264] T. J. Davies, S. Ward-Jones, C. E. Banks, J. del Campo, R. Mas, F. X. Muñoz, R. G. Compton, *J. Electroanal. Chem.* **2005**, *585*, 51-62.

[265] T. J. Davies, R. G. Compton, *J. Electroanal. Chem.* **2005**, *585*, 63-82.

[266] C. M. Welch, C. E. Banks, A. O. Simm, R. G. Compton, *Anal. Bioanal. Chem.* **2005**, *382*, 12-21.

[267] J. Ustarroz, X. Ke, A. Hubin, S. Bals, H. Terryn, *J. Phys. Chem. C* **2012**, *116*, 2322-2329.

[268] T. P. Bigioni, X. M. Lin, T. T. Nguyen, E. I. Corwin, T. A. Witten, H. M. Jaeger, *Nat. Mater.* **2006**, *5*, 265-270.

[269] M. S. Kim, J. T. Park, S.-D. Kim, H. S. Yoon, J. C. Lee, J. S. Sohn, *ECS Trans.* **2007**, *3*, 13-21.

[270] F. Duan, J. Guojun, *Introduction to Condensed Matter Physics, Vol. 1*, World Scientific, Singapore, **2005**.

[271] F. W. Campbell, S. R. Belding, R. Baron, L. Xiao, R. G. Compton, *J. Phys. Chem. C* **2009**, *113*, 9053-9062.

[272] M. Honda, T. Kodera, H. Kita, *Electrochim. Acta* **1986**, *31*, 377-383.

[273] M. Honda, T. Kodera, H. Kita, *Electrochim. Acta* **1983**, *28*, 727-733.

[274] T. Hurlen, Y. L. Sandler, E. A. Pantier, *Electrochim. Acta* **1966**, *11*, 1463-1473.

[275] E. Tomaszewska, K. Soliwoda, K. Kadziola, B. Tkacz-Szczesna, G. Celichowski, M. Cichomski, W. Szmaja, J. Grobelny, *J. Nanomater.* **2013**, *2013*, 1-10.

[276] E. Kätelhön, R. G. Compton, *Chem. Sci.* **2014**, *5*, 4592-4598.

[277] J. Ellison, C. Batchelor-Mcauley, K. Tschulik, R. G. Compton, *Sens. Actuators, B* **2014**, *200*, 47-52.

[278] J. J. Yoo, J. Kim, R. M. Crooks, *Chem. Sci.* **2015**, *6*, 6665-6671.

[279] D. A. Robinson, J. J. Yoo, A. D. Castaneda, B. Gu, R. Dasari, R. M. Crooks, K. J. Stevenson, *ACS Nano* **2015**, *9*, 7583-7595.

[280] J. Albery, *Electrode Kinetics* Oxford University Press, **1975**.

[281] S. V. Sokolov, E. Kätelhön, R. G. Compton, *J. Phys. Chem. C.* **2016**, *120*, 10629-10640.

[282] Y. V. Pleskov, V. Y. Filinovskii, *The rotating disk electrode*, New York: Consultants Bureau, **1976**.

[283] J. J. Roberts, J. A. Westgard, L. M. Cooper, R. W. Murray, *J. Am. Chem. Soc.* **2014**, *136*, 10783-10789.

[284] T. Noyhouzer, D. Mandler, *Electroanal.* **2013**, *25*, 109-115.

[285] H. Deng, G. J. V. Berkel, *Electroanal.* **1999**, *11*, 857-865.

[286] T. M. Alligrant, M. J. Anderson, R. Dasari, K. J. Stevenson, R. M. Crooks, *Langmuir* **2014**, *30*, 13462-13469.

[287] S. G. Weber, *Anal. Chem.* **1989**, *61*, 295-302.

[288] R. C. Matos, M. A. Augelli, C. L. Lago, L. Angnes, *Anal. Chim. Acta* **2000**, *404*, 151-157.

[289] J. S. Rossier, H. H. Girault, *Lab Chip* **2001**, *1*, 153-157.

[290] J. V. Macpherson, P. R. Unwin, *Anal. Chem.* **1998**, *70*, 2914-2921.

[291] J. Jiang, X. Huang, L. Wang, *J. Colloid Interface Sci.* **2016**, *467*, 158-164.

[292] J. C. Lees, J. Ellison, C. Batchelor-McAuley, K. Tschulik, C. Damm, D. Omanovic, R. G. Compton, *ChemPhysChem* **2013**, *14*, 3895-3897.